UNIVERSITY OF CALIFORNIA,
IRVINE

Ligand Effects on Kinetic and Thermodynamic Properties of Complexes of the Non-Traditional Rare-Earth (II) Ions

DISSERTATION

submitted in partial satisfaction of the requirements
for the degree of

DOCTOR OF PHILOSOPHY

in Chemistry

by

Samuel Alexander Moehring

Dissertation Committee:
Professor William J. Evans, Chair
Professor Andy S. Borovik
Professor Alan Heyduk

2019

DEDICATION

To the Triune God,

"Who alone possesses immortality and dwells in unapproachable light,
Whom no man has seen or can see,"
(1 Timothy 6:16)

Who is
"the God who made the world and all things in it,"
(Acts 17:24)

Who rightly spoke through the Preacher, that
"writing of many books is endless,
and excessive devotion to books is wearying to the body,"
(Ecclesiastes 12:12)

and through Solomon says
"The fear of the Lord is the beginning of wisdom,
And the knowledge of the Holy One is understanding;"
(Proverbs 9:10)

To Him who promises that
"at the name of Jesus every knee will bow,
of those who are in heaven and on earth and under the earth,
and that every tongue will confess that Jesus Christ is Lord,
to the glory of God the Father:"
(Philippians 2:10–11)

"To Him who sits on the throne, and to the Lamb,
be blessing and honor and glory and dominion forever and ever!"
(Revelation 5:13)

I ask, receive the work of my hands, which You have given me the means and strength to do,
as worship to You, that You may be glorified in my labor,
in anticipation of the Day when
"the elements will be destroyed with intense heat, and the earth and its works will be burned up,"
(2 Peter 3:10–12)

and when I will behold, as your servant John did,
by the grace of Our Lord Jesus Christ and His atoning death,
"a new heaven and a new earth; for the first heaven and the first earth passed away."
(Revelation 21:1, New American Standard Bible)

Come, Lord Jesus!

TABLE OF CONTENTS

LIST OF FIGURES

LIST OF TABLES

ACKNOWLEDGMENTS

My advisor and thesis chair, Prof. William Evans, has given me the gift of real mentorship and the tools to keep learning. What he has taught me (both by example and by instruction) will continue to guide my further efforts, both in my trade and my dealings with others.

My committee, namely Profs. Andy Borovik and Alan Heyduk, has played a crucial part of making me into the chemist I am now. Both of these professors have urged me onto greater mastery and higher standards than would have been possible without them.

My wife, Tiffany, has been a great help in many things, graduate school being one of them. She has been with me from the start to the finish, from the days of Quantum Mechanics homework in my first year, through my qualifying exams, and even now as I prepare this thesis. Enumerating her benefits and excellencies is simply impossible; if you consider this thesis to be the fruits of my effort, consider it to be hers as well.

My parents, the patrons of my education as well as my first educators, prepared me well for this work even from my earliest memories. Love is more than feeling, it is action. Theirs is tangible.

My mother-in-law's labors have fueled many hard days of work, as my colleagues can testify, and she has shown her support and affection through braised eggplant and fried rice.

My mentor at Pyramid Laboratories, Heather Sopher, was instrumental in developing a confidence and pride in my work. Her patience and skill cannot be underestimated, and I consider that I was well-prepared by her teaching for a productive graduate school experience.

The chemistry team at Trabuco Hills High School, namely Jay Camiling, Stacey Hamamura, and Kelli Gaines, solidified my trajectory into chemistry. I can recall, almost from my first weeks in chemistry, that I had found my vocation. Their enthusiasm for the discipline amplified mine and swung open the door to many satisfying days of synthesis.

Alice Elwell, my fifth- and sixth-grade teacher, had a crucial role in the early development of my academic life. Her tutelage turned a formerly-reluctant student into one who embraced hard work and the rewards that come with it. She truly taught me to be a scholar, even from an early age.

Pastor Dave Doyle, an elder at Kindred Community Church, catechized me and also imparted to me his mind-to-mind method of teaching and learning. His own scholarship and fruitful, mindful service of God was an encouragement of my own and a fitting example to follow.

My friends, Carter Jones and Valentine Bratoff contributed tools for my research (CJHUNT and matplotlib, respectively) that proved indispensable.

CURRICULUM VITAE

Samuel Alexander Moehring

Education

University of California, Irvine — June 2015 – December 2019
Ph.D.in Chemistry – Advisor: Prof. William J. Evans; GPA 4.0
Awards: Chancellor's Fellowship (2015–2017)

University of California, Berkeley, College of Chemistry — August 2009 – May 2012
Bachelor of Science in Chemistry; GPA 3.8
Honors: Magna Cum Laude

Experience

Evans Research Group – University of California, Irvine — June 2015 – December 2019
Graduate Student Researcher

- Designed and tested hypotheses in rare-earth metal +2 chemistry and evolved hypotheses using experimental data
- Synthesized inorganic and organometallic coordination compounds of the rare-earth metals using rigorously air- and moisture-free glove box and Schlenk line techniques
- Characterized compounds using various spectroscopies (NMR, EPR, UV-visible absorbance, IR), elemental analysis, and X-ray crystallography
- Purified organic, inorganic, and organometallic starting materials and prepared them for use in strictly air- and moisture-free environments
- Safely handled pyrophoric, flammable, toxic, and alpha-emitting materials on a daily basis
- Led installation of a Vacuum Atmospheres glove box with an Agilent ATR-FTIR inside for air-free IR spectroscopy
- Maintained Vacuum Atmospheres glove boxes and vacuum line systems in working order through proper use and repairs

Evans Research Group – University of California, Irvine — November 2017 – October 2019
Safety Representative

- Prepared RUA (Radiation Use Authorization) document to support usage of ^{238}U and ^{232}Th in DOE-supported research
- Liaised between Evans Group and Environmental Health and Safety department at the University
- Managed use of hazardous materials and procedures in the Evans Group by advising users on risk management, and hazardous material disposal
- Led a "safety moment" during weekly group meetings, a short discussion among group members about hazards pertinent to the Evans Group and provided recommendations for future risk prevention
- Briefed new researchers in the Evans Group regarding safety equipment in the laboratory and hazards unique to the Evans Group
- Optimized safety procedures by evaluating findings from yearly safety surveys of other research groups

Department of Chemistry – University of California, Irvine September 2015 – September 2016
June 2017– September 2019

Teaching Assistant

- For lecture courses:
  - Led collaborative problem-solving sessions with student presentations of solutions
  - Prepared and graded problem sets weekly for problem-solving sessions
  - Answered student questions via online discussion boards and email
  - Proofread, proctored, and graded exams
  - Courses taught: 1A, B, C (general chemistry), 216 (graduate organometallic chemistry)
- For laboratory courses
  - Led two four-hour laboratory sections per week
  - Demonstrated, modeled, and enforced laboratory safety and PPE practices
  - Graded lab reports weekly with feedback
  - Administered and graded practical final exams
  - Incorporated curriculum from lecture courses into laboratory experiments
  - Courses taught: 1LD (general chemistry laboratory), 51LB (organic chemistry laboratory)

PYRAMID Laboratories, Inc. – Costa Mesa, CA June 2012 – June 2015

Chemist I

- Analyzed raw materials, manufacturing water, API, and drug products using wet chemistry, chromatographic (LC and GC), spectroscopic, and other analytical chemistry methods in a GMP environment
- Developed and qualified HPLC methods for surfactant quantitation
- Updated analytical balance use SOP and created IQ/OQ/PQ protocols to comply with USP <41> requirements
- Coordinated with manufacturing staff to ensure prompt delivery of in-process and water testing results
- Qualified client methods for use in laboratory and reported results according to FDA guidelines
- Co-authored and revised SOPs for instrument use and maintenance
- Maintained and repaired analytical instruments (HPLCs, GCs, total organic carbon analyzer)
-

Publications and Presentations

- Moehring, S. A., Beltrán-Leiva, M. J., Páez-Hernández, D., Arratia-Pérez, R., Ziller, J. W., Evans, W. J. "Rare-Earth Metal (II) Aryloxides: Structure, Synthesis, and EPR Spectroscopy of [K(2.2.2-cryptand)][Sc($OC_6H_2{}^tBu_2$-2,6-Me-4)$_3$]," *Chemistry – A European Journal.* **2018**, *24*, 18059–18067. DOI: https://doi.org/10.1002/chem.201803807
- Moehring, S. A., Ziller, J. W., Evans, W. J. "Rare-Earth Complexes of the Asymmetric Amide Ligands, N($SiMe_3$)Ph and N($SiMe_3$)Cy," *Polyhedron*. **2019**, *168*, 72–79. DOI: https://doi.org/10.1016/j.poly.2019.04.026
- Moehring, S. A., Beltrán-Leiva, M. J., Páez-Hernández, D., Arratia-Pérez, R., Ziller, J. W., Evans, W. J. "Exploring Aryloxide Ligands in the Synthesis of Complexes of New +2 Ions of the Rare-Earth Metals." 256th ACS National Meeting & Exposition, Boston, MA, United States, August 19–23, 2018.

ABSTRACT OF THE DISSERTATION

Ligand Effects on Kinetic and Thermodynamic Properties of Complexes of the Non-Traditional Rare-Earth (II) Ions

By

Samuel Alexander Moehring

Doctor of Philosophy in Chemistry

University of California, Irvine, 2019

Professor William J. Evans, Chair

This dissertation details investigations into ligand effects on the non-traditional rare-earth(II) ions, *i.e.*, those with $4f^n5d^1$ electron configurations (as well as $3d^1$ Sc(II) and $4d^1$ Y(II)) instead of $4f^{n+1}$. Specifically, effects on kinetic stability and the reducing ability of complexes of these ions are explored as a function of ligand set and metal. Chapter 1 describes the synthesis and characterization of rare-earth(II) complexes of the aryloxide ligand 2,6-^{t}Bu$_2$-4-Me-C$_6$H$_2$O and sets forth the hypothesis that kinetic stability of rare-earth(II) compounds depends on the steric saturation of the metal center. Chapter 2 expands on the steric argument made in Chapter 1 by synthesizing Y(III) and Y(II) complexes of the bulky aryloxide 2,6,-(1-adamantyl)$_2$-4-^{t}Bu-C$_6$H$_2$O; the crystallographically-characterized Y(II) complex is kinetically stabilized compared to the thermally unstable Y(II) complex with 2,6-^{t}Bu$_2$-4-Me-C$_6$H$_2$O in Chapter 1, which is detected only spectroscopically. Chapter 3 reports the synthesis of rare-earth(III) compounds of the asymmetric amide ligands N(SiMe$_3$)R, where R = phenyl or cyclohexyl, which prove to be insufficiently sterically-saturating ligands for rare-earth(II) compound isolation. Chapter 4 compares the reducing power of Th(II) and U(II) complexes to Y(II) and La(II) complexes using

EPR spectroscopy. Chapter 5 continues these comparisons with a wider range of rare-earth (II) compounds, varying the metal involved as well as the ligand set, and also describes ligand exchange reactivity leading to EPR evidence for heteroleptic rare-earth (II) compounds.

INTRODUCTION

The rare-earth metals (abbreviated Ln; Sc, Y, and the lanthanides; excluding radioactive Pm for this work) are ubiquitous in both consumer and industrial applications, thanks to their unique properties. For example, compounds of Eu(III), Ce(III), and Tb(III) are used as phosphors in lighting and display technologies owing to their emission properties which are essentially matrix-independent.[1,2] This is possible because of one of the unique features of the lanthanides: their valence 4f electrons are radially contracted and do not extend past the inert gas electron configuration [Xe].[3] This leaves the electronic structure and thus optical transitions largely unperturbed by crystal field effects, leading to the insensitivity of the lanthanide(III) emission spectra to the lattice the ions are contained in. This insensitivity to crystal field effects also leads to the 4f orbitals being essentially degenerate in energy, which means that the orbital angular momentum is not quenched by crystal-field induced orbital energy splitting as it is in transition metals.[3–7] *L*-*S* coupling thus leads to large values of *J* and high magnetic moments, which enables the use of the lanthanides in applications requiring strong magnetism such as in wind turbine generators.[8] In fact, $Nd_2Fe_{14}B$ is the strongest permanent magnet known.[8]

All of these these properties are representative of the +3 oxidation state, which is the most stable for all of the Ln.[9] The +4 oxidation state is known for Ce[10] and Tb[11,12] in molecular complexes and for Pr[13] in solid-state materials; oxidation of Ce(III) to Ce(IV) is used in the separation of Ce from other Ln in their ores.[14] The +2 oxidation state is known for all the lanthanides. One class of these +2 ions, the "traditional" set, Sm(II), Eu(II), Tm(II), and Yb(II),[15] have electron configurations $4f^{n+1}$, where $4f^n$ is the electron configuration of the corresponding +3 ion. Compounds of these ions were the first Ln(II) compounds discovered and find their use in a

variety of organic transformations.[16,17] Furthermore, the accessibility of the Eu(III/II) redox couple (−0.35 V vs SHE)[15,18] in water is a key step in the separation of Eu from other Ln[14].

Another set of "non-traditional" Ln(II) ions, Sc(II), Y(II), La(II), Ce(II), Pr(II), Gd(II), Tb(II), Ho(II), Er(II), and Lu(II), have electron configurations approximated as $4f^n5d^1$ for the lanthanides with $3d^1$ Sc(II) and $4d^1$ Y(II). This discovery of these oxidation states was made after experiments where reduction of Ln(III) starting materials under a dinitrogen atmosphere led to the reduction of N_2 to compounds containing the reduced dinitrogen moieties $(N_2)^{2-}$ and $(N_2)^{3-}$, eq 1, where OAr = 2,6-^{t}Bu$_2$C$_6$H$_2$O. [19]

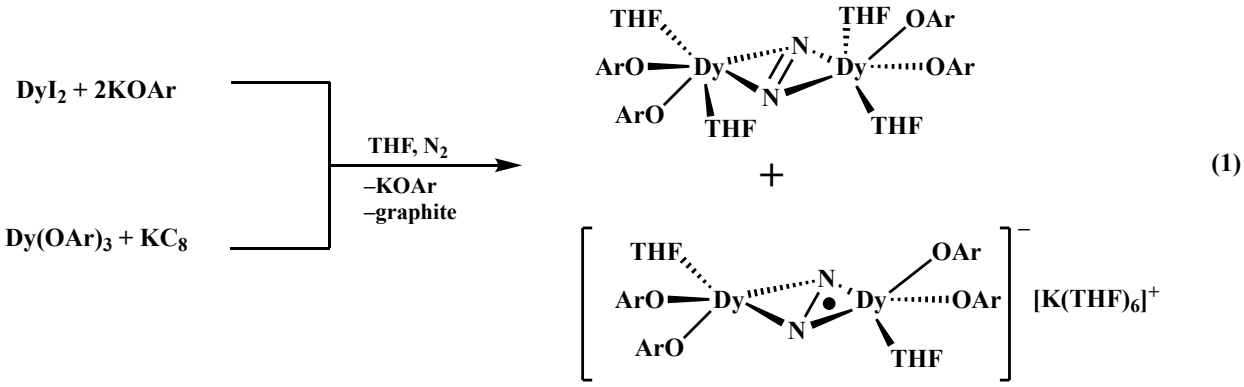

(1)

The KC_8 used in eq 1 does not perform these transformations on dinitrogen. These findings, combined with the observation of what was assigned to be a Y(II) species by EPR,[20] suggested that it should be possible to form Ln(II) species for more metals than the "traditional" set. The isolation of complexes containing $\{La^{II}[1,3\text{-}(SiMe_3)_2C_5H_3]_3\}^{1-}$ and $\{Ce^{II}[1,3\text{-}(SiMe_3)_2C_5H_3]_3\}^{1-}$ and their assignment as compounds with $5d^1$ and $4f^15d^1$ electron configurations, respectively,[21] then led to the isolation of the compounds $[Ln^{II}(C_5H_4SiMe_3)_3]^{1-}$ for Y and all the lanthanides and the identification of the "non-traditional" set of Ln(II) compounds.[22–25]

Compounds of Nd(II) and Dy(II) deserve special notice as the "configurational crossover" ions. These ions were found in DyI_2 and NdI_2, where their electron configurations were assigned as $4f^{10}$ and $4f^4$, respectively,[25] like the "traditional" set and were formed by solid-state reactions of

metal and iodine.[26] DyI_2 was also used in the dinitrogen reduction chemistry in eq 1 and the ability of DyI_2 and the reduction of a Dy(III) precursor to carry out the same transformation suggested that if reduction of other rare-earth (III) precursors could reduce dinitrogen, Ln(II) compounds with these other metals could be possible, even if no compounds of these metals in their +2 oxidation state were known. Though in their diiodides Dy(II) and Nd(II) had "traditional" electron configurations, in compounds $[Dy^{II}(C_5H_4SiMe_3)_3]^{1-}$ and $[Nd^{II}(C_5H_4SiMe_3)_3]^{1-}$, their electron configurations were assigned as "non-traditional" $4f^n5d^1$ configurations. The ligand-dependent electron configurations of Dy(II) and Nd(II) thus earned them the designation of "configurational crossover" ions.[25]

The discovery of Ln(II) compounds for all the lanthanides with the $C_5H_4SiMe_3$ led to further investigation into whether other ligand sets could stabilize the new "non-traditional" ions and what their physical and chemical properties would be.[27–31] Especially since the electron configurations of Nd(II) and Dy(II) are ligand-dependent, exploration into other ligand sets may expand the set of ions which can experience the "configurational crossover." Since the gamut of oxidation states available to an element is one of the most fundamental properties of an element, advances in this area open up new horizons in both reactivity and electronic structure studies. The "non-traditional" ions have already distinguished themselves by displaying qubit behavior[32] as well as the complexes [Li(2.2.2-cryptand)][$Ho^{II}(C_5H_4SiMe_3)_3$] and {K(2.2.2-cryptand)}{$Dy^{II}[N(SiMe_3)_2]_3$}having the highest single-ion magnetic moment (11.67 μ_B).[28,33] Furthermore, seeing that the unique oxidation states available to Eu and Ce are used to separate these elements from the other rare-earth metals during processing of their ores, research towards oxidation state diversity in the rare-earth metals could lead to improved separation technology for these elements; the mining, beneficiation, and separation of these elements stands to benefit from

improved efficiency, as these processes involve creation of radioactive and otherwise hazardous wastes in order to separate the chemically-similar Ln(III) ions, both from each other and other elements in the ore.[34] More unique applications may present themselves as more rare-earth(II) compounds are synthesized.

Dissertation Outline. This thesis describes the effect that ligands have on the kinetic properties of rare-earth(II) compounds like their thermal stability and thermodynamic properties like their reducing power. This research is oriented towards discovering a set of principles that can guide design of rare-earth(II) materials with desired properties. Chapter 1 details the evaluation of the OAr′ ligand (= 2,6-^{t}Bu$_2$-4-MeC$_6$H$_2$O) for synthesizing Ln(II) complexes (Ln = rare-earth metal). While spectroscopic evidence, supported by TD-DFT and CASSCF calculations, support the formation of "[Ln(OAr′)$_3$]$^{1-}$" complexes, the resulting materials are thermally unstable and could not be crystallographically characterized, except in the case of [K(2.2.2-cryptand)][Sc(OAr′)$_3$]. A hypothesis is developed that steric saturation is a factor controlling the kinetic stability of Ln(II) complexes, and that the (OAr′)$_3$ ligand set can only stabilize a Ln(II) complex with the smallest rare earth, Sc. Chapter 2 describes the synthesis and structural analysis of Y(III) and Y(II) complexes of the bulky aryloxide OAr* (= 2,6-(1-adamantyl)$_2$-4-^{t}Bu-C$_6$H$_2$O). The OAr* ligand was used as a more sterically-saturating, yet electronically similar analogue of OAr′ from Chapter 1. A crystallographically-characterizable Y(II) aryloxide, [K(2.2.2-cryptand)][Y(OAr*)$_3$], is isolated that is more kinetically stable than the Y(II) complex that was reported in Chapter 1. This is attributed to the greater steric saturation afforded by the OAr* ligand compared to the OAr′ ligand, and serves as further evidence supporting the hypothesis from Chapter 1, that steric saturation is an important factor in synthesizing kinetically-stable Ln(II) complexes.

In Chapter 3, Ln(III) complexes of the asymmetric amide ligands $N(SiMe_3)$(phenyl) and $N(SiMe_3)$(cyclohexyl) are synthesized and analyzed structurally. These complexes were developed as precursors to Ln(II) complexes, but the ligands' steric bulk is postulated to be insufficient to stabilize Ln(II) complexes. Chapter 4 compares the reducing power of complexes containing $[An^{II}Cp''_3]^{1-}$ units [An = Th, U; Cp″ = 1,3-$(SiMe_3)_2C_5H_3$] to La(II) and Y(II) cyclopentadienide compounds by using these Ln(II) and An(II) compounds as reductants instead of alkali metals and observing which reduced *f*-element species are produced. EPR spectroscopy is used to detect the resulting complexes. It is observed that in the ligand sets investigated, Th(II) is as strong a reductant as La(II) and Y(II) and also that La(II) and Y(II) have nearly the same reducing power. Finally, Chapter 5 compares the reducing power of lanthanide complexes as the ligand and metal are varied using the same methods as Chapter 4. The results show that changing the ligand set can change which Ln(II) are more reducing than others, and that EPR spectroscopy can detect ligand exchange and presence of heteroleptic Ln(II) compounds. In addition, the "traditional" Ln(II) compounds are shown to be less reducing than the "non-traditional" Ln(II) complexes examined in this Chapter.

REFERENCES

(1) Ronda, C. R.; Jüstel, T.; Nikol, H. *J. Alloys Compd.* **1998**, *275–277*, 669–676.
(2) Van Loy, S.; Binnemans, K.; Van Gerven, T. *J. Clean. Prod.* **2017**, *156*, 226–234.
(3) Freeman, A. J.; Watson, R. E. *Phys. Rev.* **1962**, *127* (6), 2058–2075.
(4) Emeléus, H. J.; Sharpe, A. G. *Modern Aspects of Inorganic Chemistry*, 4th ed.; Wiley: New York, 1973.
(5) Bünzli, J.-C. G.; Choppin, G. R. *Lanthanide Probes in Life, Chemical, and Earth Sciences: Theory and Practice*; Elsevier: Amsterdam, 1989.
(6) Johnson, K. E.; Sandoe, J. N. *J. Chem. Soc. A* **1969**, 1694–1697.
(7) Dieke, G. H. *Spectra and Energy Levels of Rare Earth Ions in Crystals*; Crosswhite, H. M., Crosswhite, H., Eds.; John Wiley & Sons Inc.: New York, 1968.
(8) Kramer, M. J.; McCallum, R. W.; Anderson, I. A.; Constantinides, S. *J. Miner. Met. Mater. Soc.* **2012**, *64* (7), 752–763.
(9) Connick, R. E. *J. Chem. Soc.* **1949**, S235–S241.
(10) Anwander, R.; Dolg, M.; Edelmann, F. T. *Chem. Soc. Rev.* **2017**, *46*, 6697–6709.

(11) Rice, N. T.; Popov, I. A.; Russo, D. R.; Bacsa, J.; Batista, E. R.; Yang, P.; Telser, J.; La Pierre, H. S. *J. Am. Chem. Soc.* **2019**, *141*, 13222–13233.
(12) Palumbo, C. T.; Zivkovic, I.; Scopelliti, R.; Mazzanti, M. *J. Am. Chem. Soc.* **2019**, *141*, 9827–9831.
(13) Borchert, Y.; Sonström, P.; Wilhelm, M.; Borchert, H.; Bäumer, M. *J. Phys. Chem. C* **2008**, *112*, 3054–3063.
(14) Behrsing, T.; Deacon, G. B.; Junk, P. C. The Chemistry of Rare Earth Metals, Compounds, and Corrosion Inhibitors. In *Rare Earth-Based Corrosion Inhibitors*; Elsevier Inc., 2014; pp 1–37.
(15) Evans, W. J. *Organometallics* **2016**, *35*, 3088–3100.
(16) Evans, W. J.; Allen, N. T.; Ziller, J. W. *J. Am. Chem. Soc.* **2000**, *122*, 11749–11750.
(17) Evans, W. J.; Allen, N. T. *J. Am. Chem. Soc.* **2000**, *122*, 2118–2119.
(18) Morss, L. R. *Chem. Rev.* **1976**, *76* (6), 827–841.
(19) Evans, W. J.; Fang, M.; Zucchi, G.; Furche, F.; Ziller, J. W.; Hoekstra, R. M.; Zink, J. I. *J. Am. Chem. Soc.* **2009**, *131* (31), 11195–11202.
(20) Fang, M.; Lee, D. S.; Ziller, J. W.; Doedens, R. J.; Bates, J. E.; Furche, F.; Evans, W. J. *J. Am. Chem. Soc.* **2011**, *133*, 3784–3787.
(21) Hitchcock, P. B.; Lappert, M. F.; Maron, L.; Protchenko, A. V. *Angew. Chem. Int. Ed.* **2008**, *47*, 1488–1491.
(22) MacDonald, M. R.; Ziller, J. W.; Evans, W. J. *J. Am. Chem. Soc.* **2011**, *133*, 15914–15917.
(23) MacDonald, M. R.; Bates, J. E.; Ziller, J. W.; Furche, F.; Evans, W. J. *J. Am. Chem. Soc.* **2013**, *135*, 9857–9868.
(24) MacDonald, M. R.; Bates, J. E.; Fieser, M. E.; Ziller, J. W.; Furche, F.; Evans, W. J. *J. Am. Chem. Soc.* **2012**, *134*, 8420–8423.
(25) Fieser, M. E.; MacDonald, M. R.; Krull, B. T.; Bates, J. E.; Ziller, J. W.; Furche, F.; Evans, W. J. *J. Am. Chem. Soc.* **2015**, *137*, 369–382.
(26) Bochkarev, M. N.; Fagin, A. A. *Chem. Eur. J.* **1999**, *5* (10), 2990–2992.
(27) Angadol, M. A.; Woen, D. H.; Windorff, C. J.; Ziller, J. W.; Evans, W. J. *Organometallics* **2019**, *38* (5), 1151–1158.
(28) Ryan, A. J.; Darago, L. E.; Balasubramini, S. G.; Chen, G. P.; Ziller, J. W.; Furche, F.; Long, J. R.; Evans, W. J. *Chem. Eur. J.* **2018**, *24*, 7702–7709.
(29) Jenkins, T. F.; Woen, D. H.; Mohanam, L. N.; Ziller, J. W.; Furche, F.; Evans, W. J. *Organometallics* **2018**, *37*, 3863–3873.
(30) Huh, D. N.; Ziller, J. W.; Evans, W. J. *Dalton Trans.* **2018**, *47* (48), 17285–17290.
(31) Palumbo, C. T.; Darago, L. E.; Windorff, C. J.; Ziller, J. W.; Evans, W. J. *Organometallics* **2018**, *37*, 900–905.
(32) Ariciu, A.-M.; Woen, D. H.; Huh, D. N.; Nodaraki, L. E.; Kostopoulos, A. K.; Goodwin, C. A. P.; Chilton, N. F.; McInnes, E. J. L.; Winpenny, R. E. P.; Evans, W. J.; et al. *Nat. Commun.* **2019**, *10*, 3330.
(33) Huh, D. N.; Darago, L. E.; Ziller, J. W.; Evans, W. J. *Inorg. Chem.* **2018**, *57*, 2096–2102.
(34) Van Gosen, B. S.; Verplanck, P. L.; Seal, R. R.; Long, K. R.; Gambogi, J. *Rare-Earth Elements*; Schulz, K. J., DeYoung John H., J., Seal, R. R., Bradley, D. C., Eds.; Reston, VA, 2017.

Chapter 1

Rare-Earth Metal(II) Aryloxides: Structure, Synthesis, and EPR Spectroscopy of [K(2.2.2-cryptand)][Sc($OC_6H_2{}^tBu_2$-2,6-Me-4)$_3$]*

INTRODUCTION

Two major lines of research have been pursued in the reductive chemistry of rare-earth metals: LnA_3/M reduction reactions (Ln = Sc, Y, lanthanides; A = anionic ligand; M = alkali metal) have been conducted *under argon* to isolate complexes of new Ln(II) ions in $[LnA_3]^{1-}$ complexes,[1–9] *e.g.*, with A = $C_5H_4SiMe_3$ and $C_5H_3(SiMe_3)_2$ in eq 1.1 as well as several other cyclopentadienyl ligands (A = C_5H_4Me, C_5Me_4H, $C_5H_4C(Me)_3$)[10–13] and *under dinitrogen* to make reduced dinitrogen complexes of $(N_2)^{2-}$, eq 2.1,[14] and the first examples of $(N_2)^{3-}$.[15,16] As these studies progressed, a pattern developed. Reactions with A = silylcyclopentadienyl

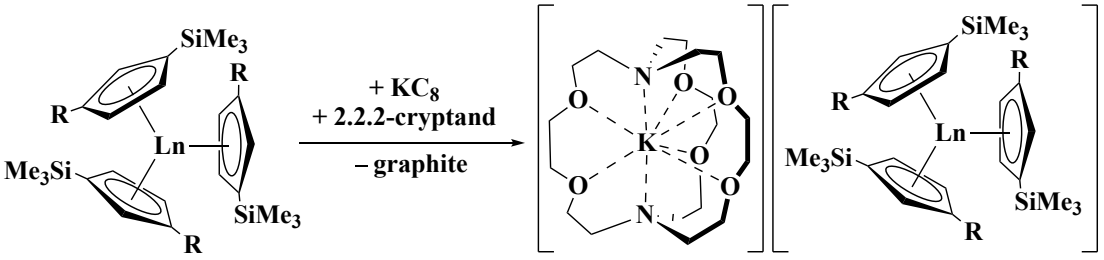

(1.1)

R = H, Ln = Y, La, Ce, Pr, Nd, Gd, Tb, Dy, Ho, Er, and Lu
R = $SiMe_3$, Ln = La, Ce, Pr, and Nd

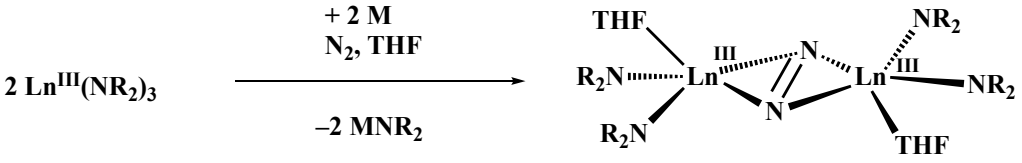

(2.1)

Ln = Y, Nd, Gd, Tb, Dy, Ho, Er, Tm, Lu
M = Na, K, or KC_8

* Portions of this Chapter have been published: Moehring, S. A.; Beltrán-Leiva, M. J.; Páez-Hernández, D.; Arratia-Pérez, R.; Ziller, J. W.; Evans, W. J. *Chem. Eur. J.* **2018**, 24, 18059–18067.

ligands[17] such as $C_5H_4SiMe_3$ and $C_5H_3(SiMe_3)_2$ under Ar gave crystallographically-characterizable Ln^{2+} complexes, eq 1.1.[1,2,4–6] Reactions with A = NR_2 (R = $SiMe_3$) on the other hand, did not at first give isolable Ln^{2+} complexes under Ar, but readily provided $(N_2)^{2-}$ and $(N_2)^{3-}$ complexes when performed under N_2, eq 2.1.[14–16] However, the isolation of complexes containing the $[Ln(NR_2)_3]^{1-}$ anion for Ln = Sc[18] and the lanthanides[19] dispelled the idea that there was a dichotomy between ligands that could stabilize Ln(II) ions and ones that could activate N_2. This suggested that many more complexes containing $[LnA_3]^{1-}$ were accessible in a diversity of ligand sets.

Reactions using the aryloxide ligand OAr (OAr = $OC_6H_3{}^tBu_2$-2,6) were important in the initial discovery of complexes containing the $(N_2)^{3-}$ radical trianion.[15,16] The first example of a $(N_2)^{3-}$ complex was synthesized from a reaction of DyI_2 with KOAr under a N_2 atmosphere and later examples were obtained using the LnA_3/M reactions with $Dy(OAr)_3$, eq 3.1.[15]

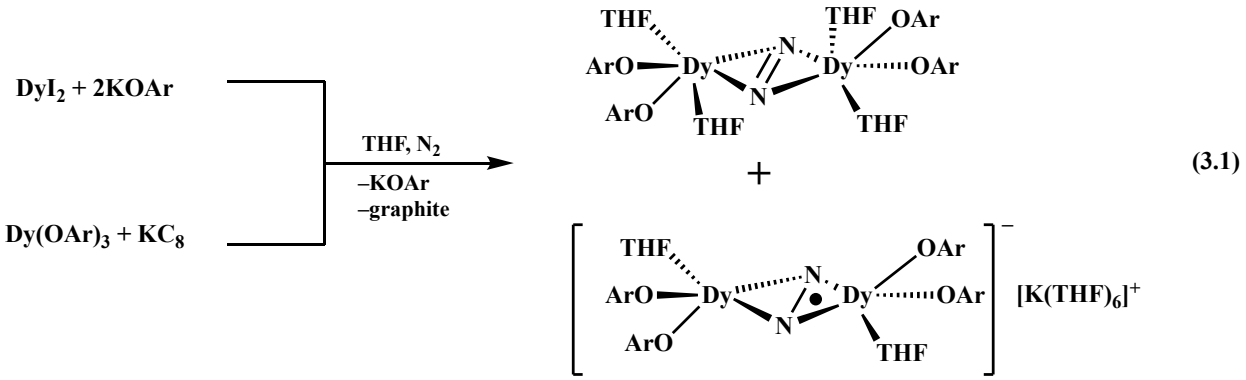

(3.1)

However, once the success of the A = NR_2 ligand in the LnA_3/M reactions under dinitrogen was established, reductive chemistry with aryloxide ligands was not developed further. This Chapter describes how that deficiency was addressed. Reductions of tris(aryloxide) rare-earth metal complexes were also of interest in light of results with the tris(aryloxide)arene ligand, $((^{Ad,Me}ArO)_3mes)^{3-}$, which has proven to be a suitable ligand for isolating Ln(II) complexes as well as +2 ions of the actinides.[20–22]

This Chapter describes how the rare-earth metals whose +2 oxidation states would be easily identifiable by EPR spectroscopy, specifically Y and Sc, were investigated to probe the suitability of the tris(aryloxide) ligand set for isolating Ln(II) rare-earth metal complexes. This approach had the extra advantage that these metals can be characterized by NMR spectroscopy in their +3 oxidation states owing to their diamagnetism. Additionally, to exclude any reactivity possible with the 4-position of OAr ligands,[23] the 4-methyl-substituted analog of OAr, namely $OC_6H_2{}^tBu_2$-2,6-Me-4 (OAr'), was explored.

RESULTS

Yttrium. $Y(OAr')_3$, **1-Y**, the precursor for the reduction described below, was prepared from YCl_3 and $LiOAr'{\bullet}OEt_2$ following literature procedures.[24,25] The complex was crystallographically characterized and found to crystallize in $P\bar{1}$ with *five* independent molecules in the unit cell, Figures 1.1 and 2.1.

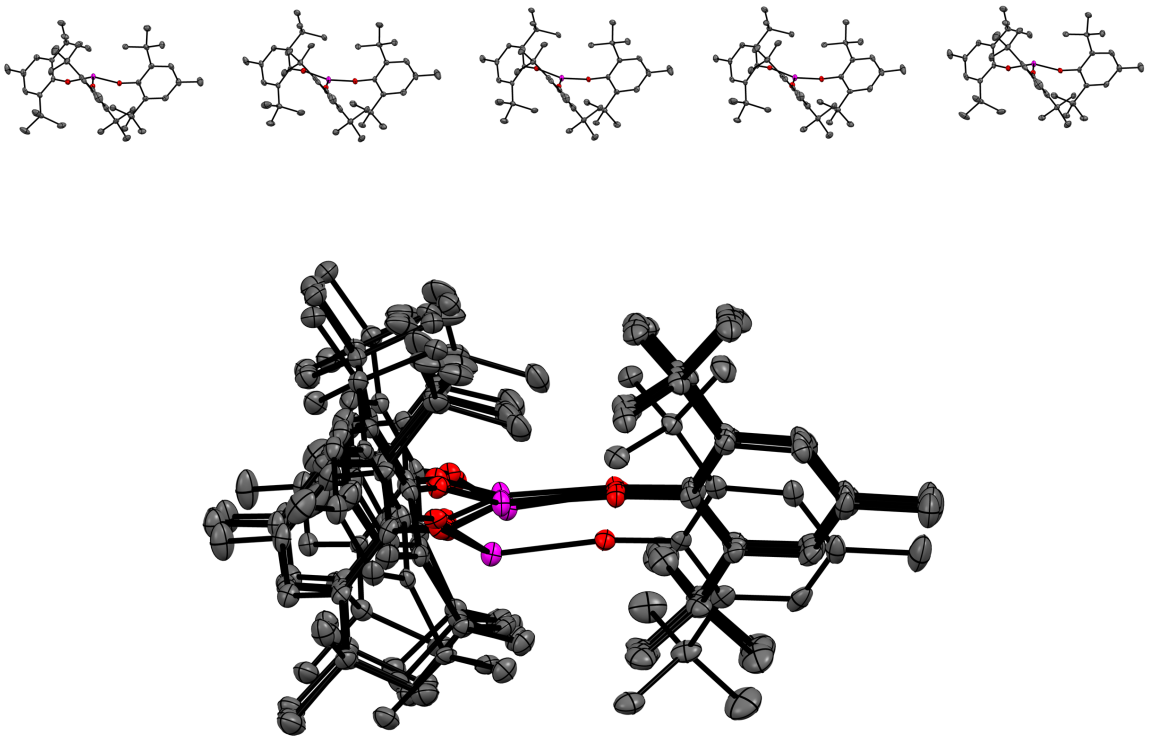

Figure 1.1. Representative thermal ellipsoid plots of **1-Y,** from the side (top) and along the axis of the 5 Y atoms (bottom). Hydrogen atoms have been removed for clarity. Thermal ellipsoids are drawn at the 50% probability level.

The five molecules have similar Y–O distances, with a range of 2.032(2)–2.053(2) Å and an average of 2.045(7) Å, but they differ significantly in the distances of the Y atom from the plane of the three donor O atoms, which has been attributed to a small energy difference between the pyramidal and planar geometries.[26] Two extreme examples are shown in Figure 2.1. The yttrium displacements from the O_3 plane are 0.009, 0.014, 0.019, 0.449, and 0.479 Å in the five molecules. The angles of the phenyl rings of the ligands with the plane of the three oxygen atoms are quite variable and range from 39.71–77.93°. The six quaternary carbons of the *tert*-butyl groups of the three OAr′ ligands form a distorted octahedron around the yttrium. Metric data for **1-Y** are summarized in Table 1.1.

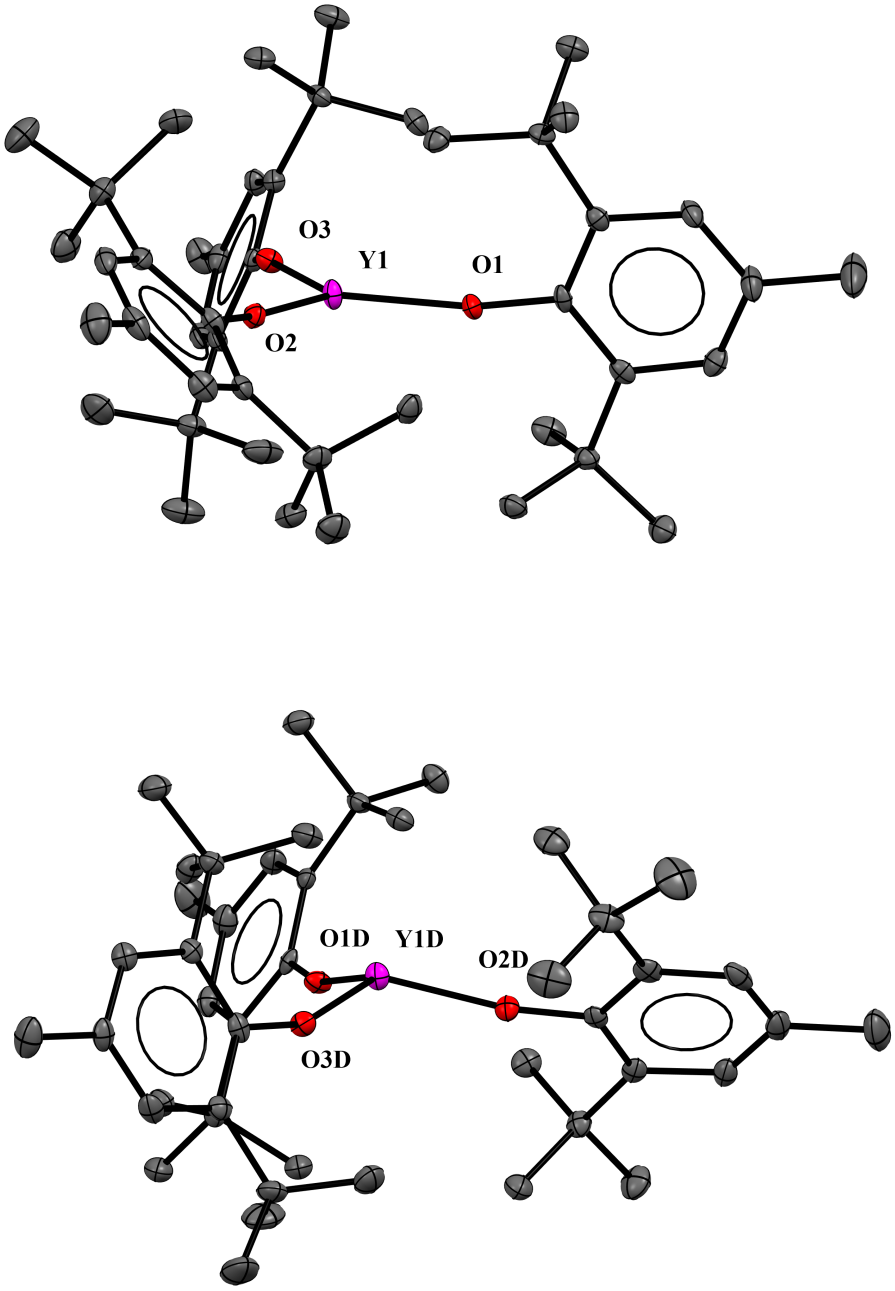

Figure 2.1: Representative thermal ellipsoid plots of two of the five molecules in the unit cell of **1-Y,** one planar (top) and one pyramidalized (bottom). Hydrogen atoms have been removed for clarity. Thermal ellipsoids are drawn at the 50% probability level.

Table 1.1. Selected metrical parameters for **1-Y**. Distances in Å, angles in °. δ = displacement of Y from the O_3 plane. Θ = angle between O_3 plane and the plane of the OAr′ ligand. Λ = distance between Y and the closest ^{t}Bu-methyl.

1-Y Unit	Y–O range	Y–O Average	Global Y–O Average	δ	Θ range	Θ average	Λ
Y1	2.043(2)–2.053(2)	2.047(3)		0.009	40–78	64	2.978(3)–4.053(3)
Y1B	2.032(2)–2.052(2)	2.043(3)		0.019	40–77	63	2.970(2)–4.069(3)
Y1C	2.041(2)–2.052(2)	2.045(3)	2.045(7)	0.014	39–77	64	2.967(3)–4.062(3)
Y1D	2.042(2)–2.045(2)	2.044(3)		0.449	49–69	61	2.905(2)–4.281(3)
Y1E	2.043(2)–2.045(2)	2.045(3)		0.479	50–68	61	2.917(2)–4.268(3)

$Y(OAr')_3$, **1-Y**, reacts at −30 °C with potassium graphite (KC_8) in THF in the presence of 2.2.2-cryptand (crypt) to form a dark blue solution, **2-Y**, analogous to that found in the synthesis of the crystallographically-characterizable Y(II) complex, [K(crypt)][YCp'_3] ($Cp' = C_5H_4SiMe_3$) in eq 1.1 under similar conditions.[2] Complex **2-Y** decomposes in ~60 seconds at room temperature, and even at −30 °C, **2-Y** fades to a clear, colorless solution in minutes. Growing crystals at −78 °C has not been successful.

To obtain EPR data on **2-Y**, a sample was prepared at –30 °C, removed from the glovebox, and frozen in liquid nitrogen within a 45 second time span. The product displays a two-line axial EPR spectrum at 77 K with $g_\perp = 1.97$, $g_\parallel = 2.00$, $A_\perp = 155.4$ G, and $A_\parallel = 148.7$ G, Figure 3.1, consistent with an unpaired electron interacting with a 100% abundant $I = 1/2$ ^{89}Y nucleus.[4] The UV-visible spectrum of **2-Y** has a single broad absorbance at 704 nm with $\varepsilon = 6500$ $M^{-1}cm^{-1}$, Figure 4.1. This is more intense than that measured for the crystallographically-characterized [K(crypt)][YCp'_3], $\varepsilon = 4500$ $M^{-1}cm^{-1}$.[2] The EPR and optical spectra are consistent with the presence of $4d^1$ Y(II) complex in solution.

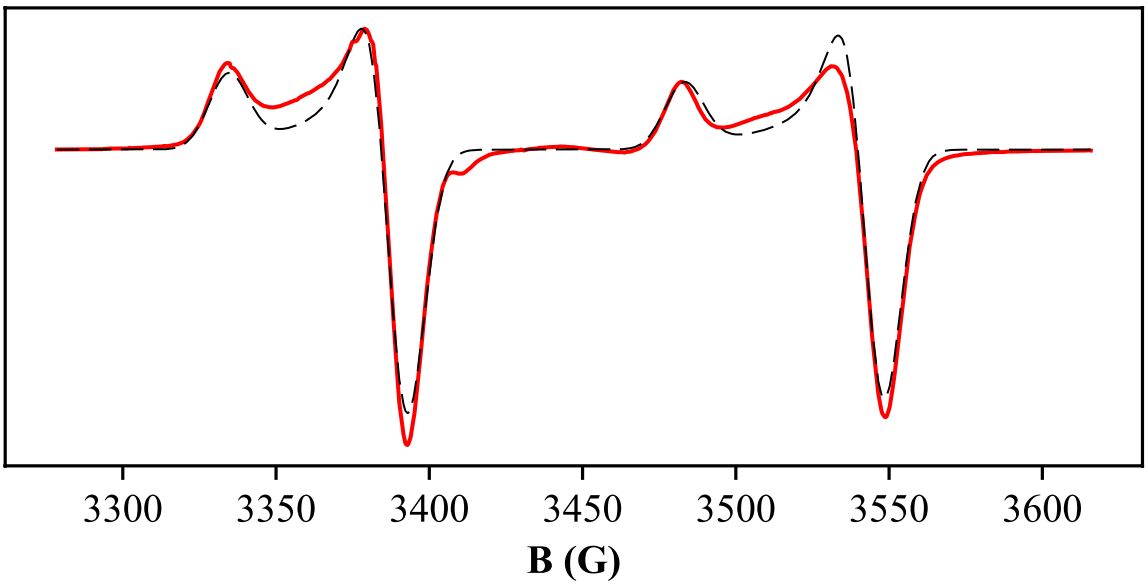

Figure 3.1. 77 K X-band EPR spectrum of **2-Y**. Experimental spectrum in red, simulated spectrum ($g_{\perp} = 1.97$, $g_{\parallel} = 2.00$, $A_{\perp} = 155.4$ G, and $A_{\parallel} = 148.7$ G) in black dashes.

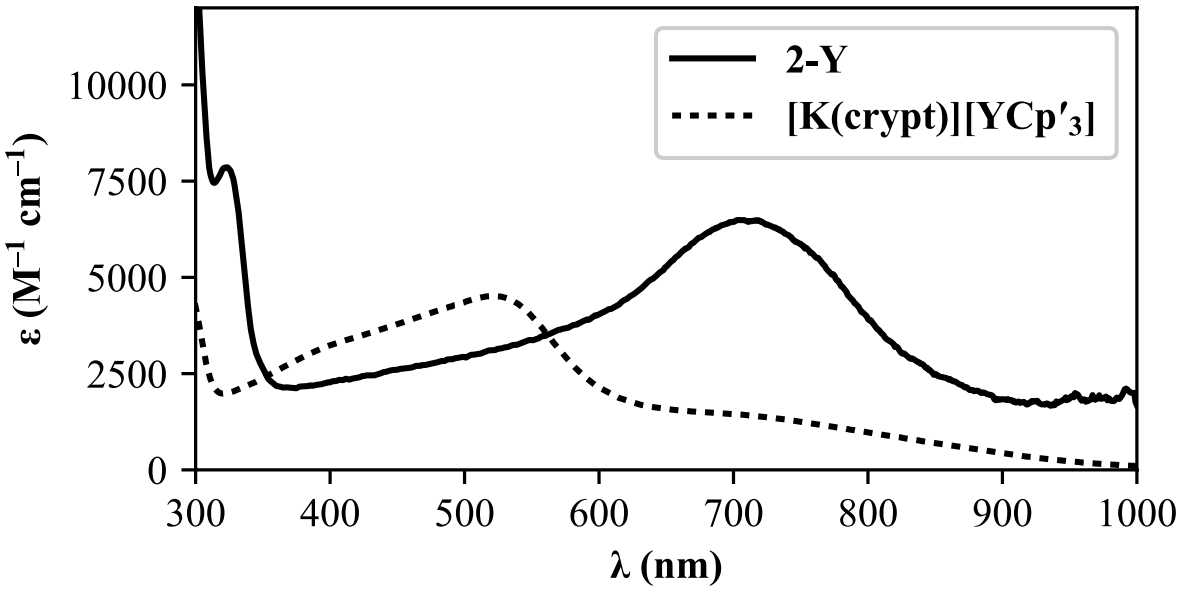

Figure 4.1. UV-visible spectrum of **2-Y** in THF at –78 °C and [K(crypt)][YCp′$_3$] in THF at room temperature.

The importance of substituting the 4-position of the aryloxide was probed by examining the reduction of Y(OAr)$_3$, **3-Y**,[27] with KC_8 in the presence of crypt. Complex **3-Y** reacted similarly to **1-Y**, forming a dark-colored solution, **4-Y**, that also had limited thermal stability similar to that of **2-Y**. The EPR spectrum of **4-Y** at 77 K was nearly identical to that of **2-Y** with $g_\perp = 1.96$, $g_\parallel = 2.00$, $A_\perp = 157.9$ G, and $A_\parallel = 149.9$ G (Figure 5.1). Evidently, the substituent on the 4-position of the aryloxide ligand does not appreciably perturb the KC_8 reactivity of the complexes or the stability of the product.

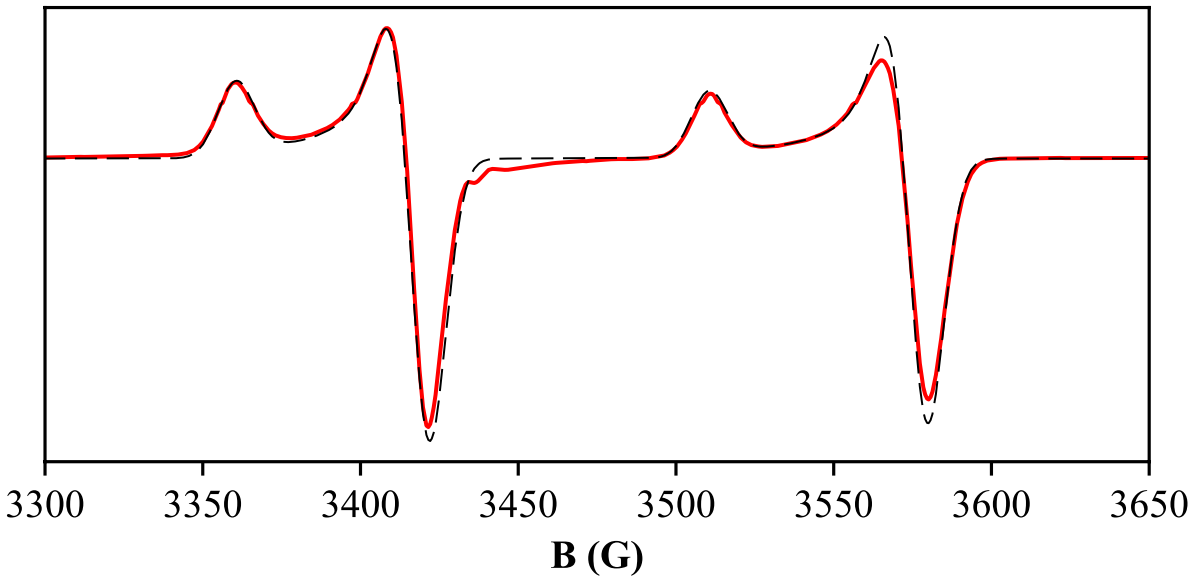

Figure 5.1. 77 K X-band EPR spectrum of **4-Y**. Experimental spectrum in red, simulated spectrum ($g_{\perp}$ = 1.96, $g_{\parallel}$ = 2.00, $A_{\perp}$ = 157.9 G, and $A_{\parallel}$ = 149.9 G) in black dashes.

Scandium. Sc(OAr′)$_3$, **1-Sc**, was prepared like **1-Y**, from $ScCl_3$ and LiOAr′•OEt_2 following literature methods.[24,25,28] **1-Sc** also reacts at −30 °C with KC_8 in THF in the presence of crypt to form a dark maroon solution, **2-Sc**. Contrary to the thermal instability of **2-Y** and **4-Y**, the deep maroon color of **2-Sc** persists after 40 minutes at room temperature and for days at −30 °C in the glovebox. EPR analysis of **2-Sc** at 77 K showed an eight-line pattern with $g_{\perp}$ = 1.98, $g_{\parallel}$ = 2.00, $A_{\perp}$ = 290.5 G, and $A_{\parallel}$ = 288.8 G. At room temperature, an eight-line pattern with g = 1.98 and A = 285.9 G is seen, Figure 6.1, which would be expected for a Sc(II) species having an unpaired electron interacting with a 100% abundant I = 7/2 ^{45}Sc nucleus.[18,29,30]

The UV-visible absorption spectrum of **2-Sc** has several strong absorptions from 327–677 nm, Figure 7.1, with molar extinction coefficients from 790–2300 $M^{-1}cm^{-1}$. The spectrum of [K(crypt)][Sc(NR$_2$)$_3$] is shown for comparison.[18]

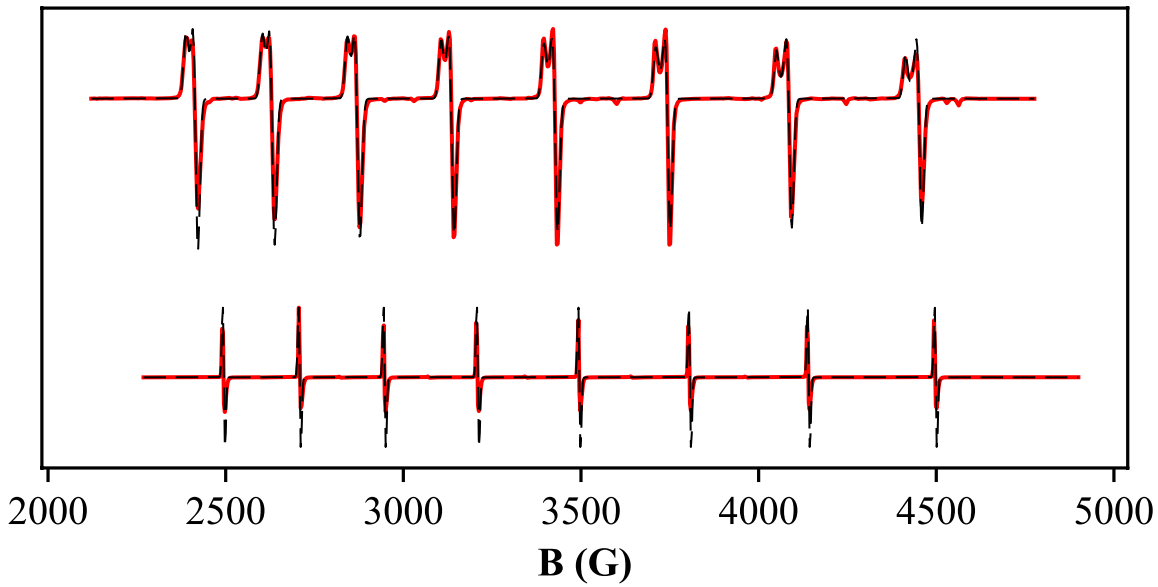

Figure 6.1. X-band EPR spectra of **2-Sc**. Experimental spectra in red, simulated spectra in black dashes. 77 K spectrum on top ($g_{\perp}$ = 1.98, $g_{\parallel}$ = 2.00, $A_{\perp}$ = 290.5 G, and $A_{\parallel}$ = 288.8 G), room temperature spectrum (g = 1.98 and A = 285.9 G) below.

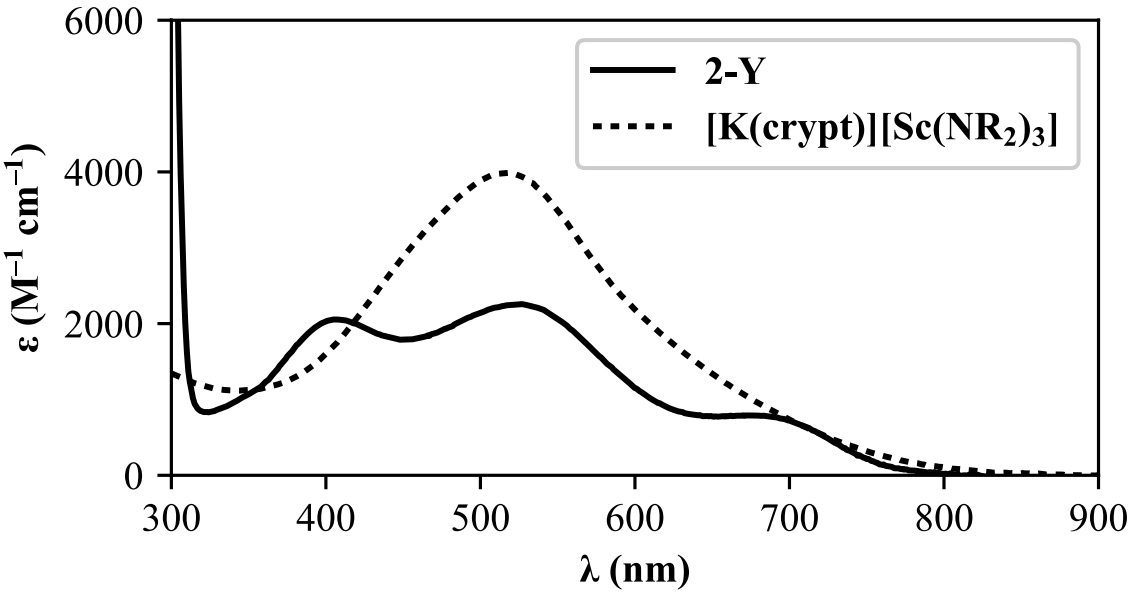

Figure 7.1. UV-visible spectrum of **2-Sc** in THF at –78 °C and [K(crypt)][$Sc(NR_2)_3$] in THF at room temperature. R = $SiMe_3$.

Crystals of **2-Sc** could be isolated by crystallization from a THF-pentane mixture and X-ray crystallography revealed the presence of [K(crypt)][$Sc(OAr')_3$], Figure 8.1, a Sc(II) complex as expected based on its EPR spectrum. The $[K(crypt)]^+$ cation is well-separated from the $[Sc(OAr')_3]^{1-}$ anion and 3.5 molecules of THF per unit cell are found in the lattice. The three oxygen donor atoms of the OAr′ ligands form a trigonal planar array around Sc with O−Sc−O angles of 117.30(6)°, 121.89(7)°, and 120.75(7)°. The Sc center is within 0.03 Å of the plane of these three oxygen atoms.

The aryl rings of the OAr′ ligands are canted with respect to the ScO_3 plane by angles of 61.11°, 63.16°, and 63.67° such that there are three tert-butyl groups above the plane and three below. The six quaternary carbons of the *tert*-butyl groups define a distorted octahedron. The 1.960(2)−1.964(2) Å Sc−O distances in **2-Sc** are substantially larger than the 1.853−1.889 Å distances in the precursor, $Sc(OAr')_3$, **1-Sc**.[28] The average C–C bond length in the OAr′ rings of **1-Sc** and **2-Sc** is the same within error: 1.40(2) and 1.40(1) Å, respectively.[28] Metrical parameters are summarized in Table 2.1.

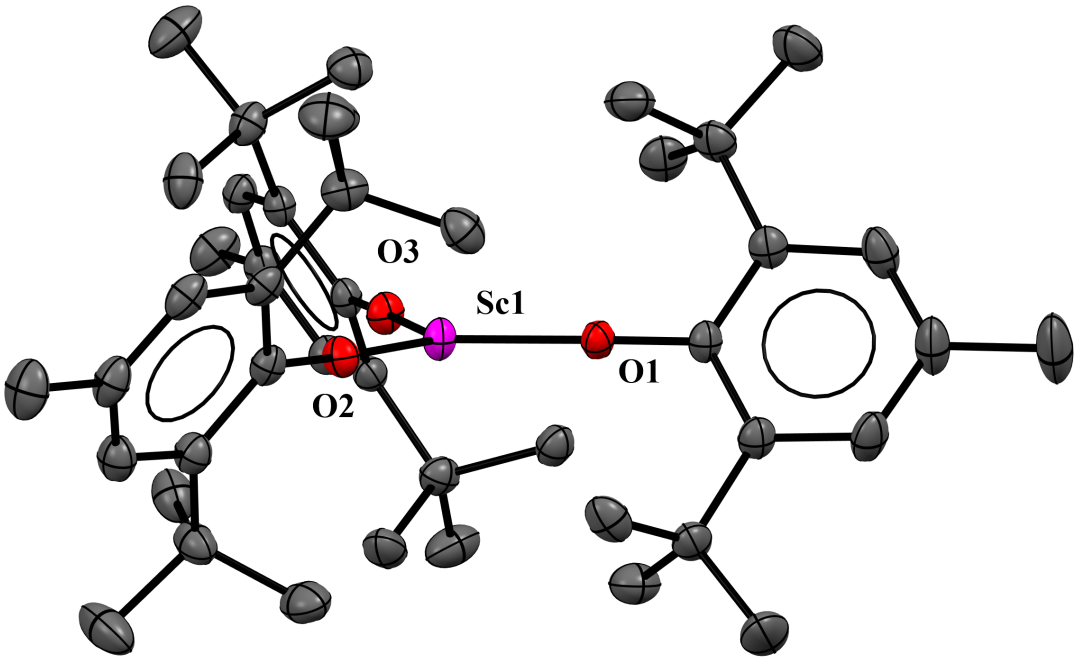

Figure 8.1. Thermal ellipsoid plot of **2-Sc**. Hydrogen atoms, the $[K(crypt)]^+$ countercation, and 3.5 molecules of lattice THF have been removed for clarity. Thermal ellipsoids are drawn at the 50% level.

Table 2.1. Selected metrical parameters for **2-Sc**. Distances in Å, angles in °. δ = displacement of Sc from the O_3 plane. Θ = angle between O_3 plane and the plane of the OAr′ ligand. Λ = distance between Sc and the closest ^{t}Bu-methyl.

Sc–O range	Sc–O Average	δ	Θ range	Θ average	Λ
1.960(2)–1.964(0)	1.962(3)	0.027	61-64	63	3.800(2)–3.870(3)

Lanthanides. The lanthanide complexes $Ln(OAr')_3$ (Ln = Gd, Dy, Ho, Er), **1-Ln**, were also reacted with KC_8 at −30 °C in THF in the presence of crypt to form deep purple solutions, **2-Ln**. These solutions had intermediate stability between **2-Sc** and **2-Y**, maintaining their deep color for about 1 day at −30 °C. Their UV-visible spectra are similar to each other and have strong, broad absorptions near 450 and 600 nm. The UV-visible spectra of $[K(crypt)][LnCp'_3]$ are presented alongside for comparison, Figure 9.1.[2]

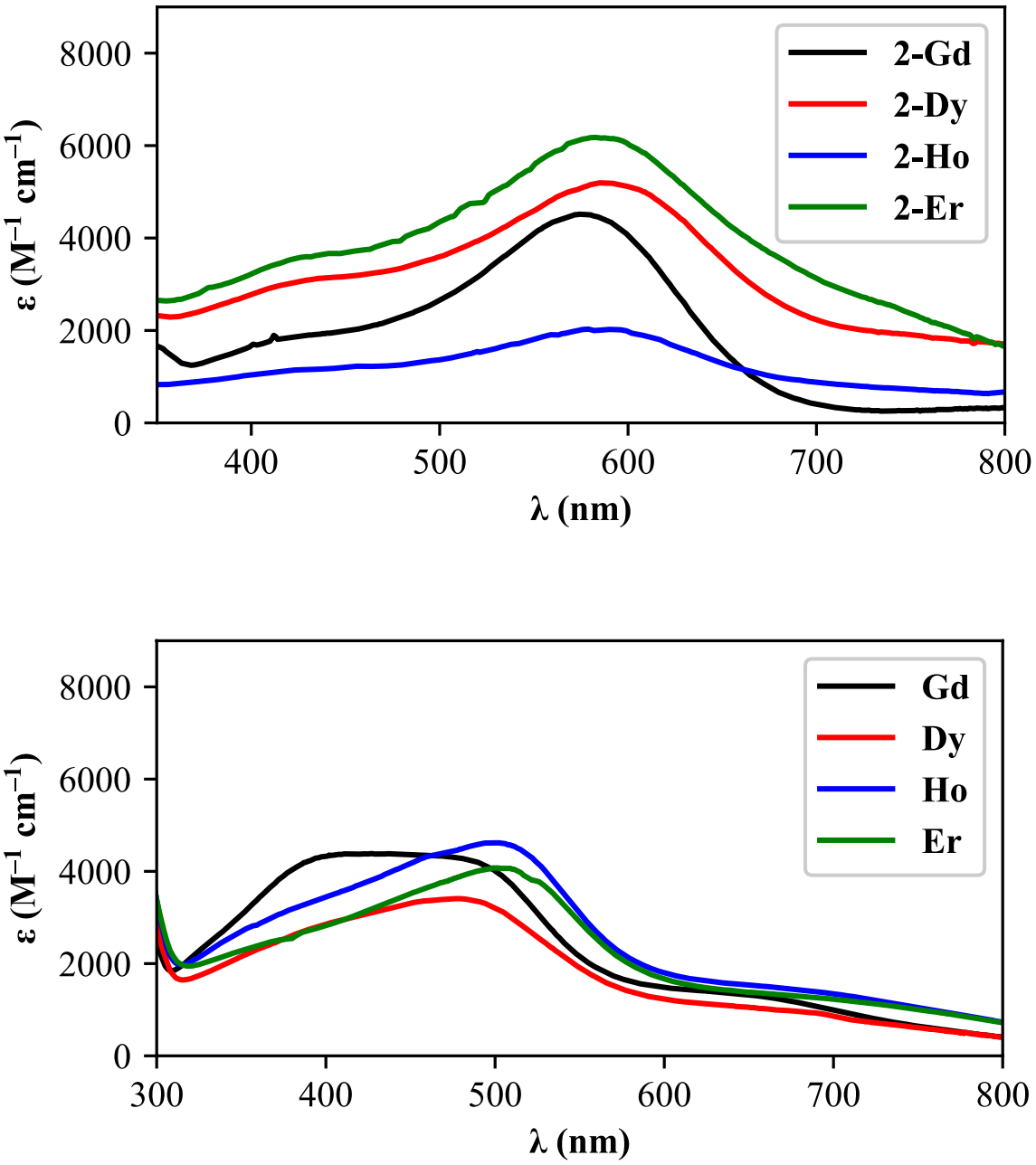

Figure 9.1: UV-visible spectra of **2-Ln** at −78 °C in THF (above) and [K(crypt)][LnCp′$_3$] in THF at room temperature (below).

Theoretical Analysis. Geometry optimizations were carried out by Maria J. Beltrán-Leiva in the group of Ramiro Arratia-Pérez at the Andres Bello University in Chile, to model a possible structure for **2-Y** in lieu of an X-ray diffraction structure. The optimized structure of "$[Y(OAr')_3]^{1-}$" is shown in Figure 10.1 and as can be observed, the oxygen atoms form a trigonal plane around the metal. Furthermore, as expected due to the homoleptic nature of the complex, all the Y–O distances are ~2.135 Å and the O–Y–O angles are ~120°. The TDDFT-simulated UV-visible spectrum agrees with the experimental spectrum.

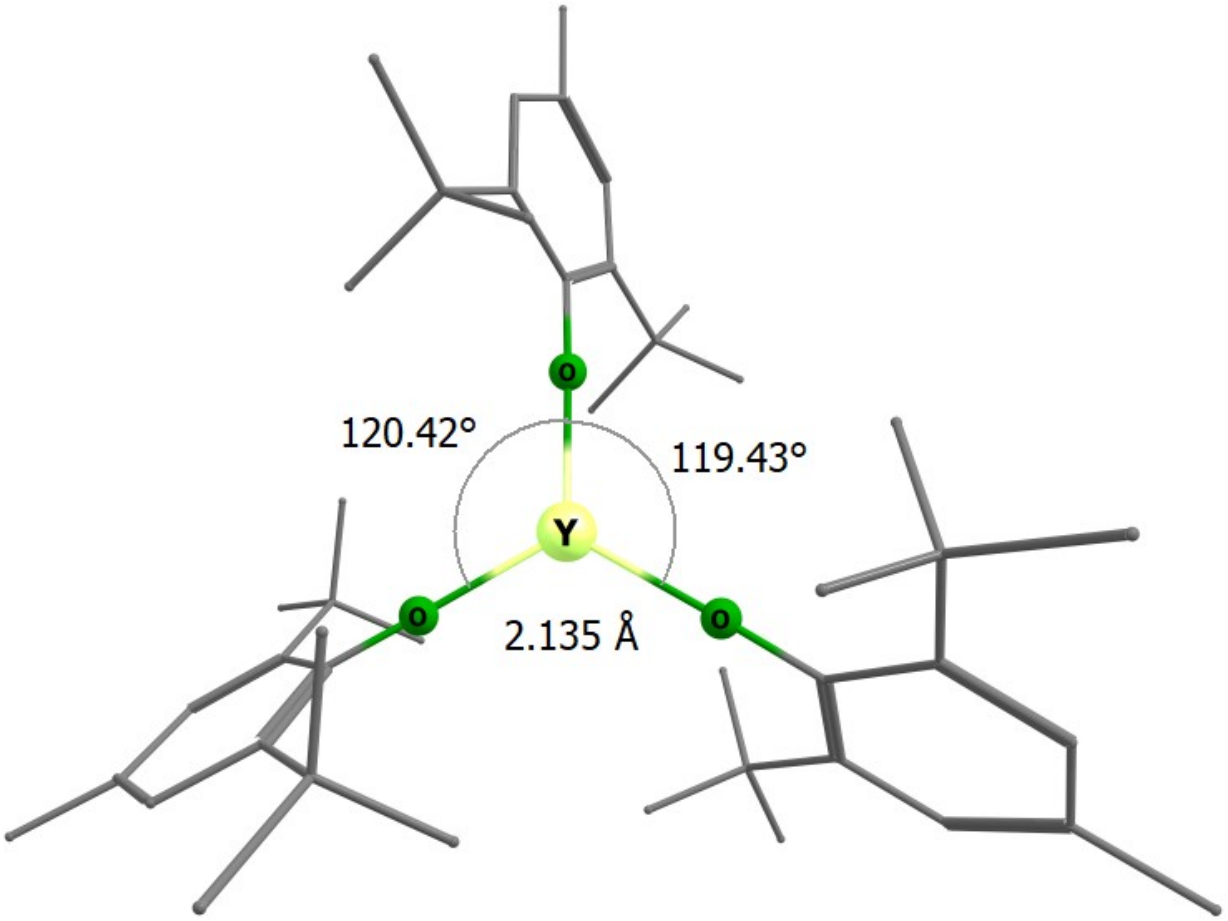

Figure 10.1. DFT optimized structure of $[Y(OAr')_3]^{1-}$.

The same calculations were performed on **2-Sc**. As with **2-Y**, all three Sc–O bonds have the same length, 1.98 Å, which matches the experimental bond length range of 1.960(2)−1.964(2) Å. All the O–Sc–O angles measure ~120°, close to the observed range of 117.30(6)–121.89(7)°. The difference between the bond lengths relative to the yttrium system is consistent with the difference in the ionic radii of these elements (~0.15 Å).[31] The calculated absorption spectrum is in good agreement with the experimental one.

In order to elucidate possible identities for the highly-absorbing compounds in solutions **2-Ln**, the UV-visible spectra were calculated using the structures of **2-Y** and **2-Sc** as starting points. The structural parameters of the modeled **2-Ln** complexes show features characteristic of homoleptic tris(aryloxide) systems. The SOMOs of **2-Gd**, **2-Er** and **2-Ho** have d_z^2 character as found earlier for the $[LnCp'_3]^{1-}$ complexes[2,5] which predict a $4f^n5d^1$ configuration for these kinds of compounds with trigonal symmetry. The simulated absorption spectra for **2-Gd**, **2-Er** and **2-Ho** properly reproduce the experimental results. However, in **2-Dy** the DFT calculation shows a SOMO with a marked *f* character, which means that in this case the dominant configuration is $4f^{10}$.

To corroborate and clarify the previous analysis, multiconfigurational CASSCF/PT2 calculations were performed on **2-Ln** in order to elucidate the nature of their ground states. In agreement with the DFT results, **2-Gd**, **2-Er** and **2-Ho** have a 100% $4f^n5d^1$ configuration as expected from the experimental UV-vis spectra and previous works, where these lanthanides were classified as $4f^n5d^1$ ions.[3] In case of **2-Dy**, the situation is more complicated because according to the DFT analysis, the ground state configuration should be $4f^{10}$, but this disagrees with the similarity observed between its spectra and those of **2-Gd**, **2-Er** and **2-Ho**. Furthermore, Dy has been classified as configurational crossover ion which increases the doubt about the DFT results.[3] According to the CASSCF/PT2 study, **2-Dy** has a 100% $4f^9 5d^1$ configuration which supports the

experimental observation. This is a more reliable result, considering the high performance of the CASSCF/PT2 methodology in the treatment of heavy elements. These results agree with the experimental UV-visible spectra for Ln(II) systems in the $(Cp')_3$ environment, where these metals were classified as $4f^n5d^1$ ions.[3]

Structural Analysis by the Method of Guzei. To explore a steric rationale for the large difference in thermal stability between **2-Y** and **2-Sc**, as well as the difference in thermal stability between **2-Y** and other Y(II) complexes,[2,4,32] the Solid-G analysis method of Guzei[33] was used to compare the degree of steric saturation afforded by cyclopentadienyl, aryloxide, and amide ligands, Table 3.1. This method provides an estimation of the percentage of the coordination sphere of the metal that is protected by the ligands by evaluating the solid angle generated by the ligands. G parameters are calculated for each compound from the crystal structure data on that compound. A G parameter of 100% indicates that the ligands completely shield the metal from exogenous substrates, while a G parameter of 50% means that the ligands cover only half the coordination sphere of the metal.

Table 3.1. G parameters (calculated around the rare-earth metal) and bond metrics for rare-earth metal complexes where R = $SiMe_3$, Cp′ = $C_5H_4SiMe_3$, Cp″ = $C_5H_3(SiMe_3)_2$-1,3 , Cp^{Me} = C_5H_4Me, Cp^t = $C_5H_4C(Me)_3$, Cp^{tet} = C_5Me_4H, and Cp = C_5H_5. Crystal structure data of the rare-earth containing molecules and ions were input into the Solid-G program excluding any lattice solvent or counterions for all the entries except (a) "$[Y(OAr')_3]^{-}$", which is based on an optimized geometry from DFT calculations, and (b) "YCp_3" whose range comes from calculation of the two "YCp_3" units in the unit cell of polymeric $[(\eta^5\text{-Cp})_2Y(\mu\text{-}\eta^5\text{:}\eta^1\text{-Cp})]_n$. †Unit cell contains multiple molecules or disorder is present in structure. *information from this work.

	Ln–donor atom or Ln–centroid range (Å)	**Average Ln– centroid or Ln–donor atom (Å)**	**G(%)**	**Ref.**
$Sc(OAr')_3$	1.8530–1.8886	1.8685	90	[28]
1-Y	2.042(2)–2.053(2)	2.045(7)	81–82†	*
2-Sc	1.961(2)–1.964(2)	1.962(3)	83	*
"$[Y(OAr')_3]^{1-}$"	2.1351–2.1353	2.1352	77	*
$Sc(NR_2)_3$	2.048(2)–2.057(2)	2.052(3)	87	[18]
$[Sc(NR_2)_3]^{1-}$	2.116(1)–2.137(2)	2.129(2)	84	[18]
$[Gd(NR_2)_3]^{1-}$	2.289(2)–2.342(2)	2.308(5)	83–84†	[19]
YCp'_3	2.403–2.409	2.405	86	[4]
$[YCp'_3]^{1-}$	2.428–2.443	2.436	86	[4]
$YCp^{Me}_3(THF)$	2.443–2.459	2.451	87	[32]
"YCp_3"	2.373–2.503	2.431	71–72†	[34]
$YCp_3(THF)$	2.438–2.455	2.449	83	[35]
$[Cp''_2YCp]^{1-}$	Cp: 2.426–2.436 Cp″: 2.421–2.468	Cp: 2.432 Cp″: 2.440	90–91†	[32]
YCp''_3	2.424–2.428	2.425	92	[36]
$[GdCp^t_3]^{1-}$	2.427–2.485	2.462	84	[12]
$[LaCp^{tet}_3]^{1-}$	2.620–2.635	2.625	79	[13]
$[TbCp^{Me}_3]^{1-}$	2.450–2.461	2.454	74	[10]

The G parameters calculated for the complexes that have been crystallographically-characterized in Table 3.1 range from 74 to 92%. In comparison, the value calculated from the structure computed by DFT for the putative "$[Y(OAr')_3]^{1-}$", which has not been isolated, is only 77%. As a calibration on these numbers, the G parameter for $Cp_3Y(THF)$, which can be readily isolated and crystallized, is 83%. The G parameter for the imaginary molecular "YCp_3" is 71%. When unsolvated "Cp_3Y" crystallizes, it is isolated as a coordination polymer, $[(\eta^5\text{-Cp})_2Y(\mu\text{-}\eta^5\text{:}\eta^1\text{-Cp})]_n$.

DISCUSSION

EPR Spectra. The two-line signals present in the EPR spectra of **2-Y** (Figure 3.1) and **4-Y** (Figure 5.1) are consistent with the presence of a $4d^1$ Y(II) complex in solution. As shown in Table 4.1, the *g* values are similar to other solutions obtained by reducing Y(III) complexes with KC_8 in THF. However, the hyperfine coupling constants (near 150 G for both **2-Y** and **4-Y**) are substantially higher than those of the only other crystallographically-characterized Y(II) complexes, [K(18-crown-6)][YCp'_3], 36.6 G, and [K(crypt)][$Cp''_2Y(C_5H_5)$], 34.6 G (Cp′ = $C_5H_4SiMe_3$, Cp″ = $C_5H_3(SiMe_3)_2$-1,3).

Table 4.1. Comparison of room-temperature EPR parameters of reduction products of YX_3 complexes (X = anion). R = $SiMe_3$, Cp′ = $C_5H_4SiMe_3$, Cp″ = $C_5H_3(SiMe_3)_2$-1,3, Cp^{Me} = C_5H_4Me, Cp^t = $C_5H_4C(Me)_3$, Cp^{tet} = C_5Me_4H, and Cp = C_5H_5. A in Gauss. † value is an average of the data at 77 K. *information from this work.

Compound Reduced	***g***	***A***	**Ref.**
Cp''_2YCp	1.99	34.6	[32]
YCp''_3	1.99	36.1	[32]
Cp''_2YCp^{Me}	1.99	36.4	[32]
YCp'_3	1.99	36.6	[4]
$YCp_3(THF)$	1.99	42.8	[32]
$YCp^{Me}_3(THF)$	1.99	46.9	[32]
YCp^t_3	1.99	51.0	[12]
YCp^{tet}_3	1.99	64.8	[13]
$Y(NR_2)_3$	1.98	110	[16]
1-Y	1.99†	152†	*
3-Y	1.98†	154†	*

The large yttrium hyperfine coupling constants are consistent with a previous correlation that the stability of solutions obtained by reducing Y(III) decreases as the hyperfine coupling constant increases.[32] The rationale was that the larger the *A* values, the more electron density that is localized on the metal center and the more reactive it becomes. The hyperfine coupling constants of **2-Y** and **4-Y** are even larger than the 110 G value for the $Y(NR_2)_3$ reduction product[16] which suggests that the OAr′ and OAr ligands put the most electron density on the metal compared to all the ligands surveyed to date.

It should be noted that crystals of "$[YCp''_3]^{1-}$" were also not isolated, although its A value of 36.1 G is between of the values of the crystallographically-characterized [K(18-crown-6)][YCp'_3][4] and [K(crypt)][$Cp''_2Y(C_5H_5)$].[32] This indicates that factors other than those affecting A values must be operative in affecting the stability of the Ln(II) complexes. In this "$[Cp''_3Y]^{1-}$" case, it likely that steric factors are involved as described below.

In the case of scandium, both the EPR spectra and the X-ray crystal structure of **2-Sc** are consistent with a Sc(II) complex. The eight line EPR-spectrum of **2-Sc** is similar to that of crystallographically-characterized [K(crypt)][$Sc(NR_2)_3$],[18] and the 285.9 G hyperfine coupling constant value for **2-Sc** is higher than the 225 G value for [K(crypt)][$Sc(NR_2)_3$]. This is consistent with the trend shown in Table 4.1 for the yttrium aryloxides vs yttrium amide. The A value for **2-Sc** is also larger than those found for the Sc(II) complexes Sc(η-^{t}Bu$_3$C$_6$H$_3$)(η^6:η^1-^{t}Bu$_2$[CMe$_2$CH$_2$]C$_6$H$_3$)H (A = 13.45 G)[30] and Sc(η^5-$P_2C_3{}^t$Bu$_3$)$_2$ ($A_\perp$ = 29.9 G, $A_{/\!/}$ = 52.9).[29]

Sc Structure. The average Sc−O bond distances in [K(crypt)][$Sc(OAr')_3$], **2-Sc**, are 0.09 Å larger than those in the Sc(III) precursor, $Sc(OAr')_3$, **1-Sc**.[28] Comparison of the $Ln^{III}Cp'_3$/$[Ln^{II}Cp'_3]^{1-}$ series of eq 1.1 showed differences in Ln–ligand distances of only 0.03 Å for Ln(II) ions that had $4f^n5d^1$ electron configurations and 0.1−0.2 Å for Ln(II) that had $4f^{n+1}$ configurations (*i.e.*, the traditional Ln(II) ions of Eu, Yb, Sm, and Tm).[2,3] The increase in Sc−O distance from Sc(III) to Sc(II) with these aryloxides is in between these two ranges even though scandium has no *f* orbitals. The C–C bond lengths in the OAr′ rings in **1-Sc** and **2-Sc** do not differ from one another, consistent with the unpaired electron in **2-Sc** being Sc-based as opposed to ligand-based. The 0.08 Å difference in Sc–N bond distances of $Sc^{III}(NR_2)_3$ and [K(crypt)][$Sc^{II}(NR_2)_3$] (R = $SiMe_3$) is

similar[18] to that of the aryloxides. Hence, care must be taken in assigning electron configurations for new Ln(II) ions solely on the basis of the difference in bond distances for Ln(III) vs Ln(II).

UV-Visible Spectra. The UV-visible spectrum of **2-Y** (Figure 4.1) has a single strong feature in the visible region, with an extinction coefficient of 6,500 $M^{-1}cm^{-1}$, greater than those of **2-Sc** (2,300 $M^{-1}cm^{-1}$) and the $[Cp'_3Ln]^-$ complexes in eq 1.1 (~5,000 $M^{-1}cm^{-1}$).[2] In contrast, **2-Sc** (Figure 7.1) shows several strong absorptions in the visible region which differs from that of $[K(crypt)][Sc(NR_2)_3]$ and the $[LnCp'_3]^{1-}$ ($Cp' = C_5H_4SiMe_3$, Ln = Pr, Gd, Tb, Ho, Er, Lu, and Y) complexes which have only a single feature in the same region. The solutions of **2-Ln** have spectra that have a single strong feature plus a shoulder, in contrast to the single feature of the $[LnCp'_3]^{1-}$ in eq 1.1 [2,3,18]

The simulated spectra properly reproduce the experimental data for most of the studied systems As explained above, in **2-Dy** the spectrum was not correctly assigned at DFT level because of problems with the prediction of its ground state nature. However, this was corrected when the electron correlation was included via CASSCF calculations.

Guzei Analysis. The Solid-G analysis points out a difference in **2-Y** and **2-Sc** that may be related to their difference in stability. It should be noted that the G parameters are probably best utilized for comparison of complexes within a similar series of ligands. Since the G parameter calculates the total area of the metal coordination sphere shielded by the ligands without distinguishing whether the steric crowding is near or far from the metal center, it is likely best used to compare the steric saturation of ligands with similar shapes. For example, the Cp''_3Ln complexes have all six Me_3Si substituents above and below the plane made by the metal and the centroids, which is

different from the three Me_3Si group in Cp'_3Ln which has two above and one below the plane. It is interesting to note that although $Y(OAr')_3$ crystallizes with five different molecules in the unit cell, the G parameters of these five variations are all between 81% and 82%.

The 83% G parameter of [K(crypt)][$Sc(OAr')_3$], **2-Sc**, falls within the range found for a variety of other stable Ln(III) compounds with values roughly between 80% and 90%.[2,19] However the 77% value estimated for "$[Y(OAr')_3]^{1-}$" , based on the optimized structure from DFT calculations, is outside the current range of stable species. This means that $[Y(OAr')_3]^{1-}$ is significantly less sterically saturated than the currently-isolable complexes of Y(II), [K(crypt)][YCp'_3] and [K(crypt)][$Cp''_2Y(C_5H_5)$], which have G parameters of 86% and 90–91%, respectively. It is possible that relatively low coverage of ligands on $[Y(OAr')_3]^{1-}$ makes it too reactive to isolate. The Tb(II) complex $[K_2(18\text{-crown-}6)_2Cp^{Me}][TbCp^{Me}_3]$[10] ($Cp^{Me} = C_5H_4Me$), however, has a G parameter of 74%, even lower than the 77% estimate for $[Y(OAr')_3]^{1-}$, but was still able to be crystallographically characterized; the authors note that it "[decomposes] within seconds at temperatures above −35 °C." Thus, the trend holds, that Ln(II) complexes with insufficient steric saturation tend to be kinetically unstable. Since kinetic stability can also depend on the mechanism of decomposition of a given Ln(II) complex, the optimum degree of steric saturation for a Ln(II) complex is likely sensitive to the ligand set. In some complexes that would normally have low G parameters, agostic interactions can aid in stabilizing the complex. In the case of $[Y(OAr')_3]^{1-}$, this type of intramolecular interaction would be disfavored by the charge on the complex and the d electron on the metal center. The charge on the complex would also make less favorable the intermolecular interactions of the type found for the polymeric $[(\eta^5\text{-Cp})_2Y(\mu\text{-}\eta^5{:}\eta^1\text{-Cp})]_n$.[34]

The transient existence of **2-Dy**, **2-Ho**, and **2-Er** can also be explained by a lack of steric saturation since the size of these metals is similar to that of yttrium. **2-Gd** would be even more sterically unsaturated. To evaluate the Guzei parameter further, the half-life data on the crystallographically characterized [K(crypt)][LnCp′$_3$] complexes[2] were plotted against their G parameters, Figure 11.1.[2,6] The optimum thermal stability for this series is found for Ln = Pr, which is neither the most sterically saturated nor unsaturated complex. The range of G parameters may be too narrow to make a definitive correlation, but Figure 11.1 suggests that within a given series, there could be an optimum G parameter that correlates with stability. More data will be needed to determine if this analysis is more generally applicable. Since OAr′ is a less sterically saturating ligand than Cp′, the only isolable [Ln(OAr′)$_3$]$^{1-}$ complex in the rare earth series may be with the smallest metal, scandium.

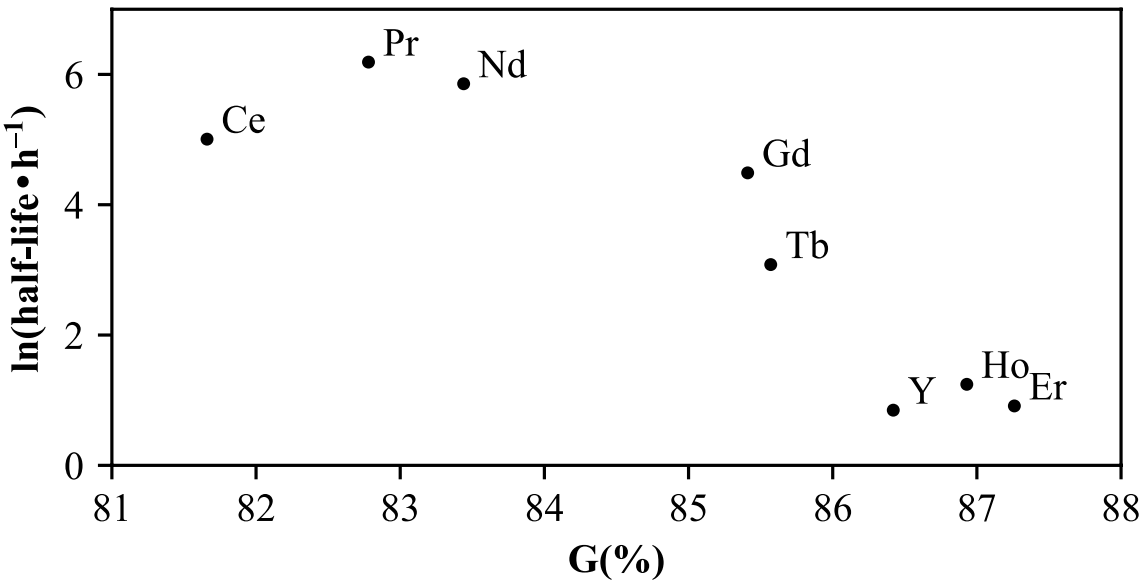

Figure 11.1. Plot of ln(half-life•h^{-1}) vs. G parameter of the Ln-containing anion for [K(crypt)][LnCp′$_3$].

CONCLUSION

Reduction of $Ln(OAr')_3$ complexes with KC_8 under argon in THF provides EPR evidence for $[Ln(OAr')_3]^-$ complexes of Sc(II) and Y(II) and UV-vis data suggest that similar complexes are generated in solution for Gd, Dy, Ho, and Er. However, only in the case of the smallest metal, Sc, is a crystallographically-characterizable Ln(II) complex isolated: $[K(crypt)][Sc(OAr')_3]$. The hyperfine coupling constants suggest that more electron density is on the metal in these $[Ln(OAr')_3]^{1-}$ anions than in analogous complexes of cyclopentadienyl or amide ligands. Analysis of the amount of steric saturation in these aryloxide complexes using the method of Guzei suggests the only with the smallest metal is there sufficient steric saturation to have the necessary thermal stability for crystallization at temperatures above −78 °C. These data provide calibration points to evaluate the effects of steric and electronic factors on the accessibility of Ln(II) complexes as the ligands are varied.

EXPERIMENTAL

All manipulations and syntheses described below were conducted with the rigorous exclusion of air and water using standard Schlenk line and glovebox techniques under an argon atmosphere. Solvents were sparged with UHP argon and dried by passage through columns containing Q-5 and molecular sieves prior to use. Deuterated NMR solvents were dried over NaK alloy or Na/benzophenone, degassed by three freeze-pump-thaw cycles, and vacuum transferred before use. ^1H and $^{13}C\{^1H\}$NMR spectra were recorded on a Bruker AVANCE600 spectrometer (^1H operating at 600 MHz, $^{13}C\{^1H\}$ at 151 MHz) at 298 K unless otherwise stated and referenced internally to residual protio-solvent resonances. Elemental analyses were conducted on a Perkin-Elmer 2400 Series II CHNS elemental analyzer. UV−visible spectra were collected in THF at −78 °C using a Varian Cary 50 Scan UV-visible spectrophotometer. EPR spectra were collected using X-band

frequency (9.3−9.8 GHz) on a Bruker EMX spectrometer equipped with an ER041XG microwave bridge, and the magnetic field was calibrated with DPPH (g = 2.0036). Infrared (IR) transmittance measurements were taken as compressed solids on a Thermo Scientific Nicolet iS5 spectrophotometer with an iD5 ATR attachment. LiOAr′•OEt_2 was synthesized by a literature procedure.[37] HOAr′ (Acros) was sublimed before use. 4,7,13,16,21,24-hexaoxa-1,10-diazabicyclo[8.8.8]hexacosane, 2.2.2-cryptand (crypt, VWR) was dried under reduced pressure (10^{-3} Torr) before use. KC_8 was synthesized according to literature methods.[38] $LnCl_3$ were prepared according to a literature preparation.[39] EPR spectra were simulated using EasySpin.[40]

Ln(OAr′)$_3$, 1-Ln. In an adaptation of a literature procedure,[25,41] $LnCl_3$ (1 equiv) and LiOAr′ •OEt_2 (3 equiv) were refluxed overnight in THF under an Ar flow. After cooling to RT, solvent was removed *in vacuo* to give oily solids. These solids were heated in a boiling water bath and vacuum was applied until solvent evaporation was no longer detected on the vacuum gauge, yielding brittle, dry solids. These solids were loaded into a glass sublimation tube and a plug of glass wool was installed above the solids. The solids were sublimed at 10^{-5} Torr and 260 °C overnight. Solids appeared where the tube exited the furnace. The tube was placed deeper into the furnace to re-sublime the solids overnight once more. The resulting highly oxygen- and moisture-sensitive solids were isolated from the sublimation tube in a glove box. The sublimation steps are crucial for purity of the materials.

1-Sc.[28] This complex was prepared as described above by combining $ScCl_3$ (420 mg, 2.7 mmol) with LiOAr′•OEt_2 (2.38 g, 7.94 mmol) with a yield of 1.2 g (66%) of straw-colored solids. ^{1}H NMR (C_6D_6, Figure 12.1): δ 7.08 (s, 6H, *m-H*), 2.24 (s, 9H, C_6H_2*Me*), 1.58 ppm (s, 54H, ^{t}*Bu*$_2$). ^{13}C{^{1}H} NMR (C_6D_6, Figure 13.1): δ 158.2 (*i*-C), 137.2 (*o*-C), 127.5 (*p*-C), 126.3 (*m*-C), 35.1

(*C*Me$_3$), 32.3 (C*Me$_3$*), 21.5 ppm (C$_6$H$_2$*Me*). IR (Figure 14.1): 3069w br, 2956m br, 2919m, 2874w, 2820w, 2734w, 1751w, 1477w, 1456m, 1420s, 1384m, 1354m, 1294w br, 1261m, 1237s br, 1215m, 1120m, 1041w br, 1023w br, 950m, 925w br, 887w, 859s br, 808m br, 777w sh, 772m cm^{-1}. Anal. Calcd. For $C_{45}H_{69}O_3Sc$: C, 76.88; H, 9.89. Found: C, 74.21; H, 9.48. Results formulate as $C_{45}H_{69}$ but low % composition results across several analyses suggest incomplete combustion of the sample.[42–44]

1-Y. This complex was prepared as described above by combining YCl_3 (760 mg, 3.9 mmol) with LiOAr′•OEt_2 (3.53 g, 11.8 mmol) with a yield of 2.3 g (78%) of white solids. X-ray quality crystals could be grown by slow evaporation of a pentane solution by diffusing the pentane into toluene at −30 °C (Table 5.1). ^{1}H NMR (C_6D_6, Figure 15.1): δ 7.10 (s, 6H, *m-H*), 2.29 (s, 9H, C$_6$H$_2$*Me*), 1.55 ppm (s, 54H, ^{t}*Bu$_2$*). ^{13}C{^{1}H} NMR (C_6D_6, Figure 16.1): δ 158.5 (*i*-C), 136.8 (*o*-C), 126.2 (*p*-C), 126.0 (*m*-C), 34.8 (*C*Me$_3$), 32.1 (C*Me$_3$*), 21.5 ppm (C$_6$H$_2$*Me*). IR (Figure 17.1): 3065w br, 2956m br, 2912m br, 2873w, 2920w sh, 2731w, 1756w, 1514w, 1477w sh, 1457m, 1422s, 1390w sh, 1358m, 1358w sh, 1350m, 1325w, 1295w br, 1253s, 1244s, 1213m, 1196w sh, 1120m, 1204w, 949w, 922w br, 888m, 865w sh, 859w, 844s, 805m, 778m, 774m cm^{-1}. Anal. Calcd. For $C_{45}H_{69}O_3Y$: C, 72.36; H, 9.31. Found: C, 69.50; H, 8.96. Multiple attempts gave incomplete combustion as is sometimes observed with rare-earth metal complexes.[42–44] However, the observed CH ratio, $C_{45}H_{69}$, matches the calculated.

1-Gd. This complex was prepared as described above by combining $GdCl_3$ (98 mg, 0.37 mmol) with LiOAr′•OEt_2 (310 mg, 1.0 mmol) with a yield of 87 mg (30%) of white solids. Anal. Calcd. For $C_{45}H_{69}O_3Gd$: C, 66.29; H, 8.53. Found: C, 66.15; H, 8.58.

1-Dy. This complex was prepared as described above by combining $DyCl_3$ (760 mg, 2.8 mmol) with LiOAr′•OEt_2 (2.45 g, 8.17 mmol) with a yield of 1.5 g (66%) of beige-to-pink solids.

IR (Figure 18.1): 3061w, 2955m, 2913m, br, 1821w br, 2821w, 2731w, 1456s, 1385m, 1359w sh, 1350w, 1327w, 1297w, 1244s br, 1312m, 1194w sh, 1120m, 1023w, 949w, 924w, 888w, 865w, 860w, 842s, 804m, 778w, 774w cm^{-1}. Anal. Calcd. For $C_{45}H_{69}DyO_3$: C, 65.87; H, 8.48. Found: C, 65.53; H, 8.90.

1-Ho. This complex was prepared as described above by combining $HoCl_3$ (300 mg, 1.1 mmol) with LiOAr′•OEt_2 (1.01 g, 3.35 mmol) with a yield of 280 mg (30%) of pink solids. IR (Figure 19.1): 3674w br, 3640w sh, 3626w br, 3071w br, 2953s br, 2912s br, 2871m br, 2731w, 1753w br, 1480m sh, 1456m, 1420s, 1384m, 1361w, 1349w, 1315w sh, 1294w sh, 1246s br, 1214m, 1201w sh, 1152m br, 1120m, 1039w, 1027w, 949w, 935w, 922w, 889w, 866w, 861w, 842w, 805w, 791w, 774w, 769w cm^{-1}. Anal. Calcd. For $C_{45}H_{69}HoO_3$: C, 65.68; H, 8.45. Found: C, 51.36; H, 6.78. Incomplete combustion was observed with this compound, but the observed CH ratio, $C_{45}H_{71}$, was close to the calculated.[42–44]

1-Er.[41] This complex was prepared as described above by combining $ErCl_3$ (770 mg, 2.8 mmol) with LiOAr′•OEt_2 (2.46 g, 8.19 mmol) with a yield of 1.5 g (65%) of pink-red solids. IR (Figure 20.1): 3066w br, 2960m br, 2916m br, 2867w br, 2814w, 2730w, 1755w br, 1477w sh, 1457m. 1422s, 1385m, 1369w, 1358w sh, 1351w br, 1295w br, 1251s br, 1245s br, 1213m, 1196m sh, 1120m, 1024w, 949w, 922w br, 889w, 884w sh, 859m, 843s, 805m, 778m, 774m cm^{-1}.

[K(crypt)][Sc(OAr′)$_3$] 2-Sc. **1-Sc** (100 mg, 0.14 mmol) and crypt (56 mg, 0.15 mmol) were dissolved in a 1:1 THF:Et_2O solution (3 mL) with a glass stir bar and chilled to −30 °C. KC_8 (29 mg, 0.21 mmol, 1.5 equiv) was tapped into the solution with stirring and the mixture immediately turned black. After ~1 minute of stirring, the mixture was filtered and the resulting dark maroon solution was layered under – 30 °C hexane (10 mL) and stored at – 30 °C overnight. The solvent was removed *in vacuo* to give black solids, which were chilled to –30 °C and triturated

with −30 °C pentane (3 x 1 mL). The pentane was removed in vacuo to give black-purple solids, **2-Sc** (97 mg, 49% yield). X-ray quality crystals could be grown from a THF solution (6 mL) layered under pentane (3 mL), and stored at – 30 °C for four days (Figure 8.1, Table 6.1). EPR (Figure 6.1) (THF, 77 K): $g_{\perp} = 1.98$, $g_{\parallel} = 2.00$, $A_{\perp} = 290.5$ G, $A_{\parallel} = 288.8$ G. (THF, RT): $g = 1.98$ and $A = 285.9$ G. UV-vis (THF, −78 °C, Figure 7.1) λ_{max} (ε): 406 (2100), 522 (2300), 679 nm (790 $M^{-1}cm^{-1}$). IR (Figure 21.1): 3739w, 1636w, 2952m br, 2891m br, 2817w sh, 2358w, 1604w, 1477m br, 1456m, 1445w br, 1416s, 1383m, 1374w sh, 1358w sh, 1354m, 1292w sh, 1276m, 1258s, 1248s, 1219m, 1200m br, 1132m, 1103s, 1078m, 1059w, 1025w br, 949m, 932m, 890m, 840m sh, 834m, 807m, 783m, 753m br cm^{-1}. Anal. Calcd. For $C_{63}H_{105}KN_2O_9Sc$: C, 67.65; H, 9.46; N, 2.50. Found: C, 64.71; H, 9.22; N, 2.42. Incomplete combustion was observed with this sample but the observed CHN ratio, $C_{63}H_{107}N_2$, matches the calculated.[42–44]

2-Ln. A solution of **1-Ln** and crypt (1 equiv) was made in THF (~1–10 mM, ~15 mL). A flash reduction column[2,5] was prepared in a glass pipette by tightly packing pieces of a Kimwipe into the bottom of the pipette, with loosely packed Kimwipe above the tightly packed wad, followed by an excess of KC_8 on top of the Kimwipe. The solution, along with the flash reduction column and another glass pipette, were chilled to −30 °C for at least 1 hour. The solution of **1-Ln** and crypt was then added to the flash reduction column using the chilled pipette and mixed with the KC_8 by repeatedly drawing the solution into the chilled pipette and back into the flash column. The solution became a black suspension and then was forced through the Kimwipe to filter it and yield dark-colored **2-Ln**. If the solution was analyzed by UV-visible spectroscopy, the solution was expressed into a pre-chilled cuvette (1 mm or 1 cm) with a Teflon stopcock, sealed, then placed in a dry ice/isopropanol bath at −78 °C until the spectrum could be acquired. If the solution was analyzed by EPR spectroscopy, the solution was expressed into a chilled EPR tube in a chilled

hexane bath. The EPR tube was then stoppered, quickly removed from the glove box, and frozen in liquid nitrogen.[16]

2-Y. Deep-blue solution. At room temperature, solution fades to colorless in ca. 1 minute. EPR (Figure 3.1) (THF, 77 K): $g_{\perp} = 1.97$, $g_{\parallel} = 2.00$, $A_{\perp} = 155.4$ G, $A_{\parallel} = 148.7$ G. UV-Vis (THF, −78 °C, Figure 4.1): λ_{max} (ε): 704 nm (6,500 $M^{-1}cm^{-1}$).

2-Gd. Deep-purple solution. UV-Vis (THF, –78 °C): λ_{max} (ε): 574 (4,500), 434 nm (1,900 sh $M^{-1}cm^{-1}$).

2-Dy. Deep-purple solution. UV-Vis (THF, –78 °C): λ_{max} (ε): 587 (5,200), 432 nm (3,100 sh $M^{-1}cm^{-1}$).

2-Ho. Deep-purple solution. UV-Vis (THF, –78 °C): λ_{max}, nm (ε, $M^{-1}cm^{-1}$): 579 (2,000), 432 (1,200 sh).

2-Er. Deep-purple solution. UV-Vis (THF, –78 °C): λ_{max} (ε): 583 (6,200), 431 nm (3,600 sh $M^{-1}cm^{-1}$).

Y(OAr)$_3$, 3-Y. Synthesized according to literature procedures.[27] ^{1}H NMR (C_6D_6, Figure 22.1): δ 7.25 (d, J = 7.8 Hz, 6H, *m-H*), 6.83 (t, J = 7.8 Hz, 3H, *p-H*), 1.52 (s, 54H, $^tBu_2$).

Reduction of 3-Y to Form 4-Y. Using the protocol above for producing **2-Y**, a solution of **3-Y** (51 mg, 72 μmol) and crypt (26 mg, 70 μmol) in THF (3 mL) was reduced using a KC_8 flash reduction column. EPR (Figure 5.1) (THF, 77 K): $g_{\perp} = 1.96$, $g_{\parallel} = 2.00$, $A_{\perp} = 157.9$ G, and $A_{\parallel} = 149.9$ G. If the solution was warmed to RT, the color faded in 1 minute to yield a clear, colorless solution.

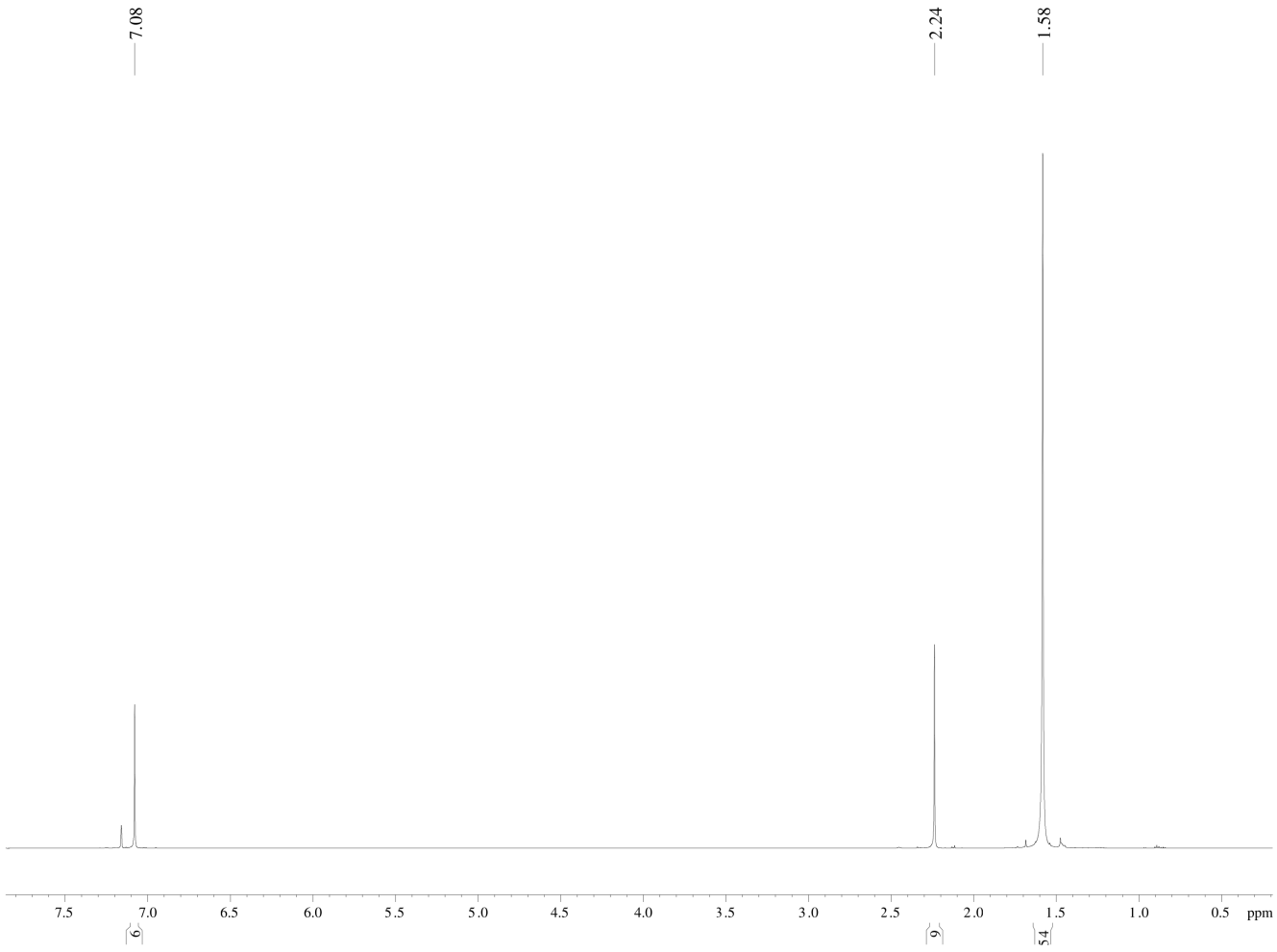

Figure 12.1. ^{1}H NMR spectrum of **1-Sc**.

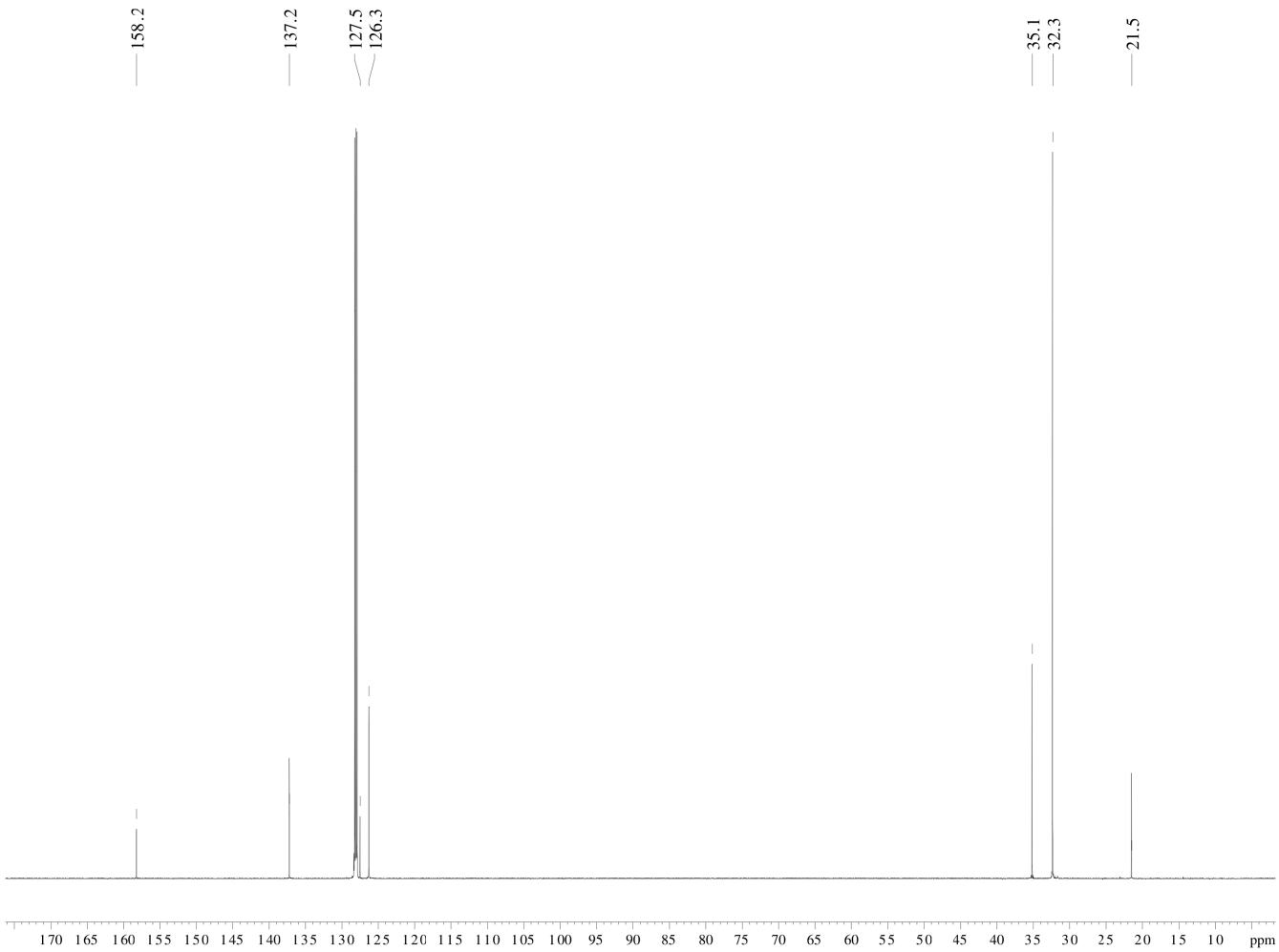

Figure 13.1. $^{13}C\{^{1}H\}$ NMR spectrum of **1-Sc**.

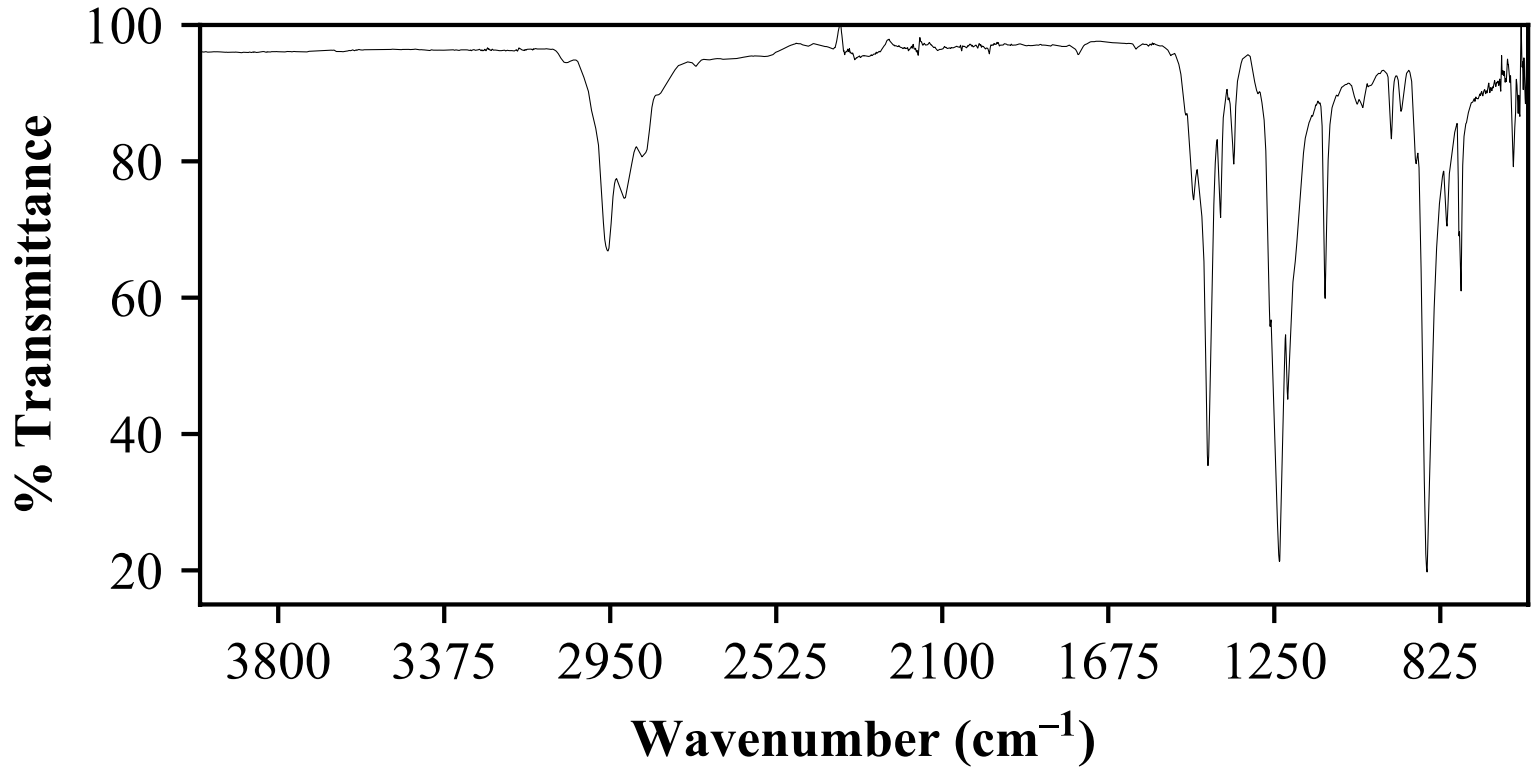

Figure 14.1. IR spectrum of **1-Sc**.

Table 5.1. Crystal data and structure refinement for **1-Y**.

Empirical formula	$C_{45}\ H_{69}\ O_3\ Y$	
Formula weight	746.91	
Temperature	88(2) K	
Wavelength	0.71073 Å	
Crystal system	Triclinic	
Space group	$P\bar{1}$	
Unit cell dimensions	a = 9.6899(5) Å	α= 76.1992(6)°.
	b = 25.0400(12) Å	β= 86.6283(7)°.
	c = 45.476(2) Å	γ = 80.9816(7)°.
Volume	10580.5(9) $Å^3$	
Z	10	
Density (calculated)	1.172 Mg/m^3	
Absorption coefficient	1.414 mm^{-1}	
F(000)	4020	
Crystal color	colorless	
Crystal size	0.322 x 0.307 x 0.120 mm^3	
Theta range for data collection	1.097 to 26.372°	
Index ranges	$-12 \le h \le 12$, $-31 \le k \le 31$, $-56 \le l \le 56$	
Reflections collected	118442	
Independent reflections	43149 [R(int) = 0.0526]	
Completeness to theta = 25.500°	99.8 %	
Absorption correction	Semi-empirical from equivalents	
Max. and min. transmission	0.7457 and 0.6481	
Refinement method	Full-matrix least-squares on F^2	
Data / restraints / parameters	43149 / 0 / 2311	
Goodness-of-fit on F^2	0.988	
Final R indices [I>2sigma(I) = 28134 data]	R1 = 0.0454, wR2 = 0.0975	
R indices (all data, 0.80 Å)	R1 = 0.0869, wR2 = 0.1114	
Largest diff. peak and hole	1.331 and -0.475 $e.Å^{-3}$	

X-ray Data Collection, Structure Solution and Refinement for **1-Y.**

A colorless crystal of approximate dimensions 0.120 x 0.307 x 0.322 mm was mounted in a cryoloop and transferred to a Bruker SMART APEX II diffractometer. The APEX2[45] program package was used to determine the unit-cell parameters and for data collection (30 sec/frame scan time for a sphere of diffraction data). The raw frame data was processed using SAINT[46] and SADABS[47] to yield the reflection data file. Subsequent calculations were carried out using the SHELXTL[48] program. There were no systematic absences nor any diffraction symmetry other than the Friedel condition. The centrosymmetric triclinic space group $P\bar{1}$ was assigned and later determined to be correct.

The structure was solved by dual space methods and refined on F^2 by full-matrix least-squares techniques. The analytical scattering factors[49] for neutral atoms were used throughout the analysis. Hydrogen atoms were included using a riding model. There were five independent molecules of the formula-unit present (Z = 10).

Least-squares analysis yielded wR2 = 0.1114 and Goof = 0.988 for 2311 variables refined against 43149 data (0.80 Å), R1 = 0.0454 for those 28134 data with $I > 2.0\sigma(I)$.

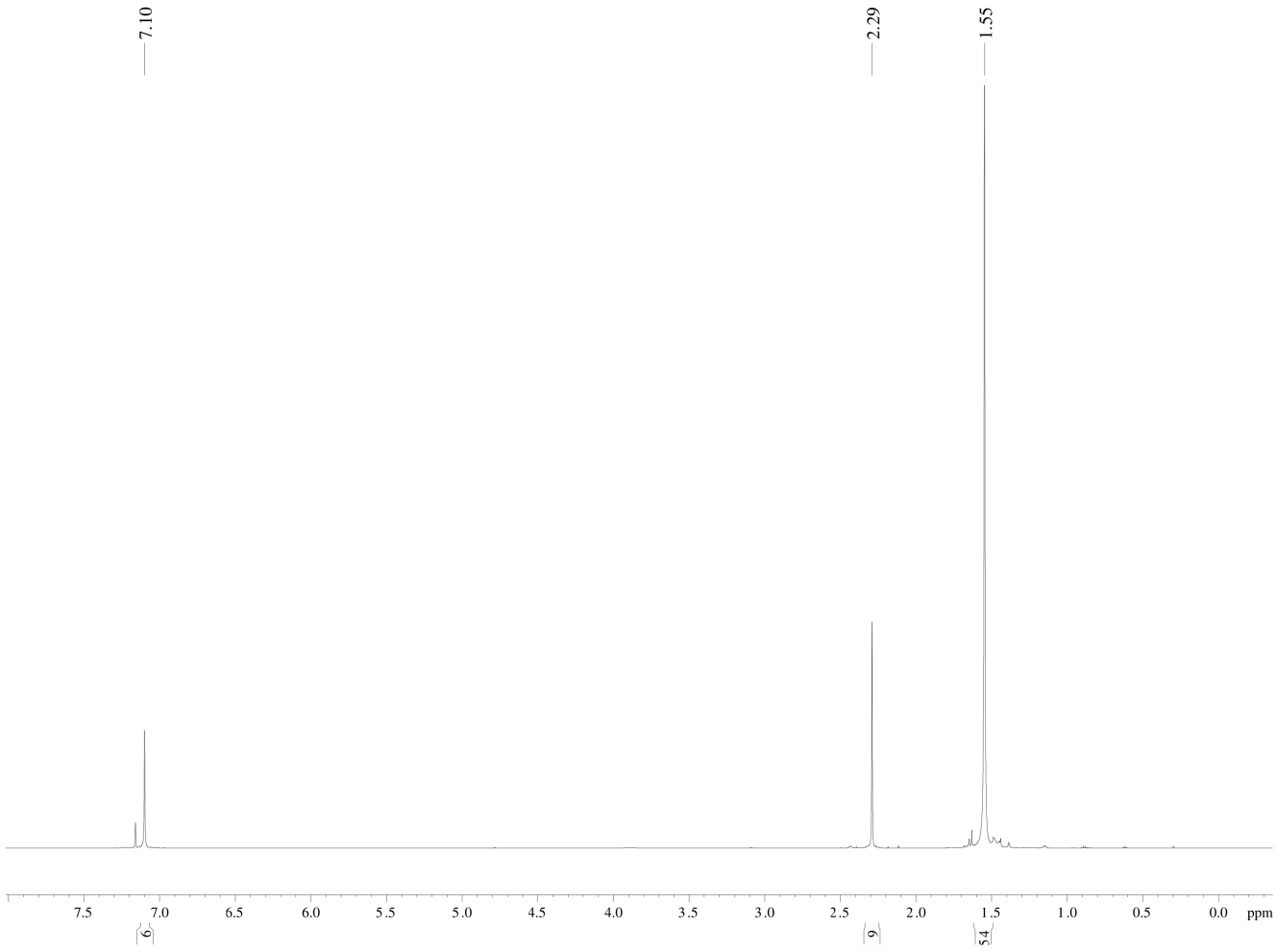

Figure 15.1. ^{1}H NMR spectrum of **1-Y**.

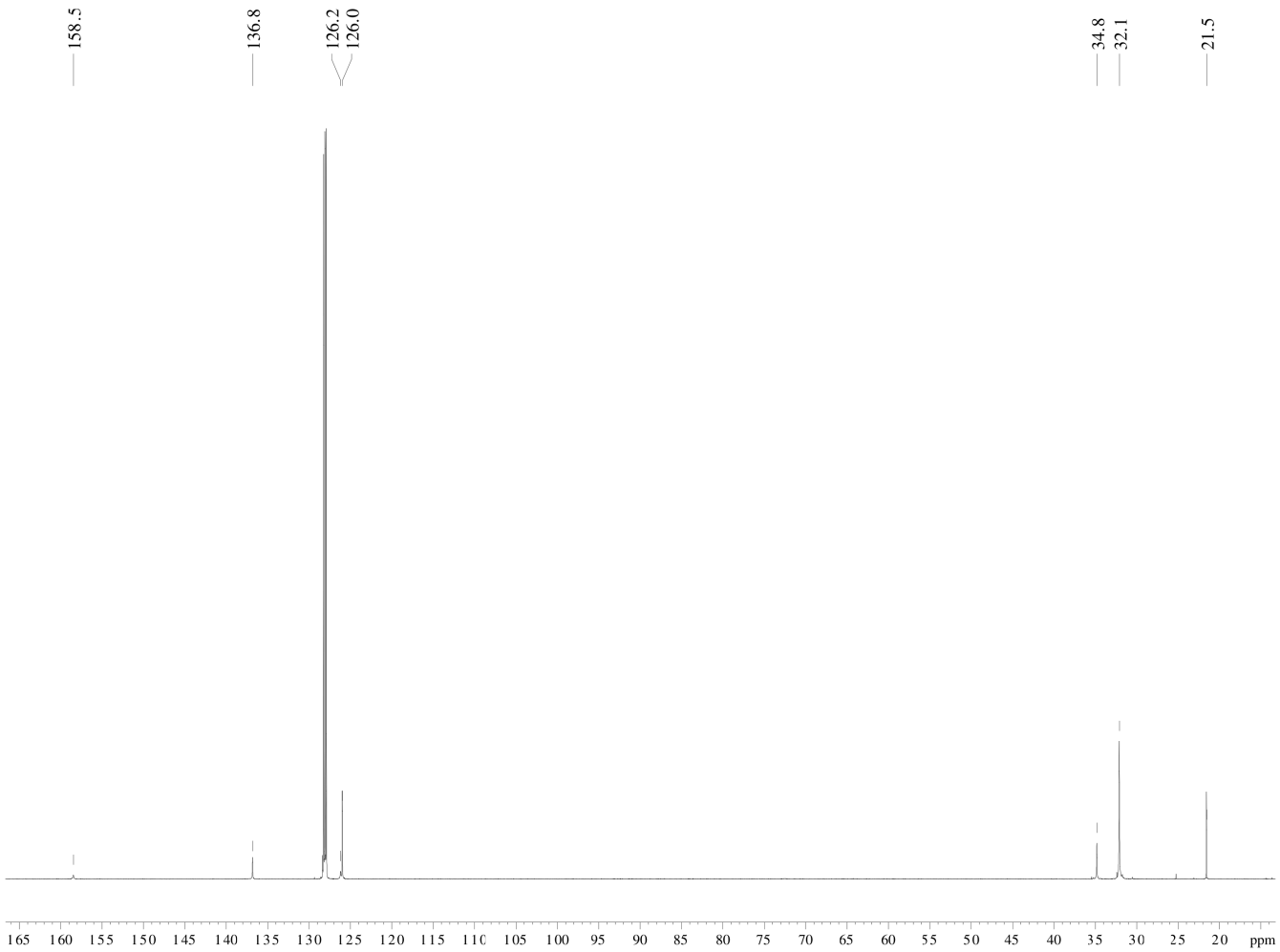

Figure 16.1. $^{13}C\{^{1}H\}$ NMR spectrum of **1-Y**.

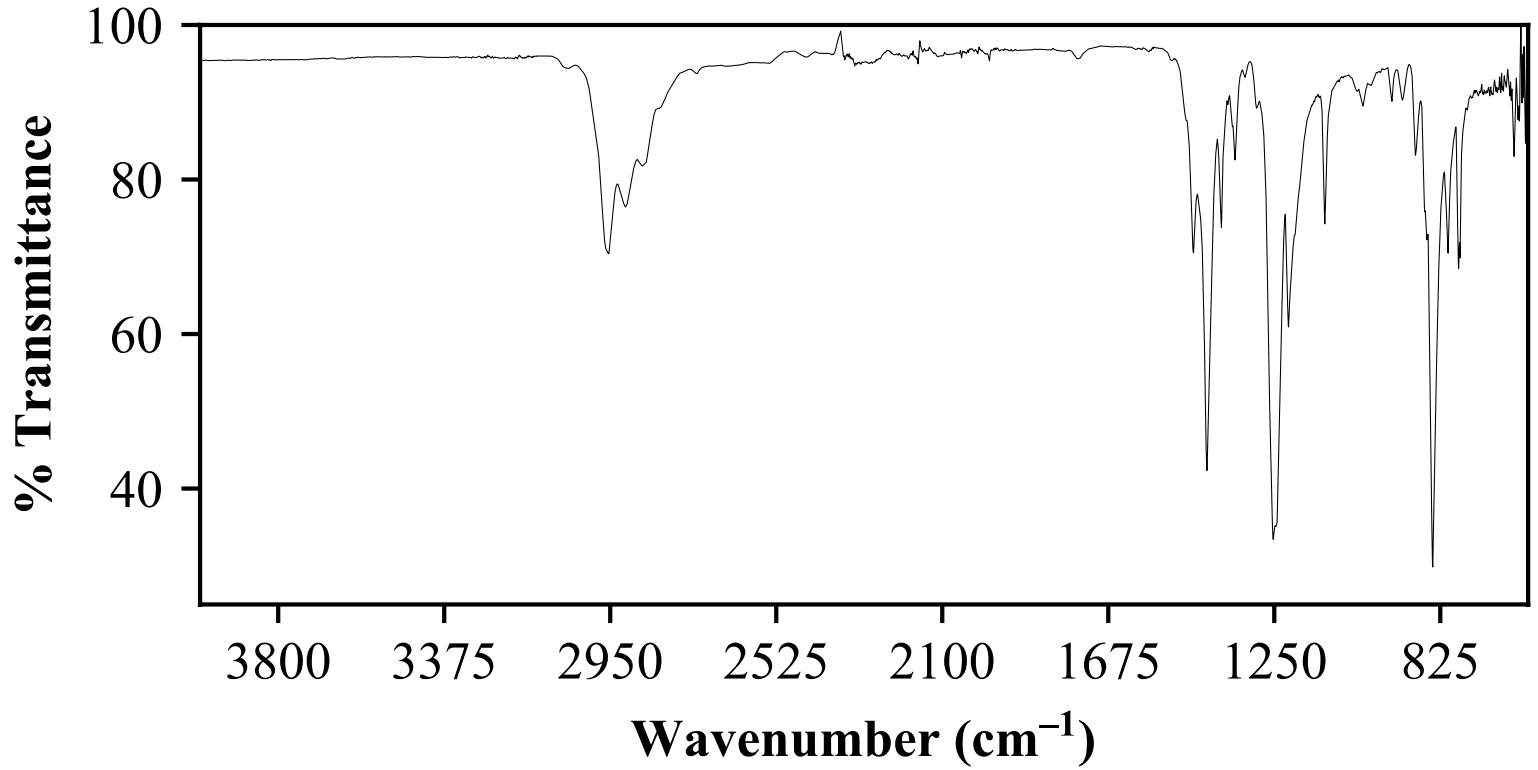

Figure 17.1. IR spectrum of **1-Y.**

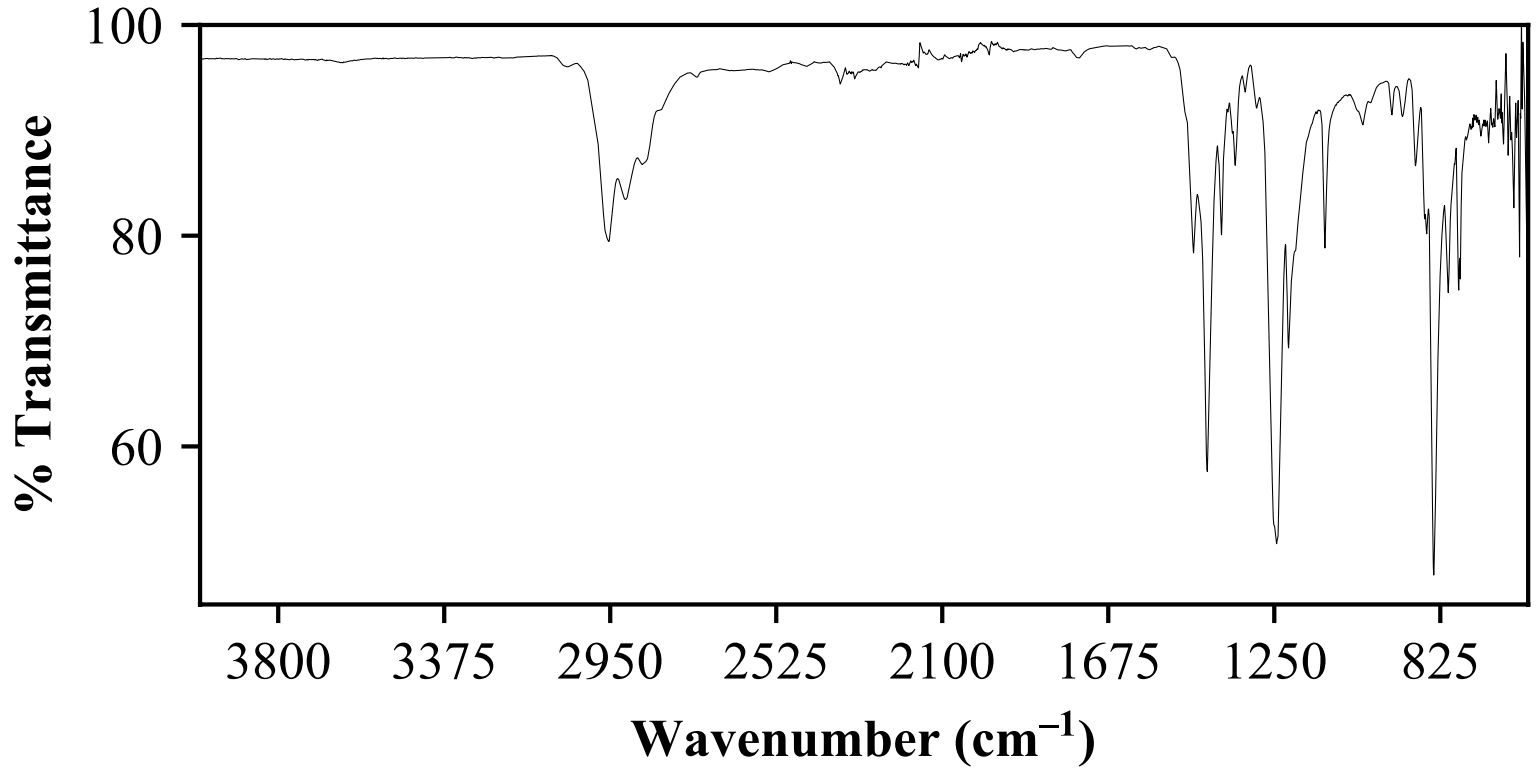

Figure 18.1. IR spectrum of **1-Dy**.

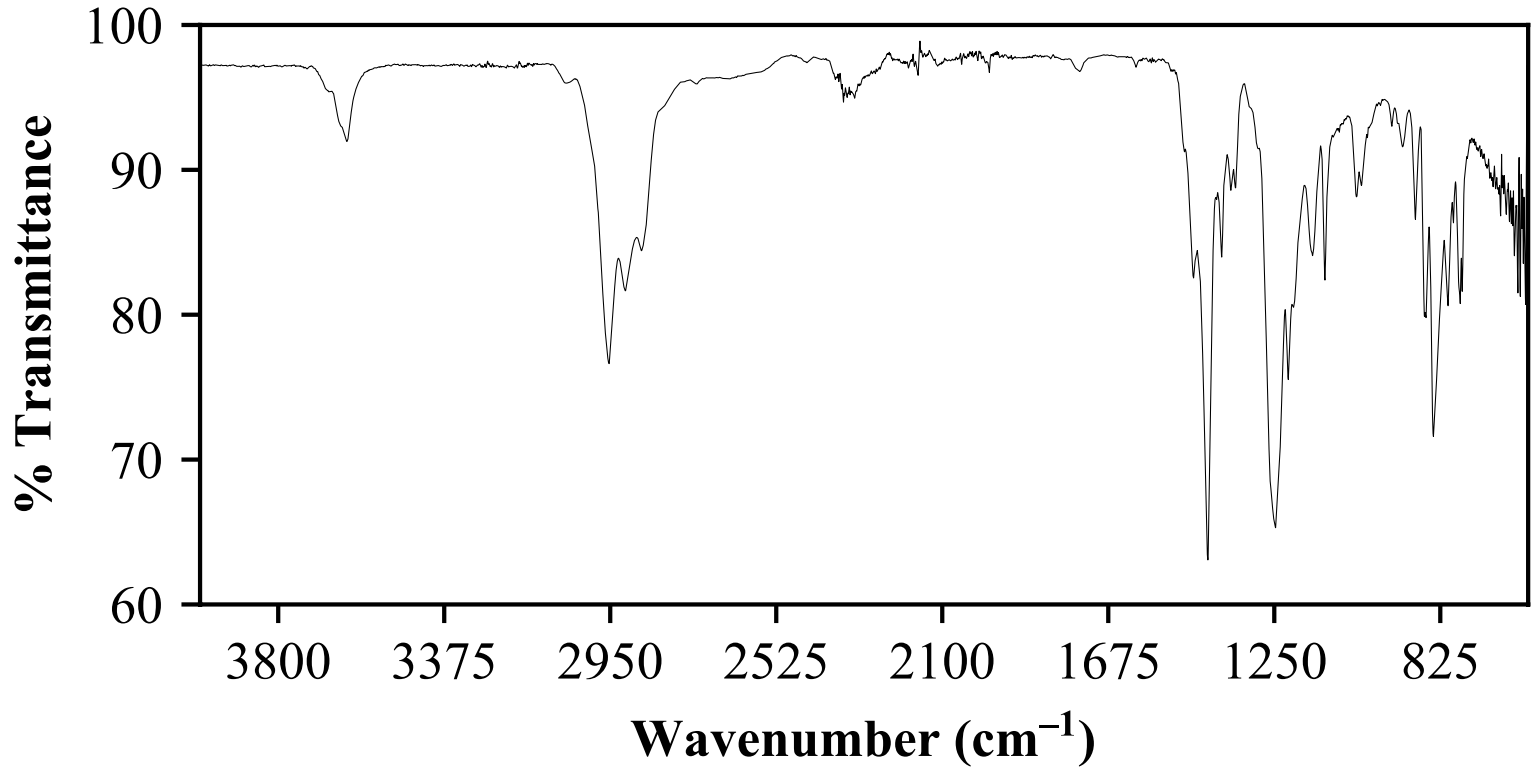

Figure 19.1. IR spectrum of **1-Ho**.

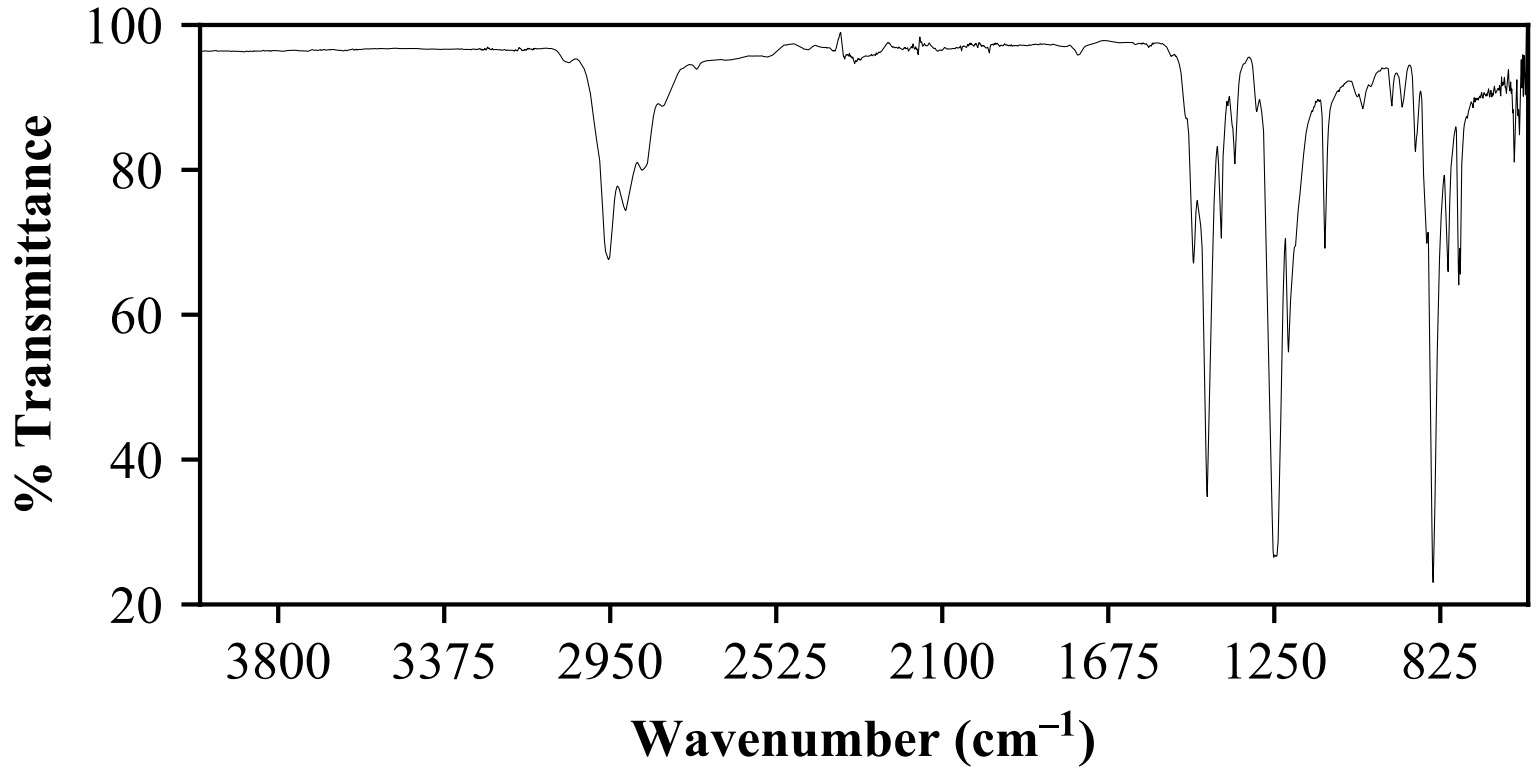

Figure 20.1. IR spectrum of **1-Er**.

Table 6.1. Crystal data and structure refinement for **2-Sc**.

Empirical formula	$C_{63}H_{105}KN_2O_9Sc \bullet 3.5(C_4H_8O)$	
Formula weight	1370.91	
Temperature	133(2) K	
Wavelength	0.71073 Å	
Crystal system	Triclinic	
Space group	$P\bar{1}$	
Unit cell dimensions	a = 14.087(3) Å	α= 105.970(3)°.
	b = 16.435(4) Å	β= 93.196(3)°.
	c = 19.453(4) Å	γ = 108.297(3)°.
Volume	4061.0(15) $Å^3$	
Z	2	
Density (calculated)	1.121 Mg/m^3	
Absorption coefficient	0.198 mm^{-1}	
F(000)	1498	
Crystal color	violet	
Crystal size	0.542 x 0.253 x 0.215 mm^3	
Theta range for data collection	1.102 to 27.103°	
Index ranges	$-18 \le h \le 18$, $-21 \le k \le 21$, $-24 \le l \le 24$	
Reflections collected	47364	
Independent reflections	17813 [R(int) = 0.0294]	
Completeness to theta = 25.500°	99.8 %	
Absorption correction	Semi-empirical from equivalents	
Max. and min. transmission	0.8015 and 0.7318	
Refinement method	Full-matrix least-squares on F^2	
Data / restraints / parameters	17813 / 0 / 839	
Goodness-of-fit on F^2	1.039	
Final R indices [I>2sigma(I) = 14306 data]	R1 = 0.0581, wR2 = 0.1520	
R indices (all data, 0.78 Å)	R1 = 0.0721, wR2 = 0.1628	
Largest diff. peak and hole	1.025 and -0.757 $e.Å^{-3}$	

X-ray Data Collection, Structure Solution and Refinement for **2-Sc.**

A violet crystal of approximate dimensions 0.215 x 0.253 x 0.542 mm was mounted in a cryoloop and transferred to a Bruker SMART APEX II diffractometer. The APEX2[45] program package was used to determine the unit-cell parameters and for data collection (60 sec/frame scan time for a sphere of diffraction data). The raw frame data was processed using SAINT[46] and SADABS[47] to yield the reflection data file. Subsequent calculations were carried out using the SHELXTL[48] program. There were no systematic absences nor any diffraction symmetry other than the Friedel condition. The centrosymmetric triclinic space group $P\bar{1}$ was assigned and later determined to be correct.

The structure was solved by dual space methods and refined on F^2 by full-matrix least-squares techniques. The analytical scattering factors[49] for neutral atoms were used throughout the analysis. Hydrogen atoms were included using a riding model. There were 3.5 molecules of tetrahydrofuran solvent present. Disordered solvents molecules were included using multiple components with partial site-occupancy-factors. One solvent molecule was disordered about an inversion center.

Least-squares analysis yielded wR2 = 0.1628 and Goof = 1.039 for 839 variables refined against 17813 data (0.78 Å), R1 = 0.0581 for those 14306 data with $I > 2.0\sigma(I)$.

There were several high residuals present in the final difference-Fourier map. It was not possible to determine the nature of the residuals although it was probable that additional tetrahydrofuran solvent was present. The SQUEEZE[50] routine in the PLATON[51] program package was used to account for the electrons in the solvent accessible voids.

Definitions:

$wR2 = [\Sigma[w(F_o^2-F_c^2)^2] / \Sigma[w(F_o^2)^2]]^{1/2}$

$R1 = \Sigma||F_o|-|F_c|| / \Sigma|F_o|$

$Goof = S = [\Sigma[w(F_o^2-F_c^2)^2] / (n-p)]^{1/2}$ where n is the number of reflections and p is the total number of parameters refined.

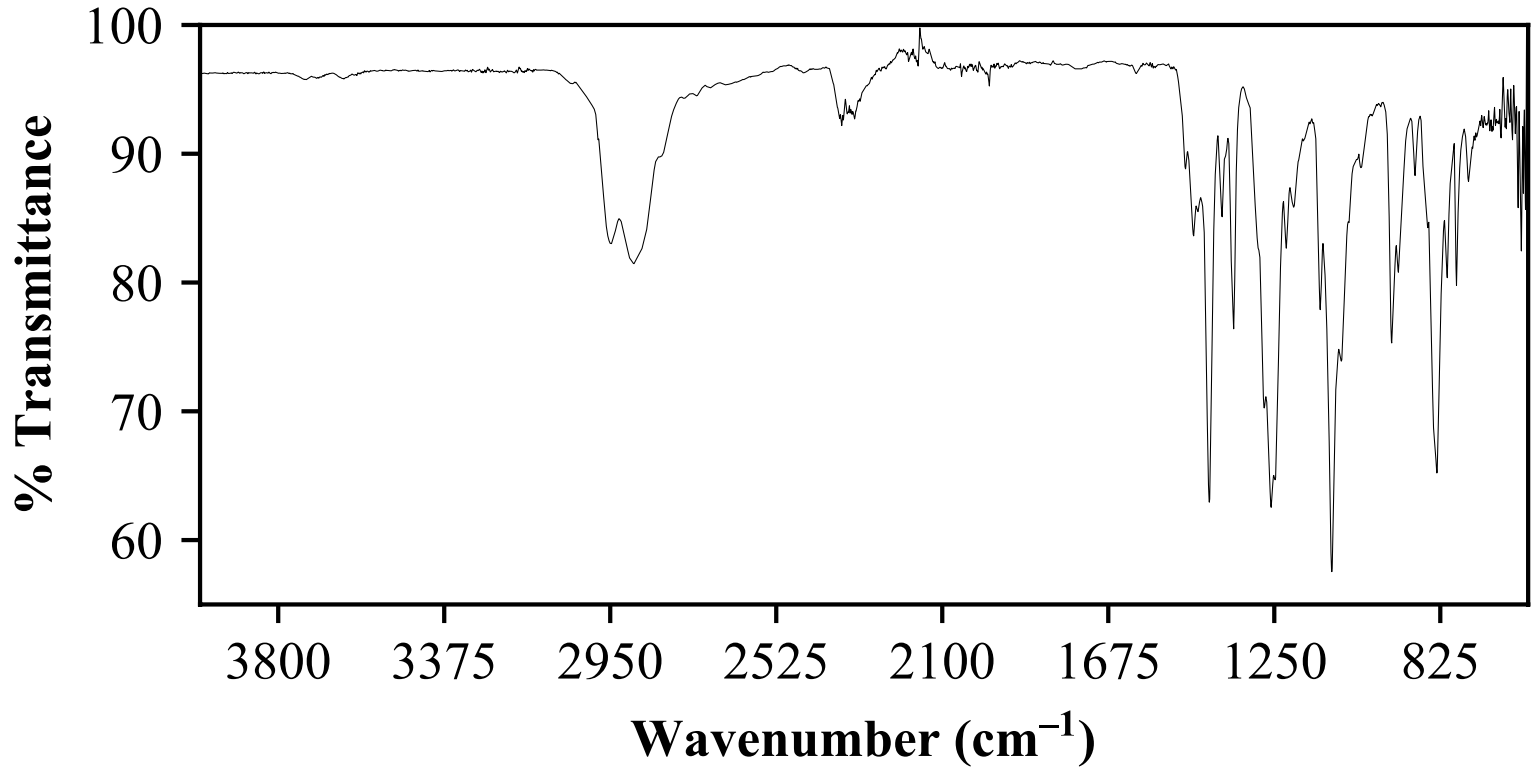

Figure 21.1. IR spectrum of **2-Sc**.

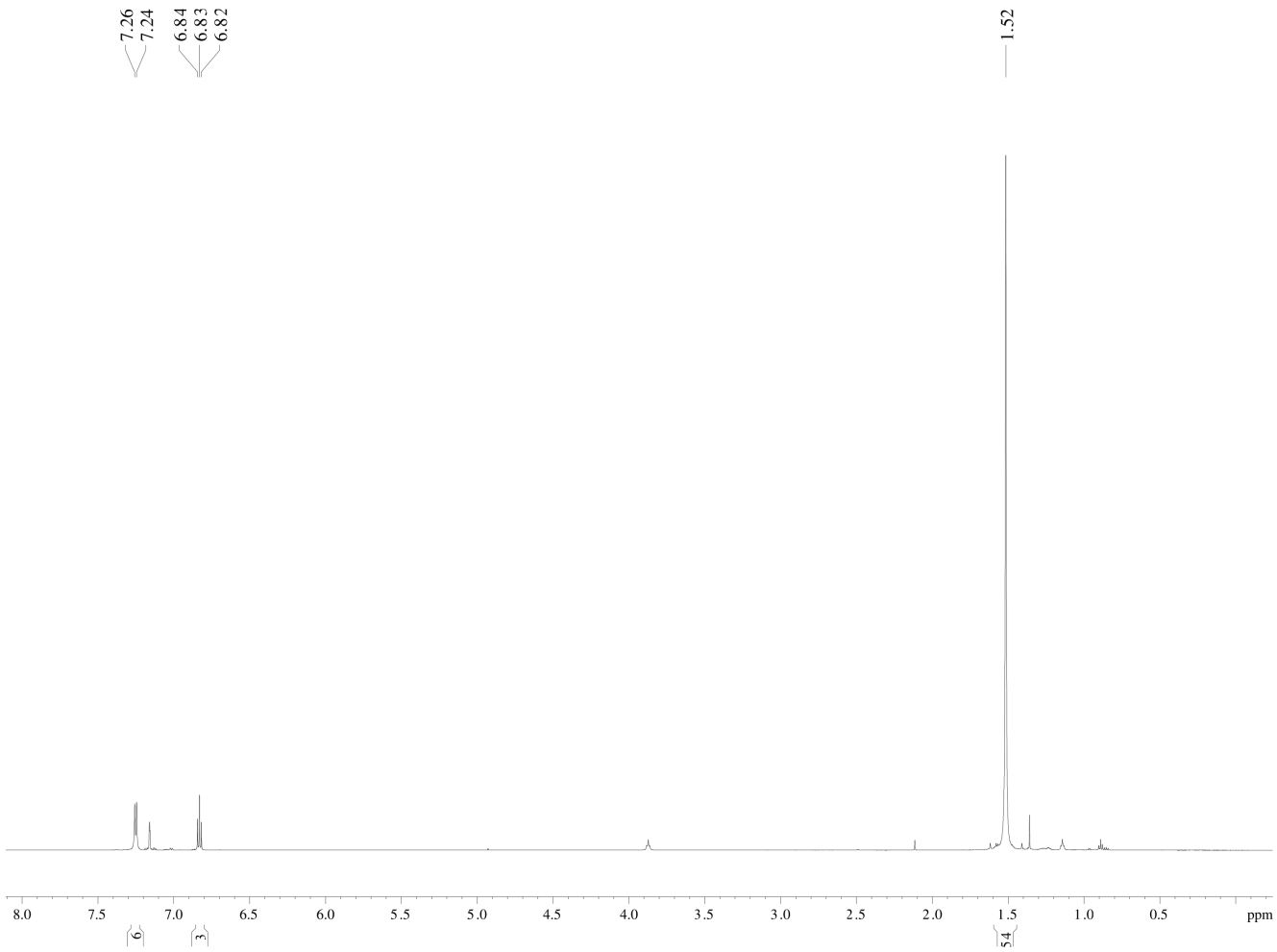

Figure 22.1. ^{1}H NMR spectrum of **3-Y**.

REFERENCES

(1) Hitchcock, P. B.; Lappert, M. F.; Maron, L.; Protchenko, A. V. *Angew. Chem. Int. Ed.* **2008**, *47*, 1488–1491.
(2) MacDonald, M. R.; Bates, J. E.; Ziller, J. W.; Furche, F.; Evans, W. J. *J. Am. Chem. Soc.* **2013**, *135*, 9857–9868.
(3) Fieser, M. E.; MacDonald, M. R.; Krull, B. T.; Bates, J. E.; Ziller, J. W.; Furche, F.; Evans, W. J. *J. Am. Chem. Soc.* **2015**, *137*, 369–382.
(4) MacDonald, M. R.; Ziller, J. W.; Evans, W. J. *J. Am. Chem. Soc.* **2011**, *133*, 15914–15917.
(5) MacDonald, M. R.; Bates, J. E.; Fieser, M. E.; Ziller, J. W.; Furche, F.; Evans, W. J. *J. Am. Chem. Soc.* **2012**, *134*, 8420–8423.
(6) Palumbo, C. T.; Darago, L. E.; Windorff, C. J.; Ziller, J. W.; Evans, W. J. *Organometallics* **2018**, *37*, 900–905.
(7) Jaroschik, F.; Momin, A.; Nief, F.; Le Goff, X.-F.; Deacon, G. B.; Junk, P. C. *Angew. Chem.* **2009**, *121*, 1137–1141.
(8) Jaroschik, F.; Nief, F.; Le Goff, X.-F.; Ricard, L. *Organometallics* **2007**, *26*, 1123–1125.
(9) Cassani, M. C.; Duncalf, D. J.; Lappert, M. F. *J. Am. Chem. Soc.* **1998**, *120*, 12958–12959.
(10) Huh, D. N.; Ziller, J. W.; Evans, W. J. *Dalton Trans.* **2018**, *47* (48), 17285–17290.
(11) Woen, D. H.; Huh, D. N.; Ziller, J. W.; Evans, W. J. *Organometallics* **2018**, *37*, 3055–3063.
(12) Angadol, M. A.; Woen, D. H.; Windorff, C. J.; Ziller, J. W.; Evans, W. J. *Organometallics* **2019**, *38* (5), 1151–1158.
(13) Jenkins, T. F.; Woen, D. H.; Mohanam, L. N.; Ziller, J. W.; Furche, F.; Evans, W. J. *Organometallics* **2018**, *37*, 3863–3873.
(14) Evans, W. J.; Lee, D. S.; Rego, D. B.; Perotti, J. M.; Kozimor, S. A.; Moore, E. K.; Ziller, J. W. *J. Am. Chem. Soc.* **2004**, *126*, 14574–14582.
(15) Fang, M.; Bates, J. E.; Lorenz, S. E.; Lee, D. S.; Rego, D. B.; Ziller, J. W.; Furche, F.; Evans, W. J. *Inorg. Chem.* **2011**, *50*, 1459–1469.
(16) Fang, M.; Lee, D. S.; Ziller, J. W.; Doedens, R. J.; Bates, J. E.; Furche, F.; Evans, W. J. *J. Am. Chem. Soc.* **2011**, *133*, 3784–3787.
(17) Gun'ko, Y. K.; Hitchcock, P. B.; Lappert, M. F. *J. Organomet. Chem.* **1995**, *499*, 213–219.
(18) Woen, D. H.; Chen, G. P.; Ziller, J. W.; Boyle, T. J.; Furche, F.; Evans, W. J. *Angew. Chem. Int. Ed.* **2017**, *56* (8), 2050–2053.
(19) Ryan, A. J.; Darago, L. E.; Balasubramini, S. G.; Chen, G. P.; Ziller, J. W.; Furche, F.; Long, J. R.; Evans, W. J. *Chem. Eur. J.* **2018**, *24*, 7702–7709.
(20) Palumbo, C. T.; Halter, D. P.; Voora, V. K.; Chen, G. P.; Chan, A. K.; Fieser, M. E.; Ziller, J. W.; Hieringer, W.; Furche, F.; Meyer, K. *Inorg. Chem.* **2018**, *57*, 2823–2833.
(21) Fieser, M. E.; Palumbo, C. T.; La Pierre, H. S.; Halter, D. P.; Voora, V. K.; Ziller, J. W.; Furche, F.; Meyer, K.; Evans, W. J. *Chem. Sci.* **2017**, *8*, 7424–7433.
(22) Halter, D. P.; Palumbo, C. T.; Ziller, J. W.; Gembicky, M.; Rheingold, A. L.; Evans, W. J.; Meyer, K. *J. Am. Chem. Soc.* **2018**, *140*, 2587–2594.

(23) Casely, I. J.; Ziller, J. W.; Fang, M.; Furche, F.; Evans, W. J. *J. Am. Chem. Soc.* **2011**, *133*, 5244–5247.
(24) Zhang, H.; Nakanishi, R.; Katoh, K.; Breedlove, B. K.; Kitagawa, Y.; Yamashita, M. *Dalton Trans.* **2018**, *47* (2), 302–305.
(25) Lappert, M. F.; Singh, A.; Smith, R. G.; Stecher, H. A.; Sen, A. *Synthetic Methods of Organometallic and Inorganic Chemistry*; Herrmann, W. A., Ed.; Georg Thieme Verlag: New York, 1997.
(26) Haddow, M. F.; Newland, R. J.; Tegner, B. E.; Mansell, S. M. *CrystEngComm* **2019**, *21*, 2884–2892.
(27) Steele, L. A. M.; Boyle, T. J.; Kemp, R. A.; Moore, C. *Polyhedron* **2012**, *42* (1), 258–264.
(28) Hitchcock, P. B.; Lappert, M. F.; Singh, A. *J. Chem. Soc. Chem. Commun.* **1983**, 1499–1501.
(29) Arnold, P. L.; Cloke, F. G. N.; Nixon, J. F. *Chem. Commun.* **1998**, 797–798.
(30) Cloke, F. G. N.; Khan, K.; Perutz, R. N. *J. Chem. Soc. Chem. Commun.* **1991**, *0*, 1372–1373.
(31) Shannon, R. D. *Acta Crystallogr. A* **1976**, *32*, 751–767.
(32) Corbey, J. F.; Woen, D. H.; Palumbo, C. T.; Fieser, M. E.; Ziller, J. W.; Furche, F.; Evans, W. J. *Organometallics* **2015**, *34*, 3909–3921.
(33) Guzei, I. A.; Wendt, M. *Dalton Trans.* **2006**, 3991–3999.
(34) Adam, M.; Behrens, U.; Fischer, R. D. *Acta Cryst. C* **1991**, *C47*, 968–971.
(35) Rogers, R. D.; Atwood, J. L.; Emad, A.; Sikora, D. J.; Rausch, M. D. *J. Organomet. Chem.* **1981**, *216*, 383–392.
(36) Coles, M. P.; Hitchcock, P. B.; Lappert, M. F.; Protchenko, A. V. *Organometallics* **2012**, *31*, 2682–2690.
(37) Çetinkaya, B.; Gümrükçü, I.; Lappert, M. F. *J. Am. Chem. Soc.* **1980**, *102* (6), 2086–2088.
(38) Bergbreiter, D. E.; Killough, J. M. *J. Am. Chem. Soc.* **1978**, *100* (7), 2126–2134.
(39) Taylor, M. D. *Chem. Rev.* **1962**, *62* (6), 503–511.
(40) Stoll, S.; Schweiger, A. *J. Magn. Reson.* **2006**, *178*, 42–55.
(41) Zhang, H.; Nakanishi, R.; Katoh, K.; Breedlove, B. K.; Kitagawa, Y.; Yamashita, M. *Dalton Trans.* **2017**, *47*.
(42) Chilton, N. F.; Goodwin, C. A. P.; Mills, D. P.; Winpenny, R. E. P. *Chem. Commun.* **2015**, *51*, 101–103.
(43) Goodwin, C. A. P.; Joslin, K. C.; Lockyer, S. J.; Formanuik, A.; Morris, G. A.; Ortu, F.; Vitorica-Yrezabal, I. J.; Mills, D. P. *Organometallics* **2015**, *34*, 2314–2325.
(44) Goodwin, C. A. P.; Chilton, N. F.; Vettese, G. F.; Pineda, E. M.; Crowe, I. F.; Ziller, J. W.; Winpenny, R. E. P.; Evans, W. J.; Mills, D. P. *Inorg. Chem.* **2016**, *55*, 10057–10067.
(45) APEX2 Version 2014.11-0, Bruker AXS, Inc.; Madison, WI 2014.
(46) SAINT Version 8.34a, Bruker AXS, Inc.; Madison, WI 2013.
(47) Sheldrick, G. M. SADABS, Version 2014/5, Bruker AXS, Inc.; Madison, WI 2014.
(48) Sheldrick, G. M. SHELXTL, Version 2014/7, Bruker AXS, Inc.; Madison, WI 2014.
(49) *International Tables for Crystallography 1992, Vol. C*; Kluwer Adademic Publishers: Dordrecht, 1992.
(50) Spek, A. L. *Acta Crystallogr.* **2015**, *C71*, 9–18.
(51) Spek, A. L. *Acta Crystallogr.* **2009**, *D65*, 148–155.

Chapter 2

A Room-Temperature Stable Y(II) Aryloxide: Using Steric Saturation as a Ligand Design Principle to Kinetically Stabilize Y(II) Complexes

INTRODUCTION

As noted in Chapter 1, the synthesis of kinetically-stable Ln(II) (Ln = rare-earth metal) compounds is aided by steric saturation of the Ln(II) center. Using the ligand OAr′ (2,6-^{t}Bu$_2$-4-Me-C$_6$H$_2$O), the Sc(II) complex [K(crypt)][Sc(OAr′)$_3$] (crypt = 2.2.2-cryptand), which is stable for 40 minutes at room temperature, could be characterized by spectroscopy and X-ray crystallography. In contrast, its congener with Y(II), formed by reduction of the Y(III) complex Y(OAr′)$_3$, was only identified by EPR and UV-visible spectroscopy, as it had visibly decomposed at room temperature in about 1 minute. It was hypothesized that the putative Y(II) complex, "[Y(OAr′)$_3$]$^{1-}$," was kinetically unstable owing to the larger ionic radius of Y compared to Sc[1] which made the Y complex less sterically saturated .[2] In order to test this hypothesis, another aryloxide ligand was sought that would not appreciably perturb the electronic structure of a Ln(OAr^x)$_3$ complex (OAr^x = aryloxide ligand) relative to Ln(OAr′)$_3$ and would also be more sterically-demanding than OAr′. 2,4,6-Tri(alkyl)aryloxides were thus considered. It was expected that the 2 and 6 positions, which are the most metal-proximate, would be the most important substituents for controlling steric saturation. Indeed, changing the substituent at the 2 and 6 positions of aryloxide ligands has been shown to change the nuclearity of rare-earth(III) aryloxides, *e.g.*, compare Y(OAr′)$_3$ and [Y(μ-2,6-Me$_2$C$_6$H$_3$O)(2,6-Me$_2$C$_6$H$_3$O)$_2$(THF)$_2$]$_2$.[3,4]

The OAr′ ligand has ^{t}Bu groups at the 2 and 6 positions, so substituents larger than ^{t}Bu were sought. Aryloxides synthesized first by Watanabe *et al.* with 1-adamantyl groups at the 2 and 6 positions, *i.e.*, OAr^{Ad} and OAr* (OAr^{Ad} = 2,6,-Ad$_2$-4-MeC$_6$H$_2$O; OAr* = 2,6-Ad$_2$-4-^{t}Bu-

C_6H_2O; Ad = 1-adamantyl), have been used to stabilize Zr(IV) aryloxide-alkyls against C–H activation[5] and synthesize two-coordinate Fe(II) aryloxides[6]. Furthermore, to a first approximation, the adamantyl substituent, Ad, is electronically similar to ^{t}Bu in that it is bonded to the aryloxide ring by a tertiary carbon. However, Ad is sterically larger than ^{t}Bu in that Ad is nearly equivalent to adding a cyclohexyl moiety to ^{t}Bu, Figure 1.2. Previously, the OAr^{Ad} ligand has also been used to synthesize $U(OAr^{Ad})_3$, a complex of the reducing U(III) ion.[7] In this Chapter, these (adamantyl)aryloxides are assessed for their utility in stabilizing a Y(II) aryloxide complex.

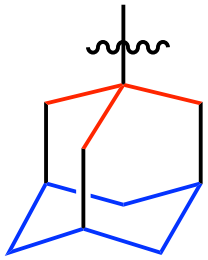

Figure 1.2. An illustration of the analogy between ^{t}Bu and Ad (1-adamantyl). The wavy line through a single bond designates a bond to an aryloxide ring carbon atom. The red portion of the drawn Ad group is the portion similar to ^{t}Bu and the blue portion is the part similar to cyclohexyl.

RESULTS

$U(OAr^{Ad})_3$ had previously been synthesized by salt metathesis of $UI_3(dioxane)_{1.5}$ with 3 equiv of $KOAr^{Ad}$•1.5 DME in benzene and this synthesis was used as a guide.[7] Salt metathesis of YX_3 compounds (X = Cl, I, OTf) in THF with 3 equiv of $KOAr^{Ad}$•1.5 DME (DME = dimethoxyethane) graciously provided by the Karsten Meyer group in Erlangen, Germany was undertaken both at room temperature and at 65 °C. Regardless of the Y(III) precursor used, $Y(OAr^{Ad})_3$ was never the major product and the crude product was consistently contaminated with $HOAr^{Ad}$. Even heating the reaction mixture at 65 °C overnight, followed by removal of solvent and heating the mixture in toluene for 48 h at 100 °C did not yield $Y(OAr^{Ad})_3$ as the major product,

nor in isolable quantities. Only protonolysis of 1.2 equiv of $Y(NR_2)_3$ (R = $SiMe_3$) with 3 equiv of $HOAr^{Ad}$ (also provided by the Karsten Meyer group) in toluene for 48 h at 100 °C gave $Y(OAr^{Ad})_3$, **1-Y**, but it was heavily contaminated by $HOAr^{Ad}$. The resulting product was only sparingly soluble in arenes (benzene, toluene, mesitylene) and obtaining X-ray quality crystals was difficult. In addition, **1-Y** and $HOAr^{Ad}$ have similar solubilities such that it is not possible to separate them by washing one component selectively out of the reaction mixture.

In an effort to increase solubility of the Y(III) aryloxide complex, as well as to effect a greater differential solubility between the phenol and the Y(III) aryloxide, the 2,6-Ad_2-4-^{t}Bu-C_6H_2O ligand (OAr*) was investigated next to see if exchanging the 4-Me in OAr^{Ad} for a 4-^{t}Bu in OAr* would confer these properties. Protonolysis of 1.2 equiv of $Y(NR_2)_3$ with 3 equiv of HOAr* in toluene for 48 h at 100 °C gave $Y(OAr^*)_3$, **2-Y**, that by ^{1}H NMR spectroscopy, was still contaminated with HOAr*. Crystallization from boiling hexane at room temperature overnight yielded colorless crystals that had an IR spectrum that only contained a weak signal for the characteristically sharp O–H stretch of HOAr* at 3628 cm^{-1}. However, the NMR spectrum of this sample was still contaminated with ~15% with HOAr*, so the HOAr* may be formed from **2-Y** in the course of preparing the NMR sample. **2-Y** was identified by ^{1}H NMR spectroscopy and X-ray crystallography, Figure 2.2. **2-Y** is sparingly soluble in benzene, toluene, and tetrahydrofuran. Unlike $Y(OAr')_3$, **2-Y** will not sublime even at 300 °C and 10^{-5} Torr.

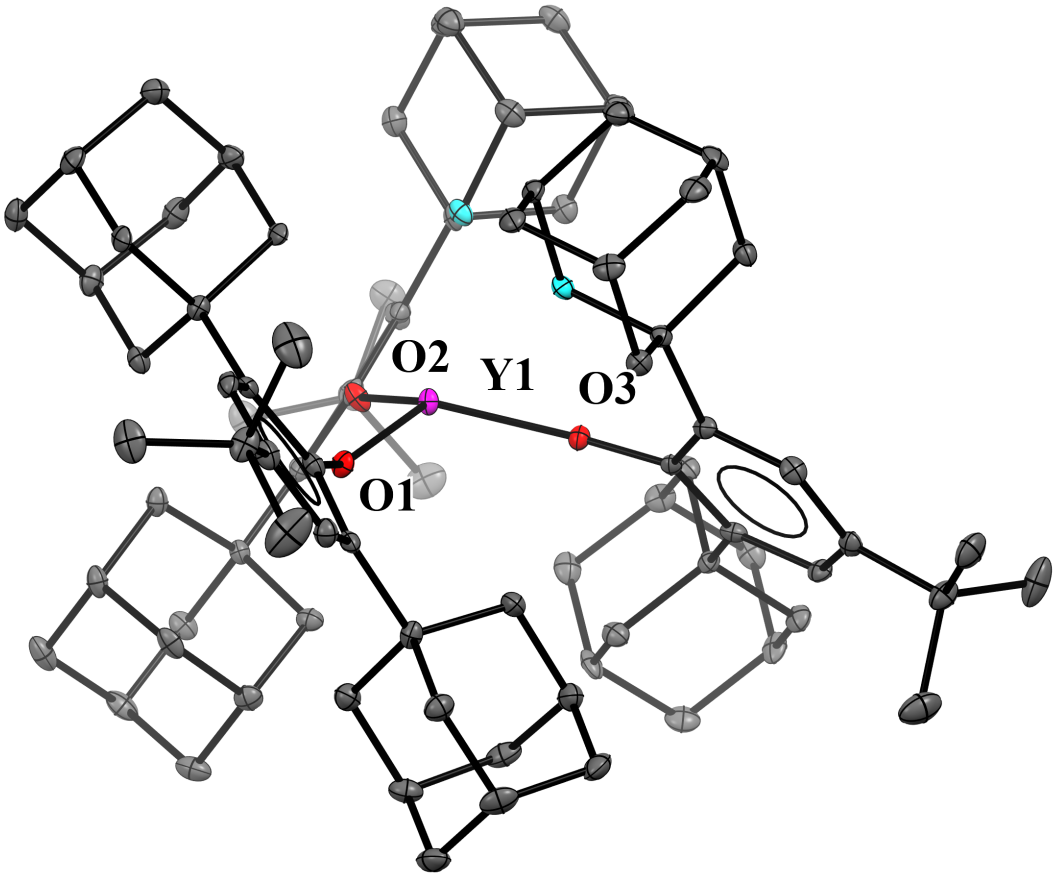

Figure 2.2. Thermal ellipsoid plot of $Y(OAr^*)_3$, **2-Y**. Hydrogen atoms and lattice hexane molecules are omitted for clarity. Carbon atoms that are colored cyan are CH_2 carbons which are directed towards the Y atom. Ellipsoids are drawn at the 50% probability level. Atoms and bonds in the foreground are more darkly shaded than those in the background.

$Y(OAr^*)_3$, **2-Y**, crystallizes in $P2_1/n$ with two equivalents of hexane in the lattice. The complex is pseudo-C_3 symmetric. Selected metrical parameters are detailed in Table 1.2 alongside those of $Y(OAr')_3$ (OAr′ =2,6-^{t}Bu$_2$-4-Me-C_6H_2O) from Chapter 1.

Table 1.2. Bond distances (Å) and angles (°) for $Y(OAr^*)_3$, **2-Y**, and $Y(OAr')_3$ (which has five molecules of $Y(OAr')_3$ in its unit cell).[2] Centroids OAr_{cent} are for the aryloxide C_6 ring. C_{exo} is the carbon atom bonded to the 4-position of the aryloxide, *i.e.*, the 4-Me carbon on OAr′ and the tertiary carbon of the 4-^{t}Bu on OAr*. δ = displacement of Y from the O_3 plane. Θ = angle between O_3 plane and the plane of the aryloxide ligand. γ = displacement of C_6 aryloxide ring carbon atoms from plane of the aryloxide ring; error is taken from the C–C bond distance error of the C_6 aryloxide rings since the C_6 plane is a calculated average and not a measured quantity. G is the Guzei G parameter and is listed in %.[8]

	$Y(OAr^*)_3$, **2-Y**	$Y(OAr')_3$
Y–O	2.038(2)–2.069(1)	2.032(2)–2.053(2)
Average Y–O	2.049(3)	2.045(7)
OAr_{cent}–C_{ipso}–O angle	175–177	176–180
Y–O–C_{ipso} angle	150.0(2) 155.3 (2) 155.7(2)	156.5(2)–171.5(2)
OAr_{cent}–C_{para}–C_{exo} angle	177–178	178–180
δ	0.431	0.009–0.479
Θ	51–60	39–78
γ	0.001(4)–0.058(4)	0.000(4)–0.027(4)
G	92	81–82

The six Ad groups in **2-Y** point toward the yttrium center in two orientations. Two of the groups have an edge of the adamantyl framework oriented toward the metal such that one CH_2 group points toward yttrium [C(38) and C(82)]. Four of the Ad groups have the open six-membered ring pointed towards the Y [groups involving C(8), C(29) C(58) and C(79)]. The OAr* ligands confer greater steric saturation on the Y(III) center than OAr′, as shown by the 92% G parameter of **2-Y** compared to the 81–82% of $Y(OAr')_3$. Despite this difference, the average Y–O distances are the same within error and the distance of the yttrium metal center out of the plane of the three oxygen donor atoms (the pyramidalization δ) in **2-Y** is similar to the value of the most-pyramidal $Y(OAr')_3$ in the unit cell. The Y–O–C_{ipso} angles in **2-Y** are 150.0(2), 155.3(2), and 155.7(2) compared to 156–172° in $Y(OAr')_3$.

There is a slightly increased distortion from planarity of aryloxide ligands in **2-Y** vs $Y(OAr')_3$ as shown by the greater deviation of the C_6 aryloxide ring carbon atoms from the C_6 aryloxide ring plane (γ value) and slightly less linear $OAr_{cent}–C_{\textit{ipso}}–O$ and $OAr_{cent}–C_{\textit{para}}–C_{\textit{exo}}$ angles. This is not accompanied with a significant deviation in C–C bond lengths in the C_6 ring of the aryloxide ligands, however, as the average C–C bond lengths are 1.40(3) Å and 1.40(1) Å for $Y(OAr')_3$ and **2-Y**, respectively. It appears that this deviation of the C_6 ring from planarity is a common feature of aryloxide complexes with the 2-6-Ad_2 substitution pattern: for example, $U(OAr^{Ad})_3$ has γ = 0.000(5)–0.064(5) Å[7], $ZrCl_2(OAr^{Ad})_2$ has γ = 0.001(5)–0.085(5) Å, and $Zr(CH_2Ph)_2(OAr^{Ad})_2$ has γ = 0.015(6)–0.067(6) Å.[5] The two-coordinate Fe(II) aryloxides $Fe(OAr^{Ad})_2$ [γ = 0.001(8)–0.009(8) Å] and $Fe(2,6\text{-}Ad_2\text{-}4\text{-}^{i}Pr\text{-}C_6H_2O)_2$ [γ = 0.001(6)–0.019(6) Å][6] display significantly less distortion of the C_6 ring, despite having a smaller ionic radius than Y(III) and U(III) (but not the highly-charged Zr(IV)).[1]

The ^1H and $^{13}C\{^1H\}$ NMR of **2-Y** are unremarkable, as expected for a complex of diamagnetic Y(III), except that the resonance for the *ipso*-carbon of the OAr* ring is split into two equal-intensity signals in C_6D_6 and in toluene-d_8 (room temperature and 3 °C). A characteristic change in the resonances of the CH_2 protons in the ^1H NMR spectrum of HOAr* compared to **2-Y** clearly indicates binding of the OAr* ligand.

Addition of KC_8 to a stirred mixture of **2-Y** and crypt in THF while under either an Ar or N_2 atmosphere results in the development of a dark blue color that deepens as the mixture is allowed to stir. The resulting blue material is more soluble in THF than **2-Y**. Removing the black solids from the blue solution by filtration and distilling off the solvent *in vacuo* from the deep-blue solution yields blue-black solids, but no crystalline material. If the reaction is run in diethyl ether instead of THF and then chilled to −35 °C, deep blue crystals of [K(crypt)][Y(OAr*)$_3$], **3-Y**, form and were identified by X-ray crystallography.

3-Y crystallizes in $P\bar{1}$ with two equivalents of diethyl ether in the lattice, Figure 3.2. The complex is pseudo-C_3 symmetric like **2-Y**. Selected metrical parameters are listed in Table 2.2 alongside those of **2-Y**, Sc(OAr′)$_3$, and [K(crypt)][Sc(OAr′)$_3$] (Sc complexes from Chapter 1). Unlike **2-Y**, all of the Ad groups in **3-Y** have a six-membered ring pointed towards Y.

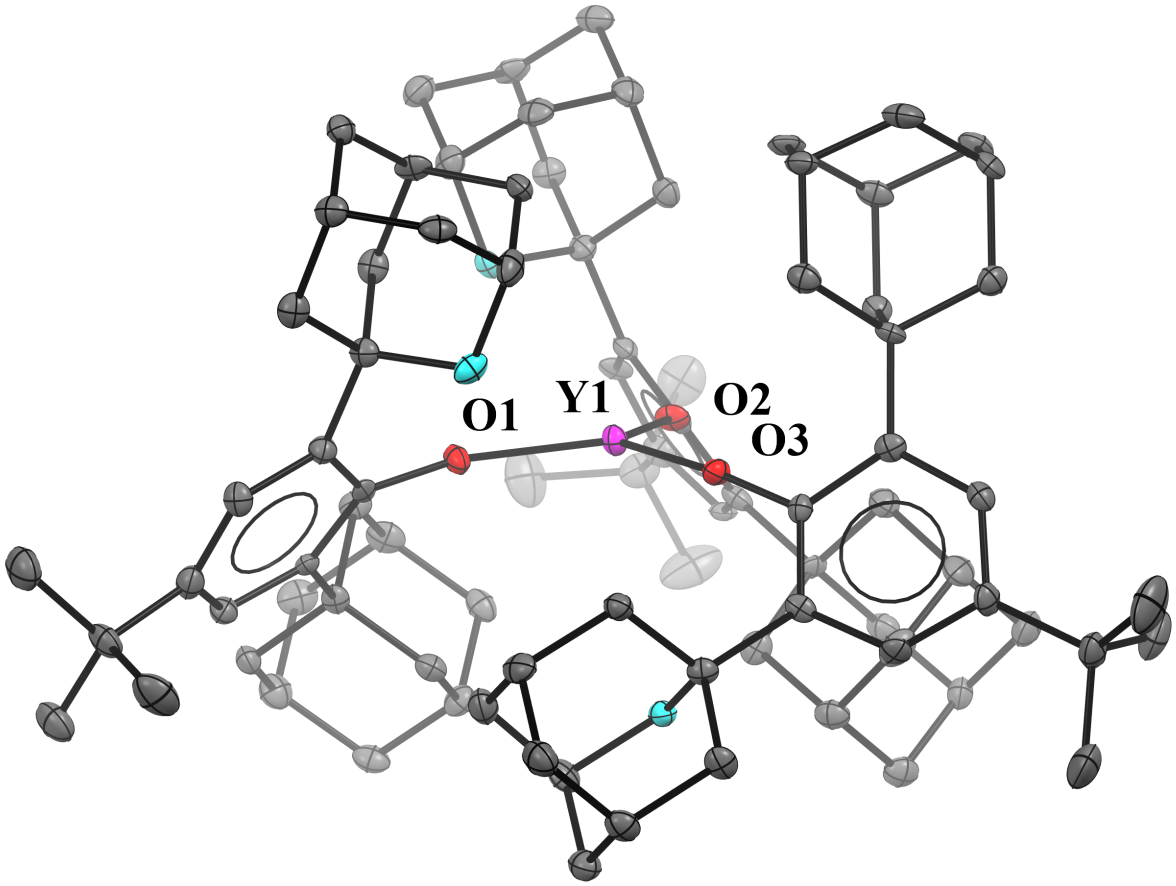

Figure 3.2. Thermal ellipsoid plot of **3-Y**. Hydrogen atoms, a $[K(crypt)]^{1+}$ counteraction, and lattice diethyl ether molecules are omitted for clarity. Carbon atoms that are colored cyan are CH_2 carbons which are closest to the Y atom. Ellipsoids are drawn at the 50% probability level. Atoms and bonds in the foreground are more darkly shaded than those in the background.

Table 2.2. Selected metrical parameters of **3-Y**, **2-Y**, $[K(crypt)][Sc(OAr')_3]^2$, and $Sc(OAr')_3$.[9] Distances in Å, angles in °. Centroids OAr_{cent} are for the aryloxide C_6 ring. C_{exo} is the carbon atom bonded to the 4-position of the aryloxide, *i.e.*, the 4-Me carbon on OAr′ and the tertiary carbon of the 4-^{t}Bu on OAr*. δ = displacement of Ln from the O_3 plane. Θ = angle between O_3 plane and the plane of the aryloxide ligand. γ = displacement of C_6 aryloxide ring carbon atoms from plane of the aryloxide ring; error is taken from the C–C bond distance error of the C_6 aryloxide ring since the C_6 plane is a calculated average and not a measured quantity. G is the Guzei G parameter and is listed in %.[8]

	3-Y	**2-Y**	$[Sc(OAr')_3]^{1-}$	$Sc(OAr')_3$
Ln–O	2.106(2)–2.118(4)	2.038(2)–2.069(1)	1.960(2)–1.964(2)	1.853–1.889
Average Ln–O	2.111(6)	2.049(3)	1.962(3)	1.869
OAr_{cent}–C_{ipso}–O angle	171–172	175–177	179–180	178–179
Ln–O–C_{ipso} angle	158.2(3) 160.2(3) 164.8(3)	150.0(2), 155.3 (2), 155.7(2)	175.6(1) 178.4(1) 179.1(1)	163.8 168.3 173.2
OAr_{cent}–C_{para}–C_{exo} angle	175–177	177–178	178–179	178
δ	0.125	0.431	0.027	0.133
Θ	55–61	51–60	61–64	41–72
γ	0.018(8)–0.088(8)	0.001(4)–0.058(4)	0.000(4)–0.004(4)	0.000–0.028
G	90	92	83	90

As is the case with $[Sc(OAr')_3]^{0/1-}$, an expansion of the Ln–O average distance is seen in the Y(II) complex compared to the Y(III) analog; in **3-Y**, the average Y–O distance is 0.06 Å larger than that in **2-Y**. These values are between those of other existing tris(ligand) compounds where both the Y(III) and Y(II) compound are crystallographically-characterized, with an increase of 0.03 Å for $[YCp'_3]^{0/1-}$ and 0.07 Å for $[Y(NR_2)_3]^{0/1-}$.[10–12] The difference in Sc–O distances in $[Sc(OAr')_3]^{1-}$ and $Sc(OAr')_3$, was larger: 0.09 Å.[2] Consistent with this, the 2% decrease in the G parameter from **2-Y** to **3-Y** is less than the 7% decrease in $[Sc(OAr')_3]^{1-}$ vs. $Sc(OAr')_3$. The Y(II) ion in **3-Y** deviates less from the O_3 plane than in **2-Y**. The value of γ does not change (within error) between **2-Y** and **3-Y** although the OAr_{cent}–C_{ipso}–O angle does deviate more from linearity. The C–C bond lengths of the C_6 aryloxide ring in **3-Y** are also the same within error as **2-Y**: 1.40(2) Å and 1.40(1) Å, respectively.

The UV-visible spectrum of **3-Y** in THF at room temperature is shown in Figure 4.2. There is a strong, broad feature at 629 nm with ε = 8100 $M^{-1}cm^{-1}$, which is consistent with other Y(II) compounds.[10,13] In THF, **3-Y** keeps its deep blue color for ~48 h at room temperature, contrary to the putative "$[Y(OAr')_3]^{1-}$", characterized by EPR spectroscopy, which decomposes in 60 seconds at room temperature in THF. Since "$[Y(OAr')_3]^{1-}$" is so thermally unstable, UV-visible spectroscopy could only be performed at –78 °C, as in Chapter 1. The UV-visible spectrum of **3-Y** at –78 °C was thus also collected in order to compare it with "$[Y(OAr')_3]^{1-}$", Figure 5.2. At −78 °C, **3-Y** has its strongest feature at 622 nm, with ε = 9700 $M^{-1}cm^{-1}$, blue-shifted from "$[Y(OAr')_3]^{1-}$" with its strongest feature at 704 nm, ε = 6500 $M^{-1}cm^{-1}$.

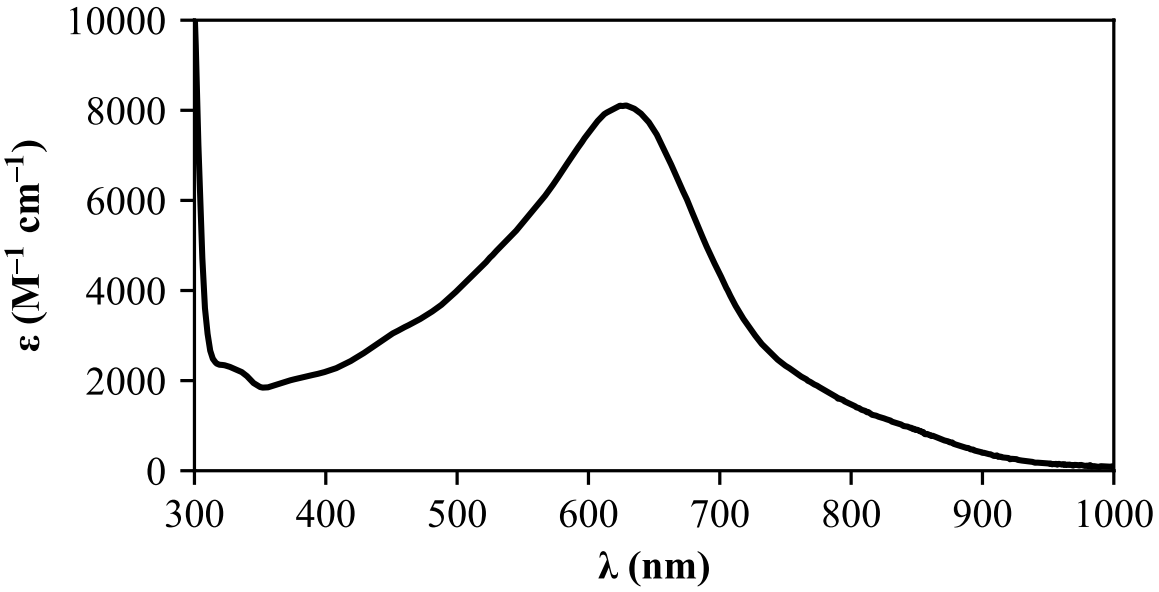

Figure 4.2. The UV-visible spectrum of **3-Y** at room temperature in THF.

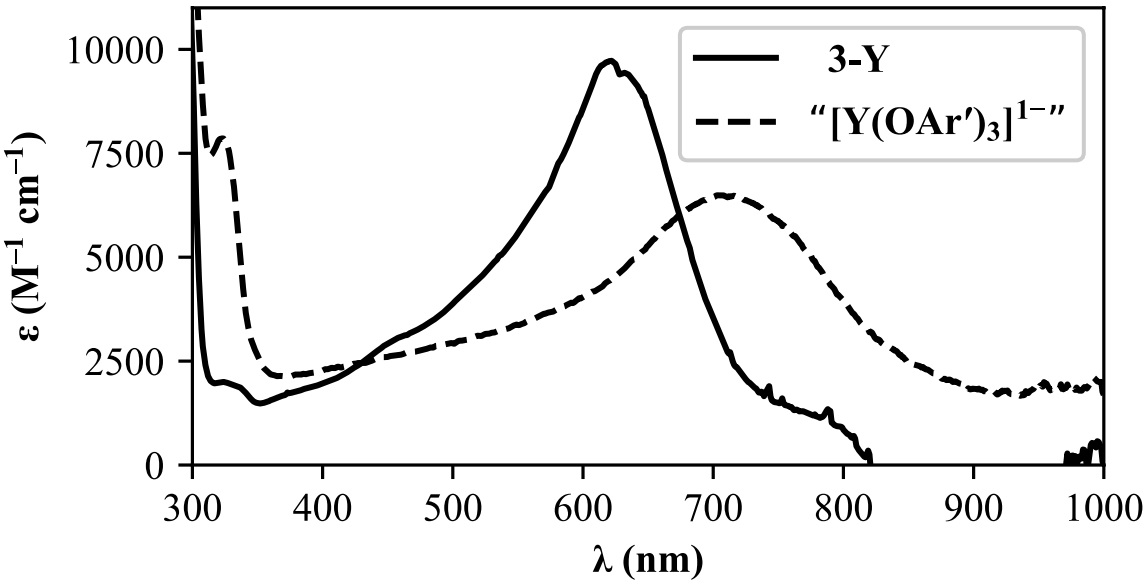

Figure 5.2. The UV-visible spectra of **3-Y** and "$[Y(OAr')_3]^{1-}$" from reduction of $Y(OAr')_3$,[2] both in THF and at −78 °C (isopropanol/CO_2(*s*)) with a film of isopropanol around the cuvette from the cold bath.

The EPR spectrum of **3-Y**, Figure 6.2, contains an axial doublet signal at 77 K with $g_\perp$ = 1.97, $g_{/\!/}$ = 2.00, $A_\perp$ = 156.5 G, and $A_{/\!/}$ = 147.8 G. At room temperature the spectrum contains a doublet with g = 1.98 and A = 153.3 G, both of which are consistent with a single unpaired electron interacting with a 100% abundant ^{89}Y nucleus (I = 1/2). The axial signal seen in the 77 K spectrum is also consistent with the pseudo-C_3 geometry of **3-Y**. The EPR spectrum presented in Chapter 1 for the putative complex "$[Y(OAr')_3]^{1-}$" formed by reduction of $Y(OAr')_3$ has similar EPR parameters at 77 K: $g_\perp$ = 1.97, $g_\parallel$ = 2.00, $A_\perp$ = 155.4 G, and $A_\parallel$ = 148.7 G.

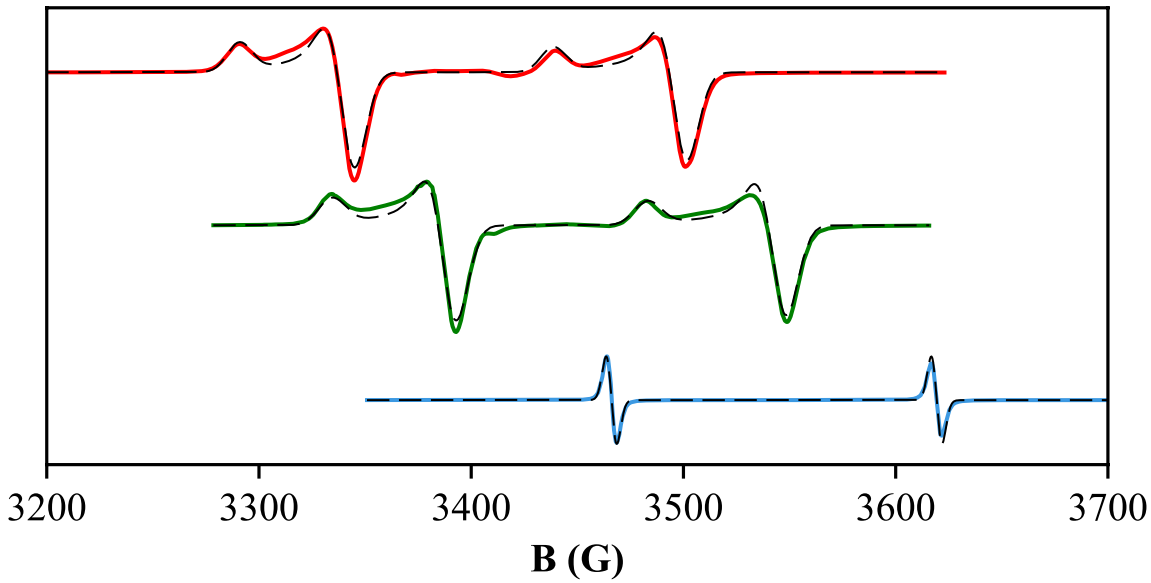

Figure 6.2. X-band EPR spectra of **3-Y** at 77 K in THF (red, top), "$[Y(OAr')_3]^{1-}$" in THF at 77 K (green, middle), and **3-Y** in THF at room temperature (blue, bottom) with associated simulated spectra in black dashed lines.

DISCUSSION

$Y(OAr^*)_3$, 2-Y, vs. $Y(OAr^{Ad})_3$. The substitution of the 4-Me position with 4-^{t}Bu in the 2,6,-Ad_2-4-R-C_6H_2O ligand had a profound effect on the synthesis and handling of the yttrium tris(aryloxide). It was less difficult to synthesize and purify the *tert*-butyl-subsituted complex, $Y(OAr^*)_3$, **2-Y**, compared to the methyl-substituted complex, $Y(OAr^{Ad})_3$, **1-Y**, even though this variation in substitution is far from the metal. This change also made it possible for **2-Y** to be characterized by X-ray crystallography. Good-quality single crystals of **1-Y** were not obtainable.

$Y(OAr^*)_3$, 2-Y, vs. $Y(OAr')_3$. The structure of **2-Y** with Ad substituents in the 2 and 6 positions bears striking resemblance to that of $Y(OAr')_3$, with tert-butyl groups in the 2 and 6 positions. The Y–O bond lengths that are the same within error and the complexes have similar deviations of the Y(III) ion out of the O_3 plane. The biggest differences are seen in the degree of steric saturation of the two complexes and the deviation of C_6 ring carbons from the C_6 plane.

$Y(OAr')_3$ has a G parameter of 81–82%, while **2-Y** has a G parameter of 92%. Alteration of the 2 and 6 substituents from ^{t}Bu to Ad effected minimal change to the primary coordination sphere (*i.e.,* the Y–O distances), but conferred much greater steric saturation.

[K(crypt)][Y(OAr*)$_3$], 3-Y, vs. "[Y(OAr′)$_3$]$^{1-}$." The reduction of **2-Y** in THF with crypt and KC_8, a common protocol for making Ln(II) complexes,[2,10,14–16] produced the dark-colored [K(crypt)][Y(OAr*)$_3$], **3-Y**, as also observed in the reduction of $Y(OAr')_3$. The EPR spectrum of **3-Y** is very similar to that of "$[Y(OAr')_3]^{1-}$," pointing to a similarity in electronic structure between the two Y(II) complexes. The axial doublet pattern agrees with the assignment of **3-Y** as a $4d^1$ complex with the single unpaired electron interacting with the 100% abundant ^{89}Y nucleus (I=1/2) in a trigonal ligand environment. This is also consistent with the theoretical prediction of the geometry and identity of "$[Y(OAr')_3]^{1-}$," which despite not being crystallographically characterized, was predicted to have a geometry similar to that of **3-Y**. The –78 °C UV-visible spectra of **3-Y** and "$[Y(OAr')_3]^{1-}$" have similar single-feature, broad spectra, but the 82 nm (1900 cm^{-1}/ 0.23 eV) difference in λ_{max} values shows that the ligand change from OAr′ to OAr* has perturbed the electronic structure somewhat.

2-Y/3-Y versus Sc(OAr′)$_3$ /[Sc(OAr′)$_3$]$^{1-}$. Upon reduction of **2-Y** to **3-Y**, structural changes occur similar to those seen when $Sc(OAr')_3$ is reduced to form $[Sc(OAr')_3]^{1-}$. Between **2-Y** and **3-Y**, the average Y–O distance expands by 0.06 Å which is slightly less than the expansion for the Sc complexes: 0.09 Å. The deviation of the Y(II) ion out of the O_3 plane decreases from 0.431 Å in **2-Y** to 0.125 Å in **3-Y** (a change of 0.306 Å), making the complex more planar. This also occurs in $Sc(OAr')_3$ and $[Sc(OAr')_3]^{1-}$ (deviation of Sc from the O_3 plane of 0.133 Å and 0.027 Å, respectively) though the change (0.106 Å) is smaller. As well, the G parameter of **3-Y** (90%) decreases from that of **2-Y** (92%), as expected from the longer Y–O bonds. This is less dramatic

than that seen for the Sc complexes, where the reduction from Sc(III) to Sc(II) decreases the G parameter from 90% to 83%. The G parameter of **3-Y** is much greater than the estimated 77% of "$[Y(OAr')_3]^{1-}$," showing how much more steric saturation is afforded by OAr* than OAr′. The geometry of the 2,6-Ad_2(aryloxide) ligands thus may be sensitive to the degree of steric crowding around a metal. While other sterically bulky aryloxide ligands may be flexible by way of rotation around bonds (*e.g.*, 2,6-(Ph_2CH)-4-Me-C_6H_2O),[7,17] it may be that 2,6-Ad_2(aryloxide) ligands are flexible through distortion of the ligand framework to accommodate a variety of coordination environments.

The greater steric saturation of **3-Y** compared to "$[Y(OAr')_3]^{1-}$" is likely the factor that confers the greater thermal stability of **3-Y**: ~48 h for **3-Y** compared to 60 seconds for "$[Y(OAr')_3]^{1-}$." Since the electronic structure and donor characteristics have not changed appreciably, this shows the power of optimizing steric saturation for synthesizing thermally-stable Y(II), and likely Ln(II), compounds.

It should be noted that simple maximization of the G parameter is not a productive strategy, as in Chapter 1 it was shown that for $[LnCp'_3]^{1-}$ ($Cp' = C_5H_4SiMe_3$) complexes, the most sterically-saturated complex, [K(crypt)][$LuCp'_3$], was not the most kinetically stable, which was [K(crypt)][$PrCp'_3$]. Hence, there appears to be an optimum value, and deviation from that value, either more or less sterically-saturated, leads to decreased room-temperature stability. Furthermore, the Y(II) complex [K(crypt)][YCp''_2Cp] ($Cp'' = 1,3\text{-}(SiMe_3)_2C_5H_3$) has a G parameter of 90–91%, but is less thermally-stable than [K(crypt)][YCp'_3] with its G parameter of 86%.[18] It is likely that significantly different ligand sets may have different optimum G parameters for stabilizing Ln(II) complexes. Furthermore, the G parameter does not take into account cation effects. The lower thermal stabilities of $[LnCp'_3]^{1-}$ (Ln = Y, Tb, Ho, Er) complexes when the

cation is $[K(18\text{-crown-6})]^{1+}$ compared to $[K(crypt)]^{1+}$,[19] constitute one example. Likewise, the sterically-undersaturated Ln(II) complexes of the small Cp^{Me} (C_5H_4Me) ligand, can be isolated with an inverse sandwich cation in the $[(18\text{-crown-6})_2K_2Cp^{Me}][LnCp^{Me}_3]$ complexes.[20] While steric saturation is clearly not the sole determiner of thermal stability of Ln(II) complexes, it is evidently important and may allow for the isolation of Ln(II) in a broader range of sufficiently sterically-saturating ligand sets.

CONCLUSION

The goal of the research in this Chapter was to modulate steric saturation, but not electronic structure of a Y(II) complex to make a more kinetically-stable complex. It has already been shown that changing the OAr′ ligands of "$[Y(OAr')_3]^-$" to OAr* in **3-Y** does not tremendously change the electronic structure, but it does change the steric saturation considerably, from an estimated 77% to 90%. This comes with a concomitant increase in thermal stability. "$[Y(OAr')_3]^{1-}$" loses its characteristic blue color in 60 seconds at room temperature, while **3-Y** maintains its color for 48 h at room temperature. Thus, optimizing the steric saturation of reactive Y(II) centers can lead to more kinetically-stable complexes that permit a greater range of characterization.

EXPERIMENTAL

All manipulations and syntheses described below were conducted with the rigorous exclusion of air and water using standard Schlenk line and glovebox techniques under an argon or dinitrogen atmosphere. Solvents were sparged with UHP argon and dried by passage through columns containing Q-5 and molecular sieves prior to use. Deuterated NMR solvents were dried over NaK alloy or Na/benzophenone, degassed by three freeze-pump-thaw cycles, and vacuum transferred

before use. ^{1}H and ^{13}C{^{1}H}NMR spectra were recorded on a Bruker AVANCE600 spectrometer (^{1}H operating at 600 MHz, ^{13}C{^{1}H} at 151 MHz) at 298 K unless otherwise stated and referenced internally to residual protio-solvent resonances. Elemental analyses were conducted on a Perkin-Elmer 2400 Series II CHNS elemental analyzer. UV−visible spectra were collected in THF at −78 °C or room temperature in a 0.1 cm cell fitted with a Teflon stopcock using an Agilent Cary 60 UV-visible spectrophotometer. EPR spectra were collected using X-band frequency (9.3−9.8 GHz) on a Bruker EMX spectrometer equipped with an ER4119HS-W1 microwave bridge and the magnetic field was calibrated with DPPH (g = 2.0036). Infrared (IR) transmittance measurements were taken as compressed solids on an Agilent Cary 630 FTIR spectrophotometer with a diamond ATR attachment. 4,7,13,16,21,24-hexaoxa-1,10-diazabicyclo[8.8.8]hexacosane, 2.2.2-cryptand (crypt, VWR) was dried under reduced pressure (10^{-3} Torr) before use. HOAr*, $Y(NR_2)_3$, and KC_8 were synthesized using published preparations.[5,21,22] EPR spectra were simulated using EasySpin.[23]

HOAr*. IR (Figure 7.2): 3628m, 2961m sh, 2946m sh, 2900s br, 2846s, 2674w, 2654w, 1756w, 1743w, 1597w br, 1476m, 1463m sh, 1454s sh, 1443s, 1420m, 1390m, 1359m, 1342mm, 1325m, 1312m, 1277m, 1262w, 1241m, 1206m, 1185m, 1170m, 1131m, 1105m, 1096m, 1078m, 1047w, 1031w, 1021w, 984m, 969m, 939m, 919w, 902w, 887w, 873m, 841w br, 820m, 803m, 779w, 786m, 740w br, 710m, 658w cm^{-1}.

Y(OAr*)$_3$, 2-Y. $Y(NR_2)_3$ (1.50 g, 2.64 mmol, 1.2 equiv) and HOAr* (2.75 g, 6.58 mmol, 3 equiv) were combined in toluene (20 mL) in a 100 mL flask fitted with a Teflon stopcock. The pale yellow mixture was heated to 100 °C in an oil bath with stirring and all the material dissolved to form a golden solution. After two days of stirring and heating, the solvent was removed *in vacuo* to form brown-yellow solids with extensive amounts of residual toluene. The solids were

suspended in 20 mL hexane and solvent was removed *in vacuo* once more to remove entrained toluene. The resulting solid were washed with pentane (3 x 20 mL) and dried *in vacuo* to give crude white solids of Y(OAr*)$_3$, **2-Y** (1.15 g, 39% crude yield), identified by NMR. Recrystallization from boiling hexane (80 mL) overnight at room temperature, followed by washing with pentane (3 x 2 mL) and removal of solvent *in vacuo* yielded colorless microcrystalline solids of **2-Y** (420 mg, 14% crystalline yield). X-ray quality crystals were present after the recrystallization from boiling hexane (Table 3.2). ^{1}H NMR (C_6D_6, Figure 8.2): δ 7.34 (s, 6H, *m-H*), 2.49 (d, J = 11.2 Hz, 18H, Ad-CH_2, proximal to C_6 ring), 2.35 (d, J = 11.3 Hz, 18H, Ad-CH_2, proximal to C_6 ring), 2.05 (s, 18H, Ad-C*H*), 1.75 (d, J = 11.9 Hz, 20H, Ad-CH_2, distal to C_6 ring), 1.66 (d, J = 12.0 Hz, 18H, Ad-CH_2, distal to C_6 ring), 1.43 (s, 28H, ^{t}*Bu*) ppm. ^{13}C{^{1}H} NMR (C_6D_6, Figure 9.2): δ 158.2 (d, *i-C*), 139.3 (*o-C*), 135.8 (*p-C*), 122.4 (*m-C*), 44.5 (Ad-*C*H$_2$, proximal to C_6 ring), 38.9, 37.3 (Ad-*C*H$_2$, distal to C_6 ring), 34.7, 32.1 (C*Me*$_3$), 29.8 (Ad-*C*H). IR (Figure 10.2): 3086w br, 2948m sh, 1896s br, 2846s, 2678w, 2654w, 1598w, 1448m sh, 1429s, 1390m, 1359m 1342m, 1314w, 1278s, 1260s, 1243s, 1230s, 1200m, 1167wm 1139m, 1100m, 1044w, 10034w, 968s, 923m, 872m, 842s, 818w, 809, 773m, 766m, 734s, 693w, 662m cm^{-1}.

[K(crypt)][Y(OAr*)$_3$], 3-Y. **2-Y** (150 mg, 0.11 mmol) was suspended in a THF (5 mL) solution of crypt (45 mg, 0.12 mmol). With stirring, excess KC_8 (40 mg, 0.30 mmol, 2.6 equiv) was added in two portions and a deep blue color developed. After stirring for 10 minutes, the black-blue solution was filtered through Kimwipe-packed glass pipettes to remove black solids (presumably graphite and excess KC_8) to give dark blue solution. The solids were washed with THF (10 mL) and the resulting filtrate was combined with the initial filtrate. solvent was removed *in vacuo* to give oily black solids, which were triturated with hexane (3 x 2 mL) and pentane (2 x 2 mL) to yield black solids, which were dried *in vacuo* to give a free-flowing black powder,

[K(crypt)][Y(OAr*)$_3$], **3-Y** (140 mg, 72%). X-ray quality crystals could be grown by using diethyl ether instead of THF (Table 4.2). EPR (Figure 6.2): (THF, 77 K) $g_{\perp}$ = 1.97, $g_{/\!/}$ = 2.00, $A_{\perp}$ = 156.5 G, $A_{/\!/}$ = 147.8 G; (THF, room temperature) g = 1.98 and A = 153.3 G. UV–vis λ (ε): (room temperature, THF, Figure 4.2) 629 nm (8100 $M^{-1}cm^{-1}$); (−78 °C, THF, Figure 5.2) 622 nm (9700 $M^{-1}cm^{-1}$). IR (Figure 11.2): 3082w br, 2945m sh, 2888s br, 2838s, 2671w, 2648w, 1734w, 1559w, 1476w, 1444m sh, 1423s, 1388w, 1353m, 1340w, 1310w, 1276s, 1269s sh, 1239s, 1210m br, 1174w, 1131m, 1100s, 1075m, 1059m sh, 1046w, 1034w, 978m, 948m, 931m, 904w, 867m, 863m, 836s, 816m, 809m, 772m, 751w, 729m, 695w, 661w cm^{-1}.

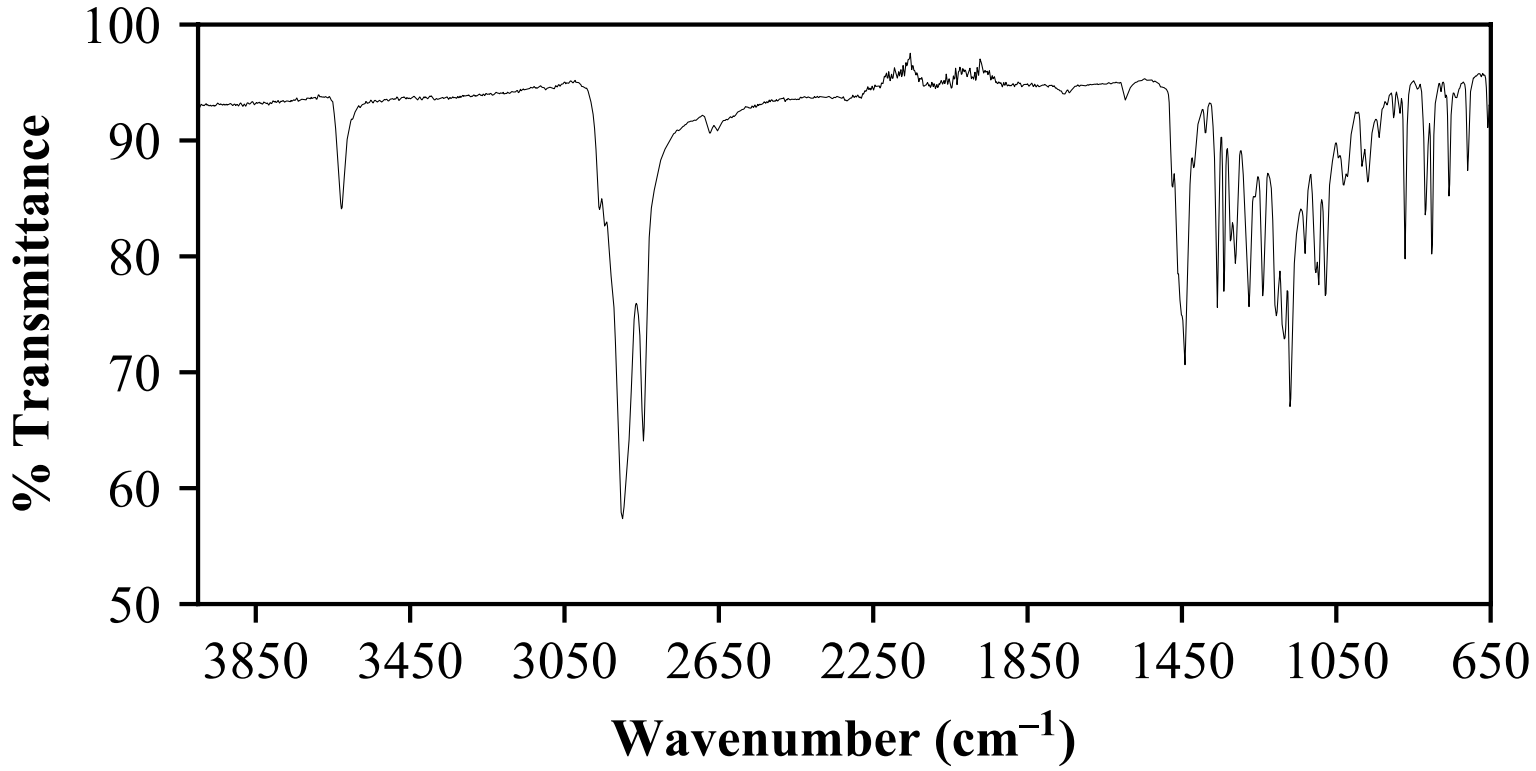

Figure 7.2. IR spectrum of HOAr*.

Table 3.2. Crystal data and structure refinement for **2-Y**.

Empirical formula	$C_{90}H_{123}O_3Y \bullet 2(C_6H_{14})$	
Formula weight	1514.13	
Temperature	88(2) K	
Wavelength	0.71073 Å	
Crystal system	Monoclinic	
Space group	$P2_1/n$	
Unit cell dimensions	a = 14.8371(7) Å	α= 90°.
	b = 28.3568(13) Å	β= 109.3636(8)°.
	c = 21.6716(10) Å	γ= 90°.
Volume	8602.2(7) $Å^3$	
Z	4	
Density (calculated)	1.169 Mg/m^3	
Absorption coefficient	0.728 mm^{-1}	
F(000)	3304	
Crystal color	colorless	
Crystal size	0.255 x 0.140 x 0.072 mm^3	
Theta range for data collection	1.228 to 28.317°	
Index ranges	$-19 \le h \le 19$, $-37 \le k \le 37$, $-28 \le l \le 28$	
Reflections collected	109141	
Independent reflections	21398 [R(int) = 0.1365]	
Completeness to theta = 25.500°	100.0 %	
Absorption correction	Semi-empirical from equivalents	
Max. and min. transmission	0.8015 and 0.7338	
Refinement method	Full-matrix least-squares on F^2	
Data / restraints / parameters	21398 / 0 / 968	
Goodness-of-fit on F^2	1.013	
Final R indices [I>2sigma(I) = 13802 data]	R1 = 0.0608, wR2 = 0.1075	
R indices (all data, ? Å)	R1 = 0.1162, wR2 = 0.1239	
Largest diff. peak and hole	1.150 and -0.920 $e.Å^{-3}$	

X-ray Data Collection, Structure Solution and Refinement for **2-Y**.

A colorless crystal of approximate dimensions 0.072 x 0.140 x 0.255 mm was mounted in a cryoloop and transferred to a Bruker SMART APEX II diffractometer. The APEX2[24] program package was used to determine the unit-cell parameters and for data collection (120 sec/frame scan time for a sphere of diffraction data). The raw frame data was processed using SAINT[25] and SADABS[26] to yield the reflection data file. Subsequent calculations were carried out using the SHELXTL[27] program. The diffraction symmetry was 2/*m* and the systematic absences were consistent with the monoclinic space group $P2_1/n$ that was later determined to be correct.

The structure was solved by dual space methods and refined on F^2 by full-matrix least-squares techniques. The analytical scattering factors[28] for neutral atoms were used throughout the analysis. Hydrogen atoms were included using a riding model. There were two molecules of *n*-hexane solvent present per formula-unit. One solvent molecule was in a general position and two half-molecules were located about inversion centers.

Least-squares analysis yielded wR2 = 0.1239 and Goof = 1.013 for 968 variables refined against 21398 data (0.75 Å), R1 = 0.0608 for those 13802 data with $I > 2.0\sigma(I)$.

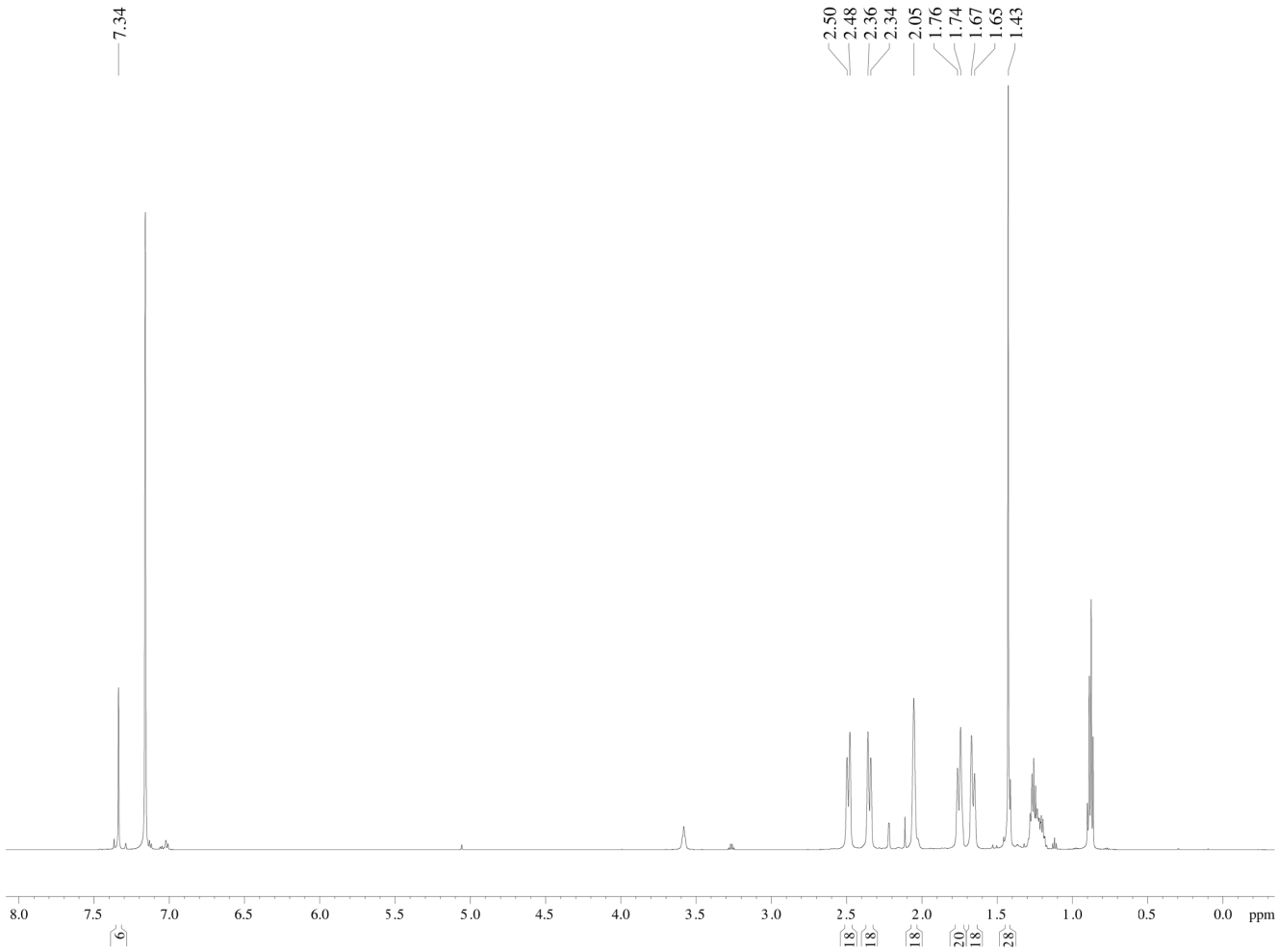

Figure 8.2. ^{1}H NMR spectrum of **2-Y**.

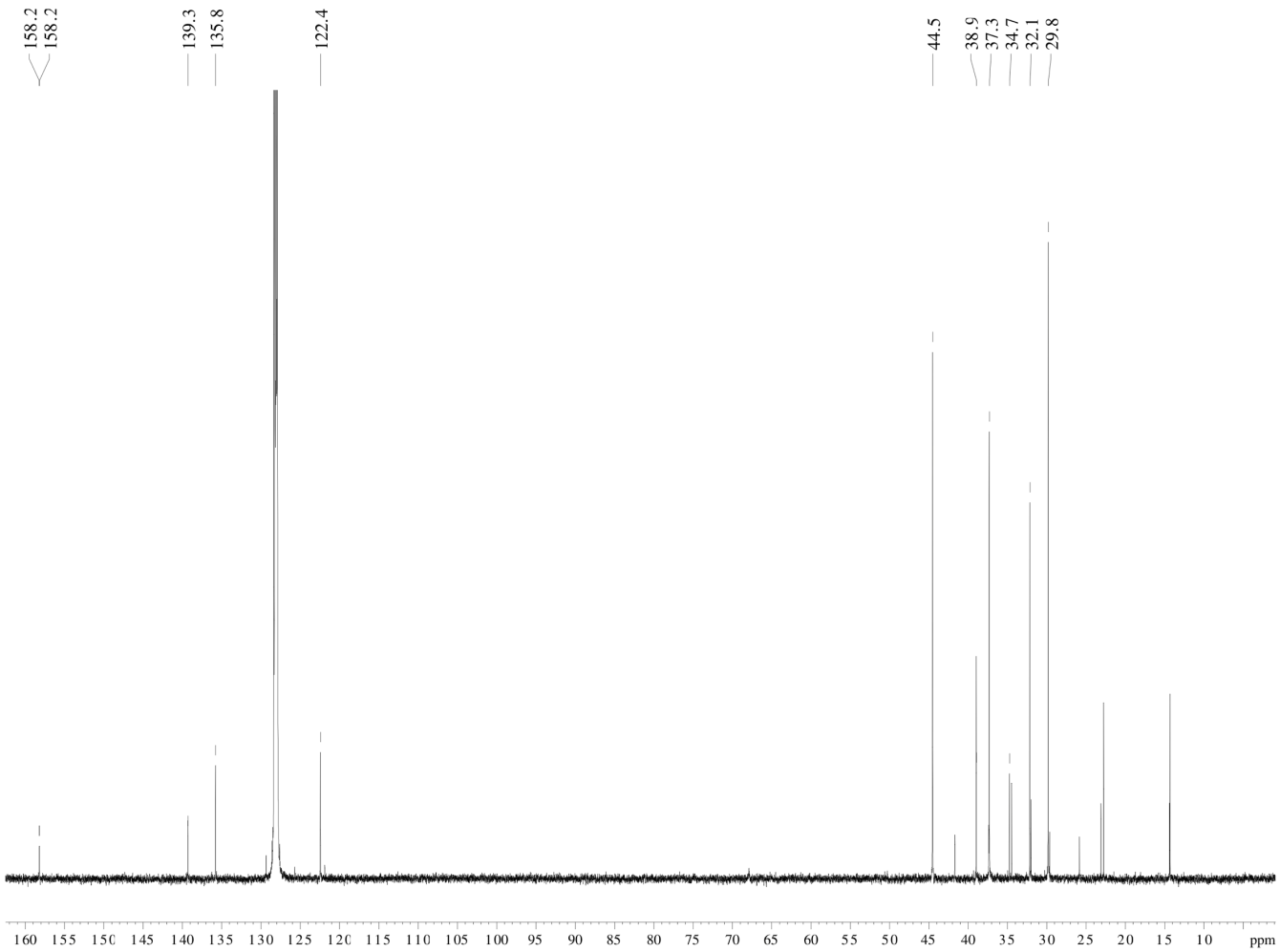

Figure 9.2. $^{13}C\{^{1}H\}$ NMR spectrum of **2-Y**.

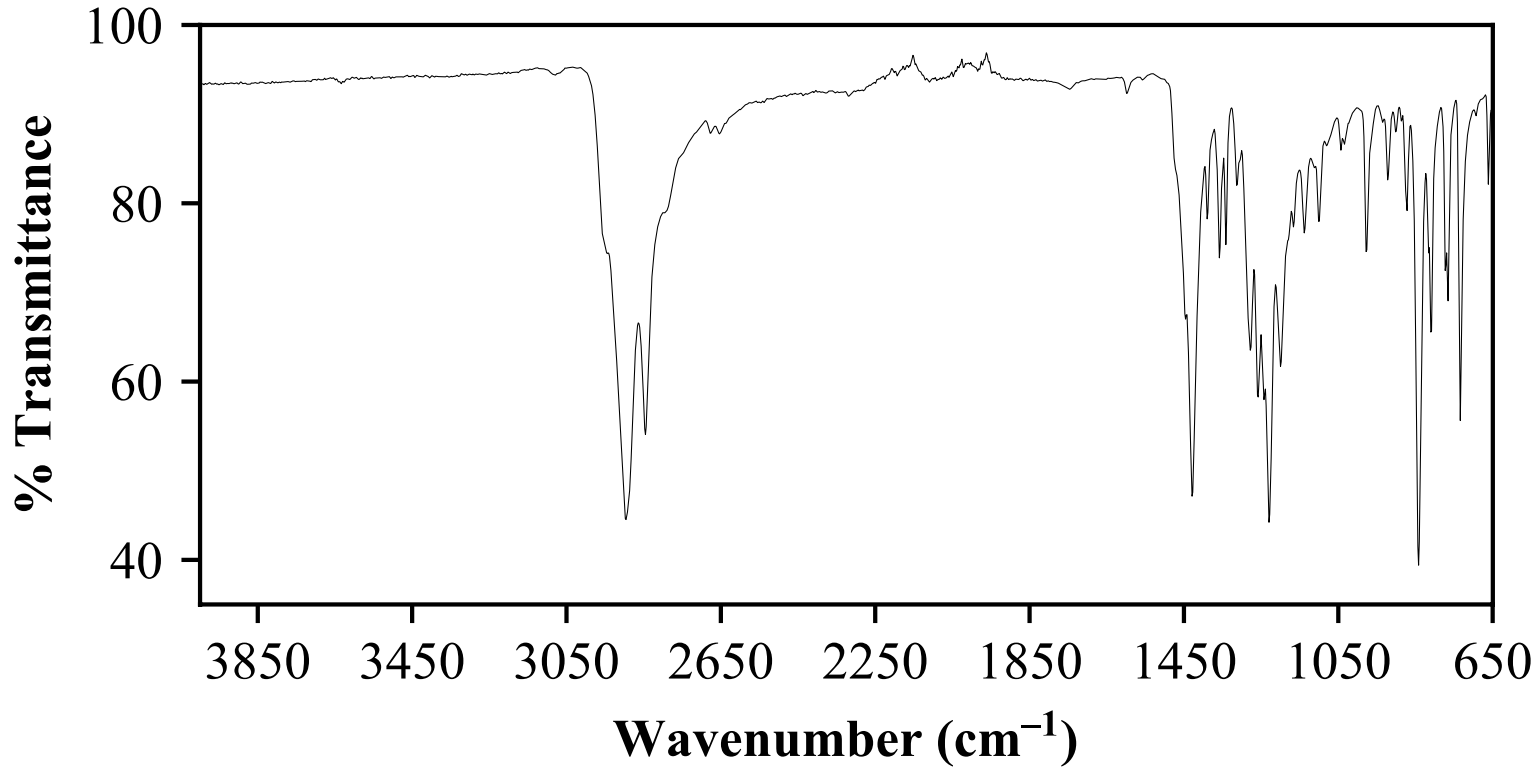

Figure 10.2. IR spectrum of **2-Y**.

Table 4.2. Crystal data and structure refinement for **3-Y**.

Empirical formula	$C_{120}\ H_{189}\ K\ N_2\ O_{12}\ Y$	
Formula weight	1979.73	
Temperature	88(2) K	
Wavelength	0.71073 Å	
Crystal system	Triclinic	
Space group	$P\bar{1}$	
Unit cell dimensions	a = 16.4167(14) Å	α= 84.4795(16)°.
	b = 16.7630(14) Å	β= 82.7936(16)°.
	c = 22.765(2) Å	γ= 62.6453(14)°.
Volume	5515.1(8) $Å^3$	
Z	2	
Density (calculated)	1.192 Mg/m^3	
Absorption coefficient	0.627 mm^{-1}	
F(000)	2154	
Crystal color	blue	
Crystal size	0.234 x 0.201 x 0.104 mm^3	
Theta range for data collection	1.369 to 25.350°	
Index ranges	$-19 \le h \le 19, -20 \le k \le 20, -27 \le l \le 27$	
Reflections collected	56912	
Independent reflections	20139 [R(int) = 0.1197]	
Completeness to theta = 25.350°	99.7 %	
Absorption correction	Semi-empirical from equivalents	
Max. and min. transmission	0.7454 and 0.6727	
Refinement method	Full-matrix least-squares on F^2	
Data / restraints / parameters	20139 / 0 / 1240	
Goodness-of-fit on F^2	1.020	
Final R indices [I>2sigma(I) = 11687 data]	R1 = 0.0764, wR2 = 0.1842	
R indices (all data, 0.83 Å)	R1 = 0.1477, wR2 = 0.2087	
Largest diff. peak and hole	1.129 and -0.610 $e.Å^{-3}$	

X-ray Data Collection, Structure Solution and Refinement for **3-Y**.

A blue crystal of approximate dimensions 0.104 x 0.201 x 0.234 mm was mounted in a cryoloop and transferred to a Bruker SMART APEX II diffractometer. The APEX2[24] program package was used to determine the unit-cell parameters and for data collection (180 sec/frame scan time for a sphere of diffraction data). The raw frame data was processed using SAINT[25] and SADABS[26] to yield the reflection data file. Subsequent calculations were carried out using the SHELXTL[27] program. There were no systematic absences nor any diffraction symmetry other than the Friedel condition. The centrosymmetric triclinic space group $P\bar{1}$ was assigned and later determined to be correct.

The structure was solved by dual space methods and refined on F^2 by full-matrix least-squares techniques. The analytical scattering factors[28] for neutral atoms were used throughout the analysis. Hydrogen atoms were included using a riding model. There were three molecules of diethyl ether solvent present per formula-unit.

Least-squares analysis yielded wR2 = 0.2087 and Goof = 1.020 for 1240 variables refined against 20139 data (0.83 Å), R1 = 0.0764 for those 11687 data with $I > 2.0\sigma(I)$.

Definitions:

$wR2 = [\Sigma[w(F_o^2-F_c^2)^2] / \Sigma[w(F_o^2)^2]]^{1/2}$

$R1 = \Sigma||F_o|-|F_c|| / \Sigma|F_o|$

$Goof = S = [\Sigma[w(F_o^2-F_c^2)^2] / (n-p)]^{1/2}$ where n is the number of reflections and p is the total number of parameters refined.

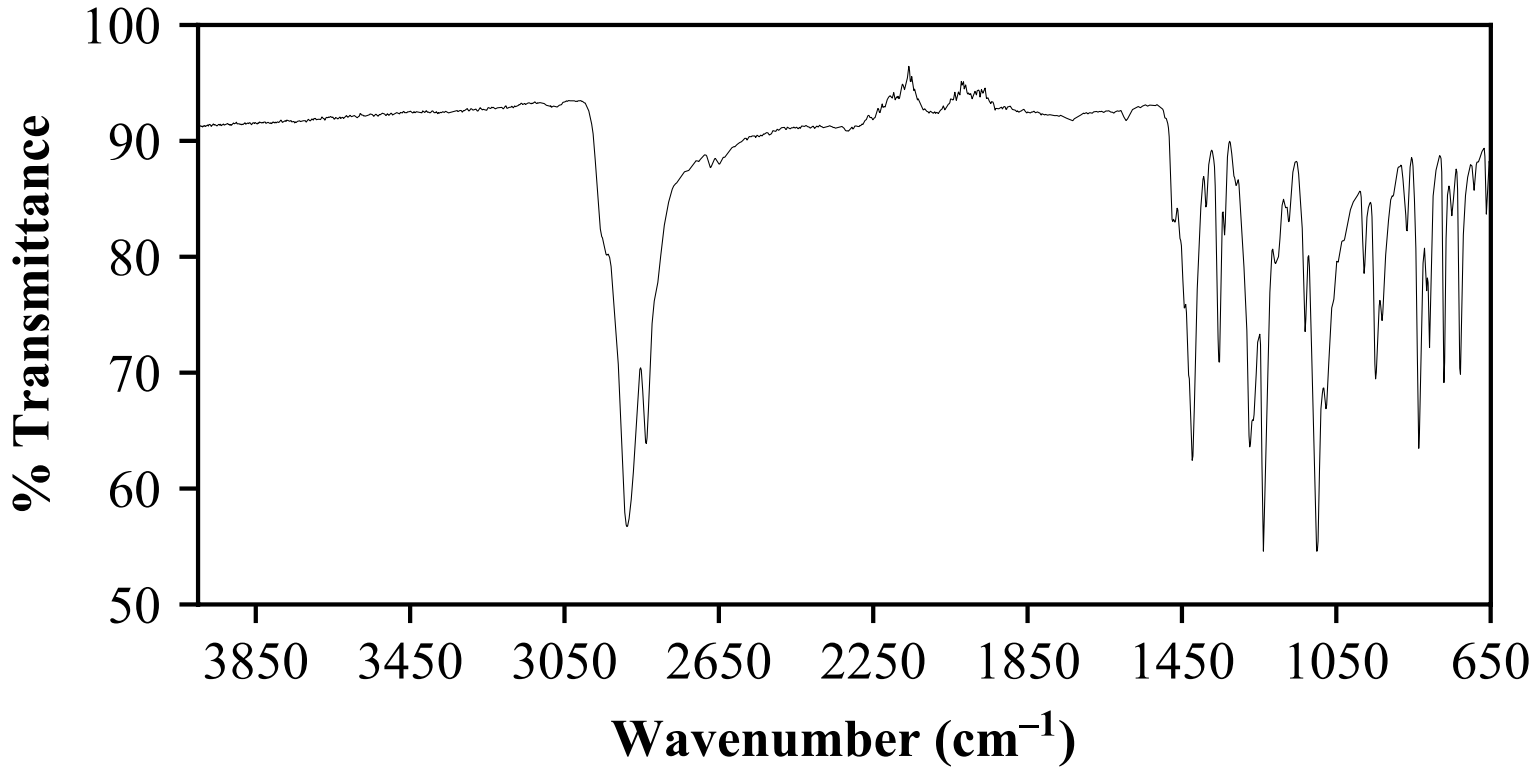

Figure 11.2. IR spectrum of **3-Y**.

REFERENCES

(1) Shannon, R. D. *Acta Crystallogr. A* **1976**, *32*, 751–767.
(2) Moehring, S. A.; Beltrán-Leiva, M. J.; Páez-Hernández, D.; Arratia-Pérez, R.; Ziller, J. W.; Evans, W. J. *Chem. Eur. J.* **2018**, *24*, 18059–18067.
(3) Evans, W. J.; Olofson, J. M.; Ziller, J. W. *Inorg. Chem.* **1989**, *28*, 4309–4311.
(4) Boyle, T. J.; Ottley, L. A. M. *Chem. Rev.* **2008**, *108* (6), 1896–1917.
(5) Watanabe, T.; Ishida, Y.; Matsuo, T.; Kawaguchi, H. *Dalton Trans.* **2010**, *39*, 484–491.
(6) Hatanaka, T.; Miyake, R.; Ishida, Y.; Kawaguchi, H. *J. Organomet. Chem.* **2011**, *696*, 4046–4050.
(7) Hoerger, C. J.; La Pierre, H. S.; Maron, L.; Scheurer, A.; Heinemann, F. W.; Meyer, K. *Chem. Commun.* **2016**, *52*, 10854–10857.
(8) Guzei, I. A.; Wendt, M. *Dalton Trans.* **2006**, 3991–3999.
(9) Hitchcock, P. B.; Lappert, M. F.; Singh, A. *J. Chem. Soc. Chem. Commun.* **1983**, 1499–1501.
(10) MacDonald, M. R.; Ziller, J. W.; Evans, W. J. *J. Am. Chem. Soc.* **2011**, *133*, 15914–15917.
(11) Westerhausen, M.; Hartmann, M.; Pfitzner, A.; Schwarz, W. *Z. Anorg. Allg. Chemie* **1995**, *621*, 837–850.
(12) Ryan, A. J.; Ziller, J. W.; Evans, W. J. *Submitted* **2019**.
(13) Fang, M.; Lee, D. S.; Ziller, J. W.; Doedens, R. J.; Bates, J. E.; Furche, F.; Evans, W. J. *J. Am. Chem. Soc.* **2011**, *133*, 3784–3787.
(14) Jenkins, T. F.; Woen, D. H.; Mohanam, L. N.; Ziller, J. W.; Furche, F.; Evans, W. J. *Organometallics* **2018**, *37*, 3863–3873.
(15) Ryan, A. J.; Darago, L. E.; Balasubramini, S. G.; Chen, G. P.; Ziller, J. W.; Furche, F.; Long, J. R.; Evans, W. J. *Chem. Eur. J.* **2018**, *24*, 7702–7709.
(16) Angadol, M. A.; Woen, D. H.; Windorff, C. J.; Ziller, J. W.; Evans, W. J. *Organometallics* **2019**, *38* (5), 1151–1158.
(17) Franke, S. M.; Tran, B. L.; Heinemann, F. W.; Hieringer, W.; Mindiola, D. J.; Meyer, K. *Inorg. Chem.* **2013**, *52* (18), 10552–10558.
(18) Corbey, J. F.; Woen, D. H.; Palumbo, C. T.; Fieser, M. E.; Ziller, J. W.; Furche, F.; Evans, W. J. *Organometallics* **2015**, *34*, 3909–3921.
(19) MacDonald, M. R.; Bates, J. E.; Ziller, J. W.; Furche, F.; Evans, W. J. *J. Am. Chem. Soc.* **2013**, *135*, 9857–9868.
(20) Huh, D. N.; Ziller, J. W.; Evans, W. J. *Dalton Trans.* **2018**, *47* (48), 17285–17290.
(21) Bergbreiter, D. E.; Killough, J. M. *J. Am. Chem. Soc.* **1978**, *100* (7), 2126–2134.
(22) Bradley, D. C.; Ghotra, J. S.; Hart, F. A. *J. Chem. Soc., Chem. Comm.* **1972**, 349–350.
(23) Stoll, S.; Schweiger, A. *J. Magn. Reson.* **2006**, *178*, 42–55.
(24) APEX2 Version 2014.11-0, Bruker AXS, Inc.; Madison, WI 2014.
(25) SAINT Version 8.34a, Bruker AXS, Inc.; Madison, WI 2013.
(26) Sheldrick, G. M. SADABS, Version 2014/5, Bruker AXS, Inc.; Madison, WI 2014.
(27) Sheldrick, G. M. SHELXTL, Version 2014/7, Bruker AXS, Inc.; Madison, WI 2014.
(28) *International Tables for Crystallography 1992, Vol. C*; Kluwer Adademic Publishers: Dordrecht, 1992.

Chapter 3

Rare-Earth Complexes of the Asymmetric Amide Ligands, N(SiMe$_3$)Ph and N(SiMe$_3$)Cy[*]

INTRODUCTION

Numerous complexes of rare earth metals and amide ligands, NR_2, have been reported in the literature.[1–3] With small alkyl R groups like Me and Et, the $Ln(NR_2)_3$ complexes are typically insoluble in common solvents and with ^{i}Pr substituents, $\{Ln[N(^iPr)_2]_4\}^{1-}$, "ate" salts can form.[2,4–8] The bis(trimethylsilyl)amide ligand originally introduced by Bradley, $N(SiMe_3)_2$,[9–11] and the dimethylsilyl analog, $N(SiHMe_2)$,[12–14] developed by Anwander, are by far the most heavily investigated amides with the rare-earth metals. The syntheses of $Ln[N(SiMe_3)Ph]_3(THF)_x$ complexes (Ln = Y, La, Nd, Sm, Eu, Tb, Dy, Er, Yb, Lu, x = 0–2) from $LnCl_3$ and $LiN(SiMe_3)Ph$ were reported in 1995, but $Nd[N(SiMe_3)Ph]_3(THF)$ was the only example that was fully defined by X-ray crystallography.[15]

This Chapter describes efforts to expand the synthetic and structural chemistry of tris(amide) rare-earth metal amides available for studies of reductive chemistry.[16–18] Specifically, the use of rare-earth metal triflate precursors to synthesize complexes with $N(SiMe_3)Ph$[15] and $N(SiMe_3)Cy$[19] ligands is demonstrated. These ligands were selected to investigate how these ligands would impact the reductive reactivity of tris(amide) rare-earth(III) complexes relative to $Ln[N(SiMe_3)_2]_3$ complexes, which are known to undergo reduction to form rare-earth(II) tris(amide) complexes.[20] The products were characterized by X-ray crystallography to generate a data base with which to evaluate steric factors using the solid angle G parameter of Guzei[21] which has proven useful in reductive chemistry[22] and in rare earth metal amide chemistry[23].

[*] Portions of this Chapter have been published: Moehring, S. A., Ziller, J. W., Evans, W. J. *Polyhedron* **2019**, 168, 72–79.

Since reduction of $N(SiMe_3)Ph$ complexes could involve reduction of the phenyl group,[24,25] complexes of $N(SiMe_3)Cy$ ligands with the rare-earth metals were also of interest. No examples of rare-earth complexes of $N(SiMe_3)Cy$ had been reported before this study.

RESULTS

$Ln[N(SiMe_3)Ph]_3(THF)$ Complexes. Rare-earth metal triflates were investigated as precursors alternative to the common lanthanide chlorides. The ionic metathesis reactions of $Ln(OTf)_3$ with $KN(SiMe_3)Ph$ in THF generate the complexes $Ln[N(SiMe_3)Ph]_3(THF)$, **1-Ln**, as shown in eq 1.3. The diamagnetic complexes of Sc, Y, La, and Lu gave unexceptional ^1H and $^{13}C\{^1H\}$ NMR spectra and the complexes exhibited the pale colors typical for the rare-earth metals in their +3 oxidation state.

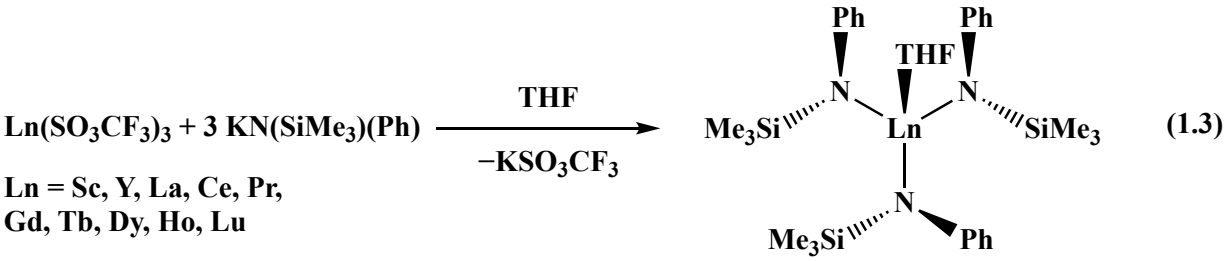

(1.3)

The $^{29}Si\{^1H\}$ NMR spectra of **1-Sc**, **1-La** and **1-Lu** exhibit a single resonance, but **1-Y** has two resonances separated by 0.01 ppm. In variable-temperature NMR experiments in THF-d_8, no change was observed in the peak-height ratio between the two peaks when the temperature is varied between 0 °C and 50 °C, but the chemical shifts vary from –10.45 and –10.46 ppm to –10.41 and –10.42 ppm, respectively. The two peaks are only visible on a 600 MHz spectrometer; only one peak is observed in a 500 MHz spectrum.

All of the **1-Ln** complexes crystallize in the *P2₁/n* space group and have similar structures, Figure 1.3. The larger metals are isomorphous with Nd[N(SiMe$_3$)Ph]$_3$(THF),[15] but **1-Sc** and **1-Lu** are different and isomorphous with V[N(SiMe$_3$)Ph]$_3$(THF).[26]

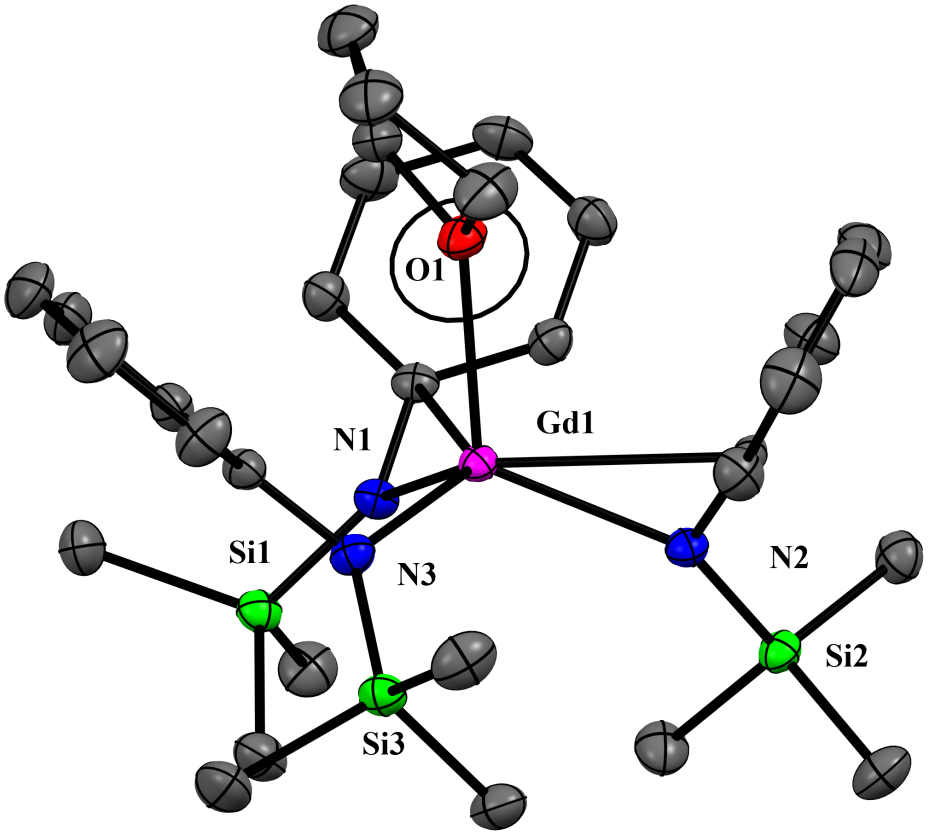

Figure 1.3. Thermal ellipsoid plot of Gd[N(SiMe$_3$)Ph]$_3$(THF), **1-Gd**, thermal ellipsoids at the 50% probability level. Hydrogen atoms are omitted for clarity. The structure is representative of all **1-Ln**.

The N(SiMe$_3$)Ph ligands in **1-Ln** are arranged so that all of the phenyl groups are on the same side of the N$_3$ donor atom plane as the coordinated THF. Hence, the THF is bound in a pocket of three phenyl rings in these complexes. The phenyl groups are not symmetry equivalent, but the donor atom arrangement is nearly ideally tetrahedral around each Ln as shown by the structural parameter τ_4' [27] in Table 1.3. Table 1 also shows the metrical parameters of **1-Ln** vs the more common Ln[N(SiMe$_3$)$_2$]$_3$.[28–33] In general, the **1-Ln** complexes have longer Ln–N distances

which is consistent with the higher formal coordination number.[34] The **1-Ln** complexes also have more variable dihedral angles between the N_3 plane and the plane defined by the Si–N–C_{ipso} atoms of the ligands in **1-Ln** or by the Si–N–Si plane in $Ln[N(SiMe_3)_2]_3$. For each metal, the 3.745(1)–4.059(2) Å Ln….C($SiMe_3$) distances of **1-Ln** are all much longer than those for the analogous $Ln[N(SiMe_3)_2]_3$ complexes such that no anagostic interactions can be claimed in the **1-Ln** series.

Reductions of **1-Ln** with KC_8 in the presence of 2.2.2-cryptand in THF at −30 °C (a protocol for forming Ln(II) complexes with extensive utility across a variety of ligand sets[20,22,35–41]) did not result in any characteristically dark-colored solutions that usually accompany Ln(II) formation. The bronze color of the KC_8 reductant did change to black, consistent with a reduction taking place with concomitant formation of graphite, but even down to temperatures as low as −78 °C, no color changes consistent with Ln(II) formation were observed.

Table 1.3. Metrical parameters of $Ln[N(SiMe_3)Ph]_3(THF)$, **1-Ln**, and $Ln(NR_2)_3$ ($R = SiMe_3$) complexes with distances in Å, angles in degrees, the Guzei G parameter in %,[21] δ = smallest Ln...C($SiMe_3$) range, and Θ = dihedral angle between the N_3 plane and the Si–N–C_{ipso} or Si–N–Si plane. Multiple sets of Θ values occur when one ligand is disordered over 2 positions. †G parameter unavailable as crystal structure excludes H atoms. *information from this work.

	Ln–N range	Average Ln–N	Shortest Ln....C($SiMe_3$) range	Ln–C_{ipso} range	τ_4'	G	Θ	Ref.
1-La	2.375(1)–2.380(1)	2.377(1)	3.794(1)–4.059(2)	2.879(1)–3.132(1)	0.91	82	49 55 58	*
1-Ce	2.342(1)–2.351(1)	2.346(2)	3.764(2)–4.041(2)	2.854(2)–3.121(2)	0.90	83	49 55 59	*
Ce(NR_2)$_3$	2.318–2.320	2.319	3.106–3.549	-	-	†	49	[29]
1-Pr	2.315(1)–2.330(2)	2.325(3)	3.782(2)–4.037(2)	2.851(2)–3.097(2)	0.91	83	49 55 58	*
1-Nd	2.298(2)–2.319(2)	2.308(3)	3.818(4)–4.039(4)	2.846(4)–3.069(4)	0.92	83	48 55 58	[15]
Nd(NR_2)$_3$	2.240–2.245	2.243	3.300	-	-	†	50	[32]
1-Gd	2.250(1)–2.274(1)	2.263(2)	3.823(2)–4.020(2)	2.864(2)–3.052(2)	0.92	85	49 55 58	*
1-Tb	2.239(2)–2.261(2)	2.251(3)	3.769(3)–4.025(3)	2.801(2)–3.068(2)	0.91	85	49 54 58	*
Tb(NR_2)$_3$	2.230	2.230	2.920–3.790	-	-	85	50	[30]
1-Dy	2.219(2)–2.243(2)	2.234(3)	3.764(2)–3.990(2)	2.813(2)–3.054(2)	0.92	86	50 54 57	*
Dy(NR_2)$_3$	2.213–2.215	2.214	2.970–3.724	-	-	85	50	[42]
1-Ho	2.214(2)–2.231(2)	2.225(3)	3.801(2)–3.988(2)	2.811(2)–3.042(2)	0.93	86	49 54 57	*
1-Y	2.216(1)–2.242(1)	2.230(1)	3.795(2)–3.988(2)	2.816(2)–3.046(2)	0.93	86	50 54 57	*
Y(NR_2)$_3$	2.222–2.224	2.223	2.977–3.736	-	-	†	50	[33]
1-Lu	2.167(2)–2.187(2)	2.180(3)	3.791(3)–3.940(3)	2.825(3)–3.011(3)	0.95	87	49 55 56	*
Lu(NR_2)$_3$	2.190–2.192	2.191	2.887–3.857	-	-	86	49	[28]
1-Sc	2.057(1)–2.085(1)	2.073(1)	3.745(1)–3.878(2)	2.798(1)–2.393(1)	0.94	90	48 55 55	*
Sc(NR_2)$_3$	2.048(2)–2.057(2)	2.052(3)	2.971(3)–3.801(3)	-	-	87	48 49 52	[40]

Ln[N(SiMe$_3$)Cy]$_3$(THF) Complexes. Reactions of Ln(OTf)$_3$ (Ln = Y, Ho) with LiN(SiMe$_3$)Cy were examined for comparison with **1-Ln**. The complexes Y[N(SiMe$_3$)Cy]$_3$(THF), **2-Y**, and Ho[N(SiMe$_3$)Cy]$_3$(THF), **2-Ho**, were similarly generated according to eq 2.3, but they proved to be more challenging to purify and crystallize than **1-Ln**. The X-ray crystal structures, Figure 2.3, are included here to report the existence of these compounds. The ^{1}H and ^{13}C{^{1}H} NMR spectra of **2-Y** are similar to those of **1-Y**. In C$_6$D$_6$, the Me$_3$Si ^{1}H resonance is at 0.40 ppm compared to 0.47 ppm in **1-Y**. The ^{29}Si{^{1}H} NMR of **2-Y** has two closely-spaced resonances as found for

1-Y.

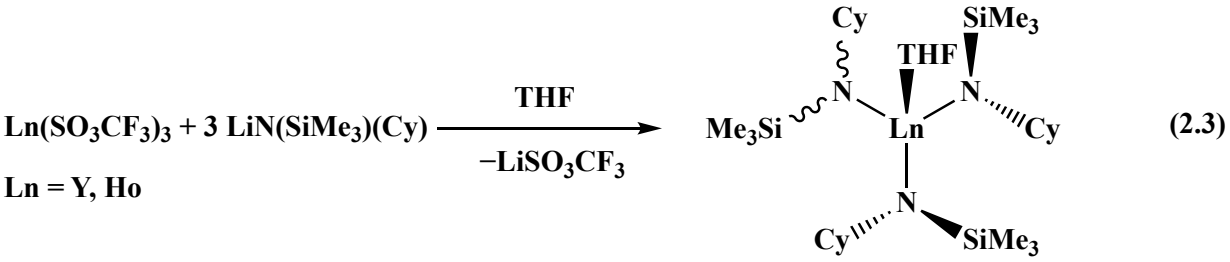

(2.3)

X-ray crystallography revealed that complexes **2-Y** and **2-Ho** both crystallize in *P2$_1$/n* and are isomorphous, Figure 2.3. In contrast to **1-Ln**, the three ligands in **2-Ln** are not ordered in a regular fashion with respect to the N$_3$ plane and the THF ligand. In **2-Ln**, two ligands are oriented with the SiMe$_3$ groups on the side of the bound THF, but the third N(SiMe$_3$)Cy ligand is disordered over two positions, as indicated by the wavy lines in eq 2.3. This third ligand has the SiMe$_3$ groups oriented on the same side as the other two with 19% and 21% occupancy for **2-Y** and **2-Ho**, respectively, and with the complementary occupancies, 81% and 79%, respectively, on the other side. As with **1-Ln**, reduction of **2-Ln** to form Ln(II) complexes was unsuccessful.

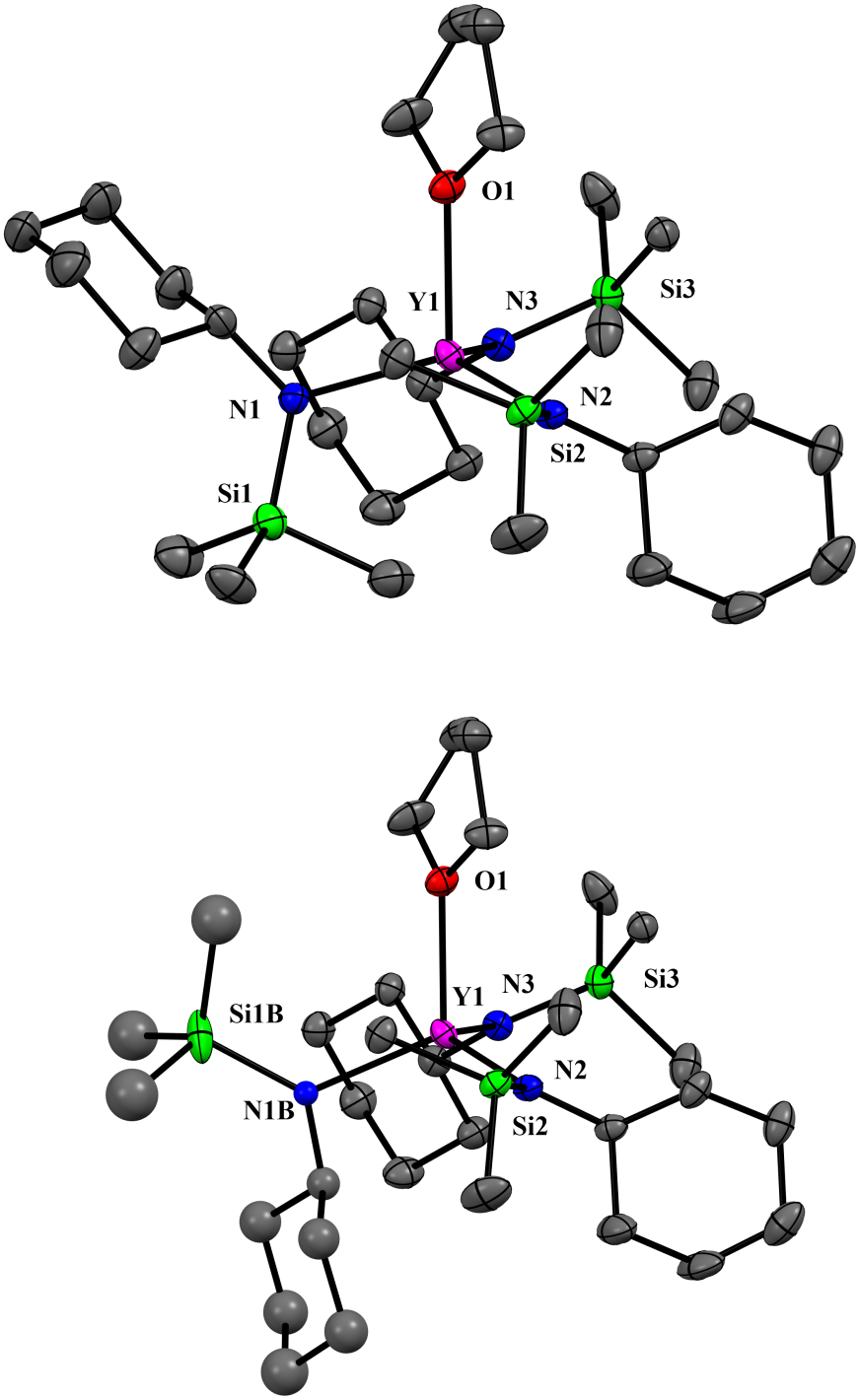

Figure 2.3 Thermal ellipsoid plots, thermal ellipsoids drawn at the 50% probability level, of the two disordered structures (top, 81% occupancy; bottom, 19% occupancy) of **2-Y** which are representative of **2-Ln**. Thermal ellipsoids were not available for the atoms in the lower-occupancy sites. Hydrogen atoms are omitted for clarity.

Table 2.3. Comparison of metrical parameters of Ln[N(SiMe$_3$)Cy]$_3$(THF), **2-Ln**, with Ln[N(SiMe$_3$)Ph]$_3$(THF), **1-Ln**, for Ln = Y, Ho along with Y[N(SiMe$_3$)$_2$]$_3$ with distances in Å, angles in degrees, the Guzei G parameter in %,[21] and Θ = dihedral angle between the N_3 plane and the Si–N–C_{ipso} or Si–N–Si plane. Multiple sets of Θ values occur when one ligand is disordered over 2 positions.

	Ln–N range	Average Ln–N	Shortest Ln....C(SiMe$_3$) range	Ln–C_{ipso} range	τ_4'	G	Θ		Ref.
1-Y	2.216(1)–2.242(1)	2.230(1)	3.795(2)–3.988(2)	2.816(2)–3.046(2)	0.93	86	50 54 57		*
2-Y	2.217(2)–2.27(2)	2.23(2)	3.169(3)–3.87(2)	2.93(1)–3.177(3)	0.87 0.88	85 83	29 31 80	25 38 87	*
Y(NR$_2$)$_3$	2.222–2.224	2.223	2.977–3.736	-	-	†	50		[33]
1-Ho	2.214(2)–2.231(2)	2.225(3)	3.801(2)–3.988(2)	2.811(2)–3.042(2)	0.93	86	59 54 57		*
2-Ho	2.204(6)–2.23(2)	2.22(2)	3.210(6)–3.85(4)	2.98(3)–3.143(6)	0.88	85 83	30 31 73	26 38 83	*

Degree of Steric Saturation. The steric saturation effected by the ligands in **1-Ln** and **2-Ln** was compared to that of Ln[N(SiMe$_3$)$_2$]$_3$ and select other rare earth amide complexes using the solid angle G parameter of Guzei,[21] previously used to measure the amount of steric saturation in lanthanide amides and main group amides.[23,43] This method provides an estimation of the percentage of the coordination sphere of the metal that is protected by the ligands. A G parameter of 100% indicates that the ligands completely shield the metal from exogenous substrates, while a G parameter of 50% means that the ligands cover only half the coordination sphere of the metal. In Figure 3.3, G parameters of Ln[N(SiMe$_3$)$_2$]$_3$ complexes were plotted alongside those of **1-Ln** and **2-Ln** for comparison.[28,30,40,42,44,45] The G parameters are plotted against the six-coordinate ionic radius[34] of the metal contained in the complex. Two G parameters are given for each **2-Ln** complex because the different orientations of the disordered ligand provide different amounts of steric saturation. As might be expected, the G parameter is

proportional to the ionic radius[34] of the Ln in these complexes and varies smoothly across the Ln series. The G parameters of the unsolvated hypothetical species, "Ln[N(SiMe$_3$)Ph]$_3$" and "Ln[N(SiMe$_3$)Cy]$_3$" were also calculated. These calculations gave G parameters from 69–74%, well outside of the range found for the isolable complexes **1-Ln** (82–90%), **2-Ln** (83–85%), Ln[N(SiMe$_3$)$_2$]$_3$ (84–87%), La[N(SiMe$_3$)(SiMe$_2$^{t}Bu)]$_3$ (87%), Ce[N(SiMe$_3$)(SiMe$_2$^{t}Bu)]$_3$ (88%), and La[N(SiMe$_2$^{t}Bu)$_2$]$_3$ (92%).

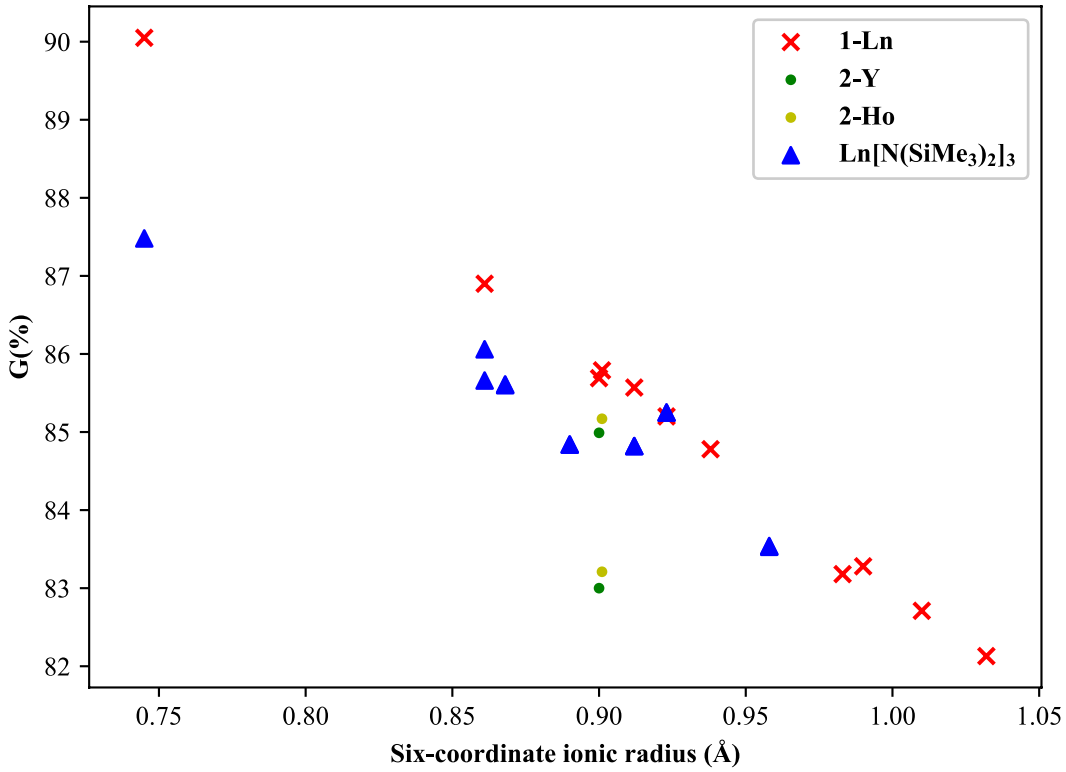

Figure 3.3. Plot of the G parameters of **1-Ln**, **2-Ln,** and Ln[N(SiMe$_3$)$_2$]$_3$ vs the six-coordinate ionic radius[34] of the corresponding Ln(III) ion. Two points are included for each **2-Ln** and some Ln[N(SiMe$_3$)$_2$]$_3$ when the data were modeled with two disordered structures, which have different G parameters.

DISCUSSION

The syntheses of $Ln[N(SiMe_3)Ph]_3(THF)$, **1-Ln**, can be accomplished from $Ln(OTf)_3$ and $KN(SiMe_3)Ph$ as well as the previously-known route from $LnCl_3$ and $LiN(SiMe_3)Ph$.[15] The ease of preparing anhydrous $Ln(OTf)_3$[46] compared to $LnCl_3$[47] may make triflates an attractive starting material for other types of lanthanide complexes. The crystal structures of **1-Ln** show that these complexes crystallize with one molecule of THF in contrast to the unsolvated $Ln[N(SiMe_3)_2]_3$ series.[28,30,40,42,44,45] Analysis of the degree of steric saturation using the Guzei G parameter indicates why the mono-solvates are isolated. Without THF, the $Ln[N(SiMe_3)Ph]_3$ and $Ln[N(SiMe_3)Cy]_3$ complexes would not have G parameters in the range found for the isolable complexes. Hence, both $N(SiMe_3)Ph$ and $N(SiMe_3)Cy$ occupy less space around the rare-earth ion than $N(SiMe_3)_2$.

The G parameter also shows that $N(SiMe_3)Cy$ with all three cyclohexyl groups on one side of the N_3 plane protects a smaller area of the metal than the other orientation of ligands in **2-Ln**. This lower degree of steric saturation may enhance reactivity and provide a channel for decomposition. This could be an Achilles heel that contributes to the difficulty of synthesizing these complexes. This disorder could also contribute to problems in crystallizing these complexes, since there is not one optimum geometry.

As noted in Chapter 1,[22] proper steric saturation of Ln(II) complexes is likely necessary to form kinetically-stable products. All of the currently-known new Ln(II) complexes described in Chapter 1 lack bound neutral ligands; if Ln(II) species formed from **1-Ln** and **2-Ln** were to be formed, they would likely have formulas $\{Ln[N(SiMe_3)Ph]_3\}^{1-}$ and $\{Ln[N(SiMe_3)Cy]_3\}^{1-}$. The low steric saturation of these unsolvated fragments of **1-Ln** and **2-Ln** may be to blame for Ln(II) formation not being observed for these complexes. Since it appears KC_8 is consumed in the

course of the reductions of **1-Ln** and **2-Ln**, it is possible that sterically-undersaturated and thus highly kinetically unstable complexes $\{Ln[N(SiMe_3)Ph]_3\}^{1-}$ and $\{Ln[N(SiMe_3)Cy]_3\}^{1-}$ are formed, but decompose so rapidly as not to be observed.

CONCLUSION

The $N(SiMe_3)Ph$ and $N(SiMe_3)Cy$ amide ligands form crystallographically characterizable complexes of the rare-earth metals like the more common $N(SiMe_3)_2$ ligands, but they are isolated as THF solvates to achieve steric saturation. $Ln[N(SiMe_3)Ph]_3(THF)$ complexes are available with both large and small metals ranging from La to Sc, but the $Ln[N(SiMe_3)Cy]_3(THF)$ complexes were isolated only for the similarly-sized Ho and Y. Salt metatheses starting with $Ln(OTf)_3$ demonstrated that triflates are viable alternatives to chloride precursors in these syntheses.

EXPERIMENTAL DETAILS

All manipulations and syntheses described below were conducted with the rigorous exclusion of air and water using standard Schlenk line and glovebox techniques under an argon atmosphere. Solvents were sparged with UHP argon and dried by passage through columns containing Q-5 and molecular sieves prior to use. Deuterated NMR solvents were dried over NaK alloy, degassed by three freeze-pump-thaw cycles, and vacuum transferred before use. ^{1}H, $^{13}C\{^{1}H\}$, $^{29}Si\{^{1}H\}$ (using the INEPT pulse sequence), and ^{89}Y NMR spectra were recorded on Bruker AVANCE600, CRYO500, or GN500 spectrometers ($^{13}C\{^{1}H\}$ NMR spectra on the CRYO500 spectrometer operating at 125 MHz, $^{13}C\{^{1}H\}$ NMR spectra on the AVANCE600 operating at 151 MHz, $^{29}Si\{^{1}H\}$ at 119 MHz on the AVANCE600, ^{89}Y at 24 MHz on the GN500) at 298 K unless otherwise stated and referenced internally to residual protio-solvent resonances, to external $SiMe_4$ for $^{29}Si\{^{1}H\}$ experiments, or to external $Y(NO_3)_3$ for ^{1}H-^{89}Y experiments. NMR

resonances were assigned with the help of HMQC and HSQC experiments. Elemental analyses were conducted on a Perkin-Elmer 2400 Series II CHNS elemental analyzer. The $Ln(OTf)_3$ precursors (Strem) were dried at 220 °C at 10^{-5} Torr for 2 days before use,[46] except for $Ce(OTf)_3$. The cerium triflate was dried at 220 °C at 10^{-5} Torr for 2 days, then pulverized and dried again at 220 °C at 10^{-5} Torr for 2 more days. $KN(SiMe_3)Ph$[48] and $LiN(SiMe_3)Cy$[19] were synthesized using published preparations.

$Ln[N(SiMe_3)Ph]_3(THF)$, 1-Ln. $Ln(OTf)_3$ (1 equiv) and $KN(SiMe_3)Ph$ (3 equiv) were suspended together in THF and stirred overnight. The solvent was removed from the suspension *in vacuo* and the solids were extracted with toluene (10–15 mL in three portions). Solvent was removed from the solution *in vacuo* and the crude solids were recrystallized in procedures detailed for each of the **1-Ln** compounds. Each complex was purified by trituration with pentane and this was done at low temperature to minimize the solubility of the complex.

1-Sc. As above, $Sc(OTf)_3$ (970 mg, 2.0 mmol) and $KN(SiMe_3)Ph$ (1.20 g, 5.91 mmol) were combined. The solids were chilled to −15 °C to form a rubbery puck of crude orange solids, which was triturated with −30 °C pentane (15 x 1 mL) to form a free-flowing powder. The solids were dried *in vacuo* to give beige $Sc[N(SiMe_3)Ph]_3(THF)$, **1-Sc** (350 mg, 29% yield). Colorless X-ray quality crystals were grown overnight from a pentane solution at −30 °C (Table 3.3). ^{1}H NMR (THF-d_8, Figure 4.3): δ 7.15 (t, J = 7.7 Hz, 6H, *m*-H), 6.95 (d, J = 7.7 Hz, 6H, *o*-H), 6.85 (t, J = 7.3 Hz, 3H, *p*-H), 3.61 (m, 6H, 2,5-THF-CH_2), 1.77 (m, 6H, 3,4-THF-CH_2), 0.11 ppm (s, 27H, SiMe_3). ^{13}C{^{1}H} NMR (THF-d_8, Figure 5.3): δ 152.8 (*i*-C), 129.5 (*m*-C), 128.4 (*o*-C), 122.0 (*p*-C), 68.2 (2,5-THF-CH$_2$), 26.4 (3,4-THF-CH$_2$), 2.2 (SiMe_3). ^{29}Si{^{1}H} NMR (THF-d_8, Figure 6.3): δ –6.02 ppm. IR (Figure 7.3): 3075w, 3047w, 2959w, 2892w, 1588m, 1565w, 1499w, 1476w, 1352m sh, 1330m, 1272m sh, 1243s, 1231s, 1217s, 1206s, 1189s sh, 1168m,

1078w, 1031s, 1003m, 933m, 912m, 901m, 884m, 848m, 831s br, 797s, 754m, 738m, 733m, 702m, 683m, 669m, 634s, 624s cm^{-1}. Anal Calcd for $Sc[N(SiMe_3)Ph]_3(THF)$ $C_{27}H_{42}N_3ScSi_3O$: C, 61.04; H, 8.26; N, 6.89. Found: C, 44.60; H, 6.19; N, 4.55. Incomplete combustion was observed with this sample as sometimes is the case with rare earth complexes,[23,49–52] but the observed CHN ratio, $C_{31}H_{31}N_3$, is close to the calculated.

1-Y. As above, $Y(OTf)_3$ (540 mg, 1.0 mmol) and $KN(SiMe_3)Ph$ (600 mg, 2.9 mmol) were combined. The crude yellow solids were chilled to −30 °C and triturated with −30 °C pentane (2 x 1 mL). Decanting the solvent and removal of the residual solvent *in vacuo* gave beige solids, $Y[N(SiMe_3)Ph]_3(THF)$, **1-Y** (260 mg, 41% yield). Colorless X-ray quality crystals were grown from a saturated pentane solution at −30 °C overnight (Table 4.3). ^1H NMR (C_6D_6, Figure 8.3): δ 7.14 (d, J = 7.6 Hz, 6H, *o*-H), 6.96 (t, J = 7.8 Hz, 6H, *m*-H), 6.53 (t, J = 7.2 Hz, 3H, *p*-H), 0.37 ppm (s, 27H, Si*Me*$_3$). $^{13}C\{^1H\}$ NMR (C_6D_6, Figure 9.3): δ 156.4 (*i*-C), 129.4 (*m*-C), 125.5 (*o*-C), 117.9 (*p*-C), 2.9 (Si*Me*$_3$) ppm. $^{29}Si\{^1H\}$ NMR (C_6D_6, Figure 10.3): δ –7.06, –7.07 ppm. ^{89}Y NMR (C_6D_6): δ 587 ppm. Lack of THF resonances in the ^1H and $^{13}C\{^1H\}$ spectra indicate desolvation may have occurred. Direct observation of the ^{89}Y nucleus was unsuccessful, but the signal could be observed in 2D ^1H-^{89}Y gHMBC experiments. IR (Figure 11.3): 3691w, 3068w, 3051w, 3027w, 2950m, 2895m, 2865w sh, 1584m, 1561w, 1534w br, 1489m, 1474m, 1458w, 1441w, 1396w br, 1351m, 1329w, 1299w, 1283w, 1261m sh, 1250m sh, 1238s, 1219s, 1181m, 1168m, 1153m, 1106m, 1081w, 1068w, 1041w, 1027w, 1008w, 992m, 973w, 960w, 937s, 910s, 895m, 885m, 836m sh, 824s, 802w, 788m, 752m, 740m, 726m sh, 707s, 681m, 671m, 643w, 626m, 614m cm^{-1}. Anal Calcd for $Y[N(SiMe_3)Ph]_3$ $C_{27}H_{42}N_3Si_3Y$: C, 55.74; H, 7.28; N, 7.22. Found: C, 53.28; H, 7.20; N, 5.91. Incomplete combustion was observed with this sample as sometimes is the case with rare earth complexes,[23,49–52] but the observed CHN

ratio, $C_{27}H_{43}N_3$, is close to the calculated and consistent with the loss of 1 equiv of THF as seen in the ^{1}H NMR.

1-La. As above, La(OTf)$_3$ (290 mg, 0.50 mmol) and KN(SiMe$_3$)Ph (300 mg, 1.5 mmol) were combined. The brown-yellow solids were washed with −30 °C pentane (3 x 1 mL), then recrystallized from 2 mL of 1:1 pentane:toluene to give colorless crystals of La[N(SiMe$_3$)Ph]$_3$(THF), **1-La** (50 mg, 15%). X-ray quality crystals were grown from 1:1 pentane:toluene at −30 °C in 3 hours (Table 5.3). ^{1}H NMR (C_6D_6, Figure 12.3): δ 7.03 (d, J = 7.4 Hz, 6H, *o-H*), 6.98 (t, J = 7.6 Hz, 6H, *m*-H), 6.50 (t, J = 6.99 Hz, 3H, *p*-H), 3.52 (m, 3H, 2,5-THF-C*H*$_2$), 1.40 (m, 4H, 3,4-THF-C*H*$_2$), 0.37 ppm (s, 27H, Si*Me*$_3$). ^{13}C{^{1}H} NMR (C_6D_6, Figure 13.3): δ 155.9 (*i*-C), 130.4 (*m*-C), 123.6 (*o*-C), 117.4 (*p*-C), 67.8 (2,5-THF-C), 25.8 (3,4-THF-C), 2.5 ppm (Si*Me*$_3$). ^{29}Si{^{1}H} NMR (C_6D_6, Figure 14.3): δ –8.80 ppm. IR (Figure 15.3): 3737w, 3637w, 3066w, 3047w, 2964m, 2948m, 2891m, 2880m, 2530w, 1583m, 1558w, 14788m sh, 1475s, 1397w br, 1351m, 1355w, 1296w, 1250m sh, 1239s, 1226m sh, 1183m, 1176m, 1150w, 1108m, 1076w, 1047m, 1029w, 991m, 962w, 902m, 884m, 827s, 780m, 749m, 727w, 703m, 698m, 685w, 673w, 627m, 622m cm^{-1}. Anal Calcd for $C_{31}H_{50}LaN_3OSi_3$: C, 52.89; H, 7.16; N, 5.97. Found: C, 43.86; H, 5.79; N, 4.90. Incomplete combustion was observed with this sample as noted above,[23,49–52] but the observed CHN ratio, $C_{31}H_{49}N_3$, is close to the calculated.

1-Ce. As above, Ce(OTf)$_3$ (590 mg, 1.0 mmol) and KN(SiMe$_3$)Ph (600 mg, 2.9 mmol) were combined. The yellow solids were triturated with −30 °C pentane (4 mL in portions) and dried *in vacuo* to give gold Ce[N(SiMe$_3$)Ph]$_3$(THF), **1-Ce** (340 mg, 49% yield). X-ray quality crystals were grown from 1:1 hexane:toluene at −30 °C overnight (Table 6.3). ^{1}H NMR (C_6D_6, Figure 16.3): δ 13.69 (s, 6H, *o-H*), 5.61 (d, J = 4.7 Hz, 6H, *m*-H), 4.28 (s, 3H, *p*-H), 0.33 (s, 27H,

Si*Me*$_3$) –2.04 (br, $\nu_{1/2}$ = 143 Hz, 6H, 3,4-THF-C*H*$_2$), –5.36 ppm (br, $\nu_{1/2}$ = 613 Hz, 5H, 3,4-THF-C*H*$_2$). IR (Figure 17.3): 3063w, 3023w, 2946m, 2894w, 1582s, 1558w, 1487m, 1472s, 1439w, 1396w, 1374w, 1325w, 1295w, 1254sh, 1234br, 1176m, 1167m, 1152w, 1075w, 1066w, 1025sh, 1016m, 992m, 936m, 912s, 896m, 883m, 835sh, 820s br, 798w, 779s, 751m, 738m, 729sh, 718w, 698s, 680m, 669m cm^{-1}. Anal Calcd for $C_{31}H_{50}CeN_3OSi_3$: C, 52.80; H, 7.15; N, 5.96. Found: C, 47.20; H, 6.15; N, 4.90. Incomplete combustion was observed with this sample as noted above,[23,49–52] but the observed CHN ratio, $C_{31}H_{48}N_3$, is close to the calculated.

1-Pr. As above, Pr(OTf)$_3$ (580 mg, 0.99 mmol) and KN(SiMe$_3$)Ph (600 mg, 2.9 mmol) were combined. The orange solids were triturated with −30 °C pentane (3 x 1 mL) and dried *in vacuo* to give green-yellow crystals, Pr[N(SiMe$_3$)Ph]$_3$(THF), **1-Pr** (140 mg, 20% yield). X-ray quality crystals were grown overnight from a pentane solution at −30 °C (Table 7.3). IR (Figure 18.3): 3636w, 3067w, 3048w, 2965w, 2949m, 2891m, 2880w sh, 1584s, 1560w, 1489m sh, 1475s, 1397w br, 1351m, 1335w, 1299w sh, 1281w sh, 1250m sh, 1239s, 1221s, 1183m, 1177m, 1152w, 1108m, 1076m, 1052m, 1047m, 1028w, 992m, 962w, 912m sh, 901s, 884m, 826s, 781s, 750s, 718m, 702s, 673m, 625m cm^{-1}. Anal Calcd for $C_{31}H_{50}N_3OPrSi_3$: C, 52.74; H, 7.14; N, 5.95. Found: C, 49.31; H, 6.73; N, 5.48. Incomplete combustion was observed with this sample as noted above,[23,49–52] but the observed CHN ratio, $C_{31}H_{50}N_3$, matches to the calculated.

1-Gd. As above, Gd(OTf)$_3$ (600 mg, 0.99 mmol) and KN(SiMe$_3$)Ph (600 mg, 3.0 mmol) were combined. The orange solids were triturated with −30 °C pentane (3 x 1 mL), then dissolved in 2:6:1 pentane:toluene:THF (~5 mL) and left at −30 °C overnight. The resulting colorless crystals were washed with −30 °C pentane and dried *in vacuo* to give white crystals, Gd[N(SiMe$_3$)Ph]$_3$(THF), **1-Gd** (210 mg, 29% yield). X-ray quality crystals were grown overnight from a concentrated toluene solution at −30 °C (Table 8.3). IR (Figure 19.3): 3646w,

3066w, 6048w 2960m, 2947m, 2893m, 2879m, 1584m, 1581m, 1574w sh, 1560w, 1552w, 1488m sh, 1475m, 1399w br, 1351m, 1355w, 1300w sh, 1280w, 1255m sh, 1250m sh. 1239s, 1225m, 1219m, 1183m, 1176m, 1150w, 1108m, 1080w, 1076w, 1052m, 1047m, 1028w, 992m, 962w, 920w sh, 910m sh, 901s, 883s, 827s, 781s, 749s, 727m, 703s, 698sm 685w, 673m, 642w, 626m, 611m cm^{-1}. Anal Calcd for $C_{31}H_{50}GdN_3OSi_3$: C, 51.55; H, 6.98; N, 5.82. Found: C, 49.54; H, 6.36; N, 5.33. Incomplete combustion was observed with this sample as noted above,[23,49–52] but the observed CHN ratio, $C_{31}H_{47}N_3$, is close to the calculated.

1-Tb. As above, $Tb(OTf)_3$ (500 mg, 0.83 mmol) and $KN(SiMe_3)Ph$ (500 mg, 2.5 mmol) were combined. X-ray crystals were grown overnight from a 1:6 pentane:toluene solution at −30 °C, then washed −30 °C pentane (1 x 3 mL) to yield pale yellow-green $Tb[N(SiMe_3)Ph]_3(THF)$, **1-Tb** (300 mg, 52% yield, Table 11.3). Anal Calcd for $C_{31}H_{50}N_3OSi_3Tb$: C, 51.43; H, 6.96; N, 5.80. Found: C, 50.0; H, 6.88; N, 5.66. Incomplete combustion was observed with this sample as noted above,[23,49–52] but the observed CHN ratio, $C_{31}H_{51}N_3$, is close to the calculated.

1-Dy. As above, $Dy(OTf)_3$ (610 mg, 0.98 mmol) and $KN(SiMe_3)Ph$ (600 mg, 3.0 mmol) were combined. The grey-purple solids were triturated with pentane (3 x 1 mL) and the resulting solids were dissolved in 2:6:1 pentane:toleuene:THF (~5 mL), then left at −30 °C overnight. The solution was then concentrated to ~2 mL and pentane was added. The solution was left at −30 °C for three days and crystals resulted, which were washed with −30 °C pentane (3 x 1 mL) and dried *in* vacuo to give white-grey crystals, $Dy[N(SiMe_3)Ph]_3(THF)$, **1-Dy** (100 mg, 14% yield). X-ray quality crystals were grown overnight from a concentrated toluene solution at −30 °C (Table 9.3). IR (Table 20.3): 3067w, 3039w, 2959m, 2948m, 2891m, 2879m, 1580m, 1572m sh, 1560w, 1552w, 1489m, 1475s, 1398w br, 1367w, 1351w, 1335w, 1296w sh, 1284w sh, 1251m, 1239s, 1225m, 1220m, 1183m, 1176m, 1053m, 1047m, 1028m, 992m, 962w, 922w sh, 812m sh,

901s, 883s, 827s, 787s, 781s, 748m, 702m, 699m, 685m, 673s, 626m, 609w cm^{-1}. Anal Calcd for Dy[N($SiMe_3$)Ph]$_3$, a loss of 1 molecule of THF; $C_{27}H_{42}DyN_3Si_3$: C, 49.48; H, 6.46; N, 6.41. Found: C, 45.23; H, 5.78; N, 5.62. Incomplete combustion was observed with this sample as noted above,[23,49–52] but the observed CHN ratio, $C_{27}H_{41}N_3$, is close to the calculated.

1-Ho. As above, Ho(OTf)$_3$ (310 mg, 0.50 mmol) and KN($SiMe_3$)Ph (300 mg, 1.5 mmol) were combined. X-ray quality crystals were grown overnight from a 1:2 pentane:toluene solution at −30 °C to give Ho[N($SiMe_3$)Ph]$_3$(THF), **1-Ho** (160 mg, 44% crystalline yield, Table 10.3). Anal Calcd for $C_{31}H_{50}HoN_3OSi_3$: C, 51.01; H, 6.90; N, 5.76. Found: C, 46.10; H, 6.75; N, 5.19. Incomplete combustion was observed with this sample as noted above,[23,49–52] but the observed CHN ratio, $C_{31}H_{54}N_3$, is close to the calculated.

1-Lu. As above, Lu(OTf)$_3$ (310 mg, 0.50 mmol) and KN($SiMe_3$)Ph (300 mg, 1.5 mmol) were combined. The light-brown solids were washed with pentane (3 x 1 mL) then dissolved in 2:6:1 pentane:toluene:THF (5 mL) and left at −30 °C. Small, colorless crystals precipitated, which were washed with −30 °C pentane (3 x 1 mL) and dried *in vacuo* to give Lu[N($SiMe_3$)Ph]$_3$(THF), **1-Lu** (90 mg, 25% yield). X-ray quality crystals were grown overnight by recrystallizing the solids first from a solution made in pentane and toluene, then crystallizing the resulting material from a solution in a mixture of pentane, toluene, and THF at −30 °C (Table 12.3). ^{1}H NMR (C_6D_6, Figure 21.3): δ 7.20 (d, J = 7.5 Hz, 6H, *o*-H), 7.12 (t, J = 7.8 Hz, 6H, *m*–H), 6.78 (t, J = 7.3 Hz, 3H, *p*-H), 0.46 ppm (s, 27H, Si*Me*$_3$). ^{13}C{^{1}H} NMR (C_6D_6, Figure 22.3): δ 152.9 (*i*-C), 129.9 (*m*-C), 126.4 (*o*-C), 120.6 (*p*-C), 2.4 ppm (Si*Me*$_3$). ^{29}Si{^{1}H} NMR (C_6D_6, Figure 23.3): δ −5.52 ppm. IR (Figure 24.3): 3636w, 3067w, 3047w, 3024w, 2966m, 2949m, 2893m, 2877m, 1584m, 1572m sh, 1560w, 1553w, 1489m sh, 1475s, 1458m sh, 1395w br, 1351w, 1334w, 1299w sh, 1281w sh, 1250m sh, 1239s, 1226s, 1219m sh, 1183m, 1177m,

1154w, 1150w, 1108m, 1080w, 1076w, 1053m, 1047m, 1029m, 992m, 962w, 923w sh, 911m sh, 901s, 883s 827s, 786m, 782m, 749s, 723m, 703s, 699s, 685m, 674m, 626m, 609w cm^{-1}. Lack of THF resonances in the ^{1}H and $^{13}C\{^{1}H\}$ spectra indicate desolvation may have occurred. Anal Calcd for $C_{31}H_{50}LuN_3OSi_3$: C, 50.32; H, 6.81; N, 5.68. Found: C, 49.07; H, 6.64; N, 5.46. Incomplete combustion was observed with this sample as noted above,[23,49–52] but the observed CHN ratio, $C_{31}H_{50}N_3$, matches the calculated.

Y[N(SiMe$_3$)Cy]$_3$(THF), 2-Y. LiN(SiMe$_3$)Cy (0.20 g, 1.1 mmol) dissolved in THF (5 mL) was added to solid Y(OTf)$_3$ (0.20 g, 0.37 mmol). After stirring overnight, a hazy yellow solution was present. Solvent was removed *in vacuo* to give yellow-white oily solids, which were extracted with toluene (10 mL) in three portions. The resulting yellow suspension was centrifuged and the supernatant was filtered away from white solids to give a yellow solution. Solvent was removed *in vacuo* to give an orange oil, which was suspended in 1 mL toluene and left at −30 °C overnight to precipitate any entrained insoluble material. White solids were removed by filtration and the solvent was stripped from the supernatant to give orange Y[N(SiMe$_3$)Cy]$_3$(THF), **2-Y** (175 mg, 70% yield). X-ray quality colorless crystals were grown from a solution made from 0.5 mL hexane and minimum toluene left at −30 °C for six days (Table 13.3). ^{1}H NMR (C_6D_6, Figure 25.3): δ 3.83 (s, 5H, 3,5-THF-CH_2), 3.07 (m, 3H, 1-Cy-C*H*), 2.06 (d, J = 12.0 Hz, 6H, 2,6-Cy-CH_2), 1.84 (d, J = 12.2 Hz, 6H, 3,5-Cy-CH_2), 1.65 (d, J = 12.1 Hz, 3H, 4-Cy-CH_2), 1.59 (q, J = 12.1 Hz, 6H, 2,6-Cy-CH_2), 1.40 (q, J = 12.5 Hz, 6H, 3,5-Cy-CH_2), 1.25 (s, 5H, 3,4-THF-CH_2), 1.18 (q, J = 11.8 Hz, 3H, 4-Cy-CH_2), 0.40 ppm (s, 27H, Si*Me$_3$*). $^{13}C\{^{1}H\}$ NMR (C_6D_6, Figure 26.3): δ 71.8 (2,5-THF-C), 57.4 (1-Cy), 41.1 (2,6-Cy), 27.4 (3,5-Cy), 26.4 (4-Cy), 25.2 (3,4-THF-C), 4.8 ppm (Si*Me$_3$*). $^{29}Si\{^{1}H\}$ NMR (C_6D_6, Figure 27.3): δ –12.47, –12.48 ppm. IR (Figure 28.3): 3733w, 3707w, 3632w, 3595w, 2992 m sh,

2981m, 2925s, 2898sh, 2851m, 2666w, 2360w, 2342m, 2329m, 1461w, 1448w, 1325m, 1300m, 1273m sh, 1261s, 1236s, 1194m, 1178m, 1145m, 1116m sh, 1105m, 1066m sh, 1042s, 1018m sh, 986m, 916w, 893m, 872w sh, 853m, 840m, 822s, 798m, 762m, 744m, 728w, 676w sh, 668w, 661w, 635s, 620m cm^{-1}.

$Ho[N(SiMe_3)Cy]_3(THF)$, 2-Ho. $LiN(SiMe_3)Cy$ (870 mg, 4.9 mmol) was dissolved in THF (15 mL) and added to a suspension of $Ho(OTf)_3$ (1.02 g, 1.66 mmol) in THF (5 mL) to form a pink suspension. After stirring overnight, a hazy pink-brown solution resulted. Solvent was removed *in vacuo* to give brown solids. The solids were extracted with toluene (20 mL) in three portions. Each portion was centrifuged and the supernatant was filtered, reserving the pink supernatant. Solvent was removed *in* vacuo to give pink solids, which were redissolved in toluene (5 mL), centrifuged, and filtered to remove insoluble. The solution was concentrated to 2 mL and left at −30 °C overnight. The resulting pink solids were washed with −30 °C pentane (3 x 1 mL) and dried *in vacuo* to give pink $Ho[N(SiMe_3)Cy]_3(THF)$**, 2-Ho** (190 mg, 15%). Pink X-ray quality crystals could be grown from a methylcyclohexane solution at −30 °C over two days (Table 14.3). IR (Figure 29.3): 3726w, 3631w, 2997w sh, 2982w, 2951m sh, 2924s, 2898m sh, 2847m, 2362w, 2344w, 2324w, 1461w, 1447m, 1386w br, 1342w, 1327w, 1254m, 1236s, 1179w, 1144w, 1103s, 1068m, 1041w, 1013m, 985m, 917w, 906w, 893m, 851s, 840m, 819s, 798m, 760m, 745m, 724m, 694w, 673w, 662m, 636m cm^{-1}. Anal Calcd for $Ho[N(SiMe_3)Cy]_3$: $C_{27}H_{60}HoN_3Si_3$: C, 47.97; H, 8.95; N, 6.22. Found: C, 44.32; H, 8.84; N, 4.86. Incomplete combustion was observed with this sample as noted above,[23,49–52] but the observed CHN ratio, $C_{27}H_{64}N_3$, is close to the calculated.

Table 3.3. Crystal data and structure refinement for **1-Sc**.

Empirical formula	C_{31} H_{50} N_3 O Sc Si_3	
Formula weight	609.97	
Temperature	133(2) K	
Wavelength	0.71073 Å	
Crystal system	Monoclinic	
Space group	$P2_1/n$	
Unit cell dimensions	a = 10.8295(17) Å	α= 90°.
	b = 18.453(3) Å	β= 98.2595(19)°.
	c = 17.325(3) Å	γ = 90°.
Volume	3426.3(9) $Å^3$	
Z	4	
Density (calculated)	1.182 Mg/m^3	
Absorption coefficient	0.347 mm^{-1}	
F(000)	1312	
Crystal color	colorless	
Crystal size	0.427 x 0.396 x 0.243 mm^3	
Theta range for data collection	1.621 to 28.870°	
Index ranges	$-14 \le h \le 14$, $-24 \le k \le 24$, $-23 \le l \le 23$	
Reflections collected	40665	
Independent reflections	8376 [R(int) = 0.0435]	
Completeness to theta = 25.500°	99.9 %	
Absorption correction	Semi-empirical from equivalents	
Max. and min. transmission	0.8015 and 0.7245	
Refinement method	Full-matrix least-squares on F^2	
Data / restraints / parameters	8376 / 0 / 371	
Goodness-of-fit on F^2	1.034	
Final R indices [I>2sigma(I) = 7490 data]	R1 = 0.0301, wR2 = 0.0785	
R indices (all data, 0.74 Å)	R1 = 0.0345, wR2 = 0.0818	
Largest diff. peak and hole	0.389 and -0.250 $e.Å^{-3}$	

X-ray Data Collection, Structure Solution and Refinement for **1-Sc.**

A colorless crystal of approximate dimensions 0.243 x 0.396 x 0.427 mm was mounted in a cryoloop and transferred to a Bruker SMART APEX II diffractometer. The APEX2[53] program package was used to determine the unit-cell parameters and for data collection (20 sec/frame scan time for a sphere of diffraction data). The raw frame data was processed using SAINT[54] and SADABS[55] to yield the reflection data file. Subsequent calculations were carried out using the SHELXTL[56] program. The diffraction symmetry was 2/*m* and the systematic absences were consistent with the monoclinic space group $P2_1/n$ that was later determined to be correct.

The structure was solved by dual space methods and refined on F^2 by full-matrix least-squares techniques. The analytical scattering factors[57] for neutral atoms were used throughout the analysis. Hydrogen atoms were included using a riding model. C(29) was disordered and included using multiple components and partial site-occupancy-factors.

Least-squares analysis yielded wR2 = 0.0818 and Goof = 1.034 for 371 variables refined against 8376 data (0.74 Å), R1 = 0.0301 for those 7490 data with $I > 2.0\sigma(I)$.

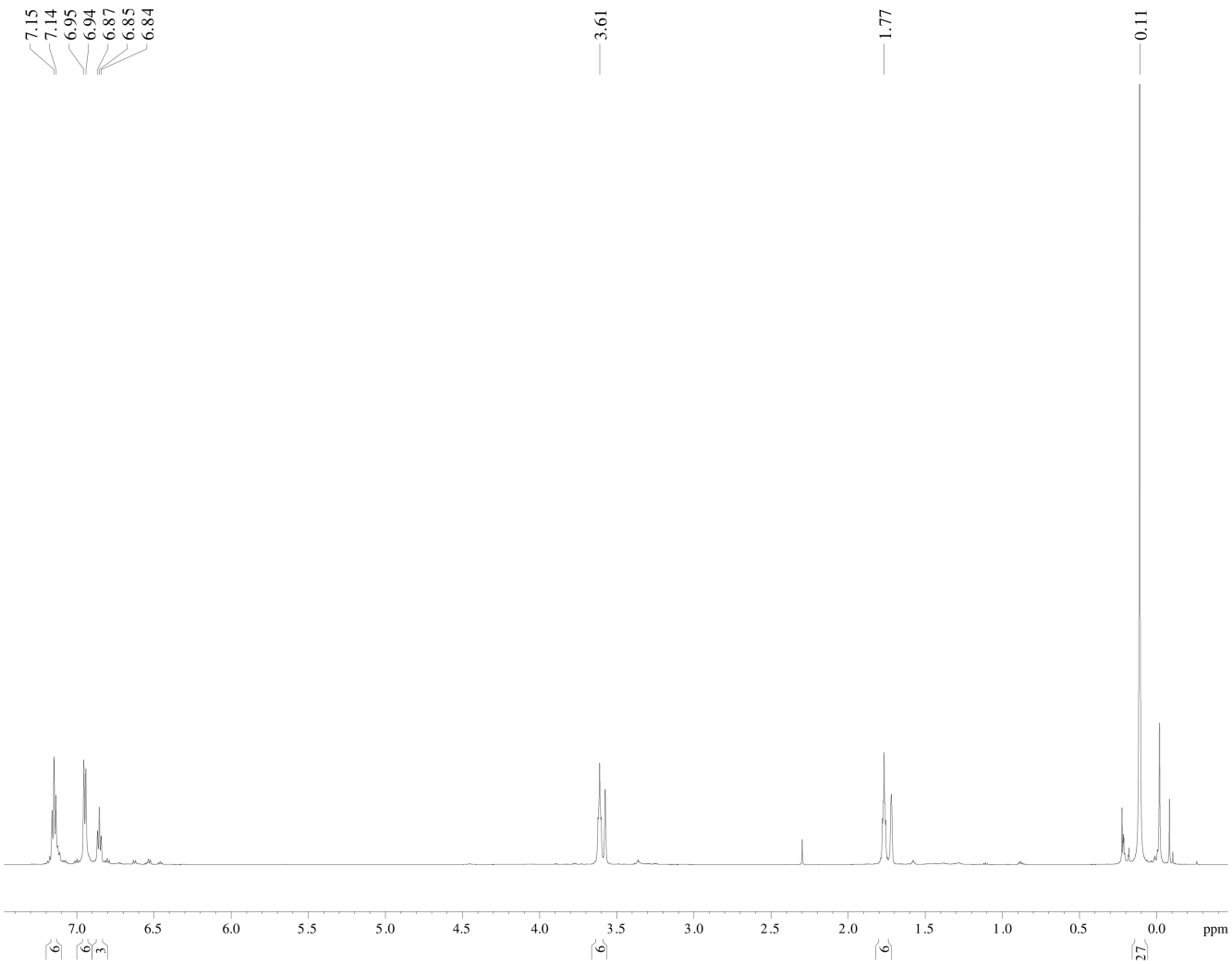

Figure 4.3. ^{1}H NMR spectrum of **1-Sc**.

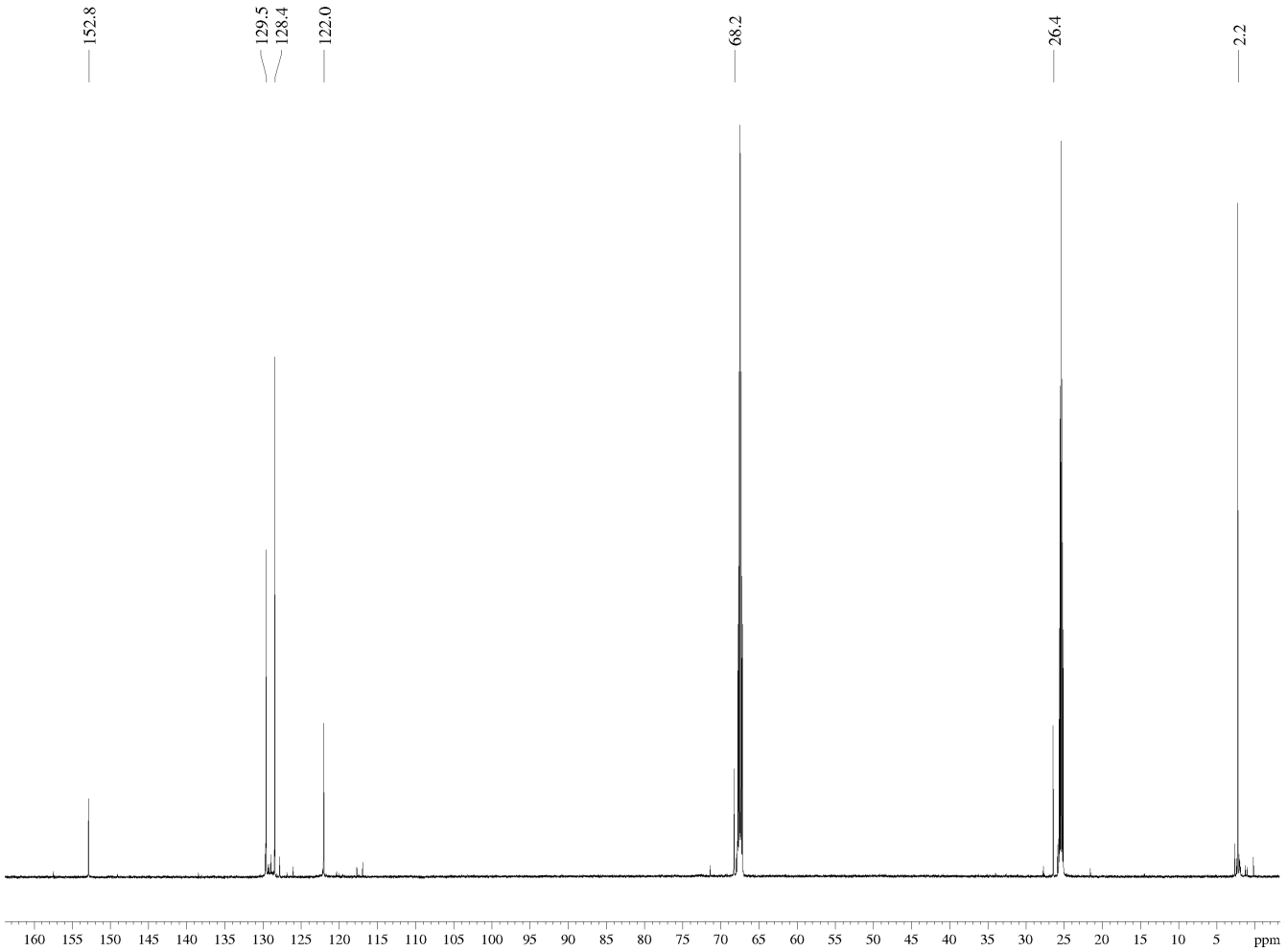

Figure 5.3. $^{13}C\{^{1}H\}$ NMR spectrum of **1-Sc**.

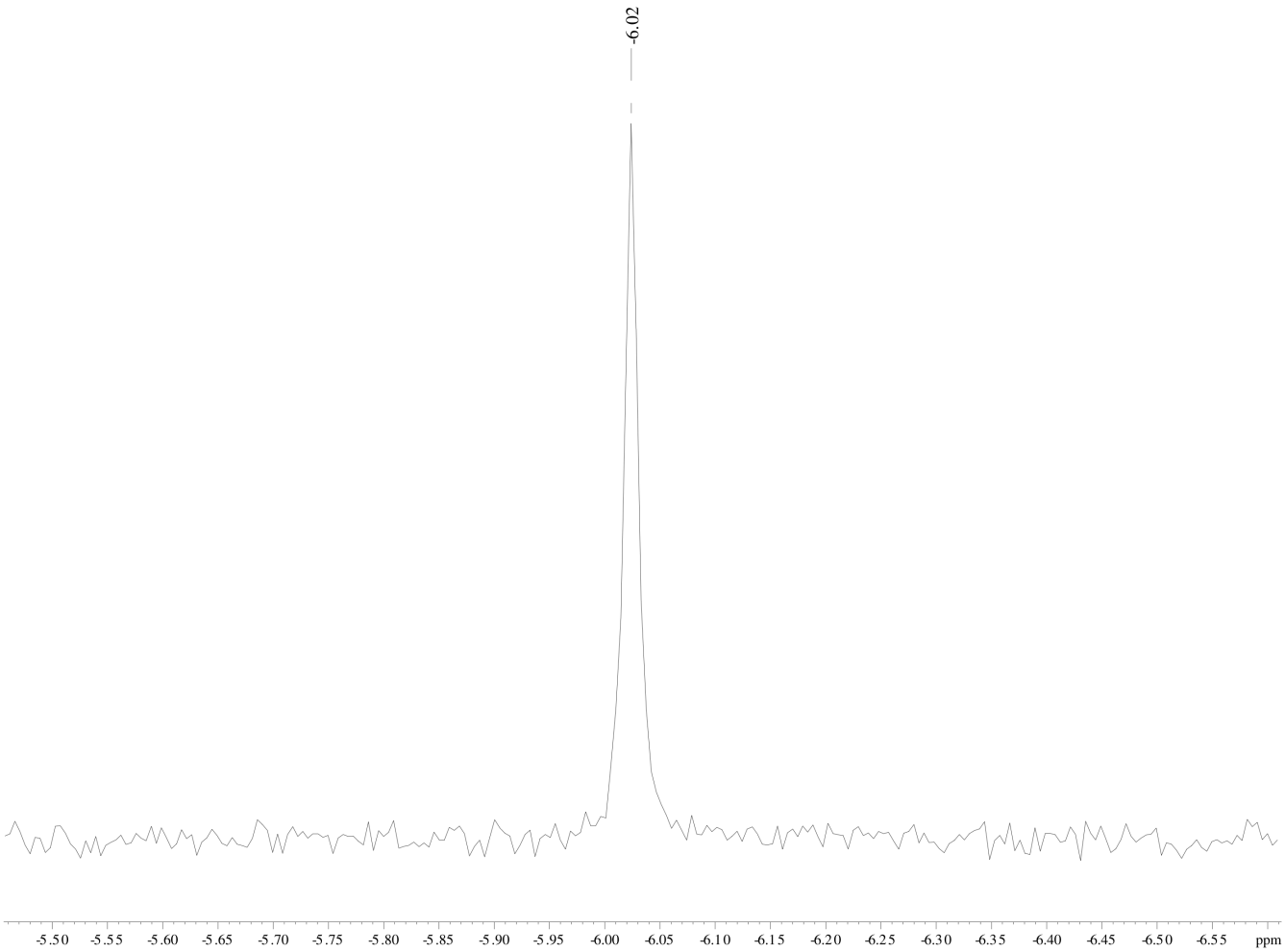

Figure 6.3. $^{29}Si\{^{1}H\}$ INEPT NMR spectrum of **1-Sc**.

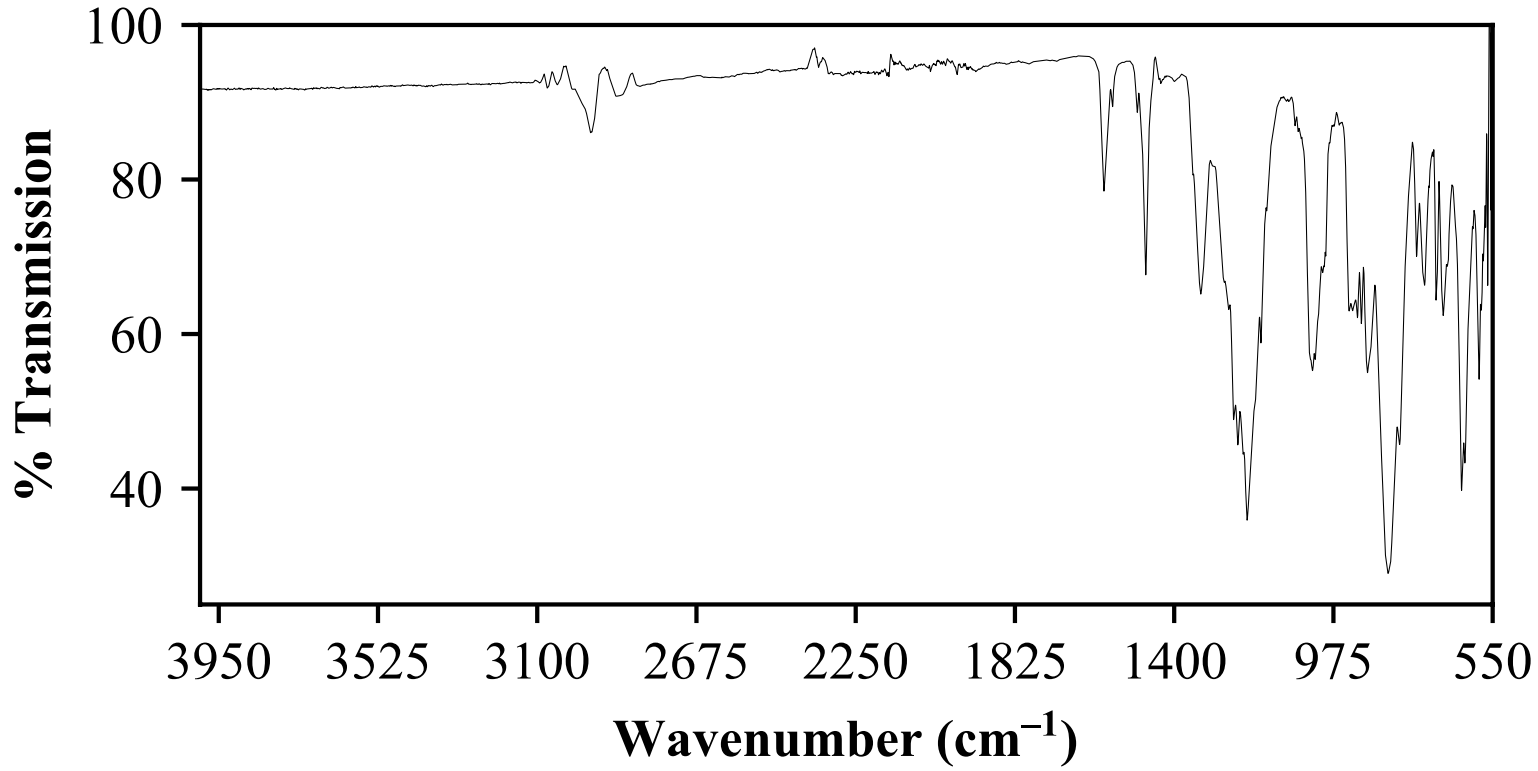

Figure 7.3. IR spectrum of **1-Sc**.

Table 4.3. Crystal data and structure refinement for **1-Y**.

Empirical formula	$C_{31}\ H_{50}\ N_3\ O\ Si_3\ Y$	
Formula weight	653.92	
Temperature	88(2) K	
Wavelength	0.71073 Å	
Crystal system	Monoclinic	
Space group	$P2_1/n$	
Unit cell dimensions	a = 11.0481(15) Å	α= 90°.
	b = 18.343(3) Å	β= 98.8909(18)°.
	c = 17.455(2) Å	γ = 90°.
Volume	3494.9(8) $Å^3$	
Z	4	
Density (calculated)	1.243 Mg/m^3	
Absorption coefficient	1.798 mm^{-1}	
F(000)	1384	
Crystal color	colorless	
Crystal size	0.319 x 0.274 x 0.220 mm^3	
Theta range for data collection	1.621 to 29.118°	
Index ranges	$-14 \le h \le 14$, $-24 \le k \le 24$, $-22 \le l \le 22$	
Reflections collected	42525	
Independent reflections	8884 [R(int) = 0.0293]	
Completeness to theta = 25.500°	100.0 %	
Absorption correction	Semi-empirical from equivalents	
Max. and min. transmission	0.7458 and 0.6913	
Refinement method	Full-matrix least-squares on F^2	
Data / restraints / parameters	8884 / 0 / 361	
Goodness-of-fit on F^2	1.034	
Final R indices [I>2sigma(I) = 7401 data]	R1 = 0.0281, wR2 = 0.0638	
R indices (all data, 0.73 Å)	R1 = 0.0416, wR2 = 0.0684	
Largest diff. peak and hole	0.463 and -0.300 $e.Å^{-3}$	

X-ray Data Collection, Structure Solution and Refinement for **1-Y**.

A colorless crystal of approximate dimensions 0.220 x 0.274 x 0.319 mm was mounted on a glass fiber and transferred to a Bruker SMART APEX II diffractometer. The APEX2[53] program package was used to determine the unit-cell parameters and for data collection (20 sec/frame scan time for a sphere of diffraction data). The raw frame data was processed using SAINT[54] and SADABS[55] to yield the reflection data file. Subsequent calculations were carried out using the SHELXTL[56] program. The diffraction symmetry was 2/*m* and the systematic absences were consistent with the monoclinic space group $P2_1/n$ that was later determined to be correct.

The structure was solved by dual space methods and refined on F^2 by full-matrix least-squares techniques. The analytical scattering factors[57] for neutral atoms were used throughout the analysis. Hydrogen atoms were included using a riding model.

Least-squares analysis yielded wR2 = 0.0684 and Goof = 1.034 for 361 variables refined against 8884 data (0.73 Å), R1 = 0.0281 for those 7401 data with $I > 2.0\sigma(I)$.

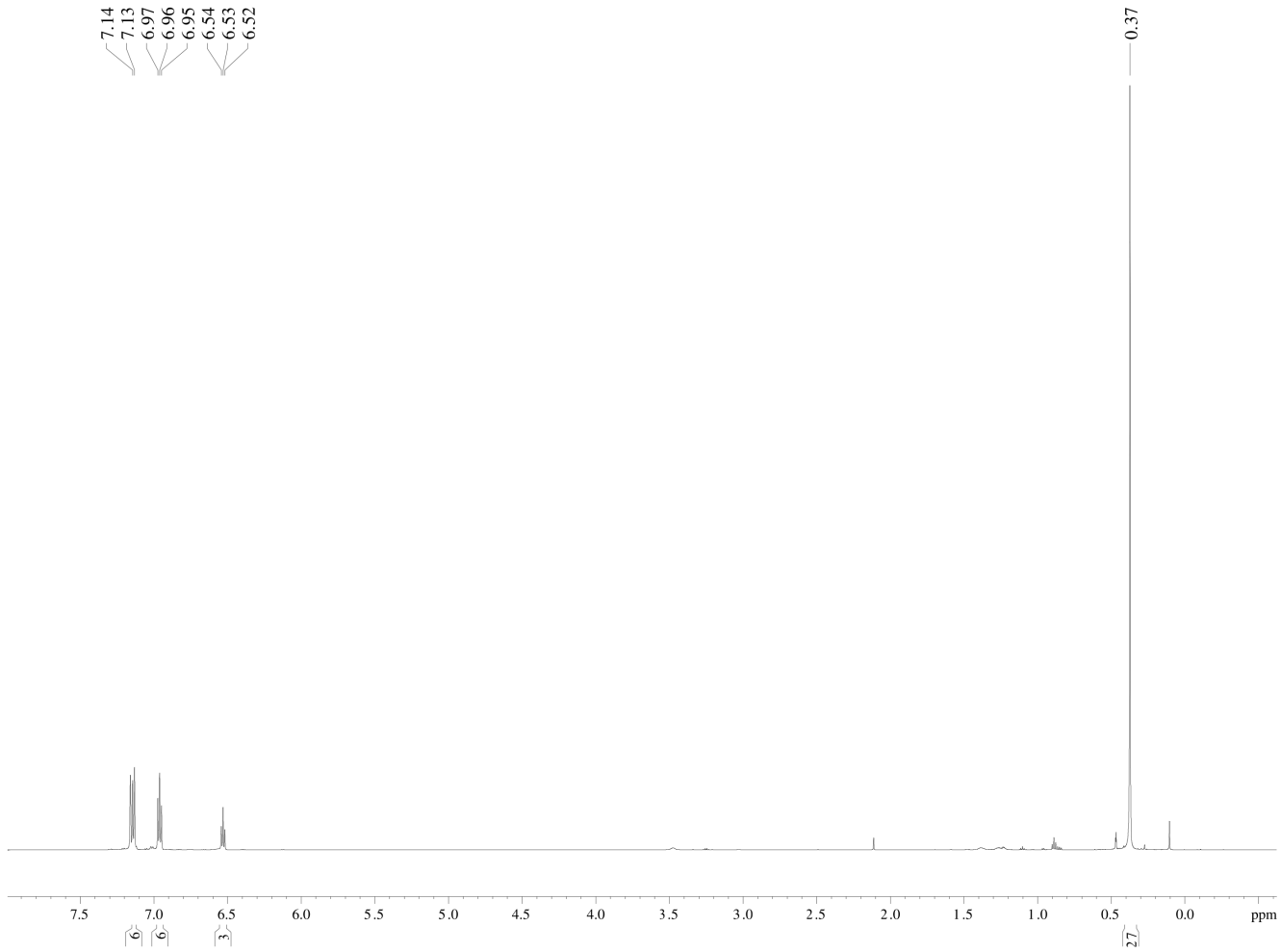

Figure 8.3. ^{1}H NMR spectrum of **1-Y**.

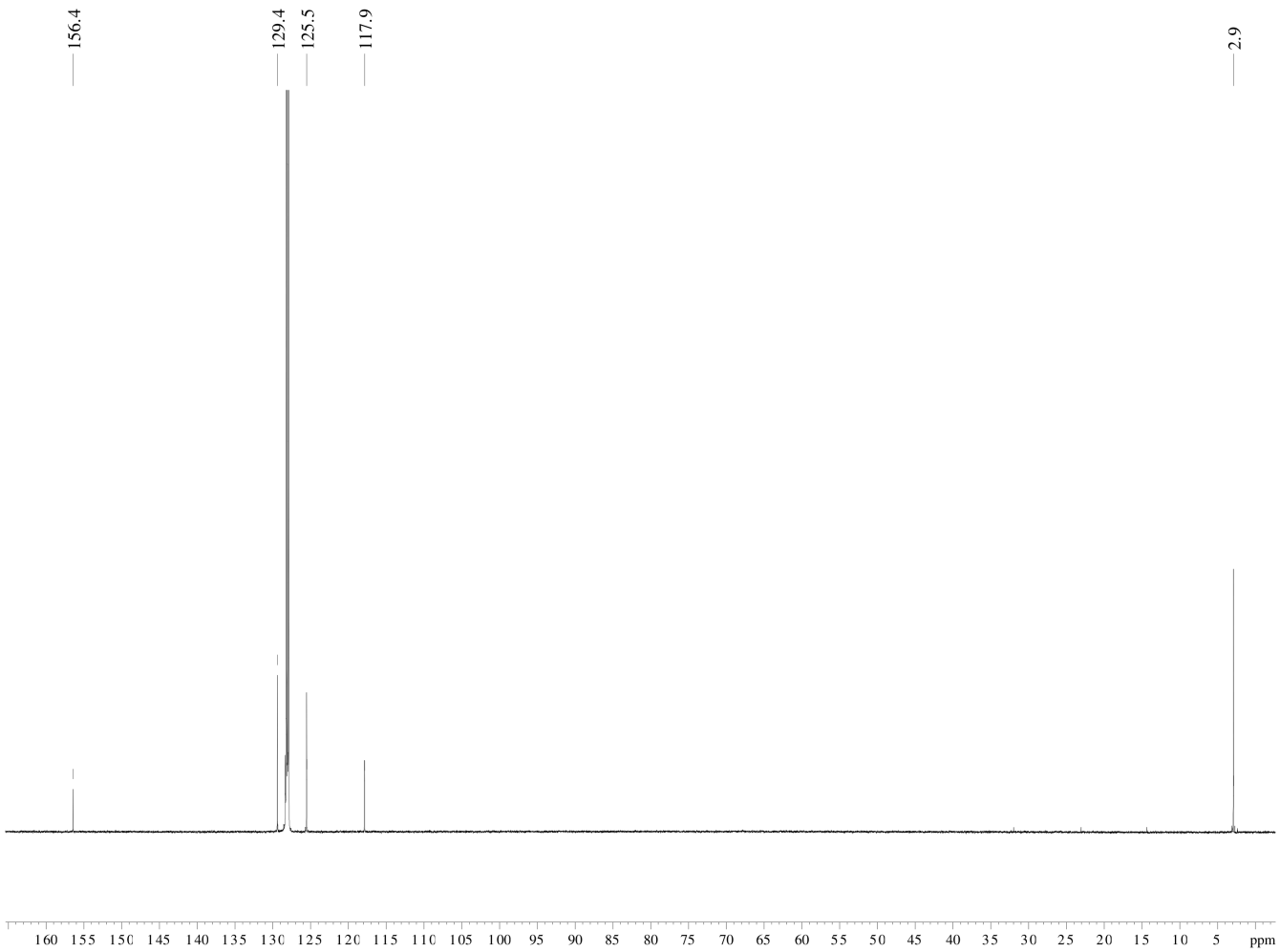

Figure 9.3. $^{13}C\{^{1}H\}$ NMR spectrum of **1-Y**.

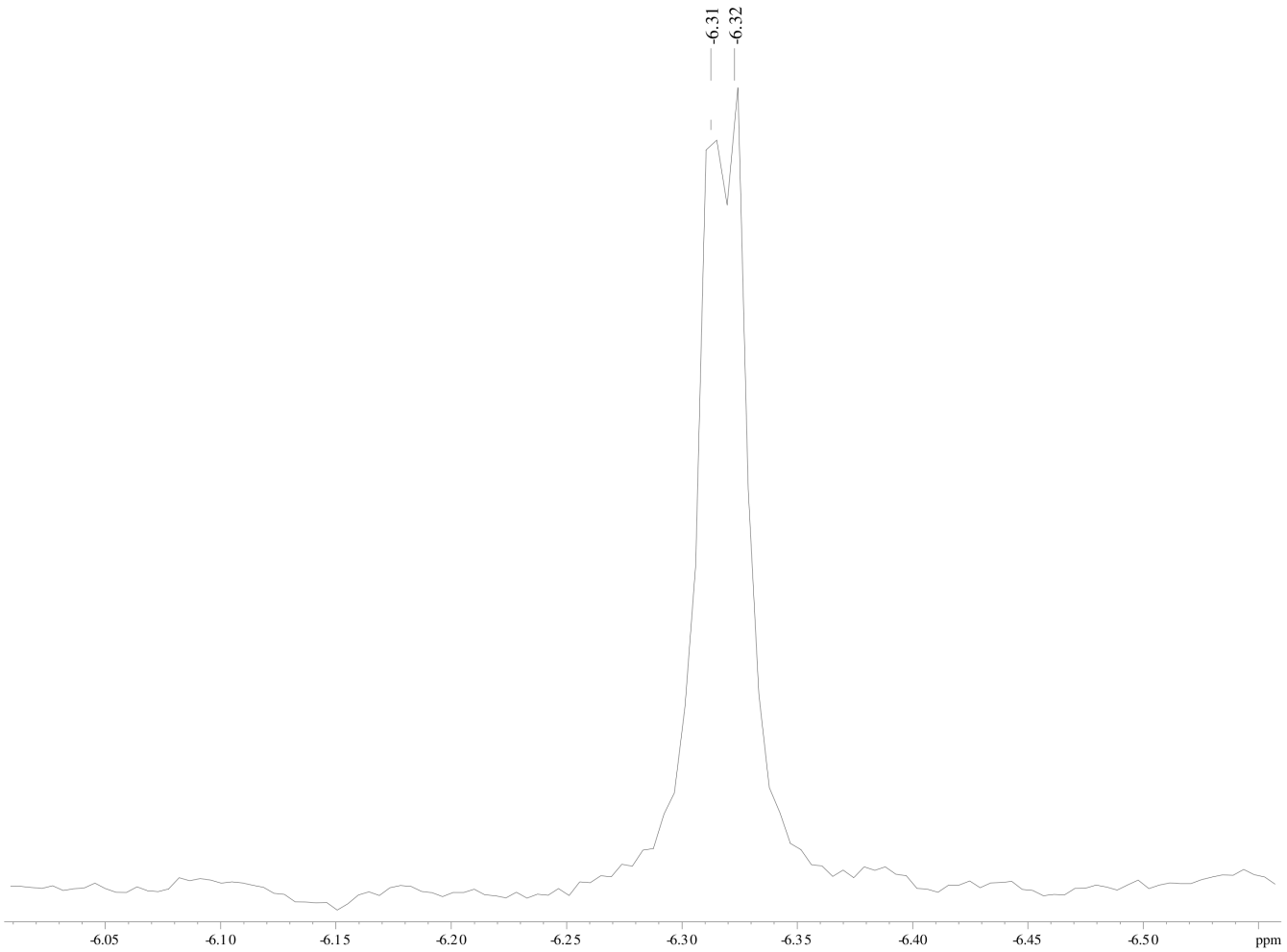

Figure 10.3. $^{29}Si\{^{1}H\}$ INEPT NMR spectrum of **1-Y**.

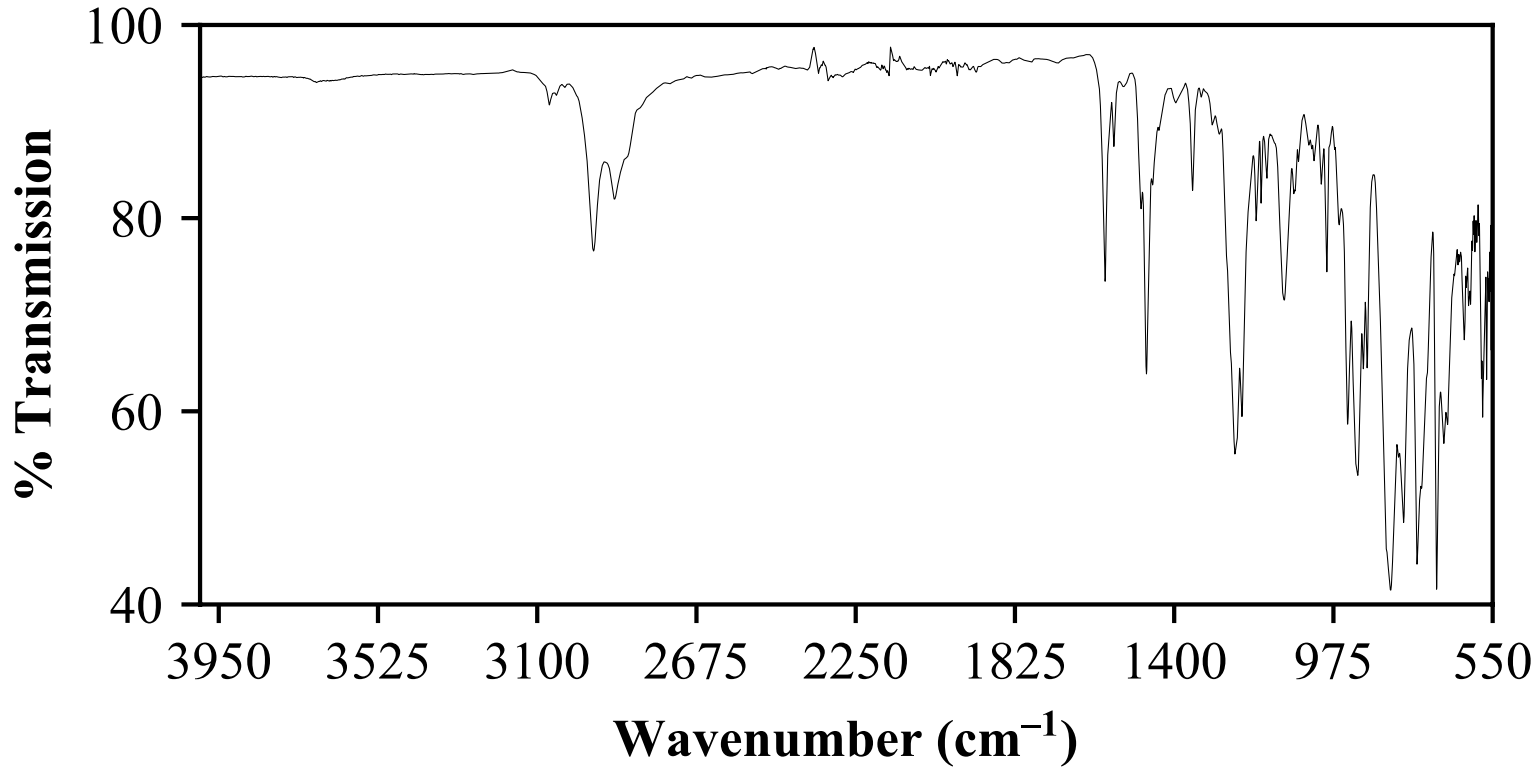

Figure 11.3. IR spectrum of **1-Y**.

Table 5.3. Crystal data and structure refinement for **1-La**.

Empirical formula	C_{31} H_{50} La N_3 O Si_3	
Formula weight	703.92	
Temperature	88(2) K	
Wavelength	0.71073 Å	
Crystal system	Monoclinic	
Space group	$P2_1/n$	
Unit cell dimensions	a = 11.2659(19) Å	α= 90°.
	b = 18.235(3) Å	β= 99.2983(19)°.
	c = 17.637(3) Å	γ = 90°.
Volume	3575.5(11) $Å^3$	
Z	4	
Density (calculated)	1.308 Mg/m^3	
Absorption coefficient	1.321 mm^{-1}	
F(000)	1456	
Crystal color	colorless	
Crystal size	0.591 x 0.402 x 0.325 mm^3	
Theta range for data collection	1.617 to 29.024°	
Index ranges	$-14 \leq h \leq 14$, $-24 \leq k \leq 24$, $-24 \leq l \leq 23$	
Reflections collected	43102	
Independent reflections	9016 [R(int) = 0.0178]	
Completeness to theta = 25.500°	99.8 %	
Absorption correction	Semi-empirical from equivalents	
Max. and min. transmission	0.4317 and 0.3647	
Refinement method	Full-matrix least-squares on F^2	
Data / restraints / parameters	9016 / 0 / 361	
Goodness-of-fit on F^2	1.054	
Final R indices [I>2sigma(I) = 8603 data]	R1 = 0.0168, wR2 = 0.0416	
R indices (all data, 0.73 Å)	R1 = 0.0180, wR2 = 0.0422	
Largest diff. peak and hole	0.626 and -0.326 $e.Å^{-3}$	

X-ray Data Collection, Structure Solution and Refinement for **1-Y**.

A colorless crystal of approximate dimensions 0.325 x 0.402 x 0.591 mm was mounted in a cryoloop and transferred to a Bruker SMART APEX II diffractometer. The APEX2[53] program package was used to determine the unit-cell parameters and for data collection (20 sec/frame scan time for a sphere of diffraction data). The raw frame data was processed using SAINT[54] and SADABS[55] to yield the reflection data file. Subsequent calculations were carried out using the SHELXTL[56] program. The diffraction symmetry was 2/*m* and the systematic absences were consistent with the monoclinic space group $P2_1/n$ that was later determined to be correct.

The structure was solved by dual space methods and refined on F^2 by full-matrix least-squares techniques. The analytical scattering factors[57] for neutral atoms were used throughout the analysis. Hydrogen atoms were included using a riding model.

Least-squares analysis yielded wR2 = 0.0422 and Goof = 1.054 for 361 variables refined against 9016 data (0.73 Å), R1 = 0.0168 for those 8603 data with $I > 2.0\sigma(I)$.

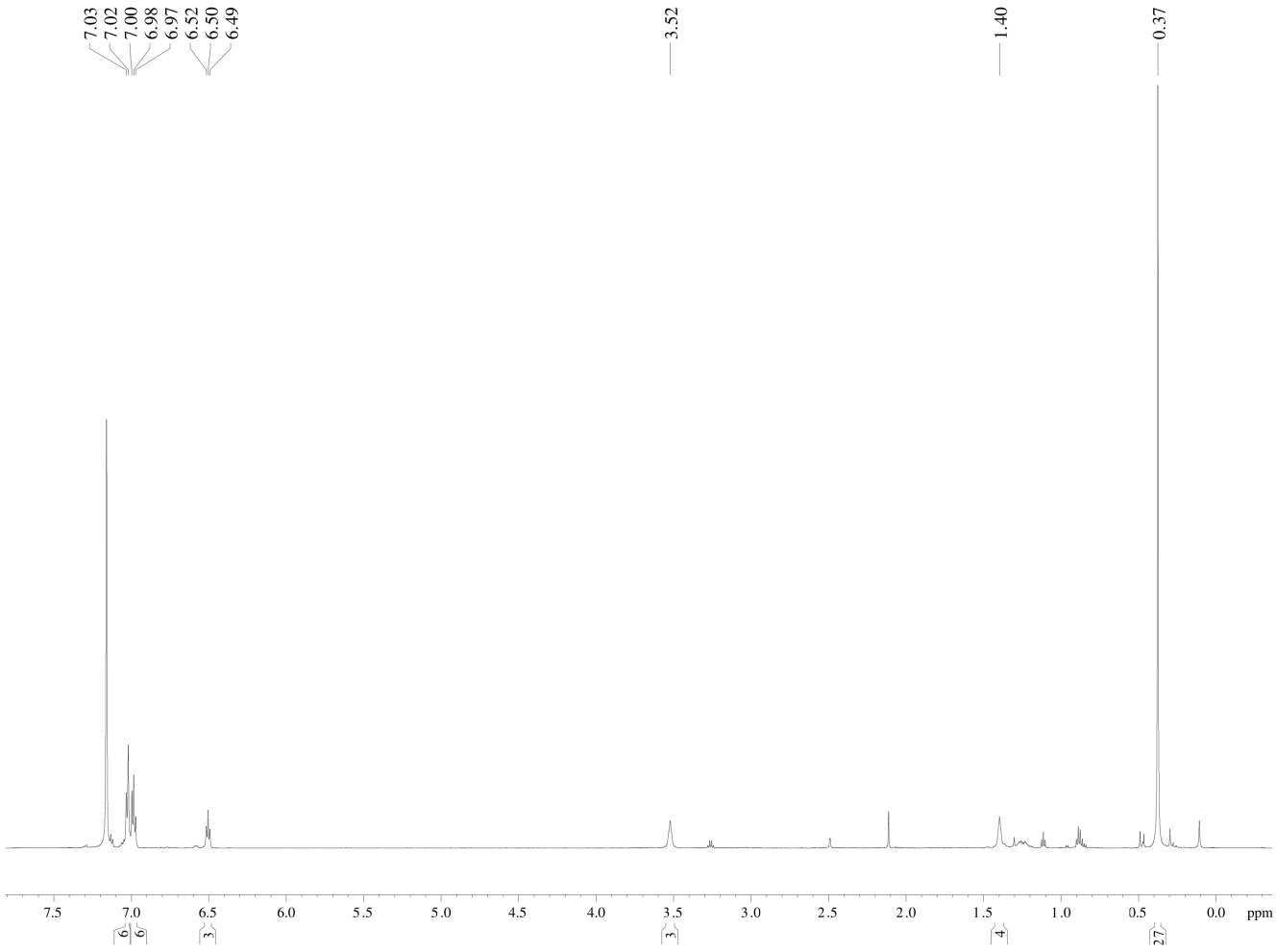

Figure 12.3. ^{1}H NMR spectrum of **1-La**.

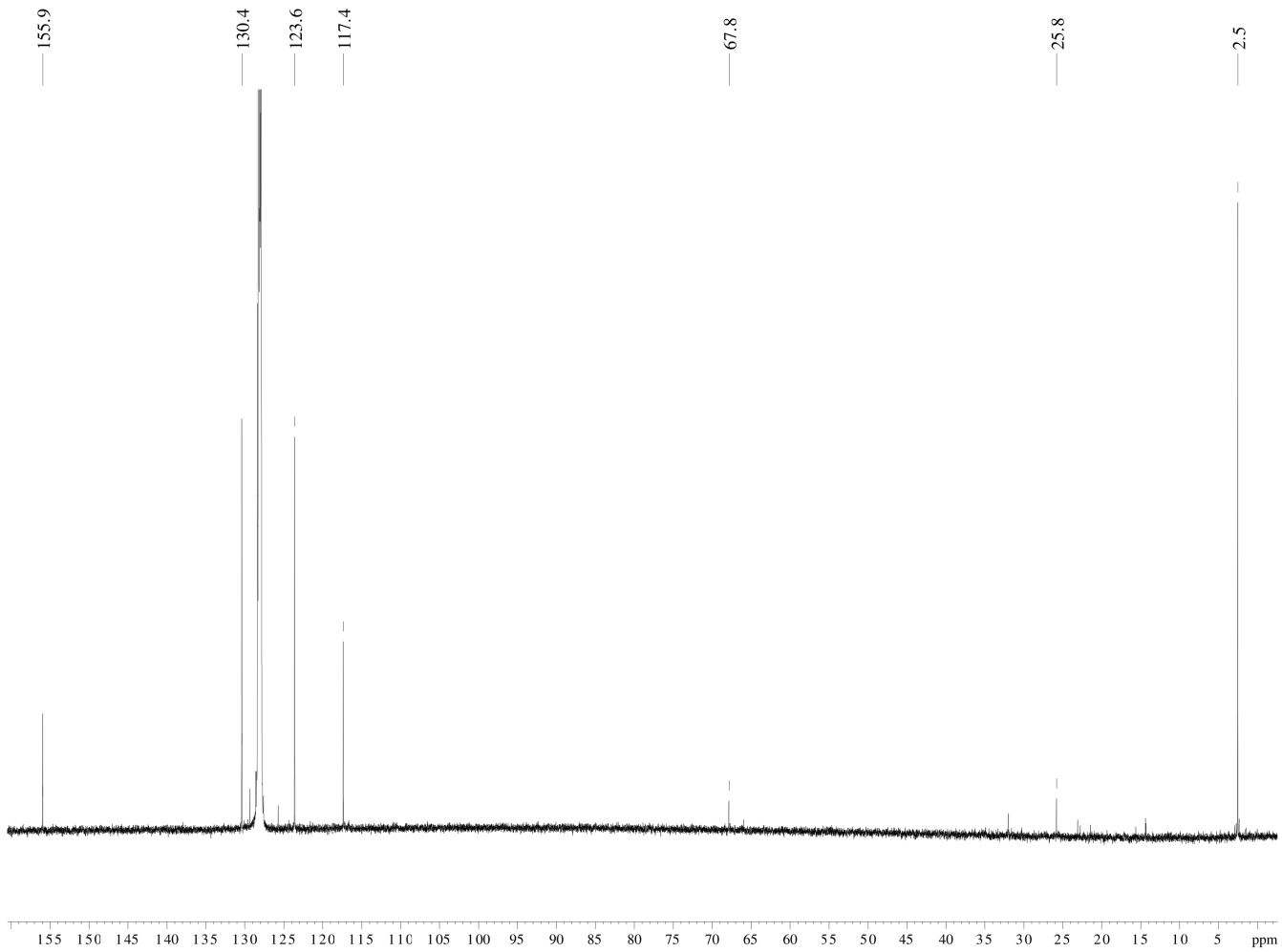

Figure 13.3. $^{13}C\{^{1}H\}$ NMR spectrum of **1-La**.

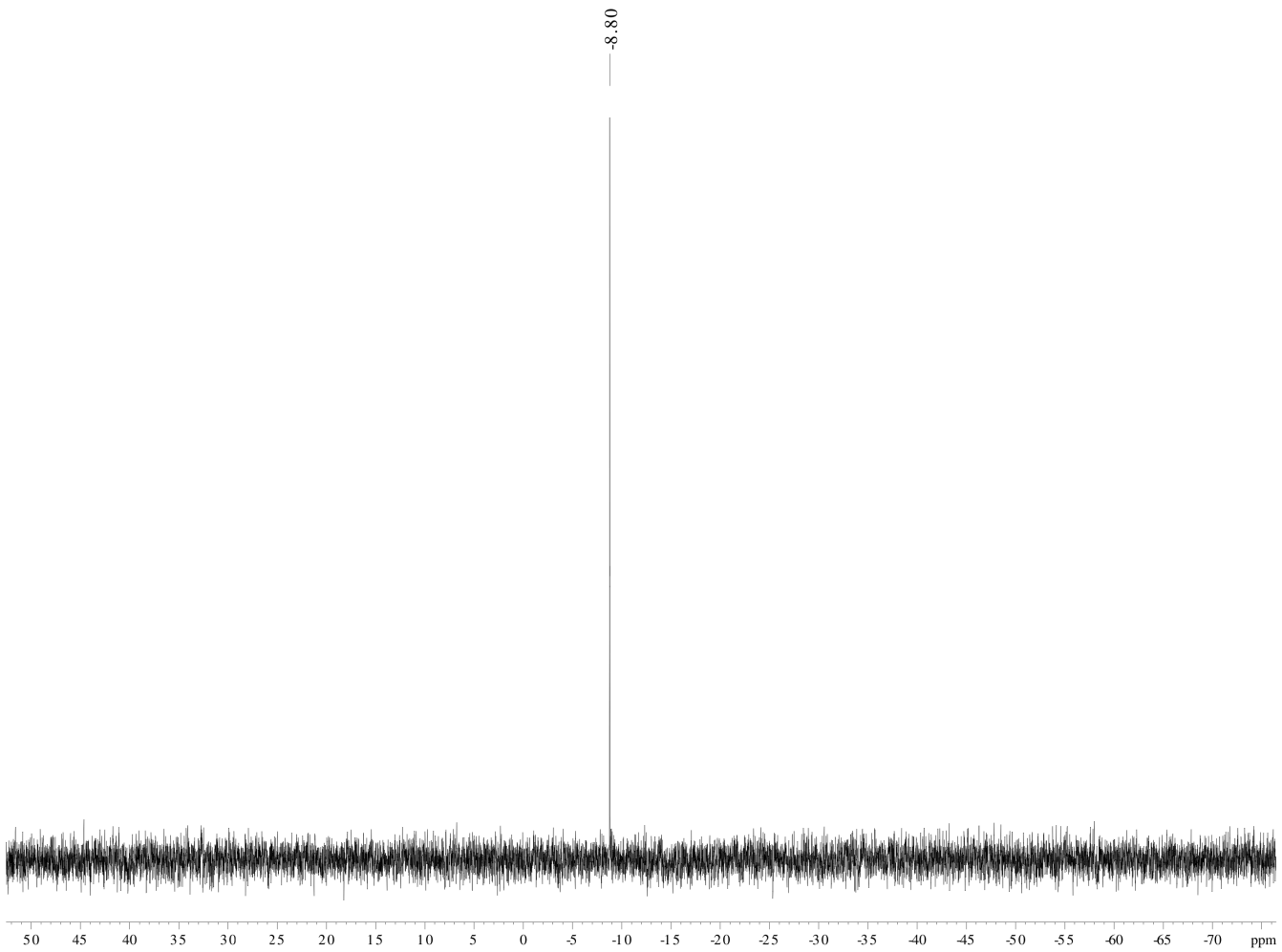

Figure 14.3. $^{29}Si\{^{1}H\}$ INEPT NMR spectrum of **1-La**.

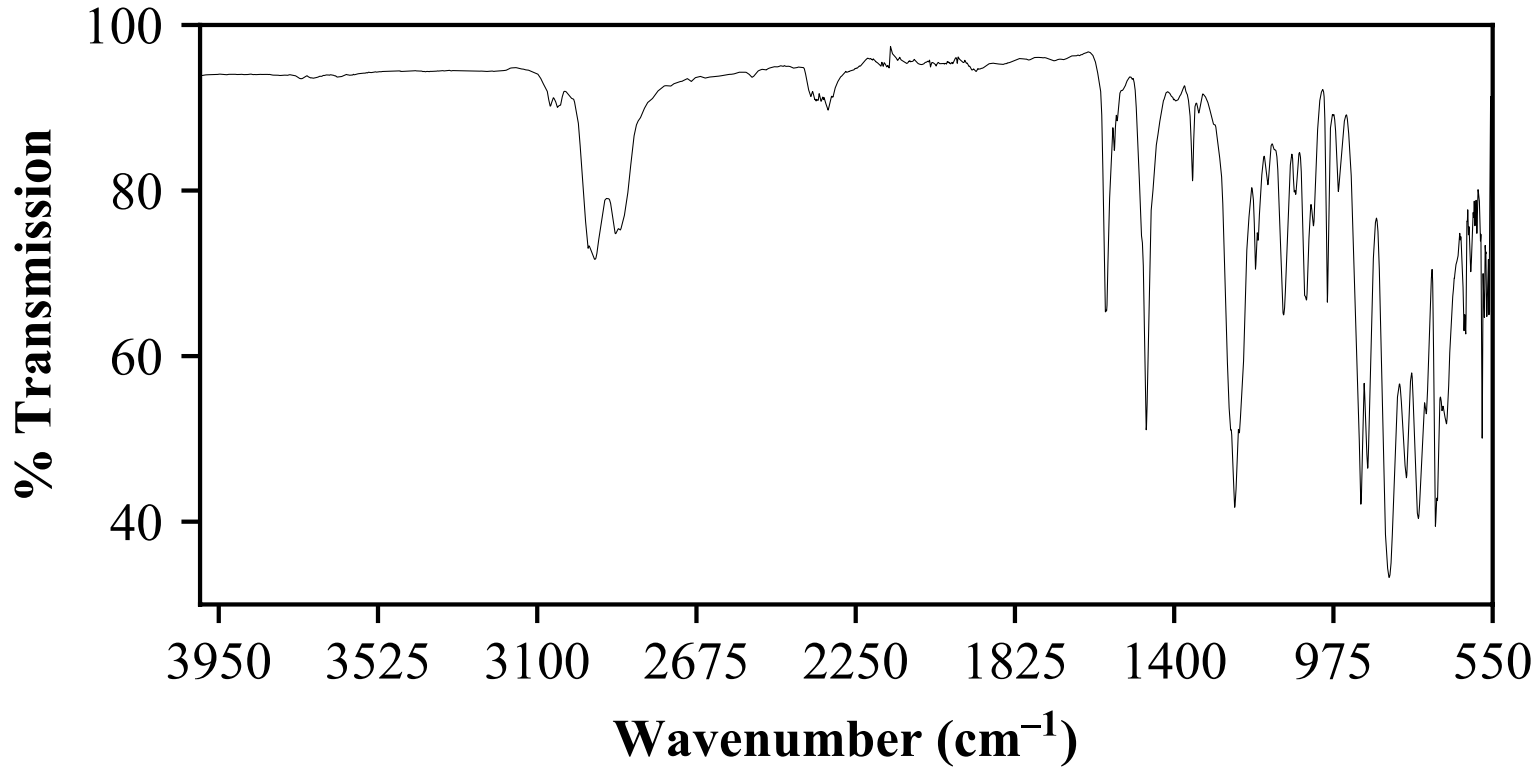

Figure 15.3. IR spectrum of **1-La**.

Table 6.3. Crystal data and structure refinement for **1-Ce**.

Empirical formula	C_{31} H_{50} Ce N_3 O Si_3	
Formula weight	705.13	
Temperature	133(2) K	
Wavelength	0.71073 Å	
Crystal system	Monoclinic	
Space group	$P2_1/n$	
Unit cell dimensions	a = 11.1829(13) Å	α= 90°.
	b = 18.267(2) Å	β= 99.4793(13)°.
	c = 17.650(2) Å	γ = 90°.
Volume	3556.4(7) $Å^3$	
Z	4	
Density (calculated)	1.317 Mg/m^3	
Absorption coefficient	1.407 mm^{-1}	
F(000)	1460	
Crystal color	yellow	
Crystal size	0.314 x 0.237 x 0.211 mm^3	
Theta range for data collection	1.616 to 28.881°	
Index ranges	$-14 \le h \le 14$, $-24 \le k \le 24$, $-22 \le l \le 23$	
Reflections collected	40674	
Independent reflections	8710 [R(int) = 0.0207]	
Completeness to theta = 25.500°	99.9 %	
Absorption correction	Semi-empirical from equivalents	
Max. and min. transmission	0.7458 and 0.6877	
Refinement method	Full-matrix least-squares on F^2	
Data / restraints / parameters	8710 / 0 / 361	
Goodness-of-fit on F^2	1.056	
Final R indices [I>2sigma(I) = 7791 data]	R1 = 0.0222, wR2 = 0.0516	
R indices (all data, 0.74 Å)	R1 = 0.0271, wR2 = 0.0544	
Largest diff. peak and hole	0.776 and -0.295 $e.Å^{-3}$	

X-ray Data Collection, Structure Solution and Refinement for **1-Ce**.

A yellow crystal of approximate dimensions 0.211 x 0.237 x 0.314 mm was mounted in a cryoloop and transferred to a Bruker SMART APEX II diffractometer. The APEX2[53] program package was used to determine the unit-cell parameters and for data collection (60 sec/frame scan time for a sphere of diffraction data). The raw frame data was processed using SAINT[54] and SADABS[55] to yield the reflection data file. Subsequent calculations were carried out using the SHELXTL[56] program. The diffraction symmetry was 2/*m* and the systematic absences were consistent with the monoclinic space group $P2_1/n$ that was later determined to be correct.

The structure was solved by dual space methods and refined on F^2 by full-matrix least-squares techniques. The analytical scattering factors[57] for neutral atoms were used throughout the analysis. Hydrogen atoms were included using a riding model.

Least-squares analysis yielded wR2 = 0.0544 and Goof = 1.056 for 361 variables refined against 8710 data (0.74 Å), R1 = 0.0222 for those 7791 data with $I > 2.0\sigma(I)$.

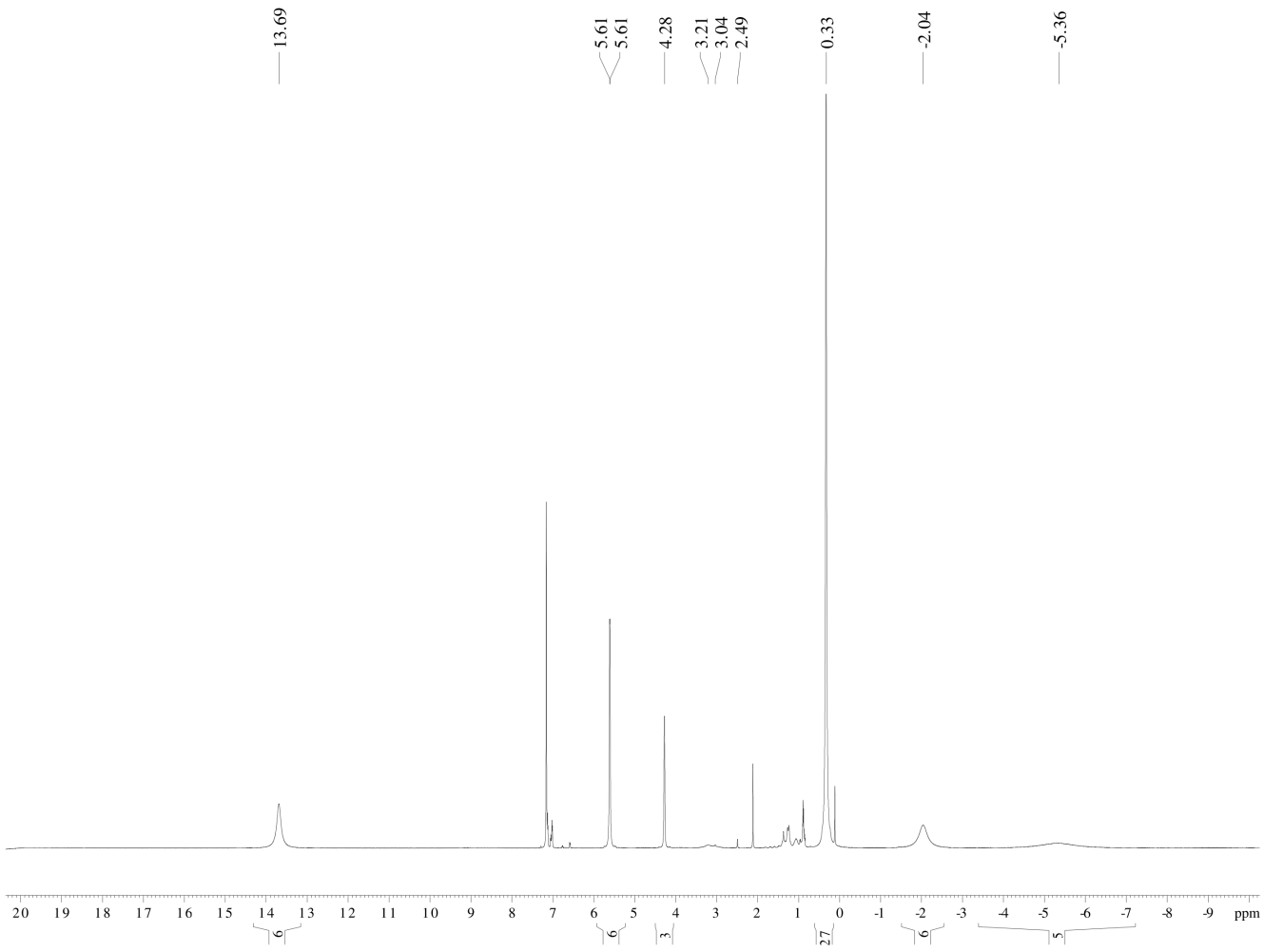

Figure 16.3. ^{1}H NMR spectrum of **1-Ce**.

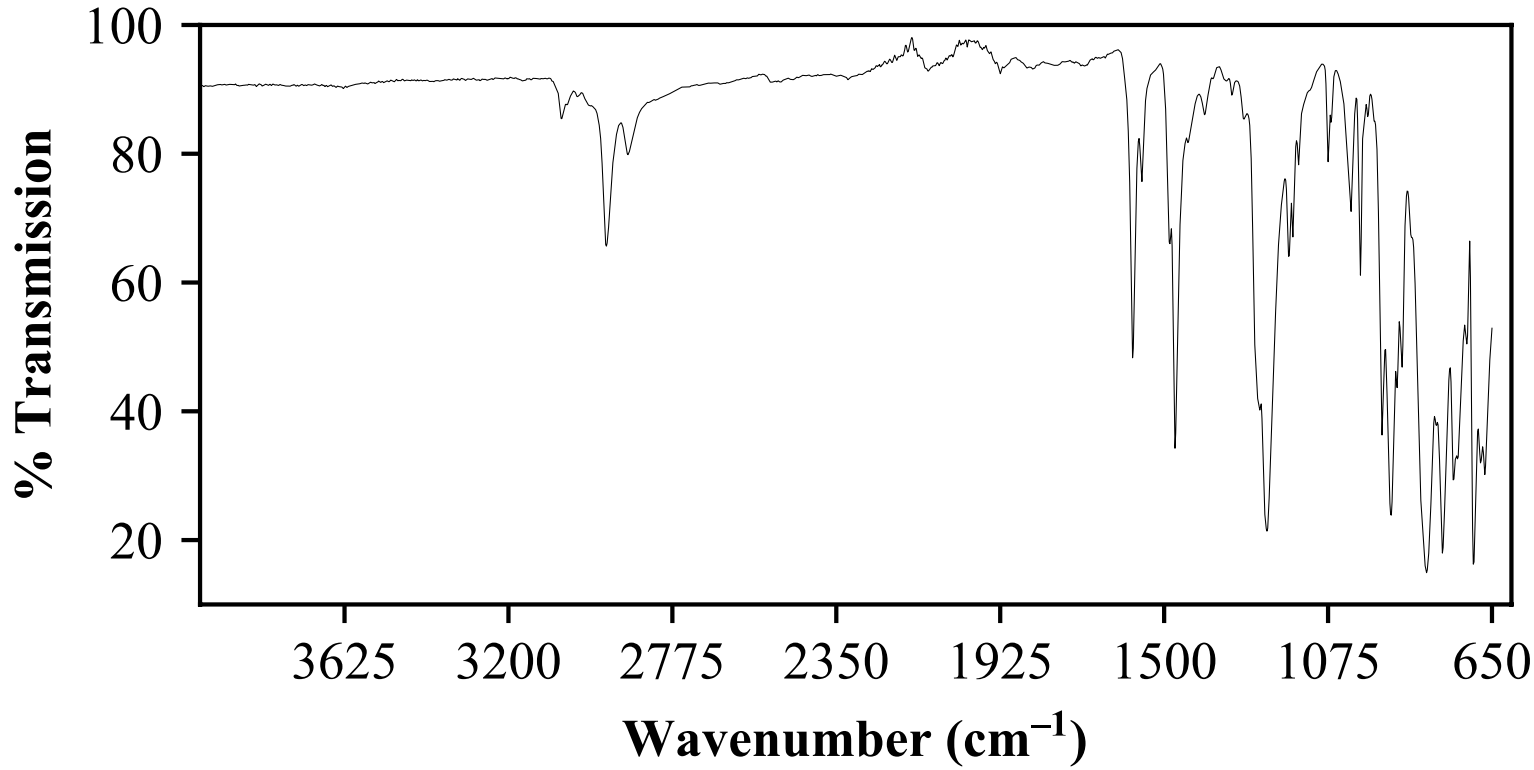

Figure 17.3. IR spectrum of **1-Ce**.

Table 7.3. Crystal data and structure refinement for **1-Pr**.

Empirical formula	$C_{31}\ H_{50}\ N_3\ O\ Pr\ Si_3$	
Formula weight	705.92	
Temperature	133(2) K	
Wavelength	0.71073 Å	
Crystal system	Monoclinic	
Space group	$P2_1/n$	
Unit cell dimensions	a = 11.1572(17) Å	α= 90°.
	b = 18.305(3) Å	β= 99.2088(18)°.
	c = 17.592(3) Å	γ = 90°.
Volume	3546.5(9) $Å^3$	
Z	4	
Density (calculated)	1.322 Mg/m^3	
Absorption coefficient	1.501 mm^{-1}	
F(000)	1464	
Crystal color	yellow	
Crystal size	0.336 x 0.294 x 0.140 mm^3	
Theta range for data collection	1.616 to 28.877°	
Index ranges	$-15 \le h \le 14$, $-24 \le k \le 24$, $-23 \le l \le 23$	
Reflections collected	41974	
Independent reflections	8755 [R(int) = 0.0274]	
Completeness to theta = 25.500°	100.0 %	
Absorption correction	Semi-empirical from equivalents	
Max. and min. transmission	0.4316 and 0.3669	
Refinement method	Full-matrix least-squares on F^2	
Data / restraints / parameters	8755 / 0 / 361	
Goodness-of-fit on F^2	1.056	
Final R indices [I>2sigma(I) = 7580 data]	R1 = 0.0227, wR2 = 0.0498	
R indices (all data, 0.74 Å)	R1 = 0.0303, wR2 = 0.0528	
Largest diff. peak and hole	0.779 and -0.319 $e.Å^{-3}$	

X-ray Data Collection, Structure Solution and Refinement for **1-Pr**.

A yellow crystal of approximate dimensions 0.140 x 0.294 x 0.336 mm was mounted in a cryoloop and transferred to a Bruker SMART APEX II diffractometer. The APEX2[53] program package was used to determine the unit-cell parameters and for data collection (30 sec/frame scan time for a sphere of diffraction data). The raw frame data was processed using SAINT[54] and SADABS[55] to yield the reflection data file. Subsequent calculations were carried out using the SHELXTL[56] program. The diffraction symmetry was 2/*m* and the systematic absences were consistent with the monoclinic space group $P2_1/n$ that was later determined to be correct.

The structure was solved by dual space methods and refined on F^2 by full-matrix least-squares techniques. The analytical scattering factors[57] for neutral atoms were used throughout the analysis. Hydrogen atoms were included using a riding model.

Least-squares analysis yielded wR2 = 0.0528 and Goof = 1.056 for 361 variables refined against 8755 data (0.74 Å), R1 = 0.0227 for those 7580 data with $I > 2.0\sigma(I)$.

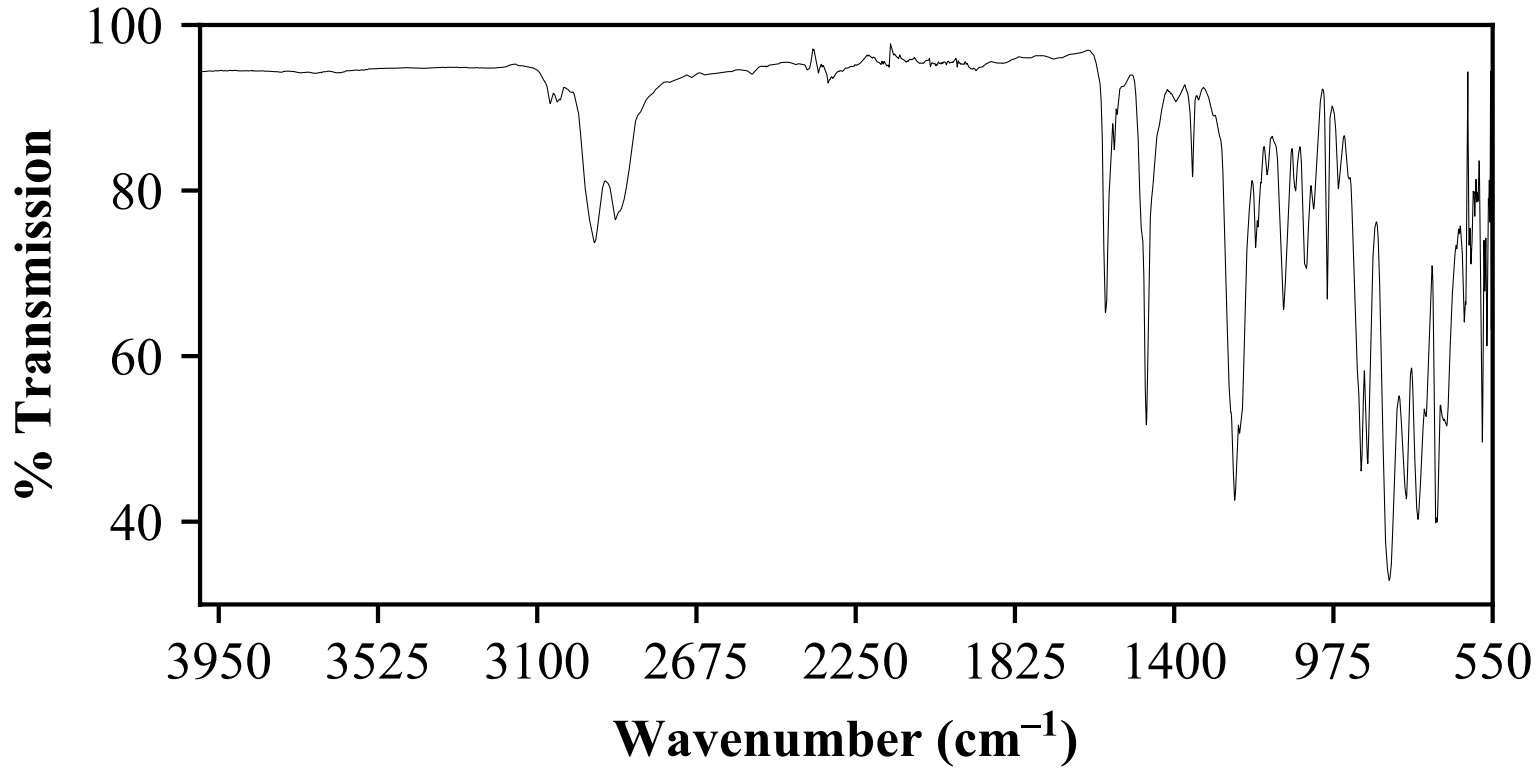

Figure 18.3. IR spectrum of **1-Pr**.

Table 8.3. Crystal data and structure refinement for **1-Gd**.

Empirical formula	C_{31} H_{50} Gd N_3 O Si_3	
Formula weight	722.26	
Temperature	153(2) K	
Wavelength	0.71073 Å	
Crystal system	Monoclinic	
Space group	$P2_1/n$	
Unit cell dimensions	a = 11.0395(14) Å	α= 90°.
	b = 18.425(2) Å	β= 99.1786(15)°.
	c = 17.560(2) Å	γ = 90°.
Volume	3526.1(8) $Å^3$	
Z	4	
Density (calculated)	1.361 Mg/m^3	
Absorption coefficient	2.009 mm^{-1}	
F(000)	1484	
Crystal color	colorless	
Crystal size	0.501 x 0.200 x 0.083 mm^3	
Theta range for data collection	1.613 to 28.846°	
Index ranges	$-14 \le h \le 14$, $-24 \le k \le 23$, $-23 \le l \le 22$	
Reflections collected	41685	
Independent reflections	8670 [R(int) = 0.0322]	
Completeness to theta = 25.500°	100.0 %	
Absorption correction	Semi-empirical from equivalents	
Max. and min. transmission	0.6945 and 0.5358	
Refinement method	Full-matrix least-squares on F^2	
Data / restraints / parameters	8670 / 0 / 361	
Goodness-of-fit on F^2	1.022	
Final R indices [I>2sigma(I) = 7733 data]	R1 = 0.0201, wR2 = 0.0459	
R indices (all data, 0.74 Å)	R1 = 0.0250, wR2 = 0.0484	
Largest diff. peak and hole	0.454 and -0.360 $e.Å^{-3}$	

X-ray Data Collection, Structure Solution and Refinement for **1-Gd**.

A colorless crystal of approximate dimensions 0.083 x 0.200 x 0.501 mm was mounted in a cryoloop and transferred to a Bruker SMART APEX II diffractometer. The APEX2[53] program package was used to determine the unit-cell parameters and for data collection (15 sec/frame scan time for a sphere of diffraction data). The raw frame data was processed using SAINT[54] and SADABS[55] to yield the reflection data file. Subsequent calculations were carried out using the SHELXTL[56] program. The diffraction symmetry was 2/*m* and the systematic absences were consistent with the monoclinic space group $P2_1/n$ that was later determined to be correct.

The structure was solved using the coordinates of the neodymium analogue[15] and refined on F^2 by full-matrix least-squares techniques. The analytical scattering factors[57] for neutral atoms were used throughout the analysis. Hydrogen atoms were included using a riding model.

At convergence, wR2 = 0.0484 and Goof = 1.022 for 361 variables refined against 8670 data (0.74Å), R1 = 0.0201 for those 7733 data with $I > 2.0\sigma(I)$.

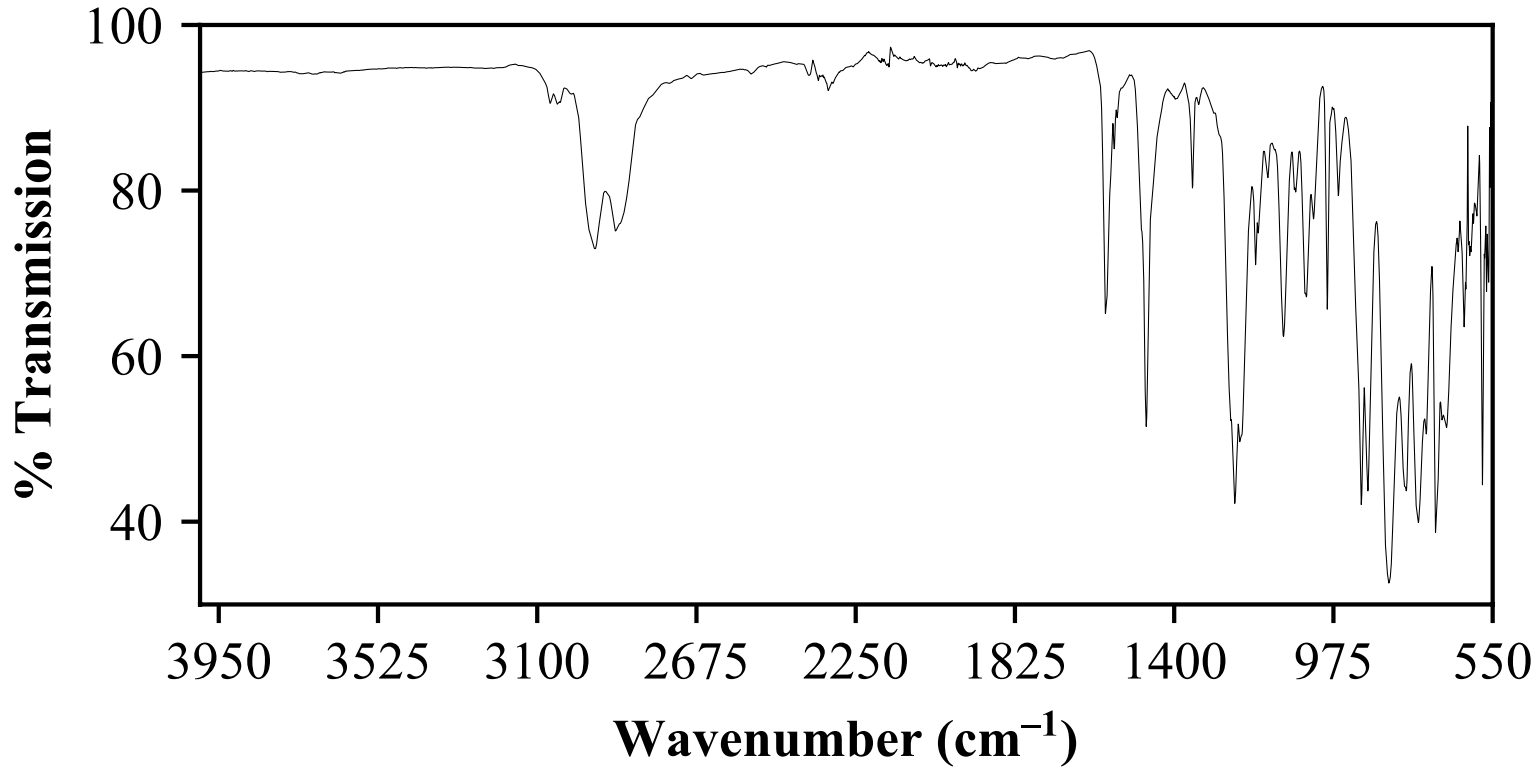

Figure 19.3. IR spectrum of **1-Gd**.

Table 9.3. Crystal data and structure refinement for **1-Dy**.

Empirical formula	C_{31} H_{50} Dy N_3 O Si_3	
Formula weight	727.51	
Temperature	133(2) K	
Wavelength	0.71073 Å	
Crystal system	Monoclinic	
Space group	$P2_1/n$	
Unit cell dimensions	a = 11.0684(10) Å	α= 90°.
	b = 18.3278(16) Å	β= 98.7870(11)°.
	c = 17.4471(15) Å	γ = 90°.
Volume	3497.8(5) $Å^3$	
Z	4	
Density (calculated)	1.382 Mg/m^3	
Absorption coefficient	2.265 mm^{-1}	
F(000)	1492	
Crystal color	colorless	
Crystal size	0.487 x 0.190 x 0.180 mm^3	
Theta range for data collection	1.622 to 28.815°	
Index ranges	$-14 \le h \le 14$, $-24 \le k \le 24$, $-23 \le l \le 23$	
Reflections collected	41160	
Independent reflections	8519 [R(int) = 0.0336]	
Completeness to theta = 25.500°	99.9 %	
Absorption correction	Semi-empirical from equivalents	
Max. and min. transmission	0.7458 and 0.5871	
Refinement method	Full-matrix least-squares on F^2	
Data / restraints / parameters	8519 / 0 / 361	
Goodness-of-fit on F^2	1.026	
Final R indices [I>2sigma(I) = 7430 data]	R1 = 0.0221, wR2 = 0.0478	
R indices (all data, 0.74 Å)	R1 = 0.0293, wR2 = 0.0509	
Largest diff. peak and hole	0.692 and -0.498 $e.Å^{-3}$	

X-ray Data Collection, Structure Solution and Refinement for **1-Dy**.

A colorless crystal of approximate dimensions 0.180 x 0.190 x 0.487 mm was mounted in a cryoloop and transferred to a Bruker SMART APEX II diffractometer. The APEX2[53] program package was used to determine the unit-cell parameters and for data collection (10 sec/frame scan time for a sphere of diffraction data). The raw frame data was processed using SAINT[54] and SADABS[55] to yield the reflection data file. Subsequent calculations were carried out using the SHELXTL[56] program. The diffraction symmetry was 2/*m* and the systematic absences were consistent with the monoclinic space group $P2_1/n$ that was later determined to be correct.

The structure was solved by dual space methods and refined on F^2 by full-matrix least-squares techniques. The analytical scattering factors[57] for neutral atoms were used throughout the analysis. Hydrogen atoms were included using a riding model.

Least-squares analysis yielded wR2 = 0.0509 and Goof = 1.026 for 361 variables refined against 8519 data (0.74 Å), R1 = 0.0221 for those 7430 data with $I > 2.0\sigma(I)$.

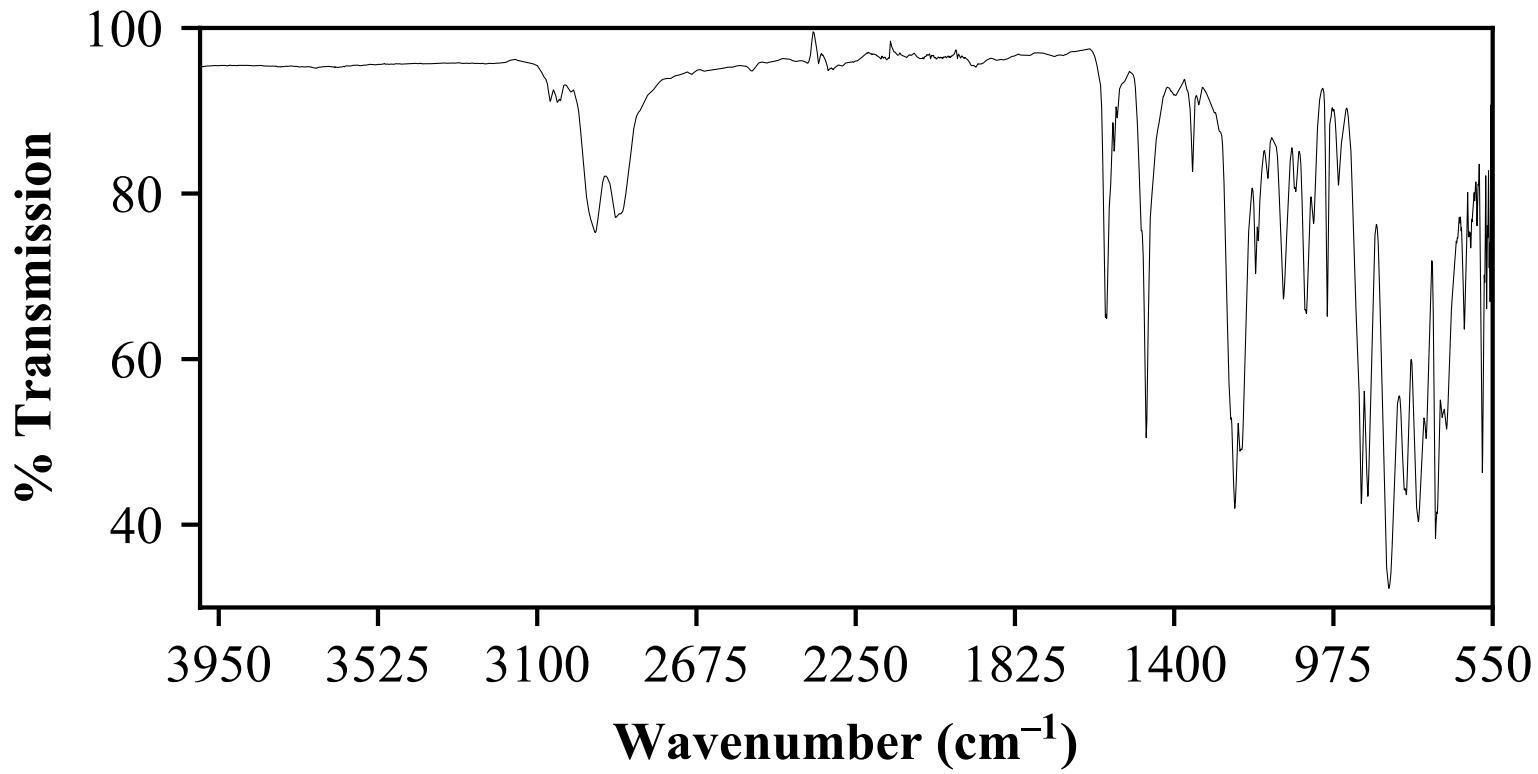

Figure 20.3. IR spectrum of **1-Dy**.

Table 10.1. Crystal data and structure refinement for **1-Ho**.

Empirical formula	C_{31} H_{50} Ho N_3 O Si_3	
Formula weight	729.94	
Temperature	88(2) K	
Wavelength	0.71073 Å	
Crystal system	Monoclinic	
Space group	$P2_1/n$	
Unit cell dimensions	a = 11.0136(9) Å	α= 90°.
	b = 18.3828(16) Å	β= 98.9547(11)°.
	c = 17.4522(15) Å	γ = 90°.
Volume	3490.3(5) $Å^3$	
Z	4	
Density (calculated)	1.389 Mg/m^3	
Absorption coefficient	2.396 mm^{-1}	
F(000)	1496	
Crystal color	yellow	
Crystal size	0.466 x 0.351 x 0.188 mm^3	
Theta range for data collection	1.619 to 29.107°	
Index ranges	$-14 \le h \le 14$, $-24 \le k \le 24$, $-23 \le l \le 23$	
Reflections collected	42438	
Independent reflections	8878 [R(int) = 0.0565]	
Completeness to theta = 25.500°	99.9 %	
Absorption correction	Semi-empirical from equivalents	
Max. and min. transmission	0.7458 and 0.5763	
Refinement method	Full-matrix least-squares on F^2	
Data / restraints / parameters	8878 / 0 / 361	
Goodness-of-fit on F^2	1.009	
Final R indices [I>2sigma(I) = 7408 data]	R1 = 0.0294, wR2 = 0.0578	
R indices (all data, 0.73 Å)	R1 = 0.0396, wR2 = 0.0618	
Largest diff. peak and hole	0.626 and -0.709 $e.Å^{-3}$	

X-ray Data Collection, Structure Solution and Refinement for **1-Ho**.

A yellow crystal of approximate dimensions 0.188 x 0.351 x 0.466 mm was mounted in a cryoloop and transferred to a Bruker SMART APEX II diffractometer. The APEX2[53] program package was used to determine the unit-cell parameters and for data collection (1 sec/frame scan time for a sphere of diffraction data). The raw frame data was processed using SAINT[54] and SADABS[55] to yield the reflection data file. Subsequent calculations were carried out using the SHELXTL[56] program. The diffraction symmetry was 2/*m* and the systematic absences were consistent with the monoclinic space group $P2_1/n$ that was later determined to be correct.

The structure was solved by dual space methods and refined on F^2 by full-matrix least-squares techniques. The analytical scattering factors[57] for neutral atoms were used throughout the analysis. Hydrogen atoms were included using a riding model.

Least-squares analysis yielded wR2 = 0.0618 and Goof = 1.009 for 361 variables refined against 8878 data (0.73 Å), R1 = 0.0294 for those 7408 data with $I > 2.0\sigma(I)$.

Table 11.1. Crystal data and structure refinement for **1-Tb**.

Empirical formula	C_{31} H_{50} N_3 O Si_3 Tb	
Formula weight	723.93	
Temperature	88(2) K	
Wavelength	0.71073 Å	
Crystal system	Monoclinic	
Space group	$P2_1/n$	
Unit cell dimensions	a = 11.0616(12) Å	α= 90°.
	b = 18.3067(19) Å	β= 99.1215(14)°.
	c = 17.4851(18) Å	γ = 90°.
Volume	3496.0(6) $Å^3$	
Z	4	
Density (calculated)	1.375 Mg/m^3	
Absorption coefficient	2.152 mm^{-1}	
F(000)	1488	
Crystal color	colorless	
Crystal size	0.560 x 0.250 x 0.153 mm^3	
Theta range for data collection	1.621 to 29.147°	
Index ranges	$-15 \le h \le 14$, $-24 \le k \le 24$, $-22 \le l \le 23$	
Reflections collected	42362	
Independent reflections	8873 [R(int) = 0.0540]	
Completeness to theta = 25.500°	100.0 %	
Absorption correction	Semi-empirical from equivalents	
Max. and min. transmission	0.7458 and 0.5108	
Refinement method	Full-matrix least-squares on F^2	
Data / restraints / parameters	8873 / 0 / 361	
Goodness-of-fit on F^2	1.022	
Final R indices [I>2sigma(I) = 7323 data]	R1 = 0.0296, wR2 = 0.0542	
R indices (all data, 0.73 Å)	R1 = 0.0421, wR2 = 0.0578	
Largest diff. peak and hole	0.532 and -0.590 $e.Å^{-3}$	

X-ray Data Collection, Structure Solution and Refinement for **1-Tb**.

A colorless crystal of approximate dimensions 0.153 x 0.250 x 0.560 mm was mounted in a cryoloop and transferred to a Bruker SMART APEX II diffractometer. The APEX2[53] program package was used to determine the unit-cell parameters and for data collection (2 sec/frame scan time for a sphere of diffraction data). The raw frame data was processed using SAINT[54] and SADABS[55] to yield the reflection data file. Subsequent calculations were carried out using the SHELXTL[56] program. The diffraction symmetry was 2/*m* and the systematic absences were consistent with the monoclinic space group $P2_1/n$ that was later determined to be correct.

The structure was solved by dual space methods and refined on F^2 by full-matrix least-squares techniques. The analytical scattering factors[57] for neutral atoms were used throughout the analysis. Hydrogen atoms were included using a riding model.

Least-squares analysis yielded wR2 = 0.0578 and Goof = 1.022 for 361 variables refined against 8873 data (0.73 Å), R1 = 0.0296 for those 7323 data with $I > 2.0\sigma(I)$.

Table 12.1. Crystal data and structure refinement for **1-Lu**.

Empirical formula	C_{31} H_{50} Lu N_3 O Si_3	
Formula weight	739.98	
Temperature	133(2) K	
Wavelength	0.71073 Å	
Crystal system	Monoclinic	
Space group	$P2_1/n$	
Unit cell dimensions	a = 10.932(2) Å	α= 90°.
	b = 18.450(4) Å	β= 98.657(2)°.
	c = 17.427(3) Å	γ = 90°.
Volume	3474.8(12) $Å^3$	
Z	4	
Density (calculated)	1.414 Mg/m^3	
Absorption coefficient	2.971 mm^{-1}	
F(000)	1512	
Crystal color	colorless	
Crystal size	0.371 x 0.221 x 0.184 mm^3	
Theta range for data collection	1.617 to 28.858°	
Index ranges	$-14 \le h \le 14$, $-24 \le k \le 24$, $-23 \le l \le 22$	
Reflections collected	41324	
Independent reflections	8573 [R(int) = 0.0468]	
Completeness to theta = 25.500°	100.0 %	
Absorption correction	Semi-empirical from equivalents	
Max. and min. transmission	0.7458 and 0.4992	
Refinement method	Full-matrix least-squares on F^2	
Data / restraints / parameters	8573 / 0 / 361	
Goodness-of-fit on F^2	1.022	
Final R indices [I>2sigma(I) = 7574 data]	R1 = 0.0302, wR2 = 0.0772	
R indices (all data, 0.74 Å)	R1 = 0.0359, wR2 = 0.0811	
Largest diff. peak and hole	3.554 and -1.877 $e.Å^{-3}$	

X-ray Data Collection, Structure Solution and Refinement for **1-Lu**.

A colorless crystal of approximate dimensions 0.184 x 0.221 x 0.371 mm was mounted in a cryoloop and transferred to a Bruker SMART APEX II diffractometer. The APEX2[53] program package was used to determine the unit-cell parameters and for data collection (30 sec/frame scan time for a sphere of diffraction data). The raw frame data was processed using SAINT[54] and SADABS[55] to yield the reflection data file. Subsequent calculations were carried out using the SHELXTL[56] program. The diffraction symmetry was 2/*m* and the systematic absences were consistent with the monoclinic space group $P2_1/n$ that was later determined to be correct.

The structure was solved by dual space methods and refined on F^2 by full-matrix least-squares techniques. The analytical scattering factors[57] for neutral atoms were used throughout the analysis. Hydrogen atoms were included using a riding model.

Least-squares analysis yielded wR2 = 0.0811 and Goof = 1.022 for 361 variables refined against 8573 data (0.74 Å), R1 = 0.0302 for those 7574 data with $I > 2.0\sigma(I)$.

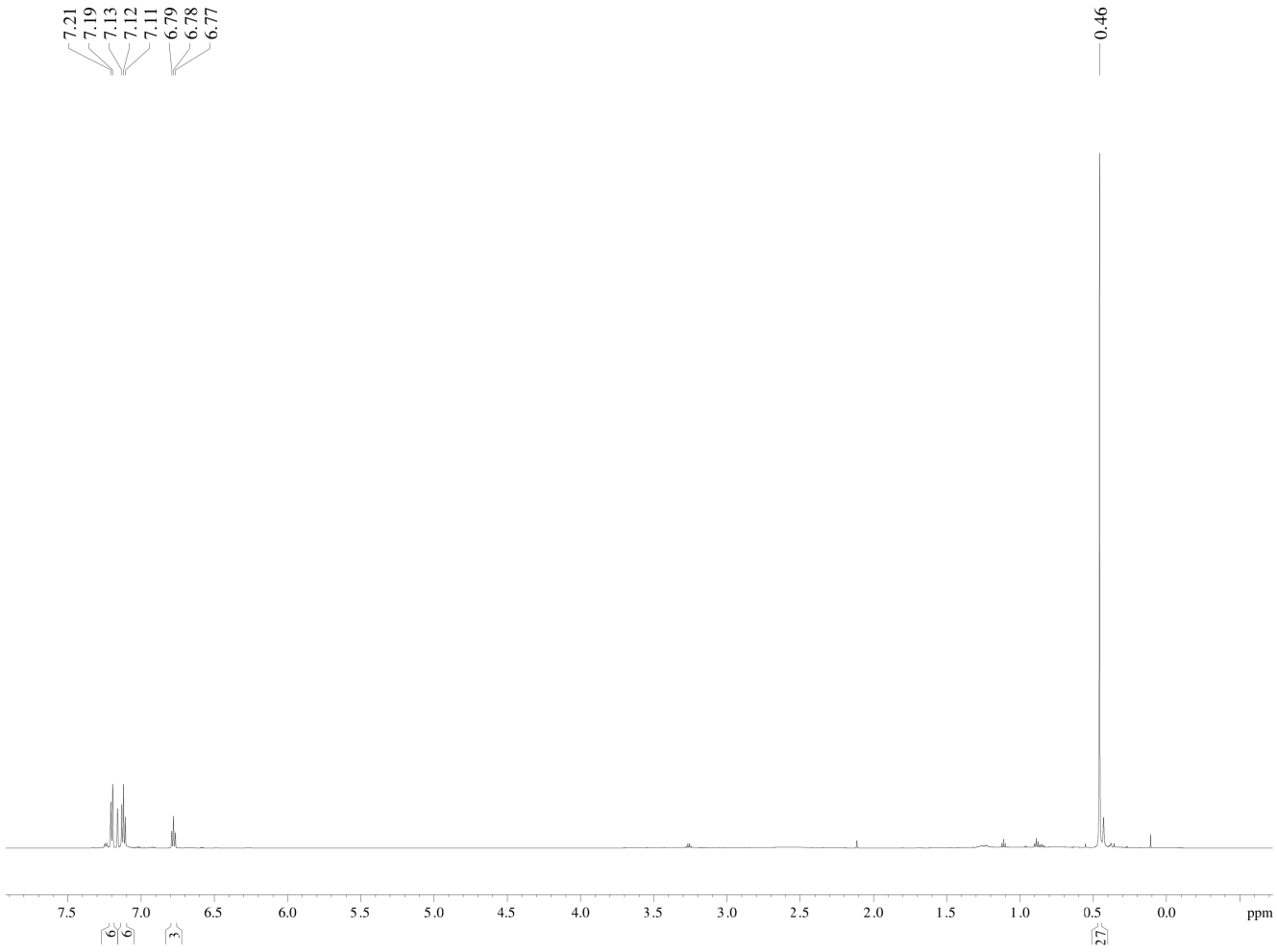

Figure 21.3. ^{1}H NMR spectrum of **1-Lu**.

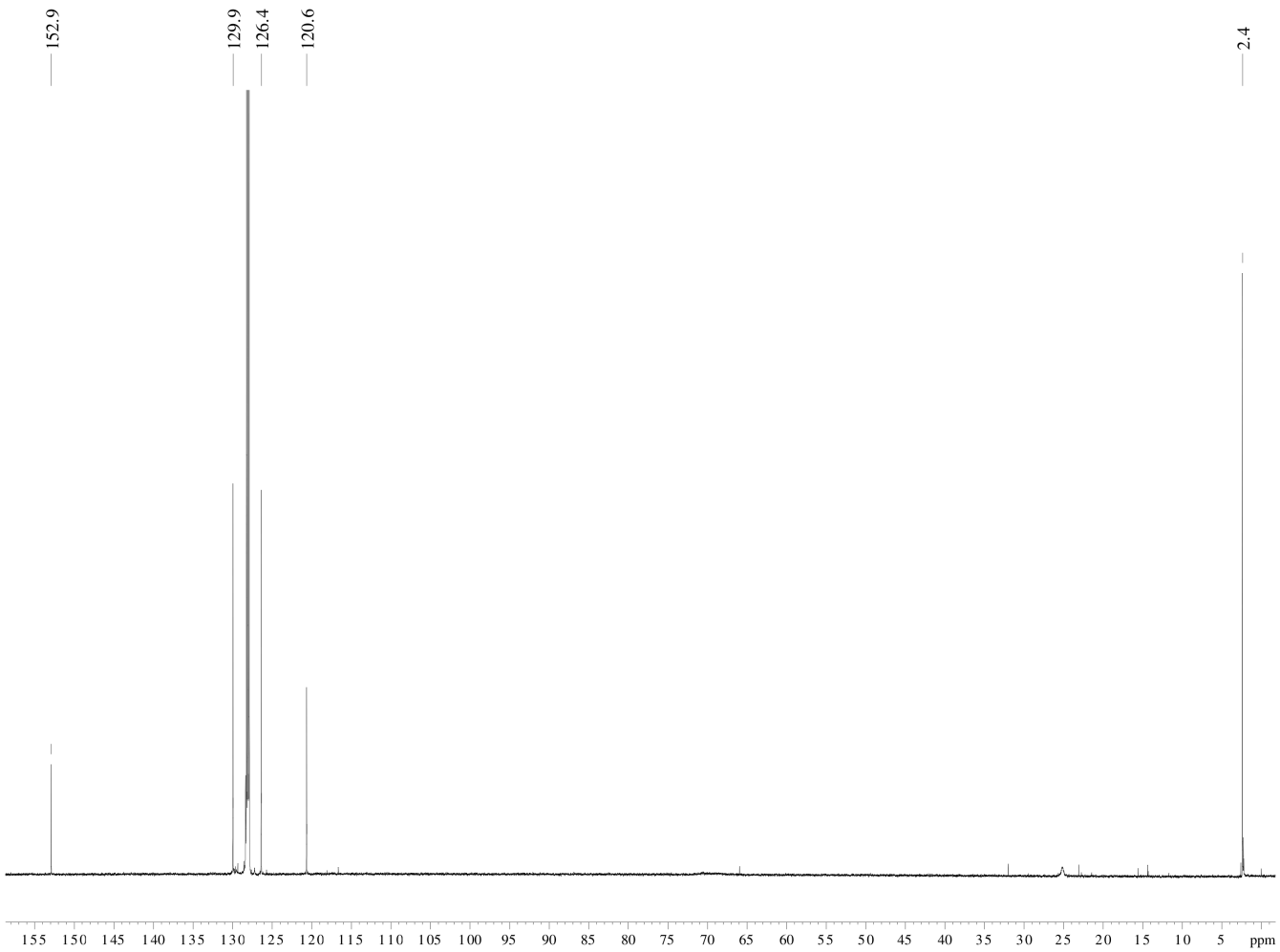

Figure 22.3. $^{13}C\{^{1}H\}$ NMR spectrum of **1-Lu**.

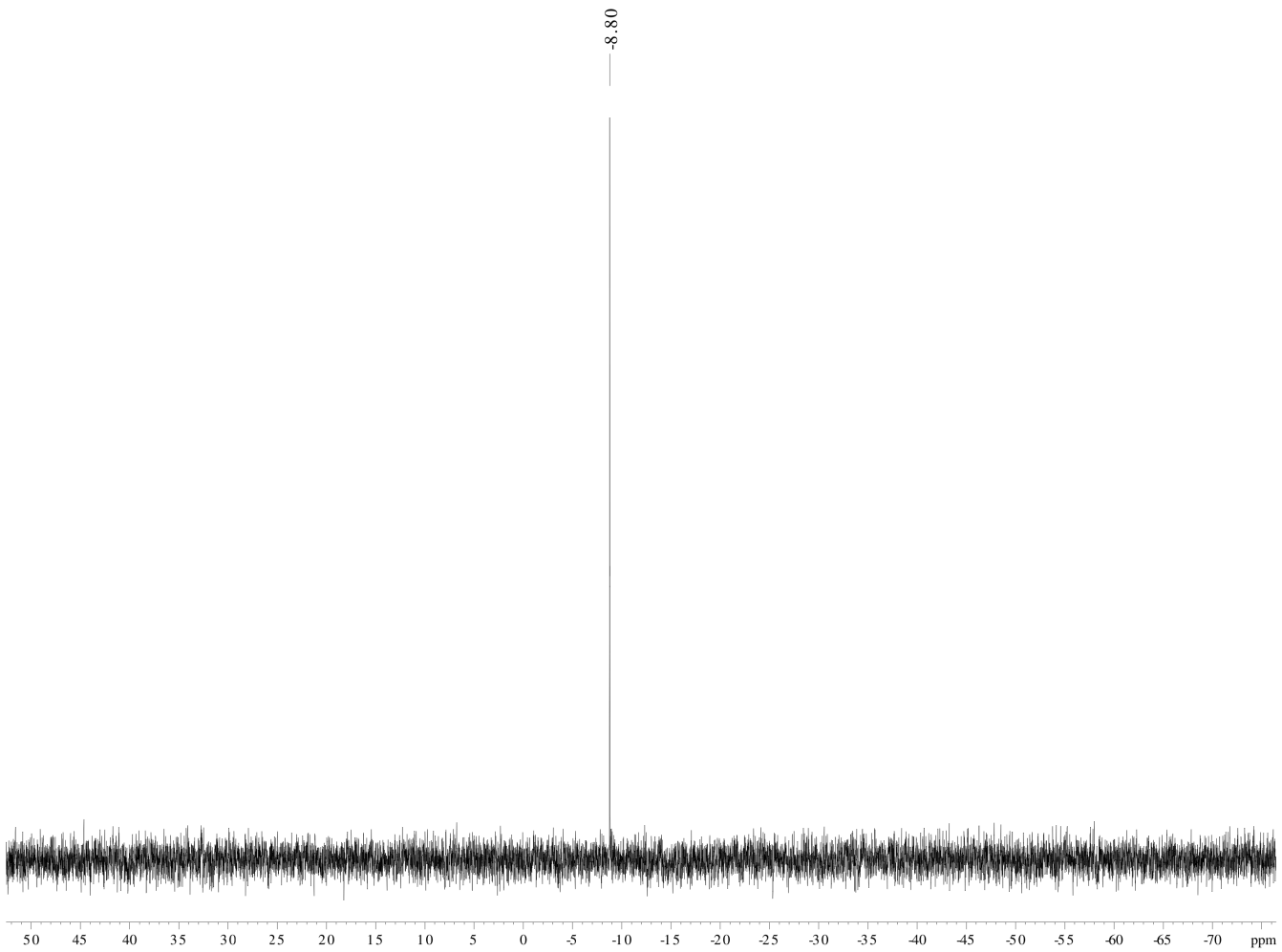

Figure 23.3. $^{29}Si\{^{1}H\}$ INEPT NMR spectrum of **1-Lu**.

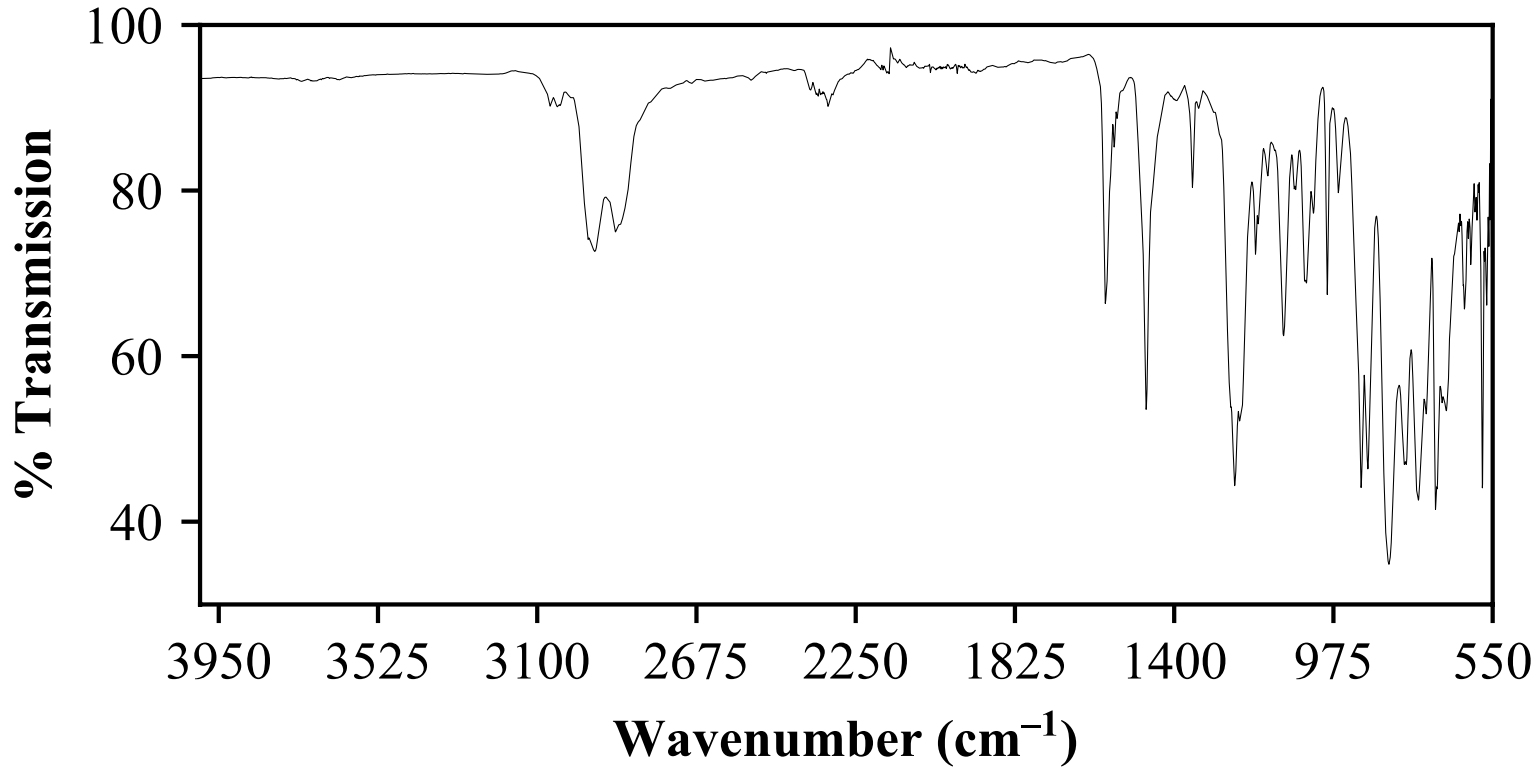

Figure 24.3. IR spectrum of **1-Lu**.

Table 13.3. Crystal data and structure refinement for **2-Y**.

Empirical formula	$C_{31}\ H_{68}\ N_3\ O\ Si_3\ Y$	
Formula weight	672.06	
Temperature	88(2) K	
Wavelength	0.71073 Å	
Crystal system	Monoclinic	
Space group	$P2_1/n$	
Unit cell dimensions	a = 10.2390(5) Å	α= 90°.
	b = 19.9308(9) Å	β= 95.1374(6)°.
	c = 18.9564(9) Å	γ = 90°.
Volume	3852.9(3) $Å^3$	
Z	4	
Density (calculated)	1.159 Mg/m^3	
Absorption coefficient	1.632 mm^{-1}	
F(000)	1456	
Crystal color	colorless	
Crystal size	0.345 x 0.272 x 0.134 mm^3	
Theta range for data collection	2.044 to 27.102°	
Index ranges	$-13 \le h \le 13$, $-25 \le k \le 25$, $-24 \le l \le 24$	
Reflections collected	44009	
Independent reflections	8498 [R(int) = 0.0356]	
Completeness to theta = 25.500°	99.9 %	
Absorption correction	Semi-empirical from equivalents	
Max. and min. transmission	0.7458 and 0.6513	
Refinement method	Full-matrix least-squares on F^2	
Data / restraints / parameters	8498 / 0 / 413	
Goodness-of-fit on F^2	1.049	
Final R indices [I>2sigma(I) = 7072 data]	R1 = 0.0374, wR2 = 0.0814	
R indices (all data, 0.78 Å)	R1 = 0.0506, wR2 = 0.0863	
Largest diff. peak and hole	0.771 and -0.546 $e.Å^{-3}$	

X-ray Data Collection, Structure Solution and Refinement for **2-Y**.

A colorless crystal of approximate dimensions 0.134 x 0.272 x 0.345 mm was mounted on a glass fiber and transferred to a Bruker SMART APEX II diffractometer. The APEX2[53] program package was used to determine the unit-cell parameters and for data collection (20 sec/frame scan time for a sphere of diffraction data). The raw frame data was processed using SAINT[54] and SADABS[55] to yield the reflection data file. Subsequent calculations were carried out using the SHELXTL[56] program. The diffraction symmetry was 2/*m* and the systematic absences were consistent with the monoclinic space group $P2_1/n$ that was later determined to be correct.

The structure was solved by dual space methods and refined on F^2 by full-matrix least-squares techniques. The analytical scattering factors[57] for neutral atoms were used throughout the analysis. Hydrogen atoms were included using a riding model. Several atoms were disordered and included using multiple components with partial site-occupancy-factors.

At convergence, wR2 = 0.0863 and Goof = 1.049 for 413 variables refined against 8498 data (0.78Å), R1 = 0.0374 for those 7072 data with $I > 2.0\sigma(I)$.

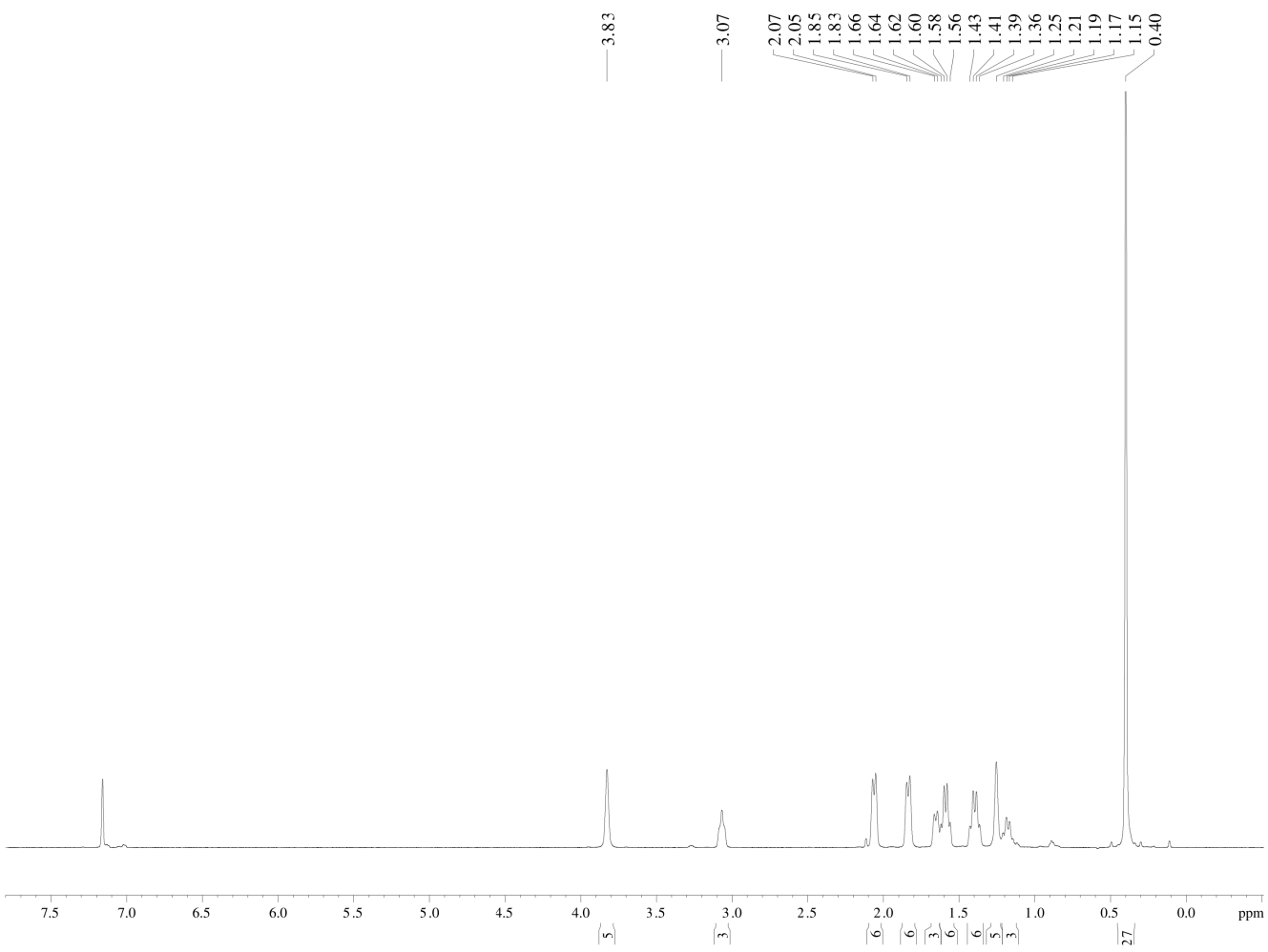

Figure 25.3. ^{1}H NMR spectrum of **2-Y**.

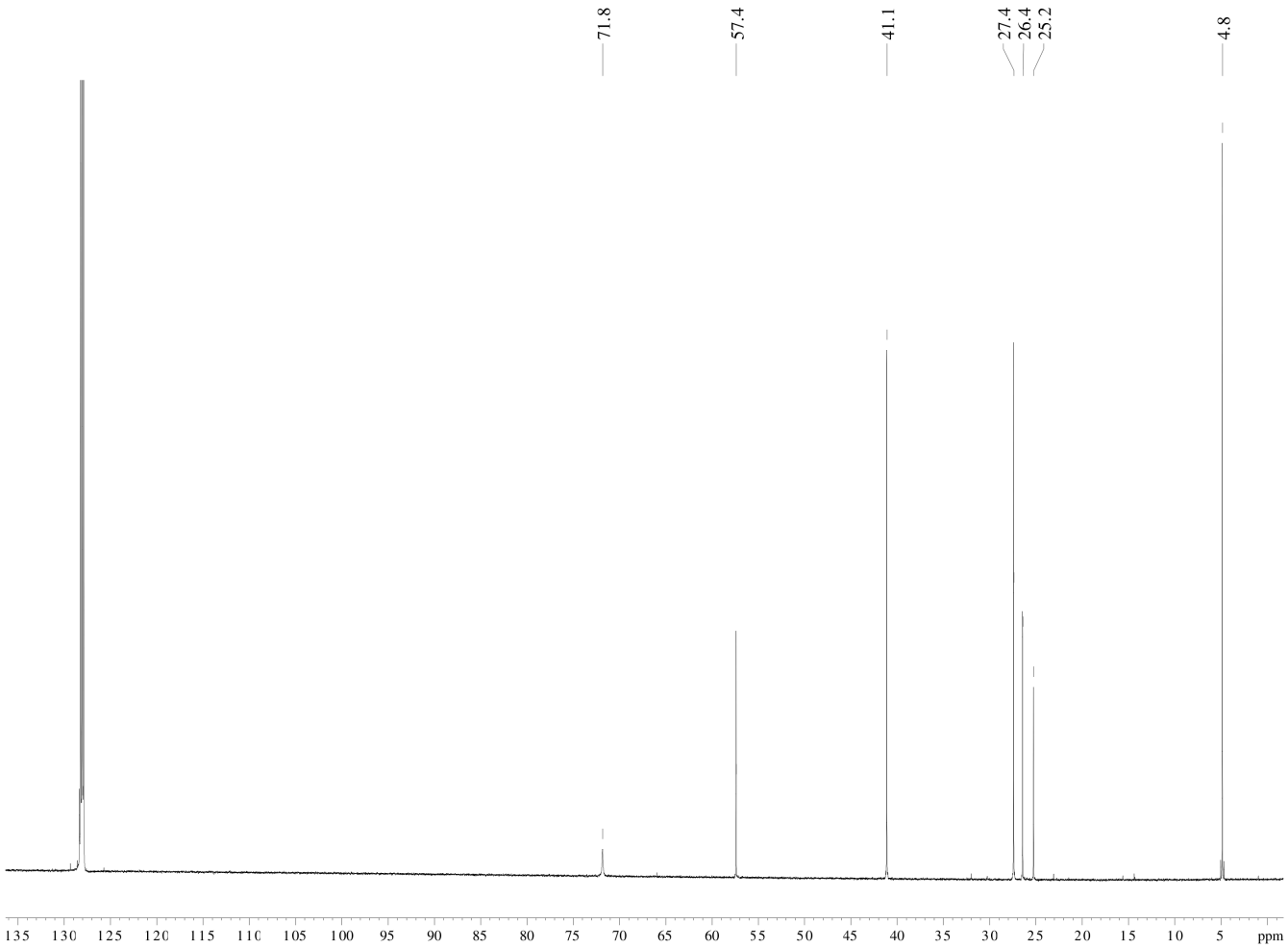

Figure 26.3. $^{13}C\{^{1}H\}$ NMR spectrum of **2-Y**.

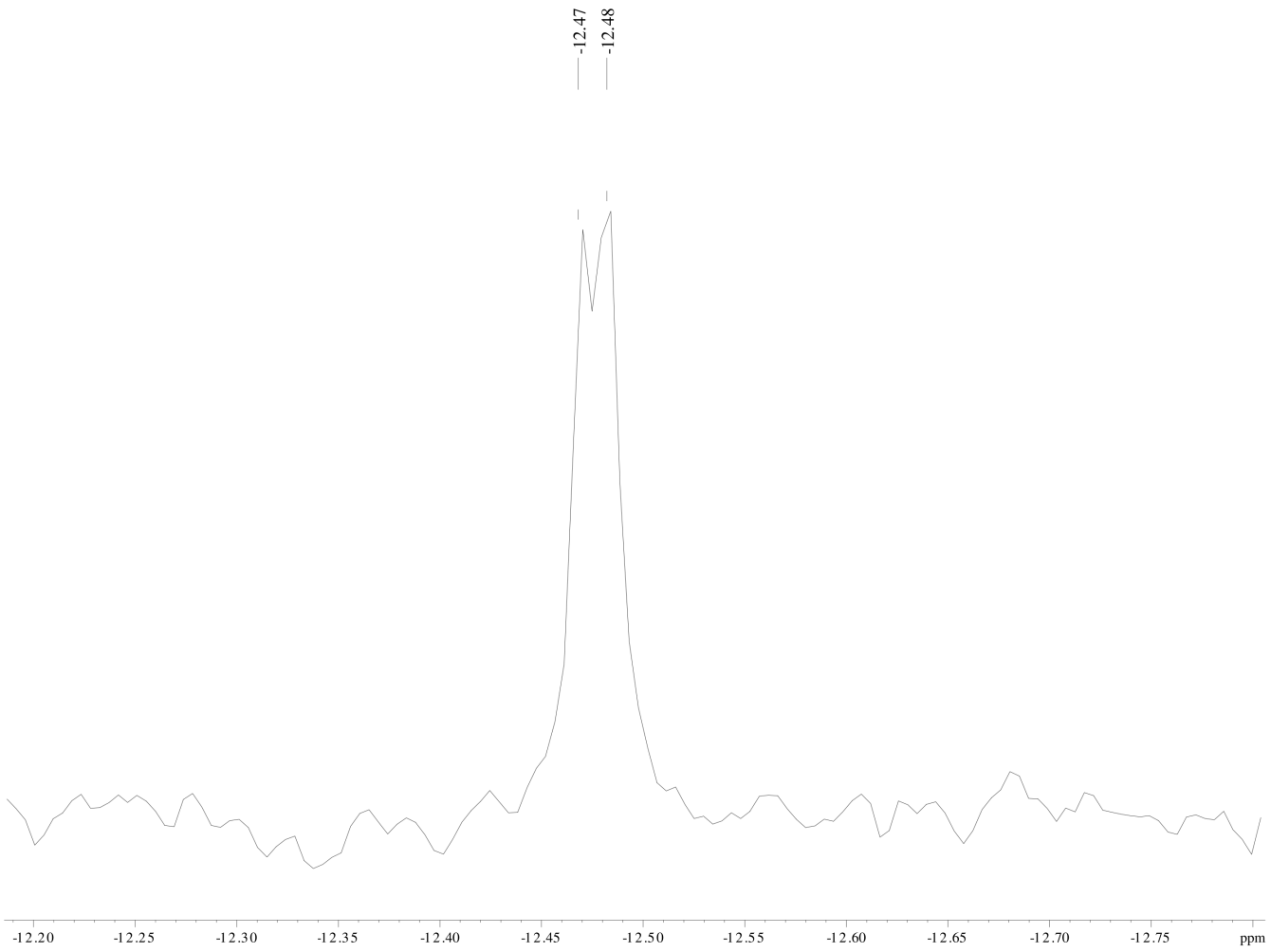

Figure 27.3. $^{29}Si\{^{1}H\}$ INEPT NMR spectrum of **2-Y**.

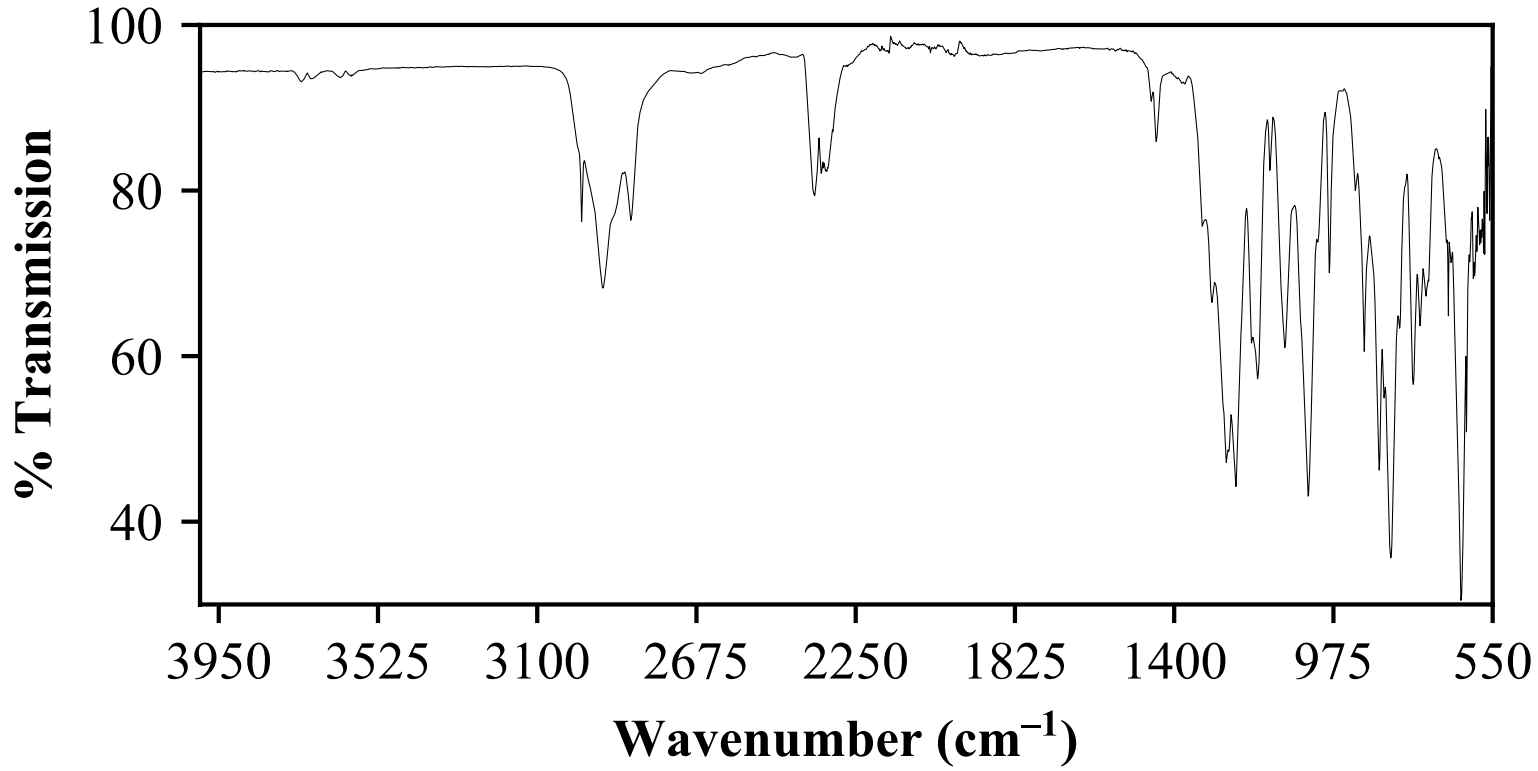

Figure 28.3. IR spectrum of **2-Y**.

Table 14.3. Crystal data and structure refinement for **2-Ho**.

Empirical formula	C_{31} H_{68} Ho N_3 O Si_3	
Formula weight	748.08	
Temperature	133(2) K	
Wavelength	0.71073 Å	
Crystal system	Monoclinic	
Space group	$P2_1/n$	
Unit cell dimensions	a = 10.2448(16) Å	α= 90°.
	b = 19.940(3) Å	β= 95.1025(19)°.
	c = 18.926(3) Å	γ = 90°.
Volume	3851.0(10) $Å^3$	
Z	4	
Density (calculated)	1.290 Mg/m^3	
Absorption coefficient	2.173 mm^{-1}	
F(000)	1568	
Crystal color	yellow	
Crystal size	0.425 x 0.225 x 0.164 mm^3	
Theta range for data collection	1.487 to 27.102°	
Index ranges	$-13 \le h \le 13$, $-25 \le k \le 25$, $-24 \le l \le 24$	
Reflections collected	38321	
Independent reflections	8501 [R(int) = 0.0552]	
Completeness to theta = 25.500°	99.9 %	
Absorption correction	Semi-empirical from equivalents	
Max. and min. transmission	0.7457 and 0.6016	
Refinement method	Full-matrix least-squares on F^2	
Data / restraints / parameters	8501 / 0 / 414	
Goodness-of-fit on F^2	1.046	
Final R indices [I>2sigma(I) = 6752 data]	R1 = 0.0384, wR2 = 0.0743	
R indices (all data, 0.78 Å)	R1 = 0.0557, wR2 = 0.0803	
Largest diff. peak and hole	1.640 and -1.056 $e.Å^{-3}$	

X-ray Data Collection, Structure Solution and Refinement for **2-Ho**.

A yellow crystal of approximate dimensions 0.164 x 0.225 x 0.425 mm was mounted in a cryoloop and transferred to a Bruker SMART APEX II diffractometer. The APEX2[53] program package was used to determine the unit-cell parameters and for data collection (10 sec/frame scan time for a sphere of diffraction data). The raw frame data was processed using SAINT[54] and SADABS[55] to yield the reflection data file. Subsequent calculations were carried out using the SHELXTL[56] program. The diffraction symmetry was 2/*m* and the systematic absences were consistent with the monoclinic space group $P2_1/n$ that was later determined to be correct.

The structure was solved by dual space methods and refined on F^2 by full-matrix least-squares techniques. The analytical scattering factors[57] for neutral atoms were used throughout the analysis. Hydrogen atoms were included using a riding model. Several atoms were disordered and included using multiple components with partial site-occupancy-factors.

At convergence, wR2 = 0.0803 and Goof = 1.046 for 414 variables refined against 8501 data (0.78Å), R1 = 0.0384 for those 6752 data with $I > 2.0\sigma(I)$.

Definitions:

$wR2 = [\Sigma[w(F_o^2-F_c^2)^2] / \Sigma[w(F_o^2)^2]]^{1/2}$

$R1 = \Sigma||F_o|-|F_c|| / \Sigma|F_o|$

$Goof = S = [\Sigma[w(F_o^2-F_c^2)^2] / (n-p)]^{1/2}$ where n is the number of reflections and p is the total number of parameters refined.

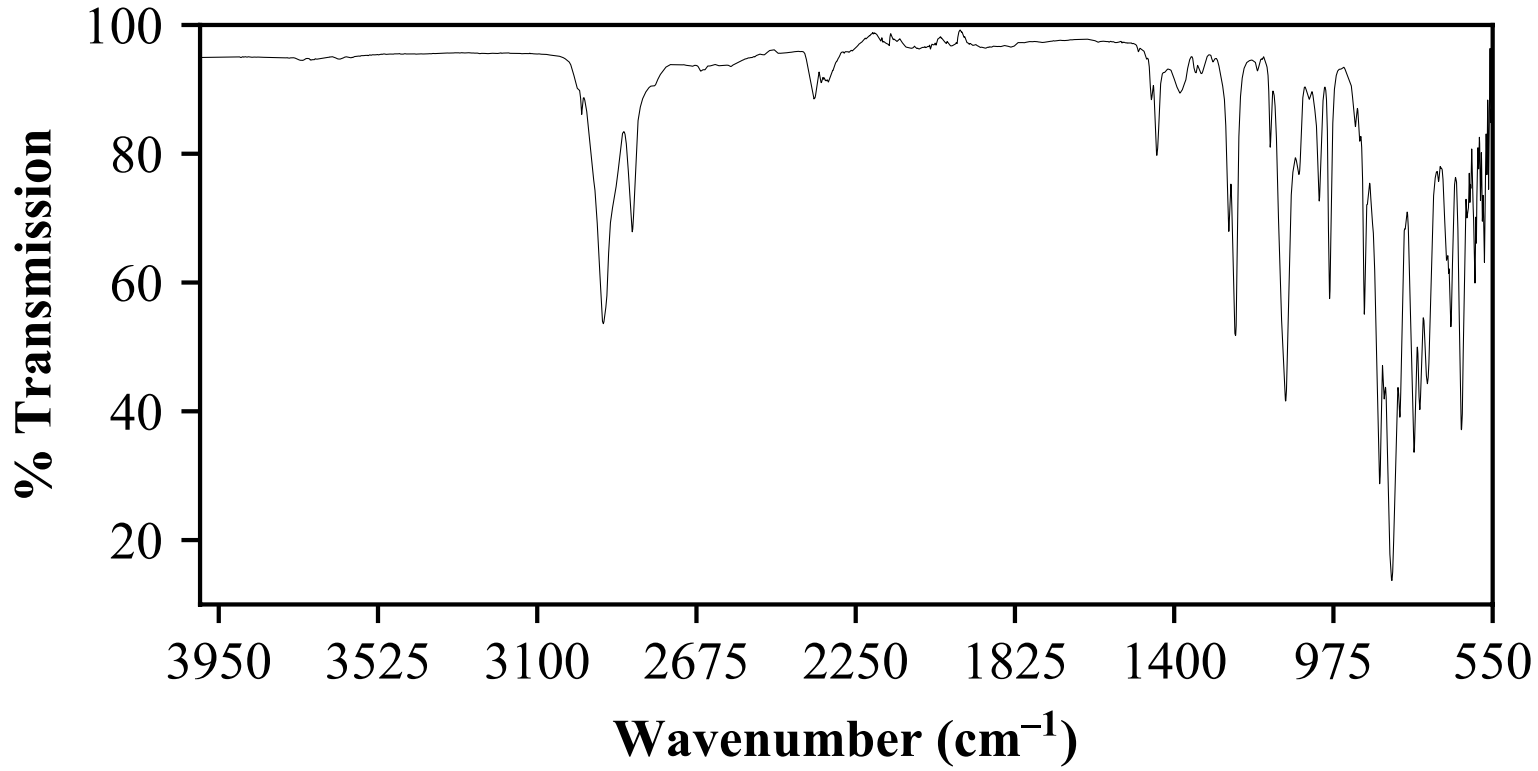

Figure 29.3. IR spectrum of **2-Ho**.

REFERENCES

(1) Lappert, M. F.; Protchenko, A. V.; Power, P. P.; Seeber, A. *Metal Amide Chemistry*; John Wiley & Sons, Ltd: Chippenham, 2008.
(2) Anwander, R. Lanthanide Amides. In *Organolanthoid Chemistry: Synthesis, Structure, Catalysis*; Springer Berlin Heidelberg: Berlin, Heidelberg, 1996; pp 33–112.
(3) Goodwin, C. A. P.; Mills, D. P. *Organomet. Chem.* **2017**, *41*, 123–156.
(4) Schneider, D.; Spallek, T.; Maichle-Mössmer, C.; Törnroos, K. W.; Anwander, R. *Chem. Commun.* **2014**, *50*, 14763–14766.
(5) Evans, W. J.; Anwander, R.; Ziller, J. W.; Khan, S. I. *Inorg. Chem.* **1995**, *34*, 5927–5930.
(6) Spallek, T.; Heß, O.; Meermann-Zimmermann, M.; Meermann, C.; Klimpel, M. G.; Estler, F.; Schneider, D.; Scherer, W.; Tafipolsky, M.; Törnroos, K. W. *Dalton Trans.* **2016**, *45*, 13750–13765.
(7) Aspinall, H. C.; Tillotson, M. R. *Polyhedron* **1994**, *13*, 3229–3234.
(8) Evans, W. J.; Anwander, R.; Doedens, R. J.; Ziller, J. W. *Angew. Chem. Int. Ed.* **1994**, *33* (15/16), 1641–1644.
(9) Alyea, E. C.; Bradley, D. C.; Copperthwaite, R. G. *J. Chem. Soc., Dalton Trans.* **1973**, 1021.
(10) Bradley, D. C.; Ghotra, J. S.; Hart, F. A. *J. Chem. Soc., Chem. Comm.* **1972**, 349–350.
(11) Bradley, D. C.; Ghotra, J. S.; Hart, F. A. *J. Chem. Soc., Dalton Trans.* **1972**, 1021–1023.
(12) Anwander, R.; Runte, O.; Eppinger, J.; Gerstberger, G.; Herdtweck, E.; Spiegler, M. *J. Chem. Soc., Dalton Trans.* **1998**, 847–858.
(13) Bienfait, A. M.; Schädle, C.; Maichle-Mössmer, C.; Törnroos, K. W.; Anwander, R. *Dalton Trans.* **2014**, *43*, 17324–17332.
(14) Meermann, C.; Gerstberger, G.; Spiegler, M.; Törnroos, K. W.; Anwander, R. *Eur. J. Inorg. Chem.* **2008**, No. 12, 2014–2023.
(15) Schumann, H.; Winterfeld, J.; Rosenthal, E. C. E.; Hemling, H.; Esser, L. *Z. Anorg. Allg. Chem.* **1995**, *621*, 122–130.
(16) Fang, M.; Bates, J. E.; Lorenz, S. E.; Lee, D. S.; Rego, D. B.; Ziller, J. W.; Furche, F.; Evans, W. J. *Inorg. Chem.* **2011**, *50*, 1459–1469.
(17) Evans, W. J.; Lee, D. S.; Rego, D. B.; Perotti, J. M.; Kozimor, S. A.; Moore, E. K.; Ziller, J. W. *J. Am. Chem. Soc.* **2004**, *126*, 14574–14582.
(18) Fang, M.; Lee, D. S.; Ziller, J. W.; Doedens, R. J.; Bates, J. E.; Furche, F.; Evans, W. J. *J. Am. Chem. Soc.* **2011**, *133*, 3784–3787.
(19) Gaul, D. A.; Just, O.; Rees Jr., W. S. *Inorg. Chem.* **2000**, *19*, 5648–5654.
(20) Ryan, A. J.; Darago, L. E.; Balasubramini, S. G.; Chen, G. P.; Ziller, J. W.; Furche, F.; Long, J. R.; Evans, W. J. *Chem. Eur. J.* **2018**, *24*, 7702–7709.
(21) Guzei, I. A.; Wendt, M. *Dalton Trans.* **2006**, 3991–3999.
(22) Moehring, S. A.; Beltrán-Leiva, M. J.; Páez-Hernández, D.; Arratia-Pérez, R.; Ziller, J. W.; Evans, W. J. *Chem. Eur. J.* **2018**, *24*, 18059–18067.
(23) Goodwin, C. A. P.; Joslin, K. C.; Lockyer, S. J.; Formanuik, A.; Morris, G. A.; Ortu, F.; Vitorica-Yrezabal, I. J.; Mills, D. P. *Organometallics* **2015**, *34*, 2314–2325.
(24) Kotyk, C. M.; Macdonald, M. R.; Ziller, J. W.; Evans, W. J. *Organometallics* **2015**, *34*, 2287–2295.
(25) Palumbo, C. T.; Darago, L. E.; Dumas, M. T.; Ziller, J. W.; Long, J. R.; Evans, W. J. *Organometallics* **2018**, *37*, 3322–3331.

(26) Desmangles, N.; Jenkins, H.; Ruppa, K. B.; Gambarotta, S. *Inorganica Chim. Acta* **1996**, *250*, 1–4.
(27) Rosiak, D.; Okuniewski, A.; Chojnacki, J. *Polyhedron* **2018**, *146*, 35–41.
(28) Scarel, G.; Wiemer, C.; Fanciulli, M.; Fedushkin, I. L.; Fukin, G. K.; Domrachev, G. A.; Lebedinskii, Y.; Zenkevich, A.; Pavia, G. *Z. Anorg. Allg. Chem.* **2007**, *633*, 2097–2103.
(29) Rees Jr., W. S.; Just, O.; Van Derveer, D. S. *J. Mater. Chem.* **1999**, *9*, 249–252.
(30) Hitchcock, P. B.; Hulkes, A. G.; Lappert, M. F.; Li, Z. *Dalton Trans.* **2004**, No. 129–136.
(31) Herrmann, W. A.; Anwander, R.; Munck, F. C.; Scherer, W.; Dufaud, V.; Huber, N. W.; Artus, G. R. J. *Z. Naturforsch. B* **1994**, *49b*, 1789–1797.
(32) Sheng, E.; Yang, G.; Dong, B. *J. Anhui Norm. Univ. Natural Sci.* **2002**, No. 3, 254–256.
(33) Westerhausen, M.; Hartmann, M.; Pfitzner, A.; Schwarz, W. *Z. Anorg. Allg. Chem.* **1995**, *621*, 837–850.
(34) Shannon, R. D. *Acta Crystallogr. A* **1976**, *32*, 751–767.
(35) MacDonald, M. R.; Ziller, J. W.; Evans, W. J. *J. Am. Chem. Soc.* **2011**, *133*, 15914–15917.
(36) MacDonald, M. R.; Bates, J. E.; Fieser, M. E.; Ziller, J. W.; Furche, F.; Evans, W. J. *J. Am. Chem. Soc.* **2012**, *134*, 8420–8423.
(37) MacDonald, M. R.; Bates, J. E.; Ziller, J. W.; Furche, F.; Evans, W. J. *J. Am. Chem. Soc.* **2013**, *135*, 9857–9868.
(38) Angadol, M. A.; Woen, D. H.; Windorff, C. J.; Ziller, J. W.; Evans, W. J. *Organometallics* **2019**, *38* (5), 1151–1158.
(39) Jenkins, T. F.; Woen, D. H.; Mohanam, L. N.; Ziller, J. W.; Furche, F.; Evans, W. J. *Organometallics* **2018**, *37*, 3863–3873.
(40) Woen, D. H.; Chen, G. P.; Ziller, J. W.; Boyle, T. J.; Furche, F.; Evans, W. J. *Angew. Chem. Int. Ed.* **2017**, *56* (8), 2050–2053.
(41) Fieser, M. E.; Palumbo, C. T.; La Pierre, H. S.; Halter, D. P.; Voora, V. K.; Ziller, J. W.; Furche, F.; Meyer, K.; Evans, W. J. *Chem. Sci.* **2017**, *8*, 7424–7433.
(42) Hermann, W. A.; Anwander, R.; Munch, F. C.; Scherer, W.; Dufaud, V.; Huber, N. W.; Artus, G. R. J. *Z. Naturforsch.* **1994**, *49b* (1789–1797), 1789–1797.
(43) Boyde, N. C.; Chmely, S. C.; Hanusa, T. P.; Rheingold, A. L.; Brennessel, W. W. *Inorg. Chem.* **2014**, *53*, 9703–9714.
(44) Brady, E. D.; Clark, D. L.; Gordon, J. C.; Hay, P. J.; Keogh, D. W.; Poli, R.; Scott, B. L.; Watkin, J. G. *Inorg. Chem.* **2003**, *42*, 6682–6690.
(45) Niemeyer, M. *Z. Anorg. Allg. Chem.* **2002**, *628*, 647–657.
(46) Sugiura, M.; Kobayashi, S. *Scandium Trifluoromethanesulfonate*; 2002.
(47) Taylor, M. D. *Chem. Rev.* **1962**, *62* (6), 503–511.
(48) Schädle, C.; Meermann, C.; Törnroos, K. W.; Anwander, R. *Eur. J. Inorg. Chem.* **2010**, 2841–2852.
(49) Goodwin, C. A. P.; Chilton, N. F.; Vettese, G. F.; Pineda, E. M.; Crowe, I. F.; Ziller, J. W.; Winpenny, R. E. P.; Evans, W. J.; Mills, D. P. *Inorg. Chem.* **2016**, *55*, 10057–10067.
(50) Hitchcock, P. B.; Lappert, M. F.; Maron, L.; Protchenko, A. V. *Angew. Chem. Int. Ed.* **2008**, *47*, 1488–1491.
(51) Chilton, N. F.; Goodwin, C. A. P.; Mills, D. P.; Winpenny, R. E. P. *Chem. Commun.* **2015**, *51*, 101–103.
(52) Gabbaï, F. P.; Chirik, P. J.; Fogg, D. E.; Meyer, K.; Mindiola, D. J.; Schafer, L. L.; You, S. L. *Organometallics* **2016**, *35* (19), 3255–3256.

(53) APEX2 Version 2014.11-0, Bruker AXS, Inc.; Madison, WI 2014.
(54) SAINT Version 8.34a, Bruker AXS, Inc.; Madison, WI 2013.
(55) Sheldrick, G. M. SADABS, Version 2014/5, Bruker AXS, Inc.; Madison, WI 2014.
(56) Sheldrick, G. M. SHELXTL, Version 2014/7, Bruker AXS, Inc.; Madison, WI 2014.
(57) *International Tables for Crystallography 1992, Vol. C*; Kluwer Adademic Publishers: Dordrecht, 1992.

Chapter 4

Evaluating Electron Transfer Reactivity of Complexes of Actinides in +2 and +3 Oxidation States using EPR Spectroscopy

INTRODUCTION

The +2 oxidation state is available in crystallographically-characterizable molecular species for many more rare-earth and actinide metals than was previously expected. Specifically, the first crystallographically-characterizable examples of Y(II), La(II), Ce(II), Pr(II), Gd(II), Tb(II), Ho(II), Er(II), Lu(II), Th(II), U(II), Np(II), and Pu(II) have been isolated from reductions of tris(silylcyclopentadienyl) complexes as shown in eq 1.4.[1–10] Additionally, examples of these new ions in other ligand environments have also been reported.[11–19]

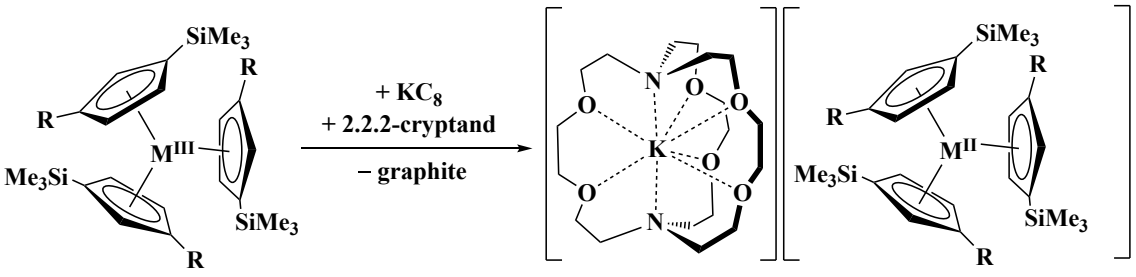

(1.4)

R = H; M = Y, La, Ce, Pr, Gd, Tb, Ho, Er, Lu, U
R = $SiMe_3$; M = La, Ce, Pr, Th, U, Np, Pu

When a new oxidation state is identified, one of the characteristics to be defined is the redox potential by which it is formed. Electrochemical analysis of the oxidation states of the rare-earth metals and the actinides has historically been challenging due to the high reactivity and oxophilicity of these species.[20–22] Frequently, chemical analysis of reductive capacity is made by examining reactions of polycyclic aromatic hydrocarbons of known reduction potential.[23–25] Since the new +2 ions can all be generated by reduction using alkali metals, it appears the reduction potentials are less negative than the −2.86 V *vs.* Fc^+/Fc, the potential of Na.[26] Electrochemical

studies of the Ln(III) complexes $Ln^{III}[(^{Ad,Me}ArO)_3mes]$ [$(^{Ad,Me}ArO)_3mes$ = 6,6′,6″-((2,4,6-trimethylbenzene-1,3,5-triyl)tris(methylene))tris(2-(adamantan-1-yl)-4-methylphenolate)], which are known to form Ln(II) compounds,[16,17] have been shown to have reduction potentials of −2.86 to −3.08 V *vs.* Fc^+/Fc in THF by cyclic voltammetry[27] and the reduction potential of $La^{III}Cp''_3$ in THF is reported to be −2.8 V vs. Fc^+/Fc;[28] furthermore, Inman and Cloke have reported Th(IV)/Th(III) reduction potentials for four compounds to be between −3.32 V and −2.96 V (*vs.* Fc^+/Fc in 0.05 M [$^n Bu_4N$][BPh_4] in THF).[29]

Due to the difficulties associated with electrochemical characterization of these species (see examples of fluoride abstraction,[20] activation of solvent,[30] and thermal instability of Ln(II) compounds generated by chemical means[31]), a series of chemical reduction reactions was sought that could be used to characterize the relative reduction potentials of the new compounds. Specifically, the reactions would use the new +2 oxidation state complexes as reductants in place of alkali metals and thereby determine which of these new compounds were most reducing. Such a study would require that clean electron transfer chemistry occurs with a minimum of ligand exchange. This study would also require that there be definitive means to identify the species involved. Since Th(III), La(II), and Y(II) have characteristic EPR signals,[4,32,33] this seemed possible with these metals.

This Chapter reports the viability of the method and provides information on the reductive reactivity of Th(II) and U(II). These results also show the power of EPR spectroscopy in identifying mixtures of low valent *f* element complexes. In the process of collecting these data, information on ligand exchange reactivity of these species was obtained. Ligand exchange as well as reductive capacity are both critical to understanding the reactivity of the new oxidation states.

RESULTS AND DISCUSSION

Methodogy. For all the electron transfer reactions reported here, a solution of a "reductant" species, either $An^{III}Cp''_3$ (An = Th, U) or $[K(crypt)][M^{II}Cp^x_3]$ [M = Y, La, Th, U; crypt = 2.2.2-cryptand; $Cp^x = C_5H_4SiMe_3$ (Cp′) or $C_5H_3(SiMe_3)_2$ (Cp″)] in THF was combined at −30 °C with a solution of the "substrate" species (*e.g.* $M^{III}Cp^x_3$) at the same concentration. The solutions were then loaded into an EPR tube and frozen in liquid nitrogen. EPR experiments were carried out at 77 K and room temperature. The solutions were made at a concentration of ~10 mM . The complexes in this study were chosen for characteristic EPR signals and similarity of ligand set. EPR signals for ^{89}Y(II) (S = 1/2, I = 1/2, 100% abundant) were observed as two-line patterns, for ^{139}La(II) (S = 1/2, I = 7/2, 99.9% abundant) as eight-line patterns, and for ^{232}Th(III) (S = 1/2, I = 0, 100% abundant) as single lines. Only when an EPR-active target compound could be detected was a reaction counted as successful. Loss of reactant signal was not sufficient. Throughout this Chapter, the equations are written to show a transformation that occurred in the forward direction since the equilibrium constants for these reactions were not determined.

All spectra were simulated with EasySpin and *g* and *A* values from these simulations are presented throughout the work.[32] This was accomplished by defining spin systems containing information about *g* and *A* values, the identity of the nucleus (or nuclei) where the electron spin is located, and empirical values for the weight (*i.e.*, the strength) and line width of the signal. These parameters were varied using the "esfit" function to find a best-fit simulated spectrum. In the cases where multiple species were present, each signal was simulated individually, then all the signals were simulated together. An example is given in Figure 10.4 for the spectrum in Figure 3.4.

An(III) vs Ln(III): An = Th, U; Ln = Y, La. Initial studies involved the reaction of $Th^{III}Cp''_3$ and $U^{III}Cp''_3$ with $La^{III}Cp''_3$ and $Y^{III}Cp'_3$ to determine if these An(III) complexes were strong enough reductants to replace alkali metals in the formation of La(II) and Y(II). Since this was unlikely at least for U(III), this served as a blank reaction. The yttrium complex $Y^{III}Cp'_3$, was used in these reactions and $[Y^{II}Cp'_3]^{1-}$ was used in the reductions described later because $[Y^{II}Cp''_3]^{1-}$ has not been isolated and does not have enough thermal stability to be a viable reagent or product.[34,35] In this series of reactions, shown in 2.4–5.4, neither of the two An(III) complexes were found to reduce the two Ln(III) substrates. Hence, the thorium reactions showed only Th(III) by EPR spectroscopy and no La(II) or Y(II). Signals for La(II) and Y(II) were also not observed in the uranium reactions.

$$\mathbf{Th^{III}Cp''_3 + La^{III}Cp''_3 \xrightarrow[Ar]{THF,\ -30\ ^\circ C} \not\rightarrow [Th^{IV}Cp''_3]^{1+} + [La^{II}Cp''_3]^{1-}} \qquad \mathbf{(2.4)}$$

$$\mathbf{Th^{III}Cp''_3 + Y^{III}Cp'_3 \xrightarrow[Ar]{THF,\ -30\ ^\circ C} \not\rightarrow [Th^{IV}Cp''_3]^{1+} + [Y^{II}Cp'_3]^{1-}} \qquad \mathbf{(3.4)}$$

$$\mathbf{U^{III}Cp''_3 + La^{III}Cp''_3 \xrightarrow[Ar]{THF,\ -30\ ^\circ C} \not\rightarrow [U^{IV}Cp''_3]^{1+} + [La^{II}Cp''_3]^{1-}} \qquad \mathbf{(4.4)}$$

$$\mathbf{U^{III}Cp''_3 + Y^{III}Cp'_3 \xrightarrow[Ar]{THF,\ -30\ ^\circ C} \not\rightarrow [U^{IV}Cp''_3]^{1+} + [Y^{II}Cp'_3]^{1-}} \qquad \mathbf{(5.4)}$$

The reverse of reaction 2.4 was approximated by treating the Th(IV) complex, $Th^{IV}Cp''_3Br$, with $[K(crypt)][La^{II}Cp''_3]$, reaction 6.4.

$$\mathbf{Th^{IV}Cp''_3Br + [K(crypt)][La^{II}Cp''_3] \xrightarrow[Ar]{THF,\ -30\ ^\circ C} Th^{III}Cp''_3 + La(III)\ products} \qquad \mathbf{(6.4)}$$

This reaction proceeds as written which shows that La(II) is a sufficiently strong reductant to reduce Th(IV) to Th(III). This is consistent with the fact that eq 2.4 does not proceed as written. Interestingly, the reduction potential of Cp''_3La^{III} was measured to be −2.8 V (*vs.* Fc^+/Fc in 0.2 M $[Bu_4N][PF_6]$ in THF)[28] and the Th(IV)/Th(III) couple for both $Th^{III}Cp''_3$ and $Th^{IV}Cp''_3Cl$ was found to be −2.96 V (*vs*. Fc^+/Fc in 0.05 M $[Bu_4N][BPh_4]$ in THF).[29]

An(II) vs. Ln(III). Reactions of $[K(crypt)][U^{II}Cp''_3]$ and $[K(crypt)][Th^{II}Cp''_3]$ with $La^{III}Cp''_3$ and $Y^{III}Cp'_3$, reactions 7.4–10.4, resulted in reduction of the Ln(III) rare earth complexes by the An(II) compounds. EPR signals were observed in reactions 7.4 and 9.4 at g = 1.96 with A values consistent with $[La^{II}Cp''_3]^{1-}$[7] and in reactions 8.4 and 10.4 at g = 1.99 with A values consistent with $[Y^{II}Cp'_3]^{1-}$[36] (36.3 G for reaction 10.4) or a ligand-exchanged $[Y^{II}Cp'_2Cp'']^{1-}$ derivative (35.6 G for reaction 10.4; compare the A value for $[Y^{II}Cp''_2Cp]^{1-}$, 34.6 G, which is not intermediate between "$[Y^{II}Cp''_3]^{1-}$," 36.1 G, and "$[Y^{II}Cp_3]^{1-}$," 42.8 G[34]).

$$\mathbf{[K(crypt)][Th^{II}Cp''_3] + La^{III}Cp''_3 \xrightarrow[Ar]{THF,\ -30\ °C} Th^{III}Cp''_3 + [K(crypt)][La^{II}Cp''_3]} \quad \mathbf{(7.4)}$$

$$\mathbf{[K(crypt)][Th^{II}Cp''_3] + Y^{III}Cp'_3 \xrightarrow[Ar]{THF,\ -30\ °C} Th^{III}Cp''_3 + [K(crypt)][Y^{II}Cp'_3]} \quad \mathbf{(8.4)}$$

$$\mathbf{[K(crypt)][U^{II}Cp''_3] + La^{III}Cp''_3 \xrightarrow[Ar]{THF,\ -30\ °C} U^{III}Cp''_3 + [K(crypt)][La^{II}Cp''_3]} \quad \mathbf{(9.4)}$$

$$\mathbf{[K(crypt)][U^{II}Cp''_3] + Y^{III}Cp'_3 \xrightarrow[Ar]{THF,\ -30\ °C} U^{III}Cp''_3 + [K(crypt)][Y^{II}Cp'_3]} \quad \mathbf{(10.4)}$$

The room-temperature EPR spectrum of the products of reaction 7.4, Figure 1.4, shows both expected EPR-active products, *i.e.,* the EPR signal for $Th^{III}Cp''_3$ (g = 1.91) can be seen simultaneously with a signal for $[La^{II}Cp''_3]^{1-}$ (g = 1.96, A = 133.6 G). A signal for another La(II) species making a minor contribution (g = 1.96, A = 143.5 G) is also observed. The identity of the

minor La(II) product is unknown, but La(II) species with *g* and *A* values similar to those in Figure 1.4 have been observed elsewhere in this study (*vide infra*).

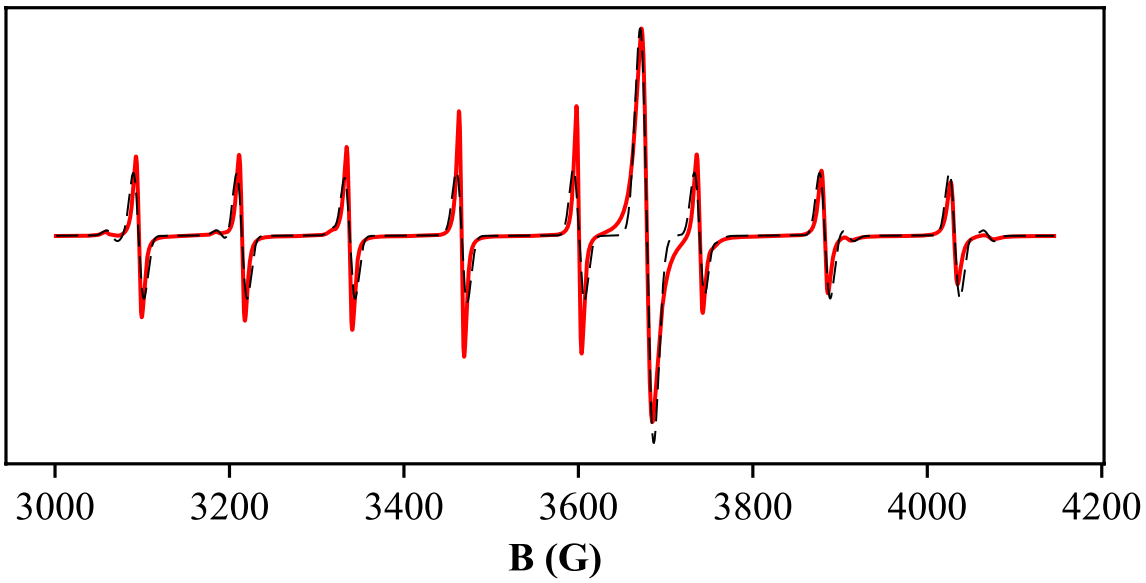

Figure 1.4. Room-temperature X-band EPR spectrum (red) and simulated spectrum (black dashes) of the products of reaction 7.4. Signals are present at $g = 1.96$, $A = 133.6$ G ($[La^{II}Cp''_3]^{1-}$), $g = 1.91$ ($Th^{III}Cp''_3$), and $g = 1.96$, $A = 143.5$ G (an unknown La(II) species).

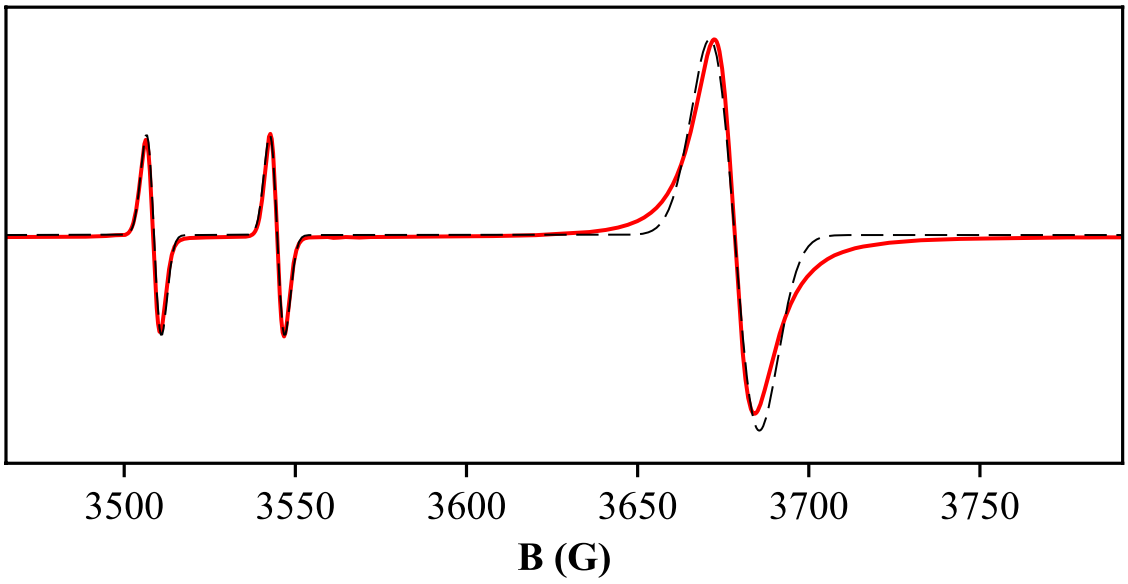

Figure 2.4. Room-temperature X-band EPR spectrum (red) and simulated spectrum (black dashes) of the products of reaction 8.4. Signals are present at $g = 1.91$ ($Th^{III}Cp''_3$) and $g = 1.99$, $A = 35.6$ G ($[Y^{II}Cp'_3]^{1-}$ has $A = 36.6$ G).

Two EPR active products, namely a Y(II) species and $Th^{III}Cp''_3$, are also observable in Figure 2.4 which shows the EPR spectrum of the products of reaction 8.4. The EPR spectra of the products of reactions 9.4 and 10.4 (Figures 5.4 and 6.4, respectively) show only the signals from the rare-earth(II) signals as expected. Attempts to examine the reverse of reactions 9.4 and 10.4. were complicated by the fact that $U^{III}Cp''_3$ is known to interfere with the NMR detection of $[K(crypt)][U^{II}Cp''_3]$.[6] Attempts to examine these reverse reactions by UV-visible spectroscopy were unsuccessful due to the broad overlapping absorptions in the spectra of $U^{II}Cp''_3$ and $[K(crypt)][U^{II}Cp''_3]$.

Ln(II) vs. Th(III). Although Cp''_3Th^{III} similarly interferes with the NMR detection of $[K(crypt)][Th^{II}Cp''_3]$, the latter complex has an especially strong, distinct absorption at 650 nm (23,000 M^{-1} cm^{-1}),[5] UV-visible spectroscopy could be used for detection of the Th(II) species. Cp''_3Th^{III} also absorbs strongly at 650 nm (5000 M^{-1} cm^{-1}), but there are other peaks in the range 470−650 nm of a similar intensity that can be used to identify the Th(III) complex if it is present. The reverse of reactions 7.4 and 8.4 were probed by UV-vis spectroscopy and reactions 11.4 and 12.4 (Figures 7.4 and 8.4, respectively) show that $[K(crypt)][La^{II}Cp''_3]$ and $[K(crypt)][Y^{II}Cp'_3]$ can reduce Cp''_3Th^{III} to $[K(crypt)][Th^{II}Cp''_3]$. These reactions, combined with the results of reactions 7.4 and 8.4 show that in these ligand sets, Th(II), La(II), and Y(II) all have similar reducing abilities.

$$\mathbf{[K(crypt)][La^{II}Cp''_3] + Th^{III}Cp''_3 \xrightarrow[\text{Ar}]{\text{THF, } -30\ ^\circ\text{C}} {}_3La^{III}Cp'' + [K(crypt)][Th^{II}Cp''_3]} \qquad \mathbf{(11.4)}$$

$$\mathbf{[K(crypt)][Y^{II}Cp'_3] + Th^{III}Cp''_3 \xrightarrow[\text{Ar}]{\text{THF, } -30\ ^\circ\text{C}} Y^{III}Cp'_3 + [K(crypt)][Th^{II}Cp''_3]} \qquad \mathbf{(12.4)}$$

La(II) vs. Y(III) and Y(II) vs. La(III). To benchmark the reducing ability of Y(II) versus La(II), reactions of $[K(crypt)][La^{II}Cp''_3]$ with $Y^{III}Cp'_3$ and $[K(crypt)][Y^{II}Cp'_3]$ with $La^{III}Cp''_3$ were carried

out, reactions 13.4–14.4. In both experiments, EPR signals for both La(II) and Y(II) were observed. These results indicate that the reduction potential of $Y^{III}Cp'_3$ is very close to that of $La^{III}Cp''_3$ such that an equilibrium mixture of complexes of La(II), Y(II), La(III), and Y(III) ions is generated. In addition, both reactions display EPR spectra indicative of the presence of multiple La(II) species, since several eight-line patterns are observed with different *g* and *A* values as shown for reaction 13.4 in Figure 3.4.

$$\mathbf{[K(crypt)][Y^{II}Cp'_3] + La^{III}Cp''_3 \xrightarrow[Ar]{THF,\ -30\ ^\circ C} Y^{III}Cp'_3 + [K(crypt)][La^{II}Cp''_3] + \text{other La(II) and Y(II) species}} \quad \mathbf{(13.4)}$$

$$\mathbf{[K(crypt)][La^{II}Cp''_3] + Y^{III}Cp'_3 \xrightarrow[Ar]{THF,\ -30\ ^\circ C} La^{III}Cp''_3 + [K(crypt)][Y^{II}Cp'_3] + \text{other La(II) species}} \quad \mathbf{(14.4)}$$

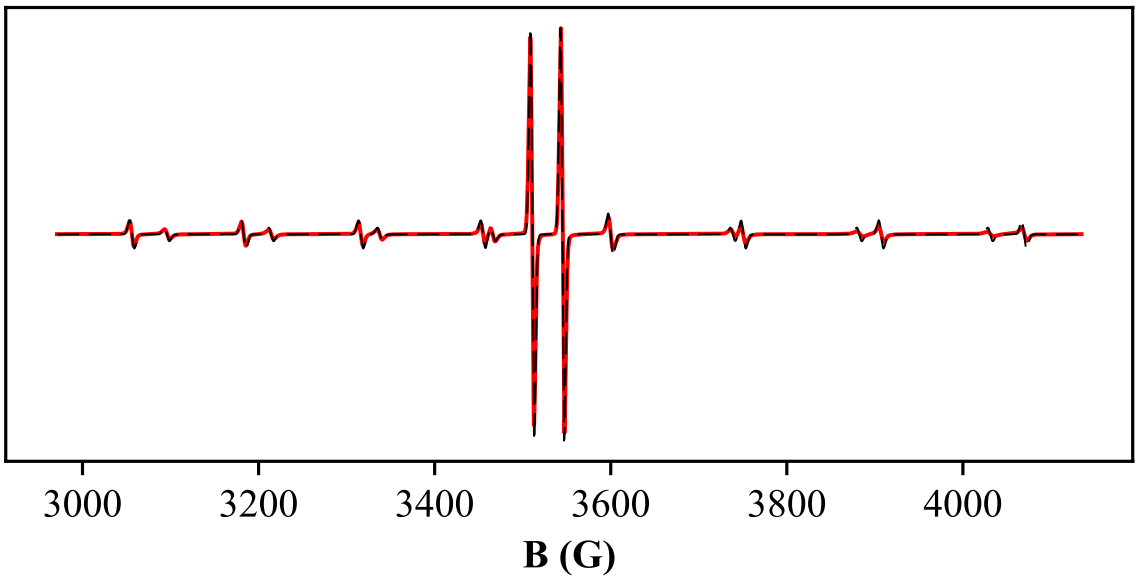

Figure 3.4. Room-temperature X-band EPR spectrum (red) and simulated spectrum (black dashes) of the products of reaction 13.4. Signals are present at $g = 1.97$, $A = 133.6$ G ($[La^{II}Cp''_3]^{1-}$), $g = 1.96$, $A = 144.7$ G (an unknown La(II) species), and $g = 1.99$, $A = 33.8$ G (an unknown Y(II) species).

Multiple Ln^{II} Species. The spectroscopic parameters for the La(II) species in reactions 13.4 and 14.4 are tabulated in Table 1.4. Both reactions have a signal whose A value corresponds to that of $[La^{II}Cp''_3]^{1-}$.[7] However, there are additional species present that do not correspond to any known La(II) compound, but which have g and A values between the values for $[La^{II}Cp''_3]^{1-}$ and $[La^{II}Cp'_3]^{1-}$.[2] The species with $g = 1.96$ and $A = 144.7/144.8$ G is produced in both reactions 13.4 and 14.4. The multiple La(II) signals observed in both reactions 13.4 and 14.4 suggest ligand exchange is occurring forming species such as $[La^{II}Cp''_2Cp']^{1-}$ and $[La^{II}Cp'_2Cp'']^{1-}$. However, the EPR spectrum of the products of reaction 7.4, Figure 1.4, shows there are more possibilities for La^{II} species. Only Cp″ ligands were used in reaction 7.4, yet another set of g and A values ($g = 1.96$, $A = 143.5$ G) not found in reactions 13.4 and 14.4 is present. A similar result was seen by Lappert et al. when $[La^{II}Cp''_3]^{1-}$ was first observed: a signal in addition to that for $[La^{II}Cp''_3]^{1-}$,

with g = 1.970 and A = 145.0 G, similar to a species in reaction 7.4, was also observed in that case and was assigned to a still-uncharacterized species $La^{II}Cp''_2(glyme)_x$.[28] In addition, Lappert found that reductions of $La^{III}Cp''_3$ in benzene gave EPR spectra with multiple signals attributed to La(II) species with g values ranging from 1.975 to greater than 1.994 and A values from 136.1 G to greater than 147.1 G.[37] The origin of these additional signals is not known, but it is possible that the high sensitivity of the EPR experiment detects minor impurities in the starting material that got reduced to form La(II) complexes. It is known that (trimethylsilyl)cyclopentadienyl ligands can lose their trimethylsilyl groups via hydrolysis.[38,39] There is also an additional two-line signal for Y(II) in Figure 3.4, reaction 13.4, with g = 1.99, A = 33.8 G. This is not attributable to either $[Y^{II}Cp'_3]^{1-}$ (g = 1.991, A = 36.6 G)[36] or "$[Y^{II}Cp''_3]^{1-}$" (g = 1.99, A = 36.1 G).[34] This value is instead closer to that for $[Y^{II}Cp''_2Cp]^{1-}$ (g = 1.99, A = 34.6 G), a rare example of a heteroleptic Y(II) compound.[34]

Table 1.4. Values of *g* and *A* (in Gauss) from the room-temperature X-band EPR spectroscopy of La(II) species in reactions 13.4 and 14.4 , $[La^{II}Cp''_3]^{1-}$,[7] and $[La^{II}Cp'_3]^{1-}$,[2] obtained by simulating the experimental data with EasySpin.[32]

	g	*A*		*g*	*A*		*g*	*A*
$[La^{II}Cp''_3]^{1-}$	1.990	133.5	**13.4**	1.97	133.6	**14.4**	1.97	133.6
				1.96	144.7		1.96	144.8
							1.97	149.8
$[La^{II}Cp'_3]^{1-}$	1.994	154						

CONCLUSION

These results show that EPR spectroscopy can be effective in characterizing reduction reactions of highly reducing actinide complexes. The data indicate that $An^{III}Cp''_3$ complexes are not strong enough reductants to reduce $La^{III}Cp''_3$ and $Y^{III}Cp'_3$ to the La(II) and Y(II) compounds, but that Th(II) and U(II) [K(crypt)][$An^{II}Cp''_3$] complexes can reduce both $La^{III}Cp''_3$ and $Y^{III}Cp'_3$ to La(II) and Y(II) products. Since [K(crypt)][$La^{II}Cp''_3$] and [K(crypt)][$Y^{II}Cp'_3$] can also reduce $Th^{III}Cp''_3$ to [K(crypt)][$Th^{II}Cp''_3$], this indicates that Th(II), La(II), and Y(II) have similar reduction potentials with these ligands. Consistent with this, studies of just [K(crypt)][$La^{II}Cp''_3$] and [K(crypt)][$Y^{II}Cp'_3$] show that they are similar reductants because they reduce $Y^{III}Cp'_3$ and $La^{III}Cp''_3$, respectively, to make mixtures of La(II) and Y(II). In these latter reactions, EPR spectroscopy indicates that some ligand exchange occurs as well as electron transfer. This suggests that there are many heteroleptic La(II) and Y(II) complexes to be discovered.

EXPERIMENTAL

All manipulations and syntheses described below were conducted with the rigorous exclusion of air and water using standard glovebox techniques under an argon atmosphere. Solvents were sparged with UHP argon and dried by passage through columns containing Q-5 and molecular sieves prior to use. EPR spectra were collected using X-band frequency (9.3−9.8 GHz) on a Bruker EMX spectrometer equipped with an ER041XG or ER4119HS-W1 microwave bridge, and the magnetic field was calibrated with DPPH (g = 2.0036). UV-visible spectra were acquired in a 0.1 cm pathlength cell fitted with a Teflon stopcock at 298 K on an Agilent Cary 60 UV-Vis spectrometer. All EPR parameters are taken from simulations of the room-temperature spectra using EasySpin.[32] $Th^{IV}Cp''_3Br$,[5] $Th^{III}Cp''_3$,[5] [K(crypt)][$Th^{II}Cp''_3$][5] (crypt = 2.2.2-cryptand), $U^{III}Cp''_3$,[40] [K(crypt)][$U^{II}Cp''_3$],[6] $La^{III}Cp''_3$,[37] [K(crypt)][$La^{II}Cp''_3$] (by adaptation of the preparation for [K(crypt)][$Y^{II}Cp'_3$]),[2] $Y^{III}Cp'_3$,[3] and [K(crypt)][$Y^{II}Cp'_3$][2] [Cp′ = $C_5H_4SiMe_3$, Cp″ = $C_5H_3(SiMe_3)_2$] were synthesized according to literature procedures. In the initial report of [K(crypt)][$La^{II}Cp''_3$], the EPR spectroscopic parameters are reported to be g = 1.990 and A = 133.5 G.[7] In all simulations in this work, reactions where [K(crypt)][$La^{II}Cp''_3$] is present (either as a reactant or product), it is best modeled as having g = 1.96 and A = 133.5 G.

Reaction 2.4. A royal-blue solution of $Th^{III}Cp''_3$ (11 mg, 13 μmol) in THF (1 mL) was combined with a colorless solution of $La^{III}Cp''_3$ (11 mg, 15 μmol) in THF (1 mL) at −30 °C. No color change was observed. The solution was loaded into an EPR tube chilled to −30 °C and set in a 25 mL conical flask filled with hexane and chilled to −30 °C, then immediately passed out of the glove box and frozen in liquid nitrogen. The EPR spectrum only contained signal for $Th^{III}Cp''_3$ (g = 1.91) and no signals for La(II) were observed.

Reaction 3.4. As in Reaction 2.4, $Th^{III}Cp''_3$ (21 mg, 24 μmol) was combined with yellow $Y^{III}Cp'_3$ (12 mg, 25 μmol) and no color change was observed. The EPR spectrum only contained signal for $Th^{III}Cp''_3$ (g = 1.91) and no signals for Y(II) were observed.

Reaction 4.4. As in reaction. 2, forest-green $U^{III}Cp''_3$ (12 mg, 14 μmol) was combined with $La^{III}Cp''_3$ (12 mg, 15 μmol) and no color change was observed. No signals for La(II) were observed in the EPR spectrum.

Reaction 5.4. As in reaction. 2, $U^{III}Cp''_3$ (21 mg, 24 μmol) was combined with $Y^{III}Cp'_3$ (12 mg, 25 μmol) and no color change was observed. No signals for Y(II) were observed in the EPR spectrum.

Reaction 6.4. As in reaction. 2, deep purple [K(crypt)][$La^{II}Cp''_3$] (19 mg, 17 μmol) was combined with beige $Th^{IV}Cp''_3Br$ (10 mg, 11 μmol). The color changed to royal blue. The EPR spectrum (Figure 4.4) contains signal for $Th^{III}Cp''_3$ (g = 1.91) and residual $[La^{II}Cp''_3]^{1-}$ (g = 1.96, A = 133.6 G).

Reaction 7.4. As in reaction. 2, aqua [K(crypt)][$Th^{II}Cp''_3$] (23 mg, 18 μmol) was combined with $La^{III}Cp''_3$ (17 mg, 23 μmol). The color did not appreciably change. The EPR spectrum (Figure 1.4) contains signals for $[La^{II}Cp''_3]^{1-}$ (g = 1.96, A = 133.6 G) and $Th^{III}Cp''_3$ (g = 1.91), as well as an unknown La(II) species (g = 1.96, A = 143.5 G).

Reaction 8.4. As in reaction. 2, [K(crypt)][$Th^{II}Cp''_3$] (23 mg, 18 μmol) was combined with $Y^{III}Cp'_3$ (10 mg, 19 μmol). The color did not appreciably change. The EPR spectrum (Figure 2.4) contains signals for $[Cp'_3Y^{II}]^{1-}$ (g = 1.99, A = 35.6 G) and $Th^{III}Cp''_3$ (g = 1.91) .

Reaction 9.4. As in reaction. 2, brown [K(crypt)][$U^{II}Cp''_3$] (20 mg, 16 μmol) was combined with $La^{III}Cp''_3$ (16 mg, 17 μmol). The color darkened. The EPR spectrum (Figure 5.4) contains

signals for $[La^{II}Cp''_3]^{1-}$ (g = 1.97, A = 133.6 G) and an unknown La(II) species (g = 1.96, A = 142.4 G).

Reaction 10.4. As in reaction. 2, [K(crypt)][$U^{II}Cp''_3$] (21 mg, 16 μmol) was combined with $Y^{III}Cp'_3$ (9 mg, 20 μmol). The color did not change appreciably. The EPR spectrum (Figure 6.4) contains the signal for $[Y^{II}Cp'_3]^{1-}$ (g = 1.99, A = 36.3 G).

Reaction 11.4. [K(crypt)][$La^{II}Cp''_3$] (11 mg, 9.8 μmol) and $Th^{III}Cp''_3$ (8 mg, 8.9 μmol) were dissolved in THF (20 mL) and loaded into a UV-visible cell. The UV-visible spectrum (Figure 7.4) contains the strong feature of [K(crypt)][$Th^{II}Cp''_3$] at 652 nm.[5]

Reaction 12.4. [K(crypt)][$Y^{II}Cp'_3$] (9 mg, 10 μmol) and $Th^{III}Cp''_3$ (9 mg, 10 μmol) were dissolved in THF (20 mL) and loaded into a UV-visible cell. The UV-visible spectrum (Figure 8.4) contains the strong feature of [K(crypt)][$Th^{II}Cp''_3$] at 653 nm.[5]

Reaction 13.4. As in reaction. 2, [K(crypt)][$Y^{II}Cp'_3$] (11 mg, 12 μmol) was combined with $La^{III}Cp''_3$ (12 mg, 15 μmol). The color changed to dark purple. The EPR spectrum (Figure 3.4) contains signals for $[La^{II}Cp''_3]^{1-}$ (g = 1.97, A = 133.6 G), an unknown La(II) species (g = 1.96, A = 144.7 G), and an unknown Y(II) species (g = 1.99, A = 33.8 G).

Reaction 14.4. As in reaction. 2, [K(crypt)][$La^{II}Cp''_3$] (23 mg, 21 μmol) was combined with $Y^{III}Cp'_3$ (11 mg, 22 μmol). The color did not change. The EPR spectrum (Figure 9.4) contains signals for $[La^{II}Cp''_3]^{1-}$ (g = 1.97, A = 133.6 G), two unknown La(II) species (g = 1.96, A = 144.8 G and g = 1.97, A = 149.8 G), and $[Y^{II}Cp'_3]^{1-}$ (g = 1.99, A = 35.8 G).

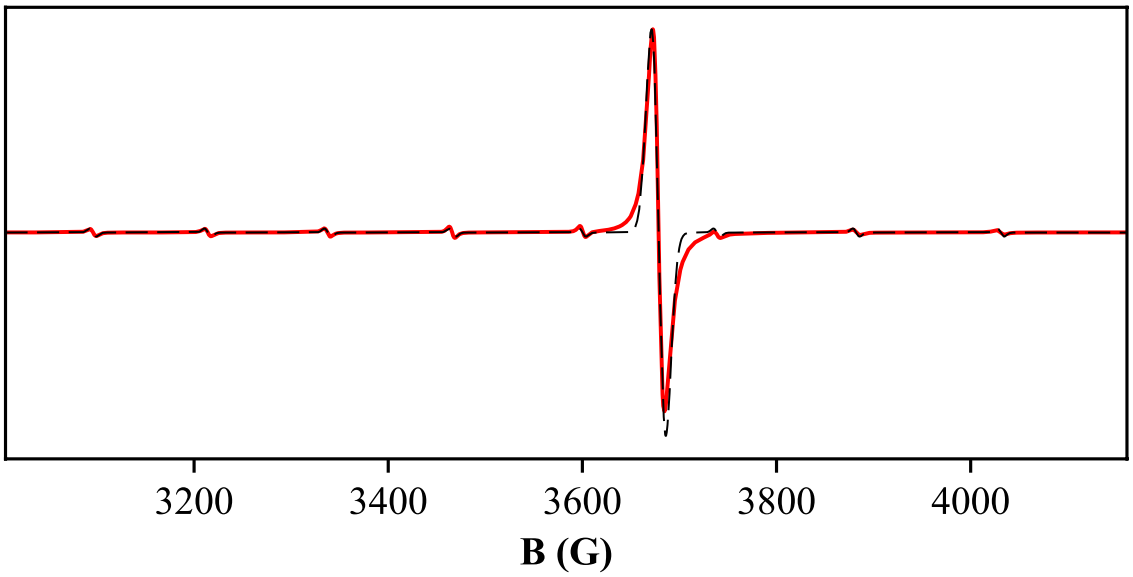

Figure 4.4. Room-temperature X-band EPR spectrum (red) and simulated spectrum (black dashes) of the products of reaction 6.4. Signals are present at g = 1.96, A = 133.6 G, ($[La^{II}Cp''_3]^{1-}$) and g = 1.91 ($Th^{III}Cp''_3$).

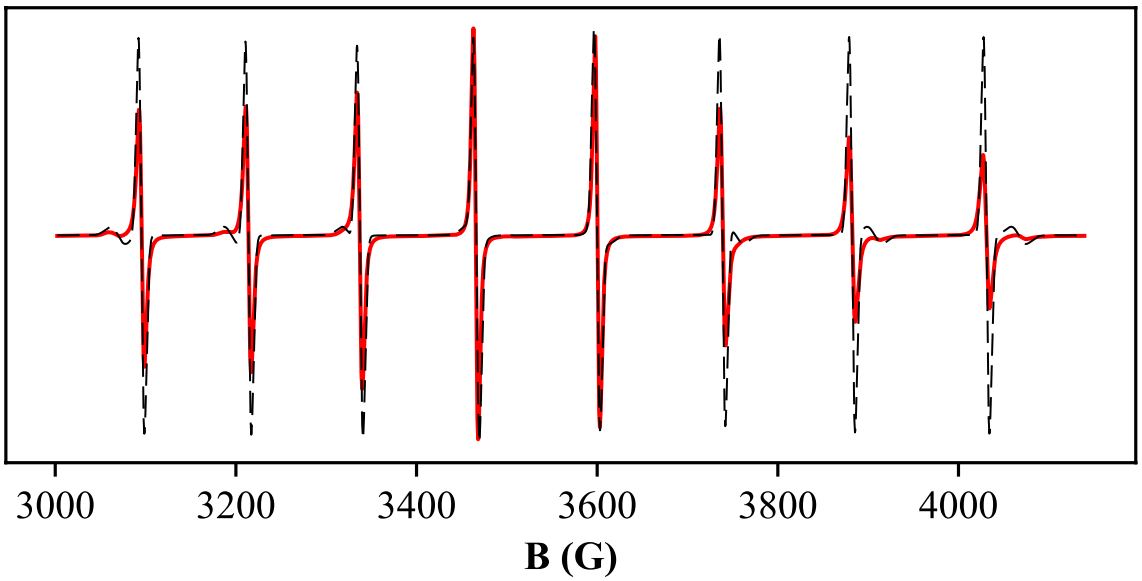

Figure 5.4. Room-temperature X-band EPR spectrum (red) and simulated spectrum (black dashes) of the products of reaction 9.4. Signals are present at g = 1.97, A = 133.6 G ($[La^{II}Cp''_3]^{1-}$) and g = 1.96, A = 142.4 G (an unknown La(II) species).

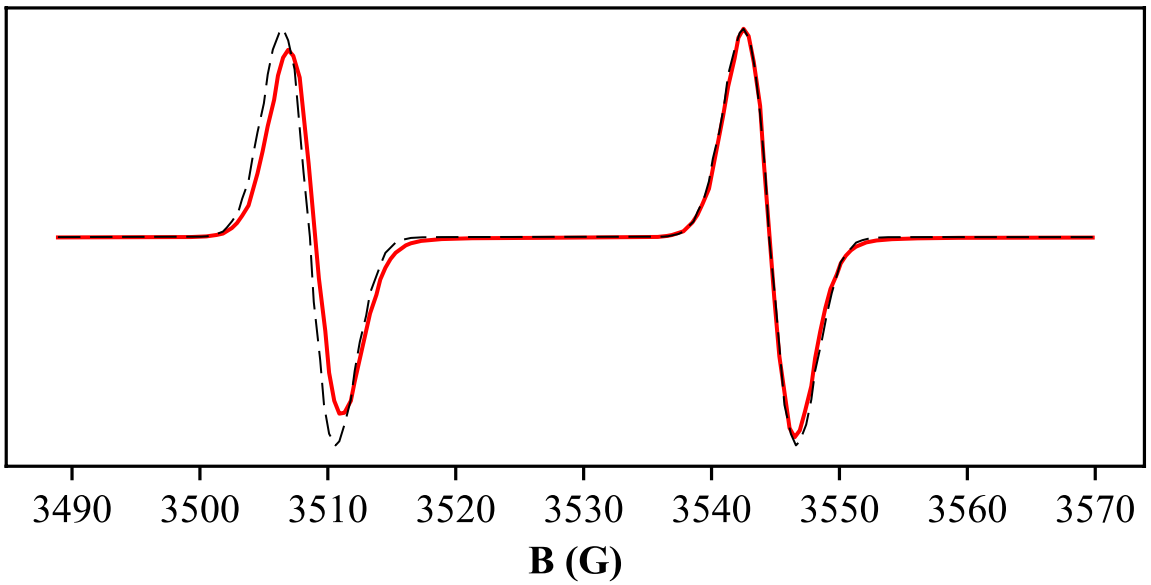

Figure 6.4. Room-temperature X-band EPR spectrum (red) and simulated spectrum (black dashes) of the products of reaction 10.4. Signal is present at $g = 1.99$, $A = 36.3$ G ($[Y^{II}Cp'_3]^{1-}$).

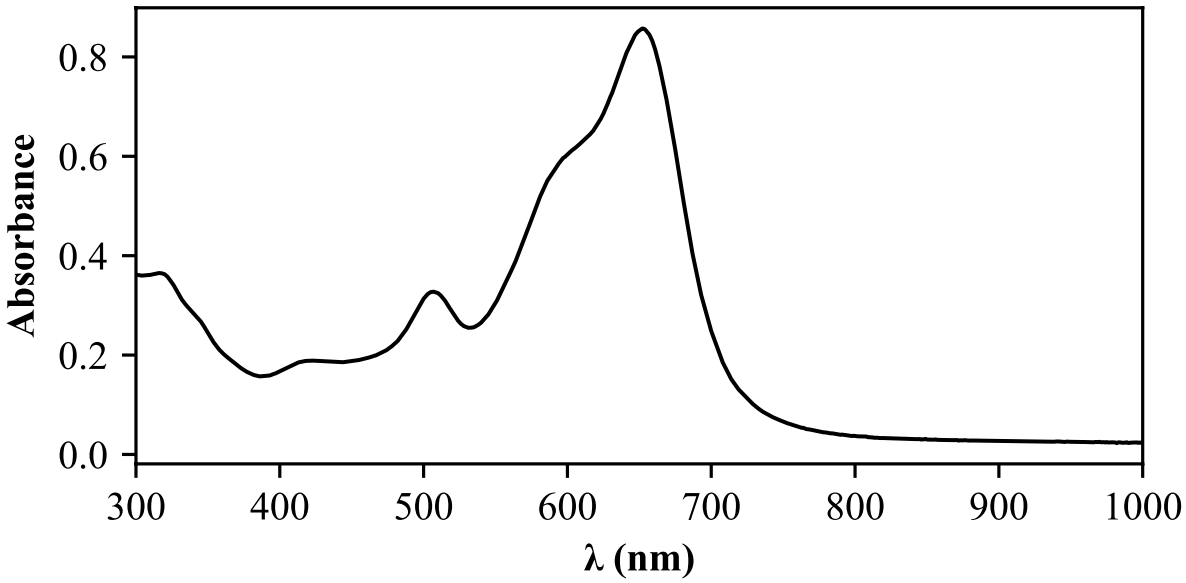

Figure 7.4. The UV-visible spectrum of reaction 11.4. The strong feature of $[K(crypt)][Th^{II}Cp''_3]$ is at 652 nm.

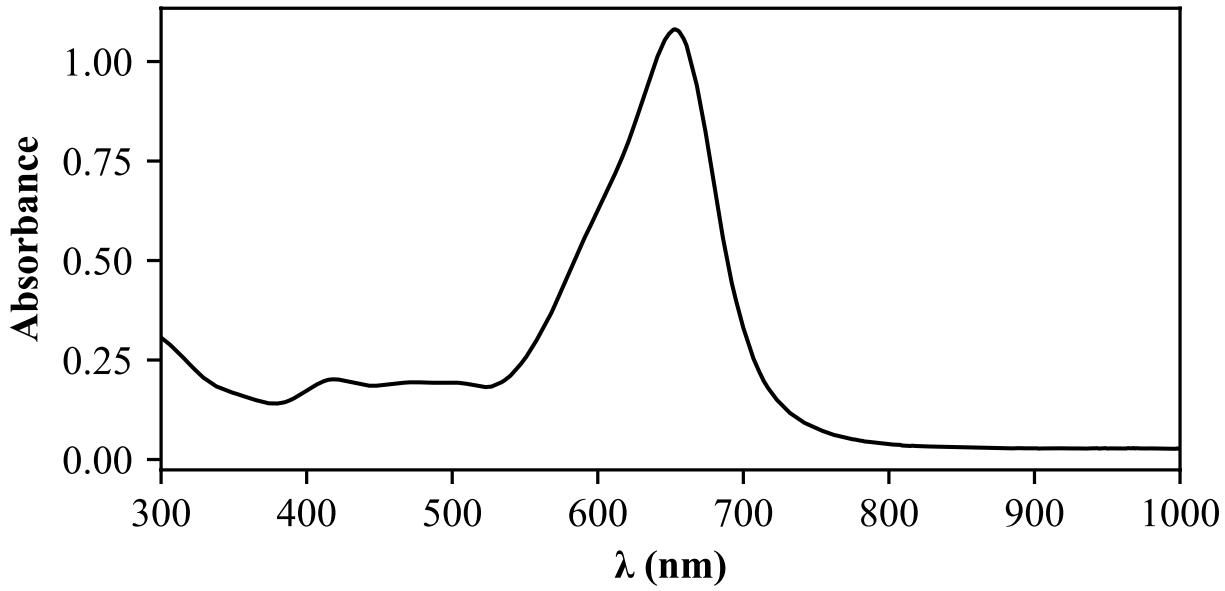

Figure 8.4. The UV-visible spectrum of reaction 12.4. The strong feature of [K(crypt)][$Th^{II}Cp''_3$] is at 653 nm.

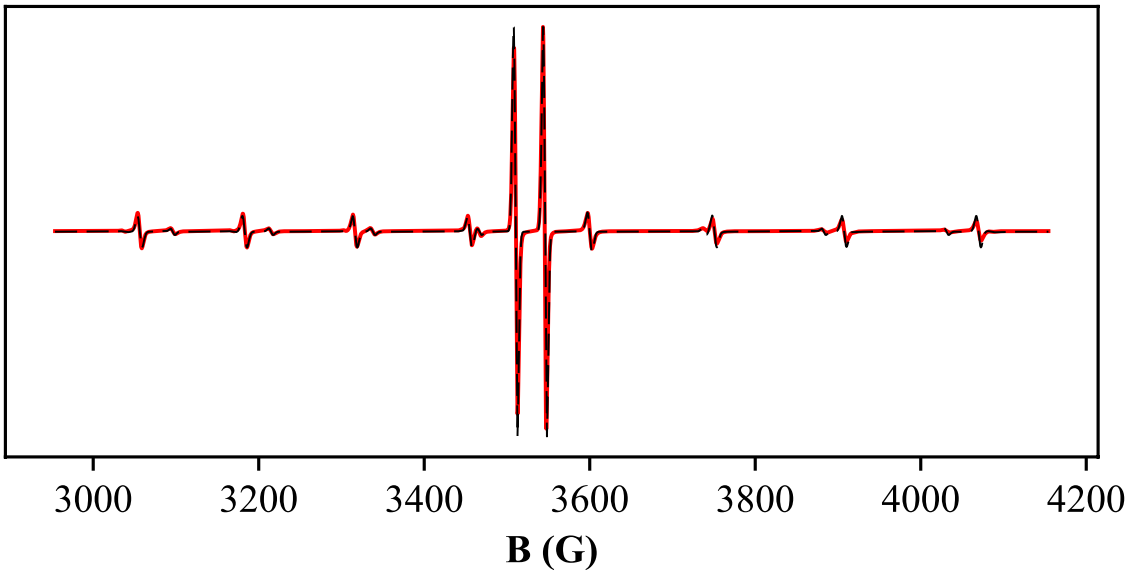

Figure 9.4. Room-temperature X-band EPR spectrum (red) and simulated spectrum (black dashes) of the products of reaction 14.4. Signals are present at $g = 1.97$, $A = 133.6$ G ($[La^{II}Cp''_3]^{1-}$), $g = 1.99$, $A = 35.8$ G ($[Y^{II}Cp'_3]^{1-}$), $g_1 = 1.96$, $A_1 = 144.8$ G, and $g_2 = 1.97$, $A_2 = 149.8$ G (two unknown La(II) species).

```
Y.g = 1.98958;
Y.A = 94.2;
Y.lwpp = 0.42492;
Y.Nucs = 'Y';
Y.weight = 1.11286;
LaP.g = 1.96509;
LaP.lwpp = 0.571824;
LaP.Nucs = '139La';
LaP.A = 367.362;
LaP.weight = 0.269556;
La2.g = 1.96454;
La2.lwpp = 0.539618;
La2.Nucs = '139La';
La2.A = 397.962;
La2.weight = 0.498112;
Exp.mwFreq = 9.824736;
Exp.Range = [297.1 413.4699966];
Exp.nPoints = 2910;
VaryY.weight = 1
VaryLaP.g = 0.02
VaryLa2.A = 50
esfit('garlic',spc,{La2,LaP,Y},{VaryLa2,VaryLaP,VaryY},Exp)
```

Figure 10.4. The EasySpin simulation of the spectrum in Figure 3.4. The systems "Y," "LaP," and "La2" are the simulated signals for the Y(II) species and the two La(II) species, respectively. The parameter "weight" defines the strength of the signal, and "lwpp" is an phenominological line-broadening function. The array "Exp" contains the experimental parameters. The array "spc" is the experimental data. The function 'garlic' is the simulation function used to generate the simulated spectrum. The function "esfit" produces a least-squares fit of the simulated systems onto the experimental data. The systems starting with "Vary" define how much "esfit" will vary the noted parameter.

REFERENCES

(1) MacDonald, M. R.; Bates, J. E.; Fieser, M. E.; Ziller, J. W.; Furche, F.; Evans, W. J. *J. Am. Chem. Soc.* **2012**, *134*, 8420–8423.
(2) Fieser, M. E.; MacDonald, M. R.; Krull, B. T.; Bates, J. E.; Ziller, J. W.; Furche, F.; Evans, W. J. *J. Am. Chem. Soc.* **2015**, *137*, 369–382.
(3) MacDonald, M. R.; Bates, J. E.; Ziller, J. W.; Furche, F.; Evans, W. J. *J. Am. Chem. Soc.* **2013**, *135*, 9857–9868.
(4) Windorff, C. J.; Chen, G. P.; Cross, J. N.; Evans, W. J.; Furche, F.; Gaunt, A. J.; Janicke, M. T.; Kozimor, S. A.; Scott, B. L. *J. Am. Chem. Soc.* **2017**, *139*, 3970–3973.
(5) Langeslay, R. R.; Fieser, M. E.; Ziller, J. W.; Furche, F.; Evans, W. J. *Chem. Sci.* **2015**, *6*, 517–521.
(6) Windorff, C. J.; MacDonald, M. R.; Meihaus, K. R.; Ziller, J. W.; Long, J. R.; Evans, W. J. *Chem. Eur. J.* **2016**, *22*, 772–782.
(7) Hitchcock, P. B.; Lappert, M. F.; Maron, L.; Protchenko, A. V. *Angew. Chem. Int. Ed.* **2008**, *47*, 1488–1491.
(8) Palumbo, C. T.; Darago, L. E.; Windorff, C. J.; Ziller, J. W.; Evans, W. J. *Organometallics* **2018**, *37*, 900–905.
(9) Macdonald, M. R.; Fieser, M. E.; Bates, J. E.; Ziller, J. W.; Furche, F.; Evans, W. J. *J. Am. Chem. Soc.* **2013**, *135*, 13310–13313.
(10) Su, J.; Windorff, C. J.; Batista, E. R.; Evans, W. J.; Gaunt, A. J.; Janicke, M. T.; Kozimor, S. A.; Scott, B. L.; Woen, D. H.; Yang, P. *J. Am. Chem. Soc.* **2018**, *140*, 7425–7428.
(11) La Pierre, H. S.; Scheurer, A.; Heinemann, F. W.; Hieringer, W.; Meyer, K. *Angew. Chem. Int. Ed.* **2014**, *53*, 7158–7162.
(12) Billow, B. S.; Livesay, B. N.; Mokhtarzadeh, C. C.; McCracken, J.; Shores, M. P.; Boncella, J. M.; Odom, A. L. *J. Am. Chem. Soc.* **2018**, *140*, 17369–17373.
(13) Kelly, R. P.; Maron, L.; Scopelliti, R.; Mazzanti, M. *Angew. Chem. Int. Ed.* **2017**, *56*, 15663–15666.
(14) Huh, D. N.; Ziller, J. W.; Evans, W. J. *Dalton Trans.* **2018**, *47* (48), 17285–17290.
(15) Jenkins, T. F.; Woen, D. H.; Mohanam, L. N.; Ziller, J. W.; Furche, F.; Evans, W. J. *Organometallics* **2018**, *37*, 3863–3873.
(16) Palumbo, C. T.; Halter, D. P.; Voora, V. K.; Chen, G. P.; Chan, A. K.; Fieser, M. E.; Ziller, J. W.; Hieringer, W.; Furche, F.; Meyer, K. *Inorg. Chem.* **2018**, *57*, 2823–2833.
(17) Fieser, M. E.; Palumbo, C. T.; La Pierre, H. S.; Halter, D. P.; Voora, V. K.; Ziller, J. W.; Furche, F.; Meyer, K.; Evans, W. J. *Chem. Sci.* **2017**, *8*, 7424–7433.
(18) Ryan, A. J.; Darago, L. E.; Balasubramini, S. G.; Chen, G. P.; Ziller, J. W.; Furche, F.; Long, J. R.; Evans, W. J. *Chem. Eur. J.* **2018**, *24*, 7702–7709.
(19) Woen, D. H.; Chen, G. P.; Ziller, J. W.; Boyle, T. J.; Furche, F.; Evans, W. J. *Angew. Chem. Int. Ed.* **2017**, *56* (8), 2050–2053.
(20) Watson, P. L.; Tulip, T. H.; Williams, I. *Organometallics* **1990**, *9*, 1999–2009.
(21) Bond, A. M.; Deacon, G. B.; Newnham, R. H. *Organometallics* **1986**, *5*, 2312–2316.
(22) Finke, R. G.; Gaughan, G.; Voegeli, R. *J. Organomet. Chem.* **1982**, *229*, 179–184.
(23) Bochkarev, M. N. *Chem. Rev.* **2002**, *102*, 2089–2117.
(24) Kotyk, C. M.; Macdonald, M. R.; Ziller, J. W.; Evans, W. J. *Organometallics* **2015**, *34*, 2287–2295.

(25) Evans, W. J.; Gonzales, S. L.; Ziller, J. W. *J. Am. Chem. Soc.* **1994**, *116*, 2600–2608.
(26) Electrochemical Series. In *CRC Handbook of Chemistry and Physics, 100th Edition (Internet Verison 2019)*; John R. Rumble, Ed.; CRC Press/Taylor & Francis: Boca Raton, FL.
(27) Halter, D. P.; Palumbo, C. T.; Ziller, J. W.; Gembicky, M.; Rheingold, A. L.; Evans, W. J.; Meyer, K. *J. Am. Chem. Soc.* **2018**, *140*, 2587–2594.
(28) Cristina Cassani, M.; Lappert, M. F.; Laschi, F. *Chem. Commun.* **1997**, 1563–1564.
(29) Inman, C. J.; Cloke, F. G. N. *Dalton Trans.* **2019**, *48*, 10782–10784.
(30) Woen, D. H.; Huh, D. N.; Ziller, J. W.; Evans, W. J. *Organometallics* **2018**, *37*, 3055–3063.
(31) Moehring, S. A.; Beltrán-Leiva, M. J.; Páez-Hernández, D.; Arratia-Pérez, R.; Ziller, J. W.; Evans, W. J. *Chem. Eur. J.* **2018**, *24*, 18059–18067.
(32) Stoll, S.; Schweiger, A. *J. Magn. Reson.* **2006**, *178*, 42–55.
(33) Blake, P. C.; Edelstein, N. M.; Hitchcock, P. B.; Kot, W. K.; Lappert, M. F.; Shalimoff, G. V.; Tian, S. *J. Organomet. Chem.* **2001**, *636*, 124–129.
(34) Corbey, J. F.; Woen, D. H.; Palumbo, C. T.; Fieser, M. E.; Ziller, J. W.; Furche, F.; Evans, W. J. *Organometallics* **2015**, *34*, 3909–3921.
(35) Coles, M. P.; Hitchcock, P. B.; Lappert, M. F.; Protchenko, A. V. *Organometallics* **2012**, *31*, 2682–2690.
(36) MacDonald, M. R.; Ziller, J. W.; Evans, W. J. *J. Am. Chem. Soc.* **2011**, *133*, 15914–15917.
(37) Laschi, F.; Hitchcock, P. B.; Gun'ko, Y. K.; Cassani, M. C.; Lappert, M. F. *Organometallics* **1999**, *18*, 5539–5547.
(38) Peterson, J. K.; MacDonald, M. R.; Ziller, J. W.; Evans, W. J. *Organometallics* **2013**, *32*, 2625–2631.
(39) Evans, W. J.; Kociok-Köhn, G.; Foster, S. E.; Ziller, J. W.; Doedens, R. J. *J. Organomet. Chem.* **1993**, *444*, 61–66.
(40) Windorff, C. J.; Evans, W. J. *Organometallics* **2014**, *33*, 3786–3791.

Chapter 5

Evaluating Electron Transfer Reactivity of Rare-Earth(II) Complexes using EPR Spectroscopy

INTRODUCTION

Redox chemistry is one of the two most fundamental types of reactivity along with acid-base chemistry. Inherent in the utilization of redox reactions is the availability of different oxidation states and the redox potentials that interconnect them. In the lanthanide metal area, new opportunities have arisen with the discovery that stable molecular complexes of +2 ions could be isolated for not only Eu, Yb, Sm, Tm, Dy, and Nd, but also for all the rest of the lanthanides except radioactive Pm, eq 1.5.[1–6] Surprisingly, the new ions made by reduction of $4f^n$ Ln(III) ions had properties consistent with $4f^n5d^1$ electron configurations rather than the $4f^{n+1}$ configurations of Eu(II), Yb(II), Sm(II), Tm(II), Dy(II), and Nd(II) obtained from reduction of $4f^n$ Ln(III) precursors.[7,8] Although these new oxidation states are being found in an increasing number of coordination environments,[9–16] information on the redox potentials of these new ions has been elusive. The highly reducing species can react with supporting electrolytes and in some cases with THF solvent. For example, $[Ln^{II}Cp^{Me}_3]^{1-}$ ($Cp^{Me1-} = C_5H_4Me^{1-}$) complexes of La and Pr ring-open THF to form $[O(CH_2)_4]^{2-}$ dianions.[17] Since these complexes can be generated with K and Na, the redox potentials must be less negative than −2.7 V vs SHE.[18] However, the relative reactivity of these species and the dependence of their redox potentials on the specific metal and the ligand remain unknown.

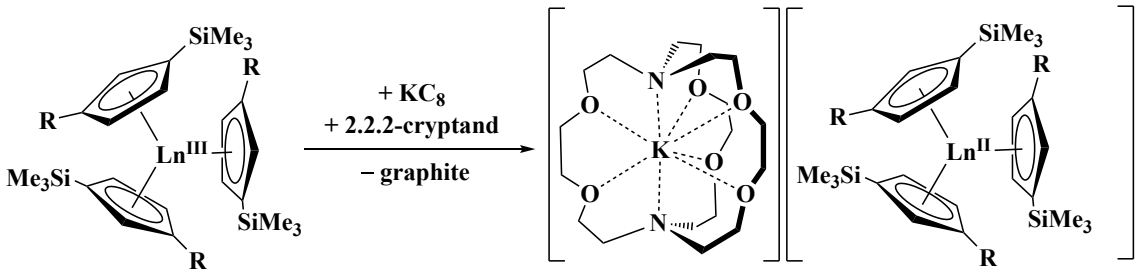

(1.5)

R = H; Ln = Y, La, Ce, Pr, Gd, Tb, Ho, Er, Lu
R = $SiMe_3$; Ln = La, Ce, Pr

To fill this gap in experimental data, reactions of $Ln^{III}A_3$ complexes that are known to form new Ln(II) ions (A = anion such as cyclopentadienyl, amide, aryloxide) with the $[Ln^{II}A_3]^{1-}$ complexes involving either different metals or different ligands were examined to evaluate their comparative reduction chemistry. To accomplish this comparison, Ln(II) systems were selected that allow EPR spectroscopy to be used to interrogate the systems. This is possible with La, Gd, Lu, Y, and Sc. It was found that EPR spectroscopy even allows characterization when complicated mixtures of products are formed. The comparative reaction data are presented along with a discussion of the implications in rare earth reduction chemistry.

RESULTS

Methods. Each reaction described below involves reaction of a solution of a $[Ln^{II}A_3]^{1-}$ complex with a solution of $Ln^{III}A_3$ where either the metal or ligand of the Ln(III) reagent differs from that of the Ln(II) reagent. Some of the $[Ln^{II}A_3]^{1-}$ complexes utilized in this study are too reactive to be isolated and have been identified only through EPR spectroscopy. In order to maintain a consistent experimental approach for both isolable and non-isolable compounds, the "reductant" $[Ln^{II}A_3]^{1-}$ species was generated by passing a THF solution (~10 mg/mL) of $Ln^{III}A_3$ through a pipette packed with KC_8 that has been chilled to –35 °C. The resulting intensely-colored solution was dripped onto a THF solution (equimolar with the "reductant" species) of a "substrate" $Ln^{III}A_3$ compound (where Ln or A was different) containing 1 equiv of 2.2.2-cryptand (crypt). In

each case, the mixture was then loaded into a chilled EPR tube and quickly frozen. This method allows unstable Ln(II) compounds to be quickly generated and trapped in the frozen solution. The whole process takes no longer than 90 seconds. The crypt is included to stabilize any Ln(II) products generated, since it has been seen in this study and in others[4] that thermal stability of Ln(II) complexes can be enhanced by the presence of crypt. Crypt could not be included in the reductant solution, however, because passing a THF solution of only crypt through KC_8 produces a deep-blue solution of an electride species that can act as a reductant itself (Figure 1.5).[19,20]

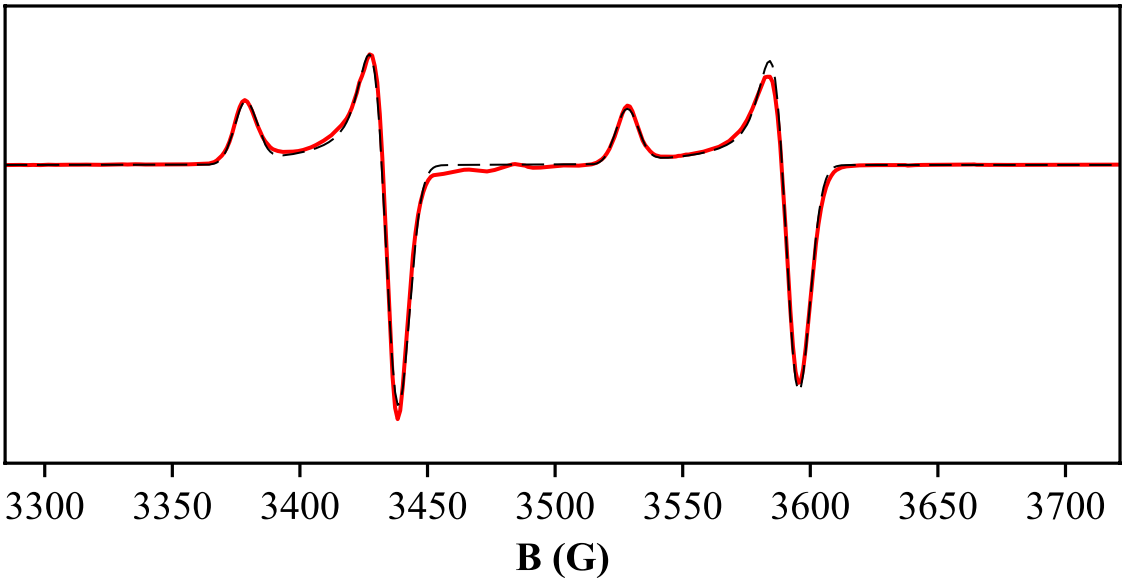

Figure 1.5. 77 K X-band EPR spectrum of the dark-blue species from adding a solution of crypt, reduced with KC_8, to Y(2,6-^{t}Bu$_2$-4-Me-$C_6H_2O)_3$. Signal is present at $g_\perp = 1.96$, $g_\parallel = 1.99$, $A_\perp = 156.8$ G, and $A_\parallel = 149.4$ G, consistent with a Y(II) species. Experimental spectrum in red, simulated spectrum in black dashes.

The reactions with DyI_2 and NdI_2 were carried out with slight modifications of the procedure, since the soluble $DyI_2(THF)_5$ and $NdI_2(THF)_5$ were first extracted from base-free DyI_2 and NdI_2 with THF at −35 °C, then these solutions were reacted with the substrate Ln(III) compounds in the same conditions as the other experiments, *i.e.,* at −35 °C in THF. Since

$DyI_2(THF)_5$ and $NdI_2(THF)_5$ are known to decompose in THF over hours at room temperature,[21] the reactions were done quickly while the colors indicative of $DyI_2(THF)_5$ and $NdI_2(THF)_5$ were still present. Signals for neither Y(II) nor La(II) were observed in the reactions with DyI_2 and NdI_2.

Reduction of an $Ln'^{III}A'_3$ substrate by a $[Ln^{II}A_3]^{1-}$ "reductant" was counted as a successful reaction only when the $[Ln'^{II}A'_3]^{1-}$ species could be detected by EPR spectroscopy, *i.e.*, loss of the EPR signal of the $[Ln^{II}A_3]^{1-}$ reactant was not sufficient. The reactions in this Chapter are written to show when a transformation occurred in the forward direction. Since equilibrium constants for these systems are not known, only reactions in the forward direction are reported. All spectra were simulated with EasySpin, which generates the *g* and *A* values reported throughout the work using the method described in Chapter 4.[22] All EPR spectra used for this study can be found in the Spectroscopic Appendix of this Chapter.

$[Ln^{II}Cp'_3]^{1-}$ Reactions with $Cp'_3Ln'^{III}$ Complexes ($Cp'^{1-} = C_5H_4SiMe_3^{1-}$). In this part of the study, this ligand set was kept constant and the metal was varied. Since the (Cp'_3) ligand set stabilizes all of the Ln(II) ions except small Sc(II) and radioactive Pm(II), this ligand set was chosen for the initial investigations.

Treatment of colorless $La^{III}Cp'_3(THF)$ with maroon $[Y^{II}Cp'_3]^{1-}$ in THF, reaction 2.5, gave a maroon mixture with an EPR spectrum that contains signals for both $[La^{II}Cp'_3]^{1-}$ and $[Y^{II}Cp'_3]^{1-}$ (Figure 2.5).[2,4] Hence, Y(II) reduced La(III), but the reaction did not form La(II) exclusively. Consistent with this, treatment of yellow $Y^{III}Cp'_3$ with maroon $[La^{II}Cp'_3]^{1-}$ forms $[Y^{II}Cp'_3]^{1-}$, *i.e.*, La(II) can reduce Y(III). These results, reaction 2.5, indicate that the reduction potentials of $La^{III}Cp'_3$ and $Y^{III}Cp'_3$ are very similar.

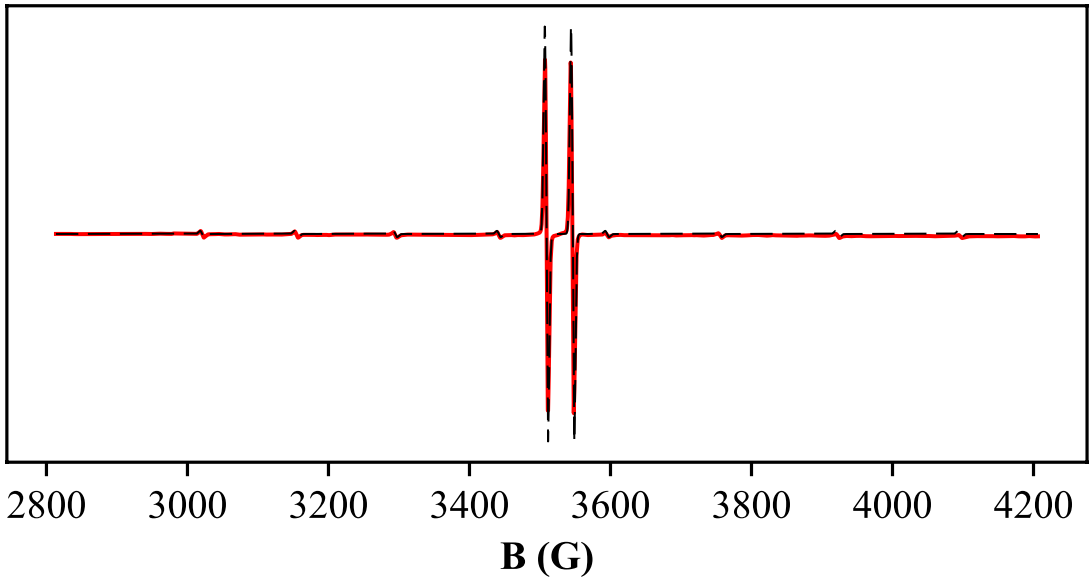

Figure 2.5. Room-temperature X-band EPR spectrum (red) and simulated spectrum (black dashes) of the products of reaction 2.5 in the forward direction. Signals are present at g = 1.99, A = 37.2 G ($[Y^{II}Cp'_3]^{1-}$) and g = 1.97, A = 153.5 G ($[La^{II}Cp'_3]^{1-}$).

The four combinations of Ln(II) reagents of Y and Lu with Ln′(III) substrates of La and Lu gave similar results, reactions 3.5–4.5.[4] Hence, $La^{III}Cp'_3(THF)$, $Y^{III}Cp'_3$, and $Lu^{III}Cp'_3$ all have similar reduction potentials. This was somewhat surprising since the measured half-lives ($t_{1/2}$) of these complexes are quite different: $[K(crypt)][Lu^{II}Cp'_3]$ decomposes in a first-order process with a $t_{1/2}$ of 19 min,[4] $[K(crypt)][Y^{II}Cp'_3]$ decomposes in a second-order process with a $t_{1/2}$ of 2.3 h at 3 mM, and $[K(crypt)][La^{II}Cp'_3]$ is more stable. The decomposition of $[K(crypt)][La^{II}Cp'_3]$ was determined for this study by the methods used to measure the other $[Ln^{II}Cp'_3]^{1-}$ complexes[4,23] and the data could be fit with either first or second order kinetics with a first-order $t_{1/2}$ of 62 h or a second-order $t_{1/2}$ of 33 h at 3 mM (Spectroscopic Appendix, Figures 53.5 and 54.5).

$$[Y^{II}Cp'_3]^{1-} + La^{III}Cp'_3(THF) \underset{\text{Ar, crypt}}{\overset{\text{THF, } -30\ ^\circ\text{C}}{\rightleftharpoons}} Y^{III}Cp'_3 + [La^{II}Cp'_3]^{1-} \quad (2.5)$$

$$[Lu^{II}Cp'_3]^{1-} + Y^{III}Cp'_3 \underset{\text{Ar, crypt}}{\overset{\text{THF, } -30\ ^\circ\text{C}}{\rightleftharpoons}} Lu^{III}Cp'_3 + [Y^{II}Cp'_3]^{1-} \quad (3.5)$$

$$[Lu^{II}Cp'_3]^{1-} + La^{III}Cp'_3(THF) \underset{\text{Ar, crypt}}{\overset{\text{THF, } -30\ ^\circ\text{C}}{\rightleftharpoons}} Lu^{III}Cp'_3 + [La^{II}Cp'_3]^{1-} \quad (4.5)$$

+2 \ +3	Y	La	Lu	Gd
Y		2.5	3.5	5.5
La	2.5		4.5	6.5
Lu	3.5	4.5		7.5
Gd				
Tb	8.5	9.5	10.5	11.5

Proceeds

Does not proceed

Figure 3.5. The results of the $[Ln^{II}Cp'_3]^{1-}$ vs. $[Ln'^{II}Cp'_3]^{1-}$ experiments in matrix form. The rows are labeled with the metal used in the reductant species and the columns with the metal used in the substrate species. The numbers in the blocks represent the number of the corresponding reaction.

In contrast to these reactions that proceed from either direction, $[Gd^{II}Cp'_3]^{1-}$ does not reduce $La^{III}Cp'_3(THF)$, $Y^{III}Cp'_3$, or $Lu^{III}Cp'_3$. Consistent with this, $Gd^{III}Cp'_3$ is reduced by $[La^{II}Cp'_3]^{1-}$, $[Y^{II}Cp'_3]^{1-}$ and $[Lu^{II}Cp'_3]^{1-}$, reactions 5.5–7.5.[4] It is not obvious why this was the case. The second order $t_{1/2}$ of $[Gd^{II}Cp'_3]^{1-}$ at 3 mM is 89 h.

To investigate if the electron configuration of Gd(II) in $[Gd^{II}Cp'_3]^{1-}$ ($4f^7 5d^1$) was involved, the Tb(II) complex $[Tb^{II}Cp'_3]^{1-}$ ($4f^8 5d^1$) was studied as a reductant to see if the nearly-half-filled subshell configuration would also make Tb(II) a weak reductant. $Tb^{III}Cp'_3$ was not used as a substrate since $[Tb^{II}Cp'_3]^{1-}$ has no known distinctive X-band EPR signal at 77 K or room temperature in this ligand set. So, only reactions where $[Tb^{II}Cp'_3]^{1-}$ was acting as a reducing agent were examined. $[Tb^{II}Cp'_3]^{1-}$reduces all of the substrates unreactive with $[Gd^{II}Cp'_3]^{1-}$, namely $La^{III}Cp'_3(THF)$, $Y^{III}Cp'_3$, or $Lu^{III}Cp'_3$, as well as $Gd^{III}Cp'_3$, reactions 8.5–11.5. This gives a ranking of these complexes, from most reducing to least reducing, as Tb(II) ≳ Y(II) ≈ La(II) ≈ Lu(II) > Gd(II). Tb(II) could be more reducing than Y(II), La(II), and Lu(II), but it is not known whether these three ions would be able to reduce Tb(III) to Tb(II) in this ligand set.

$$[Y^{II}Cp'_3]^{1-} + Gd^{III}Cp'_3 \xrightarrow[\text{Ar, crypt}]{\text{THF, } -30\ ^\circ\text{C}} Y^{III}Cp'_3 + [Gd^{II}Cp'_3]^{1-} \quad (5.5)$$

$$[La^{II}Cp'_3]^{1-} + Gd^{III}Cp'_3 \xrightarrow[\text{Ar, crypt}]{\text{THF, } -30\ ^\circ\text{C}} La^{III}Cp'_3(THF) + [Gd^{II}Cp'_3]^{1-} \quad (6.5)$$

$$[Lu^{II}Cp'_3]^{1-} + Gd^{III}Cp'_3 \xrightarrow[\text{Ar, crypt}]{\text{THF, } -30\ ^\circ\text{C}} Lu^{III}Cp'_3 + [Gd^{II}Cp'_3]^{1-} \quad (7.5)$$

$$[Tb^{II}Cp'_3]^{1-} + Y^{III}Cp'_3 \xrightarrow[\text{Ar, crypt}]{\text{THF, } -30\ ^\circ\text{C}} Tb^{III}Cp'_3 + [Y^{II}Cp'_3]^{1-} \quad (8.5)$$

$$[Tb^{II}Cp'_3]^{1-} + La^{III}Cp'_3(THF) \xrightarrow[\text{Ar, crypt}]{\text{THF, } -30\ ^\circ\text{C}} Tb^{III}Cp'_3 + [La^{II}Cp'_3]^{1-} \quad (9.5)$$

$$[Tb^{II}Cp'_3]^{1-} + Lu^{III}Cp'_3 \xrightarrow[\text{Ar, crypt}]{\text{THF, } -30\ ^\circ\text{C}} Tb^{III}Cp'_3 + [Lu^{II}Cp'_3]^{1-} \quad (10.5)$$

$$[Tb^{II}Cp'_3]^{1-} + Gd^{III}Cp'_3 \xrightarrow[\text{Ar, crypt}]{\text{THF, } -30\ ^\circ\text{C}} Tb^{III}Cp'_3 + [Gd^{II}Cp'_3]^{1-} \quad (11.5)$$

$[Ln^{II}(NR_2)_3]^{1-}$ Reactions with $Ln'^{III}(NR_2)_3$ Complexes (R = $SiMe_3$). The $(NR_2)_3$ ligand set (R = $SiMe_3$) is known to allow the isolation of complexes of Ln(II) ions for Sc, Y, Nd, Gd, Tb, Ho, and Er as well as the traditional divalent ions of Eu, Yb, Sm, and Tm.[6,9,12,24–26] Reactions of amide complexes were studied to determine if the trends in the metals' reducing ability established with Cp′ would change with different ligands. For these studies, only $[Y^{II}(NR_2)_3]^{1-}$ and $[Sc^{II}(NR_2)_3]^{1-}$ can be used to detect successful reductions, as they are the only Ln(II) compounds in this ligand set known with known EPR spectra at 77 K and room temperature.[6,27]

$$[Y^{II}(NR_2)_3]^{1-} + Sc^{III}(NR_2)_3 \xrightarrow[\text{Ar, crypt}]{\text{THF, } -30\ ^\circ\text{C}} Y^{III}(NR_2)_3 + [Sc^{II}(NR_2)_3]^{1-} \quad (12.5)$$

$$[Sc^{II}(NR_2)_3]^{1-} + Y^{III}(NR_2)_3 \xrightarrow[\text{Ar, crypt}]{\text{THF, } -30\ ^\circ\text{C}} \not\rightarrow \quad Sc^{III}(NR_2)_3 + [Y^{II}(NR_2)_3]^{1-} \quad (13.5)$$

$$[Gd^{II}(NR_2)_3]^{1-} + Y^{III}(NR_2)_3 \xrightarrow[\text{Ar, crypt}]{\text{THF, } -30\ ^\circ\text{C}} Gd^{III}(NR_2)_3 + [Y^{II}(NR_2)_3]^{1-} \quad (14.5)$$

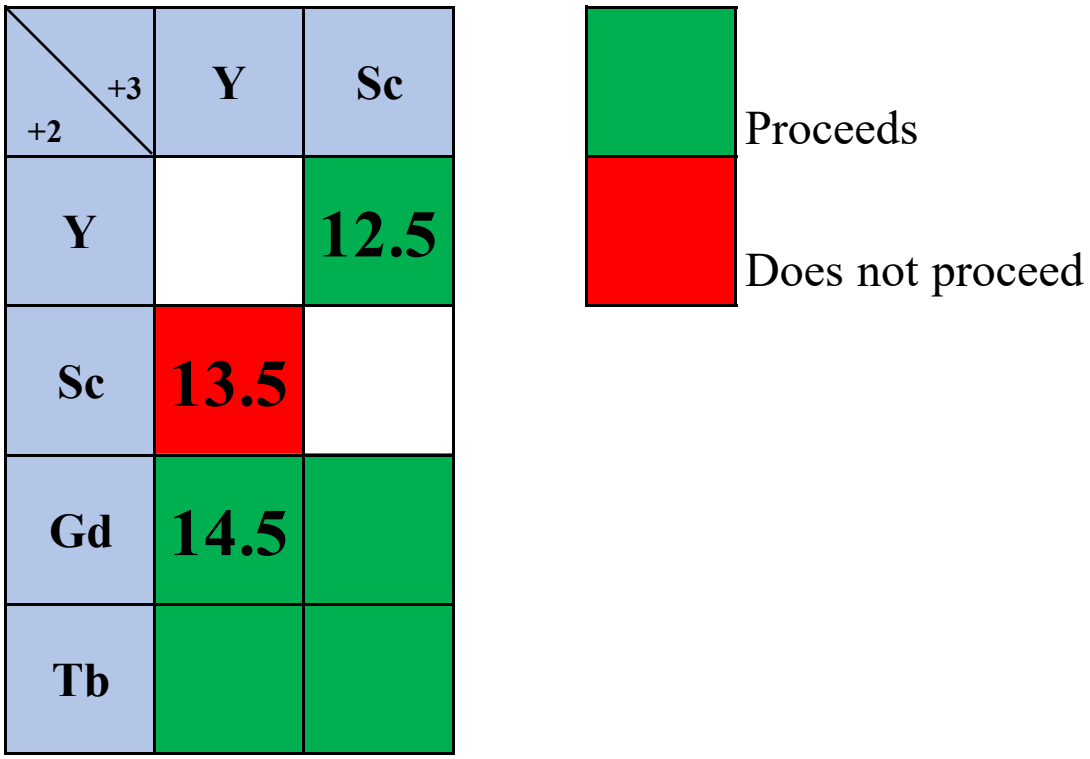

Figure 4.5. The results of the $[Ln^{II}(NR_2)_3]^{1-}$ vs. $[Ln'^{II}(NR_2)_3]^{1-}$ experiments in matrix form. The rows are labeled with the metal used in the reductant species and the columns with the metal used in the substrate species. The numbers in the blocks represent the number of the corresponding reaction.

While $[Y^{II}(NR_2)_3]^{1-}$ can reduce $Sc^{III}(NR_2)_3$ to $[Sc^{II}(NR_2)_3]^{1-}$ (reaction 12.5), the reverse reaction (reaction 13.5) does not occur (Figure 5.5). Therefore, $[Y^{II}(NR_2)_3]^{1-}$ is a stronger reductant than $[Sc^{II}(NR_2)_3]^{1-}$. Both $[Gd^{II}(NR_2)_3]^{1-}$ and $[Tb^{II}(NR_2)_3]^{1-}$ can reduce the Y(III) and

Sc(III) compounds, so these two compounds are either as reducing or more reducing than $[Y^{II}(NR_2)_3]^{1-}$. This leads to the following ranking of these complexes, from most reducing to least reducing: Tb(II) ≈ Gd(II) ≷ Y(II) > Sc(II). The Gd(II) *vs.* Y(II) results with the $(NR_2)_3$ ligand set where Y(II) is a stronger reductant than Gd(II) are opposite to those with the $(Cp')_3$ ligand set, where Y(II) is a stronger reductant than Gd(II). This indicates that the reducing ability of Ln(II) compounds is sensitive to ligand environment. To further investigate this hypothesis, experiments comparing the same Ln(II) in different ligand sets were carried out.

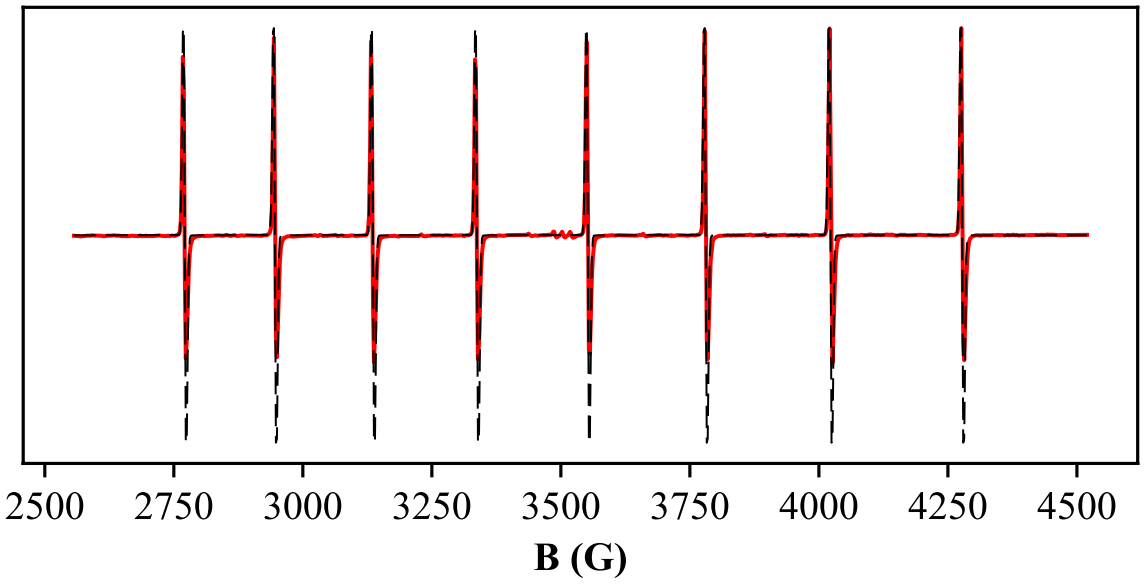

Figure 5.5. Room-temperature X-band EPR spectrum (red) and simulated spectrum (black dashes) of the products of reaction 13.5. Signal is present at $g = 1.98$, $A = 214.9$ G ($[Sc^{II}(NR_2)_3]^{1-}$). Small signals near 3500 G are not consistent with $[Y^{II}(NR_2)_3]^{1-}$ ($g = 1.97$, $A = 110.5$ G).

$[Ln^{II}A_3]^{1-}$ Reactions with $Ln^{III}A'_3$ Complexes (A, A′ = anion). The investigation of different ligand sets on the same metal was initially conducted with yttrium as this metal since a wide variety of Y(II) compounds have been identified by EPR spectroscopy. The Y(II) compounds investigated display a range of hyperfine coupling constants: $[Y^{II}Cp'_3]^{1-}$, A = 36.6 G;[2] $[Y^{II}(NR_2)_3]^{1-}$, A = 110 G,[27] and "$[Y^{II}(OAr)_3]^{1-}$," A = 156 G (OAr = 2,6-^{t}BuC$_6$H$_3$O).[13] It should be

noted that the latter complex has not been characterized by X-ray crystallography. Since the *A* value has been shown to increase with the amount of metal contribution to the SOMO,[28] it was hypothesized that a higher *A* value (i.e. more metal character in the SOMO) might increase the reducing power of the resulting Y(II) compound.

$$[Y^{II}Cp'_3]^{1-} + Y^{III}(OAr)_3 \xrightarrow[\text{Ar, crypt}]{\text{THF, } -30\ ^\circ\text{C}} \text{unknown EPR-active species} \quad (15.5)$$

$$[Y^{II}Cp'_3]^{1-} + Y^{III}(NR_2)_3 \xrightarrow[\text{Ar, crypt}]{\text{THF, } -30\ ^\circ\text{C}} \not\rightarrow \quad (16.5)$$

$$[Y^{II}(OAr)_3]^{1-} + Y^{III}Cp'_3 \xrightarrow[\text{Ar, crypt}]{\text{THF, } -30\ ^\circ\text{C}} Y^{III}(OAr)_3 + [Y^{II}Cp'_3]^{1-} + \text{other EPR-active species} \quad (17.5)$$

$$[Y^{II}(NR_2)_3]^{1-} + Y^{III}Cp'_3 \xrightarrow[\text{Ar, crypt}]{\text{THF, } -30\ ^\circ\text{C}} Y^{III}(NR_2)_3 + [Y^{II}Cp'_3]^{1-} \quad (18.5)$$

$$[Y^{II}(NR_2)_3]^{1-} + Y^{III}(OAr)_3 \xrightarrow[\text{Ar, crypt}]{\text{THF, } -30\ ^\circ\text{C}} Y^{III}(NR_2)_3 + [Y^{II}(OAr)_3]^{1-} + \text{other EPR-active species} \quad (19.5)$$

$$[Y^{II}(OAr)_3]^{1-} + Y^{III}(NR_2)_3 \xrightarrow[\text{Ar, crypt}]{\text{THF, } -30\ ^\circ\text{C}} [Y^{II}(NR_2)_3]^{1-} + Y^{III}(OAr)_3 \quad (20.5)$$

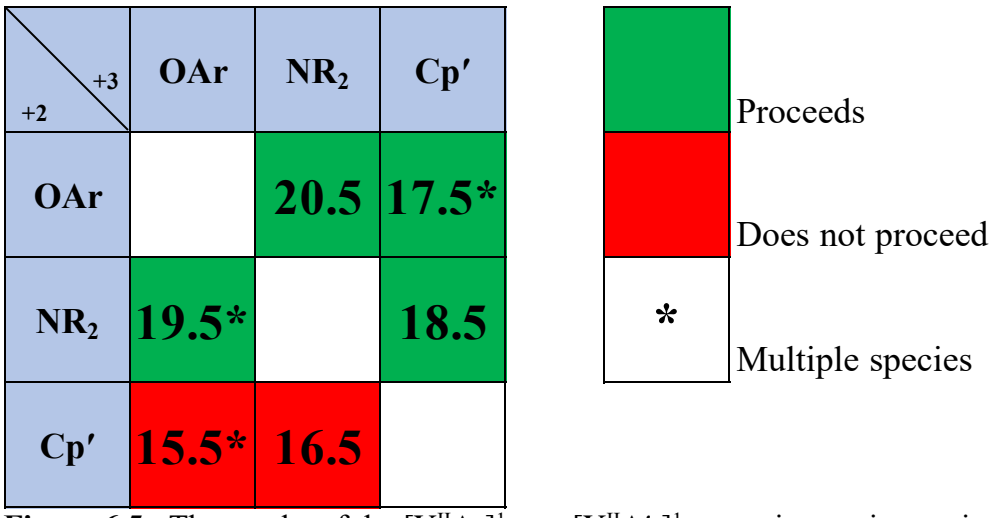

Figure 6.5. The results of the $[Y^{II}A_3]^{1-}$ vs. $[Y^{II}A'_3]^{1-}$ experiments in matrix form. The rows are labeled with the ligand used in the reductant species and the columns with the metal used in the substrate species. The numbers in the blocks represent the number of the corresponding reaction.

$[Y^{II}Cp'_3]^{1-}$ is the weakest reductant of the compounds studied with yttrium, as it cannot reduce any of the other Y(III) compounds, reactions 15.5–16.5. Consistent with this, $Y^{III}Cp'_3$ can be reduced by all of the other Y(II) species, reactions 17.5–18.5. $[Y^{II}(NR_2)_3]^{1-}$ reduces $Y^{III}(OAr)_3$ to $[Y^{II}(OAr)_3]^{1-}$, reaction 19.5, but the reverse reaction occurs as well, reaction 20.5. Therefore, the ordering of ligand sets, in terms of the reducing ability they confer on Y(II) compounds, is $(OAr)_3 \approx (NR_2)_3 > (Cp')_3$. Some of these reactions led to additional EPR signals that cannot be attributed to known Y(II) compounds. For example, the room-temperature EPR spectrum of reaction 15.5 (Figure 7.5) contains a variety of signals attributable to Y(II) complexes (by their doublet pattern), but none that can be assigned to known Y(II) compounds (the large central single line at g = 2.00 probably arises from electride[14,19,20] in the sample). The appearance of multiple Ln(II) species is observed in experiments with other metals (*vide infra*) and it will be described in more detail in those sections.

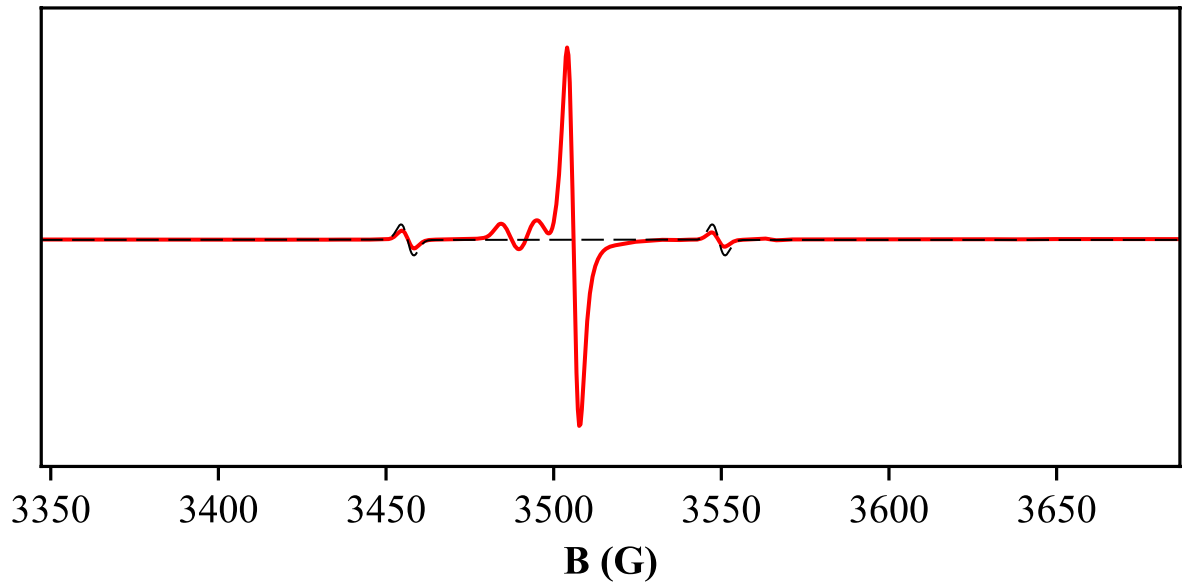

Figure 7.5. Room-temperature X-band EPR spectrum (red) and simulated spectrum (black dashes) of the products of reaction 15.5. Signals are present at ~3500 G (g = 2.00, likely electride) and g = 2.00, A = 92.8 G (the highest A value that could be simulated for this data, an unknown Y(II) species).

Comparison of different ligands on the same metal was also examined with the Sc(II) complexes $[Sc^{II}(NR_2)_3]^{1-}$ (A = 214 G) and $[Sc^{II}(OAr')_3]^{1-}$ (OAr′ = 2,6-^{t}Bu-4-Me-C_6H_2O, A = 291 G).[6,13] The Sc(II) amide and aryloxide mutually reduce one another, *i.e.,* $[Sc^{II}(NR_2)_3]^{1-}$ reduces $Sc^{II}(OAr')_3$ and $[Sc^{II}(OAr')_3]^{1-}$ reduces $Sc^{II}(NR_2)_3$, reaction 21.5. A similar situation was observed with yttrium and the these ligand sets.

$$\mathbf{[Sc^{II}(OAr')_3]^{1-} + Sc^{III}(NR_2)_3 \underset{\text{Ar, crypt}}{\overset{\text{THF, } -30\ ^\circ\text{C}}{\rightleftharpoons}} [Sc^{II}(NR_2)_3]^{1-} + Sc^{III}(OAr')_3} \qquad \mathbf{(21.5)}$$

La(II) compounds were also investigated with different ligands since several options are known: $[La^{II}Cp''_3]^{1-}$ (A = 133.5 G, Cp″ = $C_5H_3(SiMe_3)_2$),[1] $[La^{II}Cp'_3]^{1-}$ (A = 154 G),[4] and $[La^{II}Cp^{tet}_3]^{1-}$ (Cp^{tet} = C_5Me_4H, A = 291 G).[14] $[La^{II}Cp^{tet}_3]^{1-}$ can reduce $La^{III}Cp'_3(THF)$ (reaction 22.5) and $La^{III}Cp''_3$ (reaction 24.5) to their respective La(II) compounds. While $[La^{II}Cp'_3]^{1-}$ can do

the reverse reaction and reduce $La^{III}Cp^{tet}_3$ (reaction 23.5), $[La^{II}Cp''_3]^{1-}$ cannot reduce either $La^{III}Cp^{tet}_3$ or $La^{III}Cp'_3(THF)$. $[La^{II}Cp'_3]^{1-}$ can reduce $La^{III}Cp''_3$ (reaction 25.5) but $[La^{II}Cp''_3]^{1-}$ cannot reduce $La^{III}Cp'_3(THF)$ (reaction 26.5), making $[La^{II}Cp''_3]^{1-}$ a weaker reductant than $[La^{II}Cp'_3]^{1-}$ and $[La^{II}Cp^{tet}_3]^{1-}$. Thus, the ordering of reducing strength for ligand sets for La(II), in order from most reducing to least reducing is $(Cp^{tet})_3 \approx (Cp')_3 > (Cp'')_3$.

$$\mathbf{[La^{II}Cp^{tet}_3]^{1-} + La^{III}Cp'_3(THF) \xrightarrow[Ar,\ crypt]{THF,\ -30\ °C} La^{III}Cp^{tet}_3 + [La^{II}Cp'_3]^{1-} + La\text{-}A + La\text{-}B} \quad \mathbf{(22.5)}$$

$$\mathbf{[La^{II}Cp'_3]^{1-} + La^{III}Cp^{tet}_3 \xrightarrow[Ar,\ crypt]{THF,\ -30\ °C} La^{III}Cp'_3(THF) + [La^{II}Cp^{tet}_3]^{1-} + La\text{-}A + La\text{-}B} \quad \mathbf{(23.5)}$$

$$\mathbf{[La^{II}Cp^{tet}_3]^{1-} + La^{III}Cp''_3 \xrightarrow[Ar,\ crypt]{THF,\ -30\ °C} La^{III}Cp^{tet}_3 + [La^{II}Cp''_3]^{1-} + other\ La(II)\ species} \quad \mathbf{(24.5)}$$

$$\mathbf{[La^{II}Cp'_3]^{1-} + La^{III}Cp''_3 \xrightarrow[Ar,\ crypt]{THF,\ -30\ °C} La^{III}Cp'_3(THF) + [La^{II}Cp''_3]^{1-} + La\text{-}C + La\text{-}D} \quad \mathbf{(25.5)}$$

$$\mathbf{[La^{II}Cp''_3]^{1-} + La^{III}Cp'_3(THF) \xrightarrow[Ar,\ crypt]{THF,\ -30\ °C} [La^{II}Cp''_3]^{1-} + La\text{-}C + La\text{-}D} \quad \mathbf{(26.5)}$$

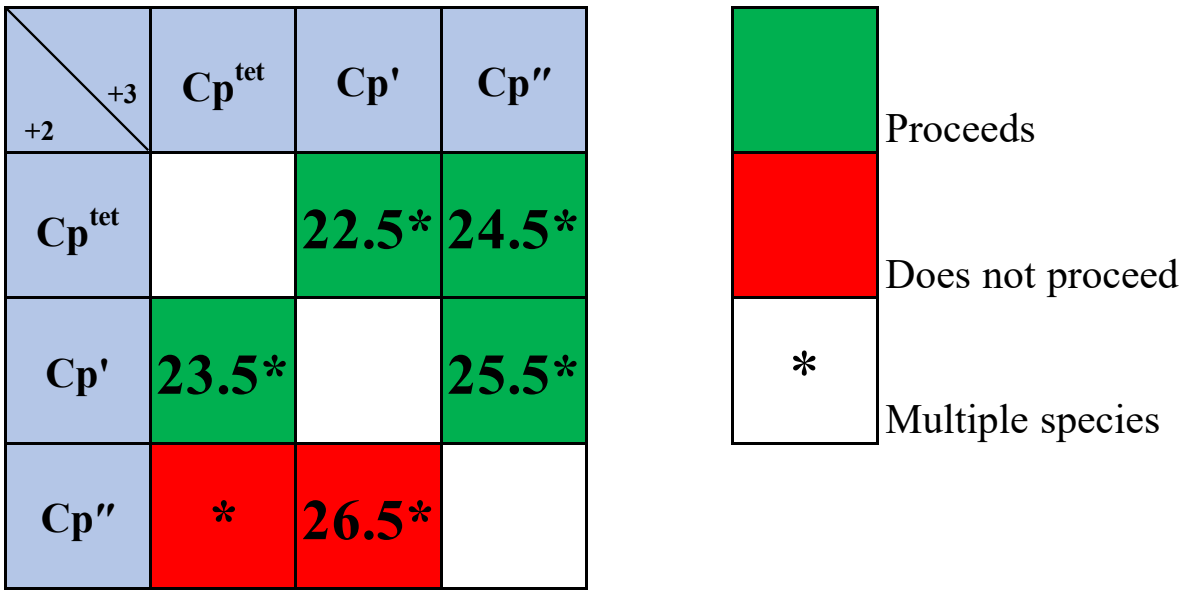

Figure 8.5. The results of the $[La^{II}A_3]^{1-}$ vs. $[La^{II}A'_3]^{1-}$ experiments in matrix form. The rows are labeled with the ligand used in the reductant species and the columns with the metal used in the substrate species. The numbers in the blocks represent the number of the corresponding reaction.

In every reaction above with lanthanum, multiple species are present. This was previously observed with reactions of yttrium complexes (*vide supra*), but this is not the case for scandium. No unidentified EPR signals are found in the Sc spectra. The EPR spectrum of reaction 22.5 contains signals for $[La^{II}Cp'_3]^{1-}$ (g = 1.97, A = 153.5 G) and two other unknown La(II) species labelled **La-A** with g_A= 1.96, A_A = 186.5 G and **La-B** with g_B = 1.96, A_B = 229.8 G (Figure 9.5) and assigned as La(II) complexes owing to the eight-line patterns.

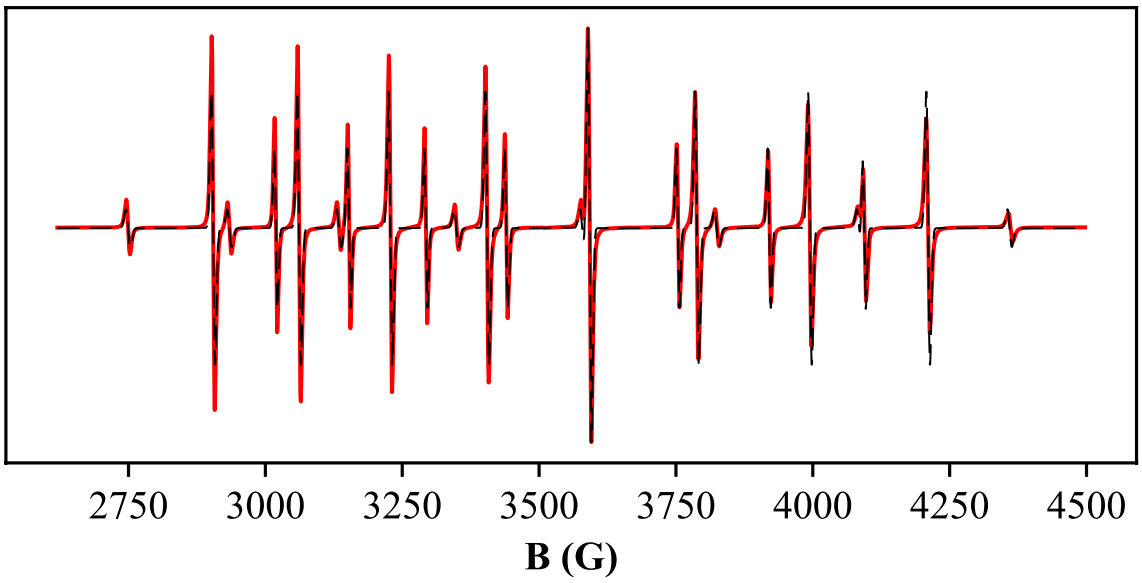

Figure 9.5. Room-temperature X-band EPR spectrum (red) and simulated spectrum (black dashes) of the products of reaction 22.5. Signals are present at g = 1.97, A = 153.4 G ($[La^{II}Cp'_3]^{1-}$), g_A = 1.96, A_A = 186.5 G (**La-A**) and g_B = 1.96, A_B = 229.8 G (**La-B**).

The EPR spectrum of the reverse of reaction 22.5, reaction 23.5, contains signals for $[La^{II}Cp'_3]^{1-}$ (g = 1.97, A = 153.7 G), $[La^{II}Cp^{tet}_3]^{1-}$ (g = 1.95, A = 290.7 G), and **La-A** and **La-B** (Figure 10.5). The detection of multiple unknown La(II) species is also seen in the pair of reactions 25.5 and 26.5. Reaction 25.5, which proceeds as written, contains signals for its target compound $[La^{II}Cp''_3]^{1-}$ (g = 1.96, A = 133.6 G) as well as two unknown La(II) species labelled **La-C** with g_C = 1.96, A_C = 144.8 G and **La-D** with g_D = 1.96, A_D = 150.0 G. Reaction 26.5, while not producing its target compound $[La^{II}Cp'_3]^{1-}$, contains the same two unknown La(II) species as reaction 25.5, *i.e.*, **La-C** and **La-D**. EPR parameters from these reactions are tabulated in Table 1.5. The La(II) species observed here with A values differing from known compounds could be heteroleptic La(II) compounds formed by ligand exchange in the course of the experiment. Support for this assessment comes from the EPR spectrum of $[Y^{II}Cp''_2Cp]^{1-}$ (g = 1.99, A = 34.6 G), which differs from both that of "$[Y^{II}Cp''_3]^{1-}$" (g = 1.99, A = 36.1 G) and "$[Y^{II}Cp_3]^{1-}$" (g = 1.99 A = 42.8 G).[28]

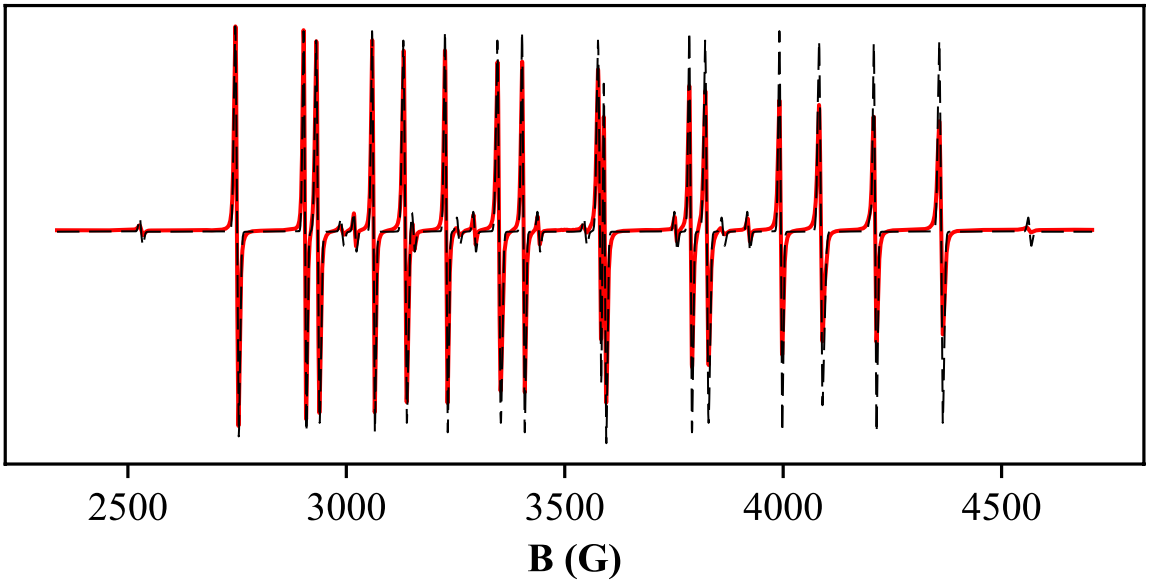

Figure 10.5. Room-temperature X-band EPR spectrum (red) and simulated spectrum (black dashes) of the products of reaction 23.5. Signals are present at $g = 1.97$, $A = 153.4$ G ($[La^{II}Cp'_3]^{1-}$), $g_A = 1.96$, $A_A = 186.3$ G (**La-A**), $g_B = 1.96$, $A_B = 230.0$ G (**La-B**), and $g = 1.96$, $A = 290.1$ G ($[La^{II}Cp^{tet}_3]^{1-}$).

$[La^{II}Cp''_3]^{1-}$ + KA (A = anionic ligand): Ligand Exchange Reactions. To investigate whether ligand exchange could be the cause of these extra signals, reactions of $[La^{II}Cp''_3]^{1-}$ with potassium salts of Cp′ and OMe were examined. Experiments were carried out with La(II) since its eight-line patterns are easier to simulate and are less prone to be obfuscated by other signals, as is the case with the two-line patterns of Y(II). $[La^{II}Cp''_3]^{1-}$ was treated with KCp′ to determine if this would lead to ligand exchange with the La(II) complex, reaction 27.5. The EPR spectrum of the product mixture contains four La(II)

$$[La^{II}Cp''_3]^{1-} + 3\ KCp' \xrightarrow[\text{Ar, crypt}]{\text{THF, } -30\ ^\circ\text{C}} [La^{II}Cp''_3]^{1-} + [La^{II}Cp'_3]^{1-} + \text{La-C} + \text{La-D} \qquad (27.5)$$

signals: those of the known $[La^{II}Cp'_3]^{1-}$ (g = 1.97, A = 153.4 G) and $[Cp''_3La^{II}]^{1-}$ (g =1.97, A = 134 G) as well as **La-C** and **La-D** (with g_C = 1.97, A_C = 144.6 G and g_D = 1.97, A_D = 149.7 G, respectively, Figure 11.5) from reactions 25.5 and 26.5. This results supports the hypothesis that these extra species observed in the EPR spectra are the result of ligand exchange. Hence, both alkali metal salts (reaction 27.5) and La(III) compounds (reactions 25.5 and 26.5) can act as Cp′ ligand transfer agents. Furthermore, if all of the EPR-detectable La(II) compounds in the reaction of reaction 27.5 are assumed to be tris(cyclopentadienyl) compounds (*N.B.* this is not true by necessity, as [K(crypt)][$La^{III}Cp'_4$] is known),[29] there is a maximum of four unique species, corresponding with the number of species seen in reaction 27.5: $[La^{II}Cp''_3]^{1-}$, $[La^{II}Cp''_2Cp']^{1-}$, $[La^{II}Cp''Cp'_2]^{1-}$, and $[La^{II}Cp'_3]^{1-}$. The results of reactions 22.5, 23.5, and 25.5–27.5 are tabulated in Table 1.5.

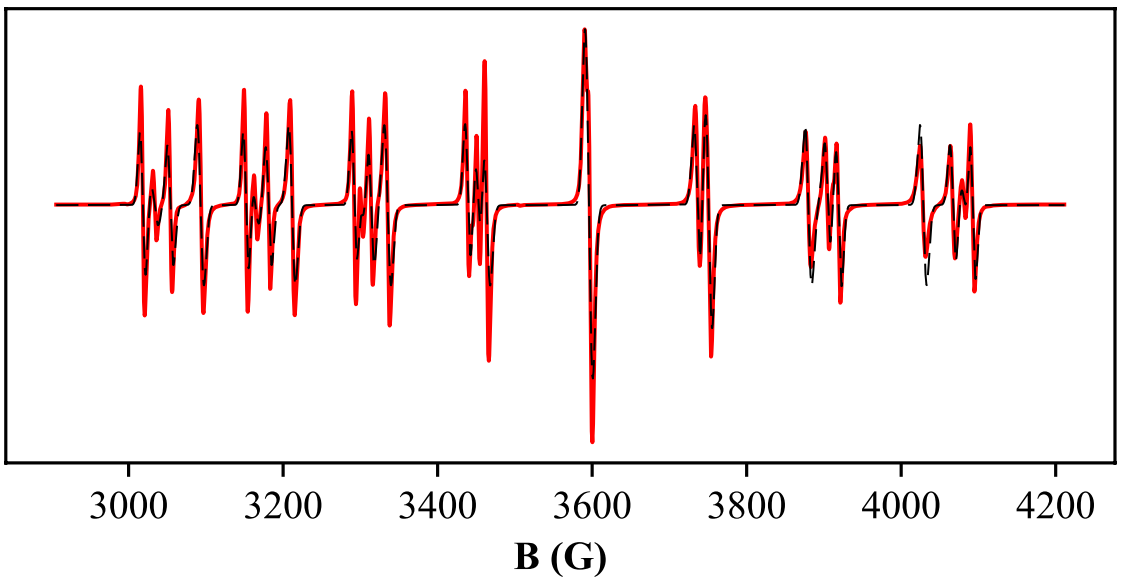

Figure 11.5. Room-temperature X-band EPR spectrum (red) and simulated spectrum (black dashes) of the products of reaction 27.5. Signals are present at g = 1.97, A = 133.6 G ($[La^{II}Cp''_3]^{1-}$), g_C = 1.97, A_C = 144.6 G (**La-C**) and g_D = 1.97, A_D = 149.7 G (**La-D**), and g = 1.97, A = 153.4 G ($[La^{II}Cp'_3]^{1-}$).

Since the signals for the putative heteroleptic La(II) compounds occur also in reactions 25.5 and 26.5, ligand exchange experiments between $La^{III}Cp''_3$ and $La^{III}Cp'_3(THF)$ were carried out in THF-d_8 and C_6D_6 to investigate by NMR whether ligand exchange occurs in the La(III) state. By NMR, new Cp″ and Cp′ environments were observed at room temperature (in the THF-d_8 experiment, one new environment each for Cp″ and Cp′; in the C_6D_6 experiment, two new environments each for Cp″ and Cp′) that were distinct from $La^{III}Cp''_3$, $La^{III}Cp'_3(THF)$, KCp″, and KCp′ (Spectroscopic Appendix, Figures 51.5 and 50.5, respectively). When the solution in THF-d_8 was reduced using KC_8 both in the presence and absence of crypt, **La-C** and **La-D** were observed.

Table 1.5. List of simulated room-temperature X-band EPR parameters of reactions of La complexes. Assignments were made based on published EPR parameters.[1,4,14] Spectra were simulated using EasySpin.[22] Values are the *A* value in Gauss, followed by the *g* value in parenthesis.

Reaction	22.5	23.5	25.5	26.5	27.5	Assignment
			133.6 (1.96)	133.7 (1.96)	133.6 (1.97)	$[La^{II}Cp''_3]^{1-}$
			144.8 (1.96)	144.8 (1.96)	144.6(1.97)	**La-C**
			150.0 (1.96)	149.6 (1.97)	149.7 (1.97)	**La-D**
	153.4 (1.97)	153.4 (1.97)			153.4 (1.97)	$[La^{II}Cp'_3]^{1-}$
	186.5 (1.96)	186.3 (1.96)				**La-A**
	229.8 (1.96)	230.0 (1.96)				**La-B**
		290.0 (1.96)				$[La^{II}Cp^{tet}_3]^{1-}$

Early attempts to synthesize $[La^{II}Cp''_3]^{1-}$ by reduction of $La^{II}Cp''_3$ in DME (DME = dimethoxyethane) led to the isolation of $[La^{III}Cp''_2(\mu\text{-OMe})]_2$ *via* cleavage of OMe groups from the DME presumably by $[La^{II}Cp''_3]^{1-}$.[30] The reported EPR spectrum of a DME solution of $[La^{II}Cp''_3]^{1-}$ at 295 K shows multiple species: one that was assigned to $[La^{II}Cp''_3]^{1-}$ (g = 1.97, A = 134.1 G) which was eventually isolated,[1] and another, that was suggested to arise from $La^{II}Cp''_2(DME)_x$ (g = 1.97, A = 145.1 G). This second species was never crystallographically authenticated. It seems possible that the second EPR signal could arise from a heteroleptic "$[La^{II}Cp''_2OMe]^{1-}$" complex formed by reduction of the $[La^{III}Cp''_2(\mu\text{-OMe})]_2$ decomposition

product formed in this reaction. The reaction of KOMe with $[La^{II}Cp''_3]^{1-}$ was examined to determine such a complex could be accessed by ligand exchange.

$$[La^{II}Cp''_3]^{1-} + 3\ KOMe \xrightarrow[Ar,\ crypt]{THF,\ -30\ °C} [La^{II}Cp''_3]^{1-} + \text{other La(II) species} \qquad (28.5)$$

The EPR spectrum of reaction 28.5 indicates the presence of two La(II) species: one assignable to $[La^{II}Cp''_3]^{1-}$ (g = 1.97, A = 133.6 G) and another species that is a near match for the second species seen in the spectrum of $[La^{II}Cp''_3]^{1-}$ in DME (g = 1.96, A = 144.8 G).

$[Ln^{II}A_3]^{1-}$ vs. Traditional Ln(II) Compounds. The reducing capacity of the traditional Ln(II) ions, Sm(II), Tm(II), Dy(II), and Nd(II), to make the new Ln(II) ions of La and Y was also investigated. This offered a chance to bracket the electrochemical potentials more precisely since a few complexes of the traditional ions already have been electrochemically characterized.[31,32] Reactions between the Sm(II) compounds $Sm^{II}I_2(THF)_5$,[33] $Sm^{II}(C_5Me_5)_2(THF)_2$,[34] $Sm^{II}(C_5Me_5)_2$,[35] and $Sm^{II}Cp''_2(THF)$[36] and the trivalent lanthanide complexes, $La^{III}Cp''_3$ and $Y^{III}Cp'_3$, did not yield any La(II) or Y(II) products. Hence, Sm(II) is less reducing than any of the new La(II) or Y(II). Eu(II) and Yb(II) complexes were not investigated, as they are known to be weaker reductants than Sm(II).[7] $TmI_2(DME)_3$,[37] DyI_2, and NdI_2[21] also failed to reduce either $La^{III}Cp''_3$ or $Y^{III}Cp'_3$ to La(II) and Y(II) products at −35 °C in THF.

DISCUSSION

Since the redox couple for $[La^{III/II}Cp''_3]^{0/1-}$ has been measured at −2.8 V (vs. Fc^+/Fc, THF, 0.2 M $[NBu_4][PF_6]$),[30] it is possible to rank other complexes' reduction potentials relative to this couple using the results of this study. $[La^{II}Cp^{tet}_3]^{1-}$ and $[La^{II}Cp'_3]^{1-}$ are stronger reductants than $[La^{II}Cp''_3]^{1-}$, so the reduction potentials of their corresponding La(III) complexes are more negative than −2.8 V. Since the potentials of $[Ln^{II}Cp'_3]^{1-}$ (Ln = Y, Lu) are similar to that of $[La^{II}Cp'_3]^{1-}$, the corresponding Ln(III) complexes can also be estimated to have reduction

potentials more negative than −2.8 V. Since $[Y^{II}(NR_2)_3]^{1-}$ and $[Y^{II}(OAr)_3]^{1-}$ are stronger reductants than $[Y^{II}Cp'_3]^{1-}$, the amide and aryloxide compounds also have reduction potentials more negative than −2.8 V.

The finding that $[La^{II}Cp''_3]^{1-}$ is the weakest reductant studied here may explain the fact that the reduction of $La^{III}Cp''_3$ can be carried out under N_2 without formation of an $(N_2)^{2-}$ complex.[2] In contrast, reductions of $La^{III}(Cp^{tet})_3$ and $La^{III}(C_5Me_5)_2(BPh_4)$ complexes under N_2 all form reduced dinitrogen complexes containing $[La^{III}_2(\mu\text{-}\eta^2\text{:}\eta^2\text{-}N_2)]^{4+}$ moieties.[38] It may be that La(II) complexes of Cp″ do not have a enough reducing capacity to activate N_2 in this fashion. If true, this demonstrate that ligand choice for Ln(II) complexes is an important parameter in determining small-molecule activation chemistry.

This study shows that NR_2 and OAr ligands give complexes that are stronger reductants than Cp′ for Y and for La, the Cp″ ligand gives the weakest reductants. This roughly follows the hyperfine coupling contact values observed in the EPR spectra of the $[Y^{II}A_3]^{1-}$ complexes, i.e. A = OAr (156 G) and NR_2 (110 G) have the highest *A* values and for the $[La^{II}A_3]^{1-}$ complexes, A = Cp^{tet} (291 G) has the highest *A* value and Cp″ (133 G) has the lowest. Interestingly, this study shows that the relative reducing capacity of one metal versus another depends on the ligand. For example, Y(II) is more reducing than Gd(II) with Cp′ ligands and the reverse is true with NR_2 ligands. This also may explain why, as above, no complexes with the $[La^{III}_2(\mu\text{-}\eta^2\text{:}\eta^2\text{-}N_2)]^{4+}$ are known with Cp″, but for Dy, the complex $(Cp''_2Dy^{III})_2(\mu\text{-}\eta^2\text{:}\eta^2\text{-}N_2)$ is known;[39] it may be that Cp″ confers greater reducing ability on Dy than La.

The results of reactions 25.5, 26.5, and 27.5 suggest that heteroleptic La(II) compounds can be formed by using La(III) or alkali metal compounds as ligand transfer agents. Since reaction

27.5 starts from a homoleptic La(II) compound, $[La^{II}Cp''_3]^{1-}$, there are several possibilities for how the ligand exchange occurs.

One possibility is that $[La^{II}Cp''_3]^{1-}$ exchanges Cp″ with Cp′ (from KCp′) in the La(II) state, eq 29.5 . Since the X-ray crystal structure of (18-crown-6)K(Cp′)$Y^{II}Cp'_2$ has the potassium ion oriented toward two carbon atoms of a Cp′ ring at K–C distances of 3.079(2) Å and 3.055(2) Å ,[2] this mechanism is not unreasonable. The structure of this compound could be considered as the model of the transition state of a Ln(II) ion exchanging ligands with a potassium salt. This motif of alkali metals interacting with *f*-element-bound cyclopentadienyls is also seen in the U(II) compound $[(THF)_2Cs(\mu\text{-}\eta^5\text{:}\eta^5\text{-}Cp'')_2U^{II}Cp'']_n$.[40]

$$\mathbf{[La^{II}Cp''_3]^{1-} + KCp' \longrightarrow [La^{II}Cp''_2Cp']^{1-} + KCp''} \qquad \mathbf{(29.5)}$$

$$\mathbf{[La^{II}Cp''_3]^{1-} \xrightarrow{-\,e^-} La^{III}Cp''_3 + KCp' \longrightarrow La^{III}Cp''_2Cp' + KCp''} \qquad \mathbf{(30.5)}$$

$$\mathbf{[La^{II}Cp''_3]^{1-} + La^{III}Cp''_2Cp' \longrightarrow [La^{II}Cp''_2Cp']^{1-} + La^{III}Cp''_3} \qquad \mathbf{(31.5)}$$

Another possibility for ligand exchanges shown in eq 30.5 and 31.5 is that $La^{III}Cp''_3$ present (either through La(III) material that did not get reduced in its passage through the KC_8 column or reduction of other components in the solution) exchanges ligands in the La(III) state. Then the resulting heteroleptic La(III) compound is reduced by $[La^{II}Cp''_3]^{1-}$ to form a heteroleptic La(II) species. Since La(III) compounds can also be used as ligand transfer reagents, as seen by the NMR ligand exchange experiments between $La^{III}Cp''_3$ and $La^{III}Cp'_3(THF)$, it is possible the mechanism of generating the heteroleptic La(II) complexes differs from when potassium cyclopentadienyls are used. Processes like those seen in eq 30.5 and 31.5 are still possible, but it is also possible that the La(II) complexes exchange ligands with one another, eq 32.5.

$$[La^{II}Cp''_3]^{1-} + [La^{II}Cp'_3]^{1-} \longrightarrow [La^{II}Cp''_2Cp']^{1-} + [La^{II}Cp''Cp'_2]^{1-} \quad (32.5)$$

$$[La^{II}Cp''_3]^{1-} + La^{III}Cp'_3(THF) \longrightarrow La^{III}Cp''_2Cp' + [La^{II}Cp''Cp'_2]^{1-} \quad (33.5)$$

However, another mechanism (not possible when potassium cyclopentadienyls are used) is that electron transfer and ligand exchange occur in a concerted fashion, eq 33.5. This scenario is suggested by the structure of $(C_5Me_5)_2Sm^{III}(\mu\text{-}\eta^5\text{:}\eta^2\text{-}C_5H_5)Sm^{II}(C_5Me_5)_2$,[41] where a C_5H_5 ligand bridges Sm^{II} and Sm^{III} centers. This complex could serve as a model of a transition state in eq 33.5, where two Ln ions in different oxidation states are bridged by a cyclopentadienyl ligand, a possible step in the process of transferring both a cyclopentadienyl ligand and an electron . If this mechanism is in operation, then the electron transfer could be considered inner-sphere, as well as those for Y compounds where multiple species are seen, Figure 7.5, reaction 15.5. Ligand exchange from Ln cyclopentadienyls is perhaps easiest to imagine, with the coordination of alkali metals and other Ln on the "back side" of the cyclopentadienyl ring, but multiple species are observed in the EPR spectra of reactions of Y(II) compounds with monodentate ligands like NR_2 and OAr, reaction 19.5. These ligands are known to form bridging structures in their complexes,[42,43] so there still exists a pathway for them to experience inner-sphere electron transfer coupled with ligand exchange. Lastly, the findings from reaction 28.5 suggest that the first report of $[La^{II}Cp''_3]^{1-}$ also reported the first EPR spectrum of "$[La^{II}Cp''_2OMe]^{1-}$," since parameters observed in that report nearly match that seen in reaction 28.5. While "$[La^{II}Cp''_2OMe]^{1-}$" has not been crystallographically authenticated here, and the EPR *A* value is far from a unique identifier of a compound, this is a plausible explanation and speaks to the diversity of Ln(II) compounds possible in heteroleptic ligand environments, as well as the power of EPR to detect them.

CONCLUSIONS

Electron transfer and ligand exchange in Ln(II) compounds was observed using EPR spectroscopy. In compounds $[Ln^{II}Cp'_3]^{1-}$, the ordering of metals from most reducing to least reducing is Tb(II) ≫ Y(II) ≈ La(II) ≈ Lu(II) > Gd(II). In compounds $[Ln^{II}(NR_2)_3]^{1-}$, the order is Tb(II) ≈ Gd(II) ≫ Y(II) > Sc(II), with Gd(II) becoming a stronger reductant than Y(II) by a change of ligand set. When $[Ln^{II}A_3]^{1-}$ compounds are compared by changing the identity of A, no clear rule determines which ligand sets are more or less reducing, but a loose correlation between high A value in the EPR spectrum and strong reducing ability is noted. Extensive ligand exchange is seen alongside electron transfer in these experiments, and it is shown that compounds of La will exchange ligands in the +3 oxidation state, and possibly in the +2 oxidation state as well. Observation of these ligand exchange products in the EPR suggests that many heteroleptic Ln(II) compounds are possible and await synthetic discovery and further characterization. Sm(II), Tm(II), $Dy^{II}I_2$, and $Nd^{II}I_2$ are unable to form non-traditional Ln(II) compounds from their corresponding Ln(III) complexes.

EXPERIMENTAL

All manipulations and syntheses were conducted with the rigorous exclusion of air and water using standard Schlenk line and glovebox techniques under an argon atmosphere. Solvents were sparged with UHP argon and dried by passage through columns containing Q-5 and molecular sieves prior to use. ^{1}H and $^{13}C\{^{1}H\}$NMR spectra were recorded on a Bruker AVANCE600 spectrometer (^{1}H operating at 600 MHz, $^{13}C\{^{1}H\}$ at 151 MHz) at 298 K unless otherwise stated and referenced internally to residual protio-solvent resonances. EPR spectra were collected using X-band frequency (9.3−9.8 GHz) on a Bruker EMX spectrometer equipped with an ER4119HS-W1 microwave bridge and the magnetic field was calibrated with DPPH (g = 2.0036). UV−visible

spectra were collected in THF at room temperature in a 0.1 cm cell fitted with a Teflon stopcock using an Agilent Cary 60 UV-visible spectrophotometer. Compounds $Ln^{III}Cp'_3(THF)_x$ (Ln = Y,[2] La,[44] Gd,[4] Tb,[4] Lu;[44] x = 1 for Ln = La, x = 0 for Y, Gd, Tb, Lu), $Ln^{III}(NR_2)_3$ (Ln = Sc, Y, Gd, Tb)[45], $Y^{III}(OAr)_3$,[46] $Sc^{III}(OAr')_3$,[13] $La^{III}Cp^{tet}_3$,[47] $La^{III}Cp''_3$,[48] KCp′,[44] $Sm^{II}I_2(THF)_5$,[33] $Sm^{II}(C_5Me_5)_2(THF)_2$,[34] $Sm^{II}(C_5Me_5)_2$,[35] $Sm^{II}Cp''_2(THF)$[36], $Dy^{II}I_2$,[21] $Nd^{II}I_2$,[21] and KC_8[49] were synthesized by published preparations. KOMe was synthesized by reacting potassium metal with a THF solution of an excess MeOH (based on potassium) overnight, then removing solvent *in vacuo* and washing the resulting white solids with hexane and diethyl ether. EPR parameters for $[Ln^{II}Cp'_3]^{1-}$ (Ln = Y,[2] La, Gd,[4] Lu[4]), $[Ln^{II}(NR_2)_3]^{1-}$ (Ln = Sc,[6] Y[27]), $[Y^{II}(OAr)_3]^{1-}$,[13] $[Sc^{II}(OAr')_3]^{1-}$,[13] $[La^{II}Cp^{tet}_3]^{1-}$,[14] and $[La^{II}Cp''_3]^{1-1}$ were taken from literature reports. In the initial report of [K(crypt)][$La^{II}Cp''_3$], the EPR spectroscopic parameters are reported to be g = 1.990 and A = 133.5 G.[1] In all simulations in this work, reactions where $[La^{II}Cp''_3]^{1-}$ is present (either as a reactant or product), it is best modeled as having g = 1.96 and A = 133.5 G. All EPR parameters are taken from simulations of the room-temperature spectra using EasySpin.[22]

SPECTROSCOPIC APPENDIX

$[Ln^{II}Cp'_3]^{1-}$ Reactions with $Cp'_3Ln'^{III}$ Complexes

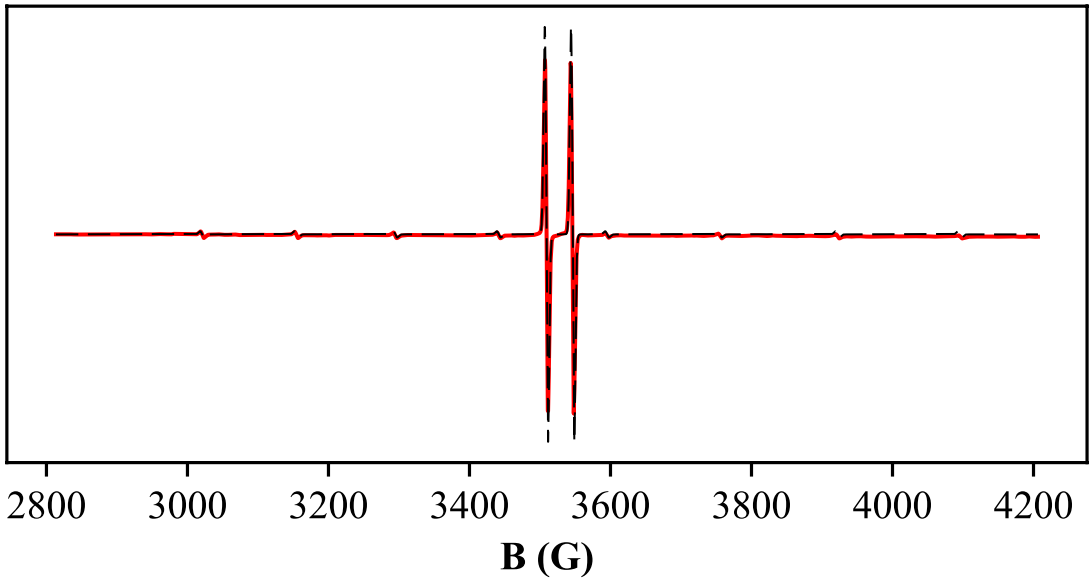

Figure 12.5. Room-temperature X-band EPR spectrum (red) and simulated spectrum (black dashes) of the products of reaction 2.5 in the forward direction. Signals are present at g = 1.99, A = 37.2 G ($[Y^{II}Cp'_3]^{1-}$) and g = 1.97, A = 153.5 G ($[La^{II}Cp'_3]^{1-}$).

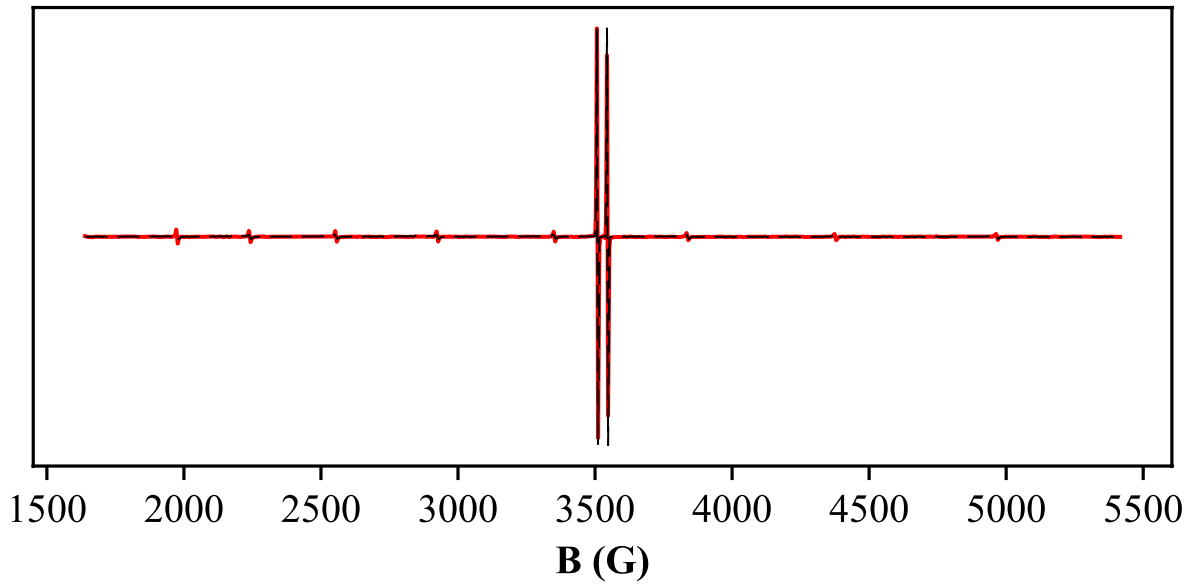

Figure 13.5. Room-temperature X-band EPR spectrum (red) and simulated spectrum (black dashes) of the products of reaction 3.5 in the reverse direction. Signals are present at g = 1.99, A = 36.8 G ($[Y^{II}Cp'_3]^{1-}$) and g = 1.97, A = 425.7 G ($[Lu^{II}Cp'_3]^{1-}$).

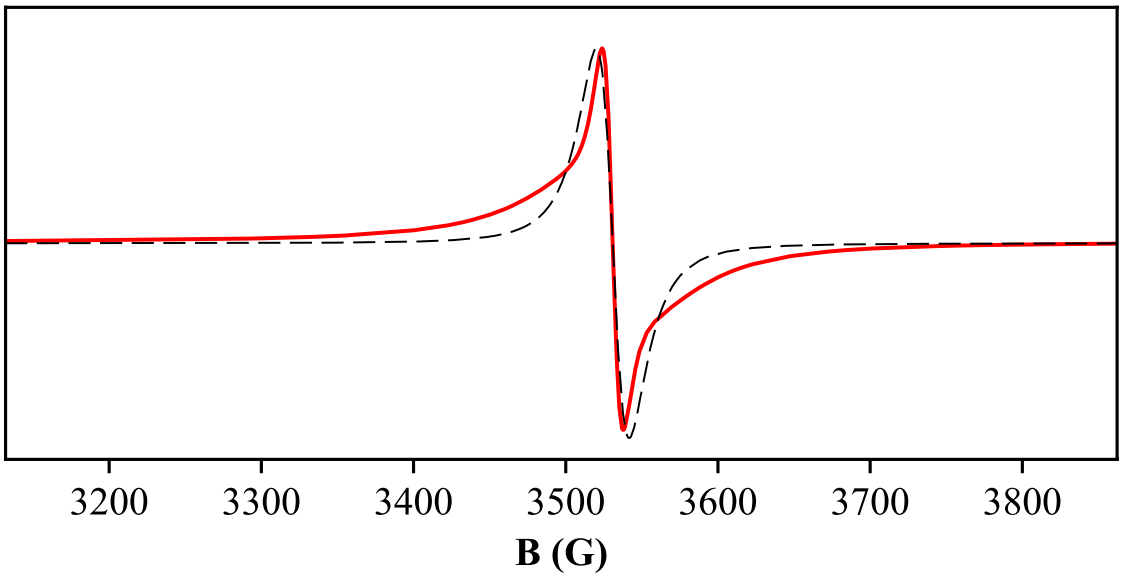

Figure 14.5. Room-temperature X-band EPR spectrum (red) and simulated spectrum (black dashes) of the products of reaction 5.5. Signal is present at g = 1.99 ($[Gd^{II}Cp'_3]^{1-}$).

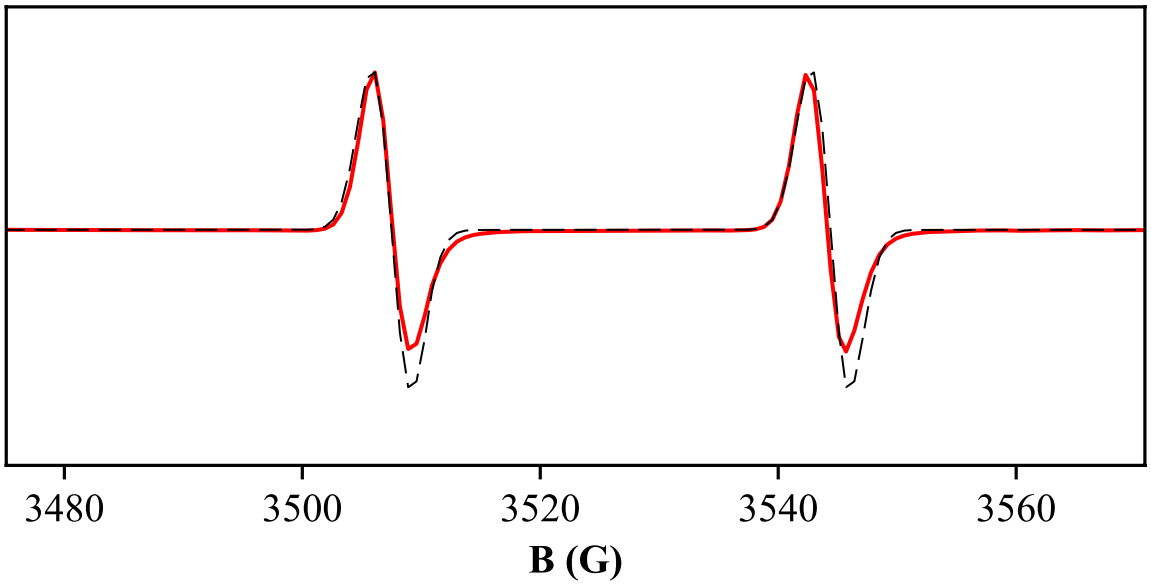

Figure 15.5. Room-temperature X-band EPR spectrum (red) and simulated spectrum (black dashes) of the products of reaction 2.5 in the reverse direction. Signal is present at g = 1.99, A = 37.3 G ($[Y^{II}Cp'_3]^{1-}$).

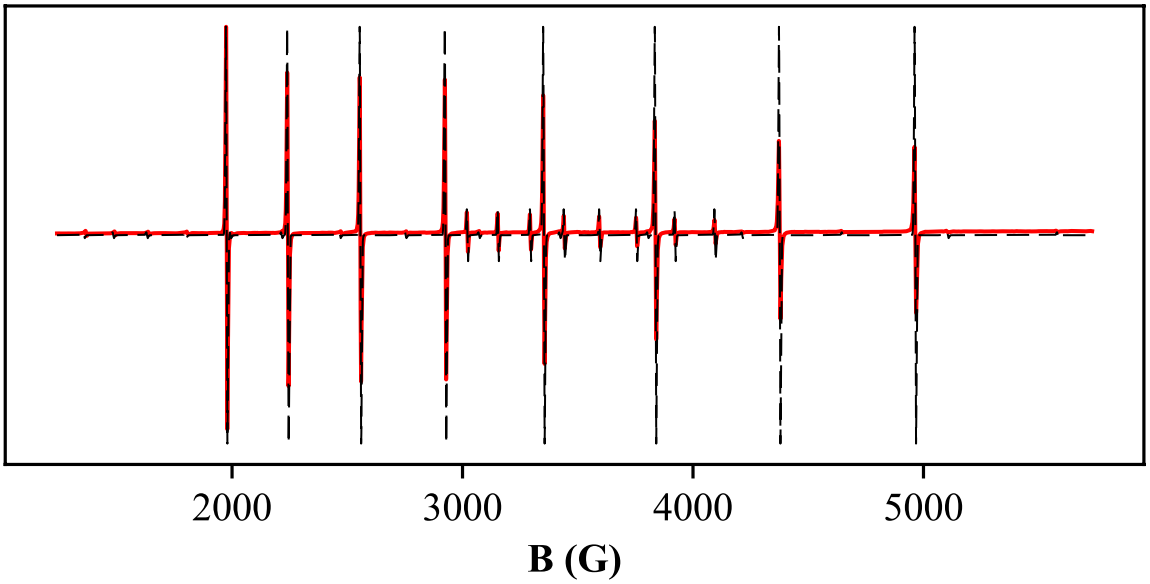

Figure 16.5. Room-temperature X-band EPR spectrum (red) and simulated spectrum (black dashes) of the products of reaction 4.5 in the reverse direction. Signals are present at $g = 1.97$, $A = 153.4$ G ($[La^{II}Cp'_3]^{1-}$) and $g = 1.97$, $A = 425.3$ G ($[Lu^{II}Cp'_3]^{1-}$).

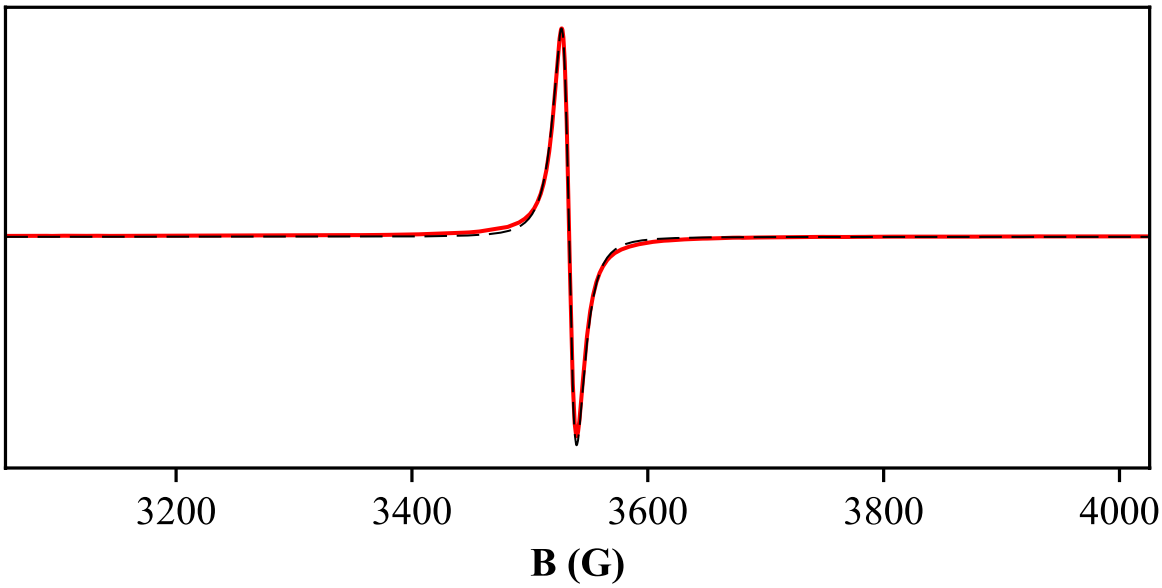

Figure 17.5. Room-temperature X-band EPR spectrum (red) and simulated spectrum (black dashes) of the products of reaction 6.5. Signal is present at $g = 1.99$ ($[Gd^{II}Cp'_3]^{1-}$).

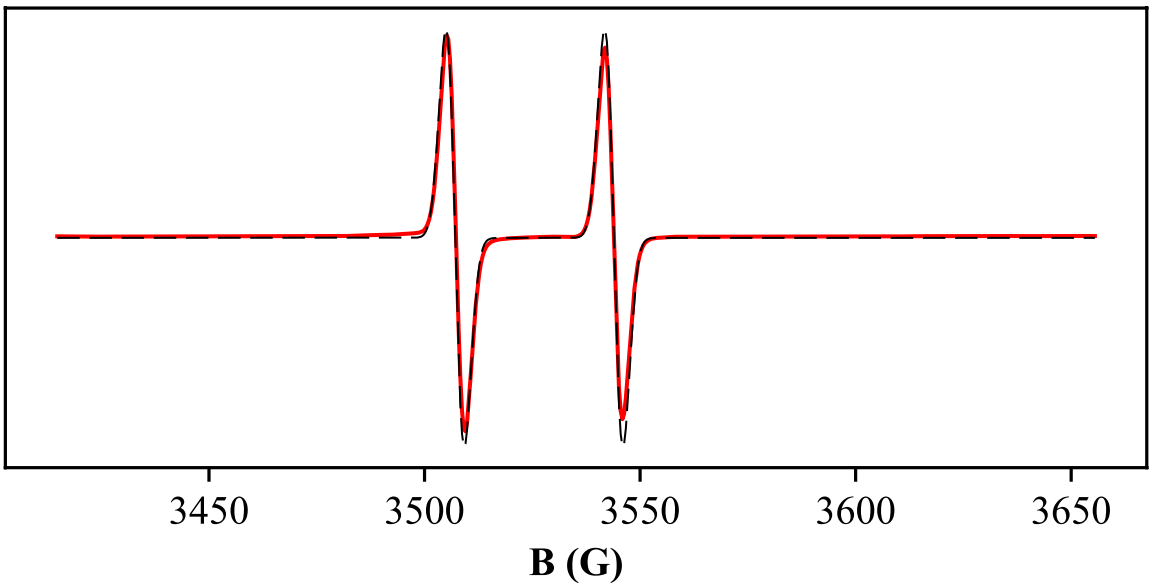

Figure 18.5. Room-temperature X-band EPR spectrum (red) and simulated spectrum (black dashes) of the products of reaction 3.5 in the forward direction. Signal is present at $g = 1.99$, $A = 37.1$ G ($[Y^{II}Cp'_3]^{1-}$).

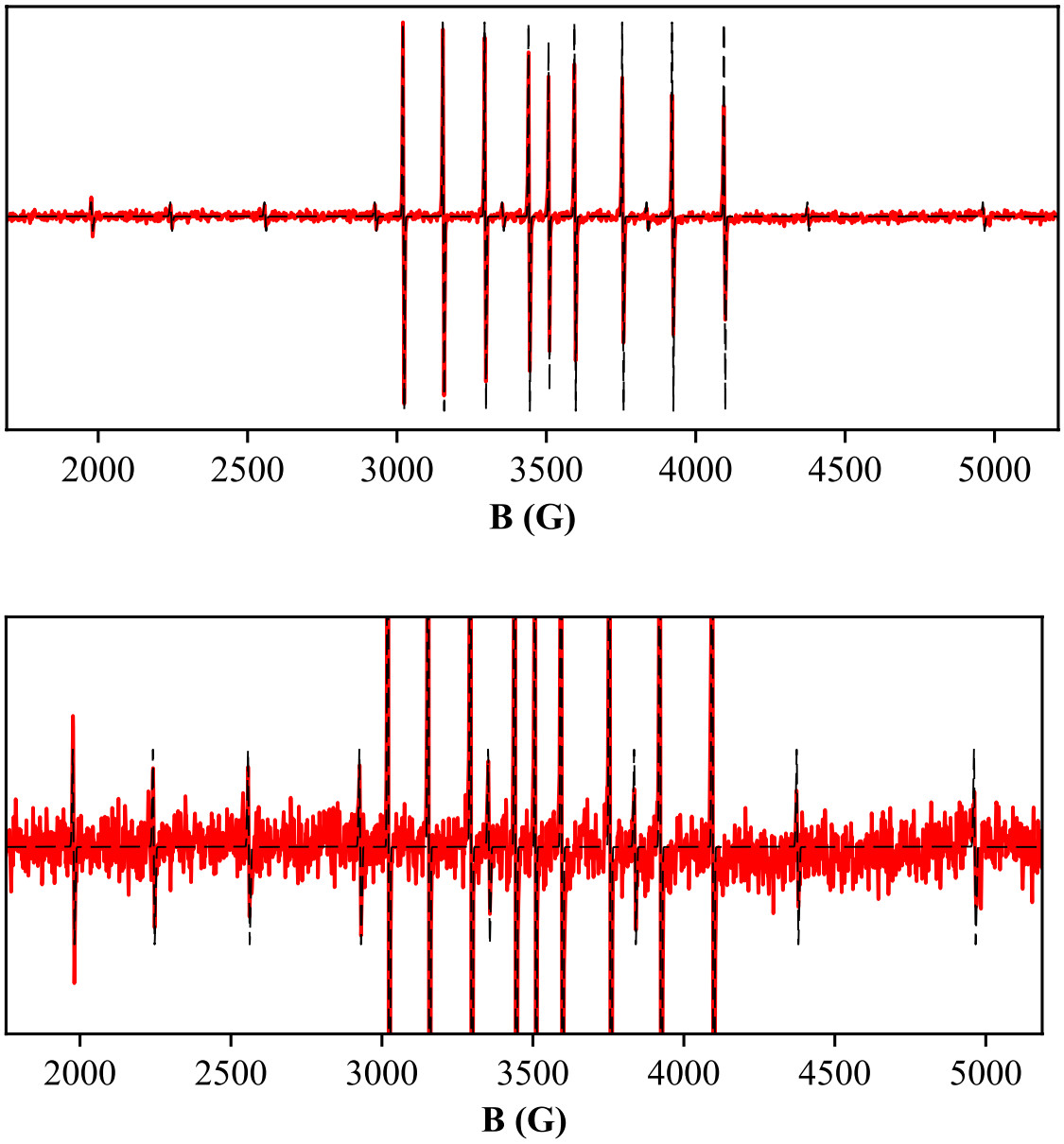

Figure 19.5. Room-temperature X-band EPR spectrum (red) and simulated spectrum (black dashes) of the products of reaction 4.5 in the forward direction. Signals are present at $g = 1.97$, $A = 153.5$G ($[La^{II}Cp'_3]^{1-}$) and $g = 1.97$, $A = 425.0$ G ($[Lu^{II}Cp'_3]^{1-}$). Top plot shows all signals, bottom plot is a scaled view of the weak signal from $[Lu^{II}Cp'_3]^{1-}$.

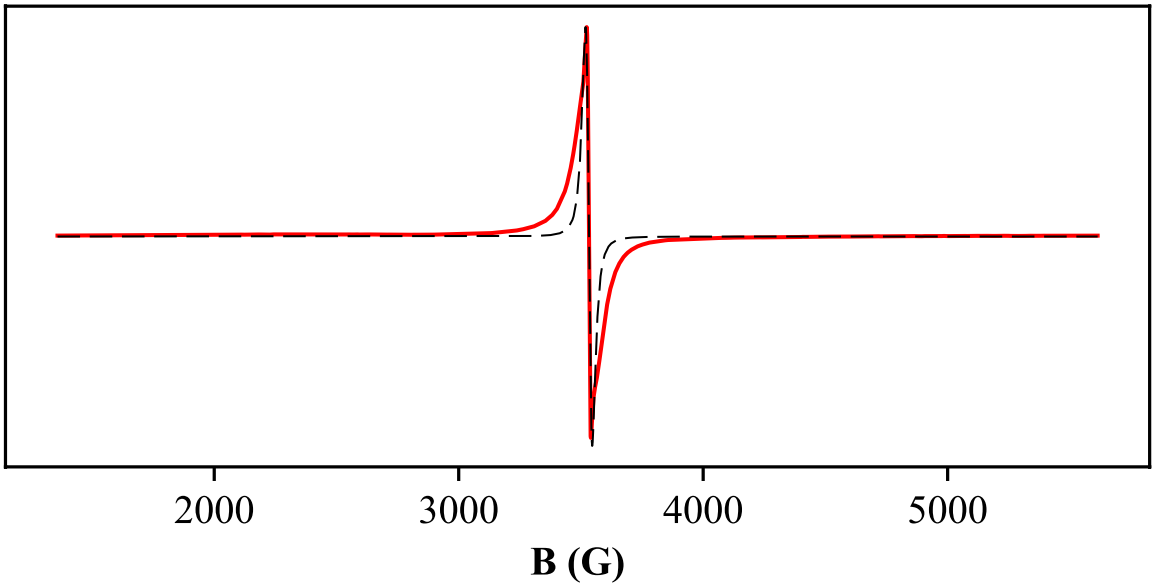

Figure 20.5. Room-temperature X-band EPR spectrum (red) and simulated spectrum (black dashes) of the products of reaction 7.5. Signal is present at $g = 1.99$ ($[Gd^{II}Cp'_3]^{1-}$).

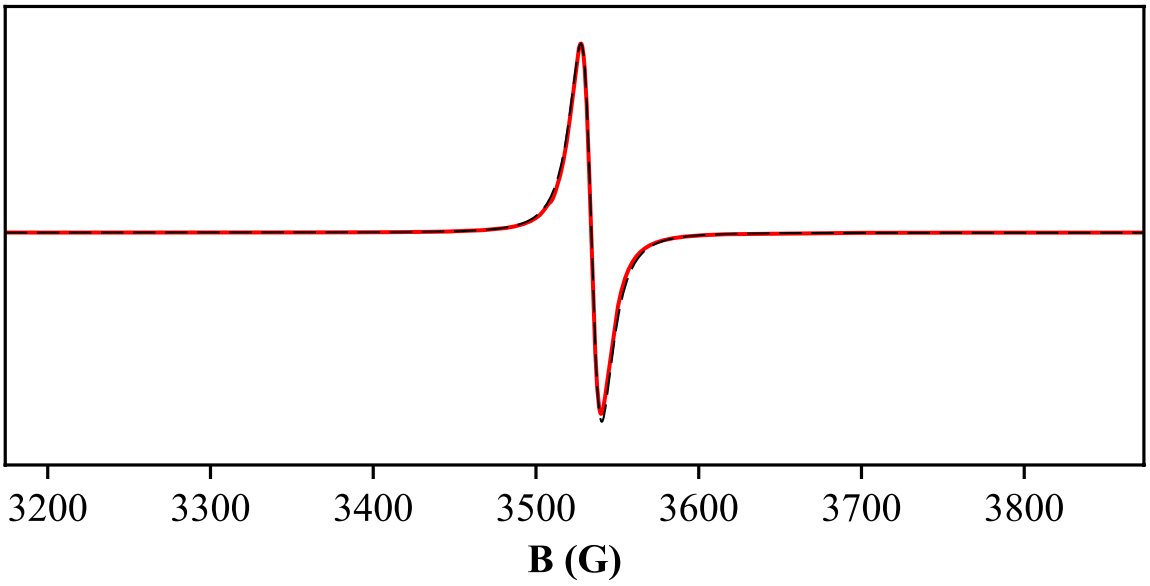

Figure 21.5. Room-temperature X-band EPR spectrum (red) and simulated spectrum (black dashes) of the products of reaction of $[Gd^{II}Cp'_3]^{1-}$ with $Y^{III}Cp'_3$. Signal is present at $g = 1.99$ ($[Gd^{II}Cp'_3]^{1-}$).

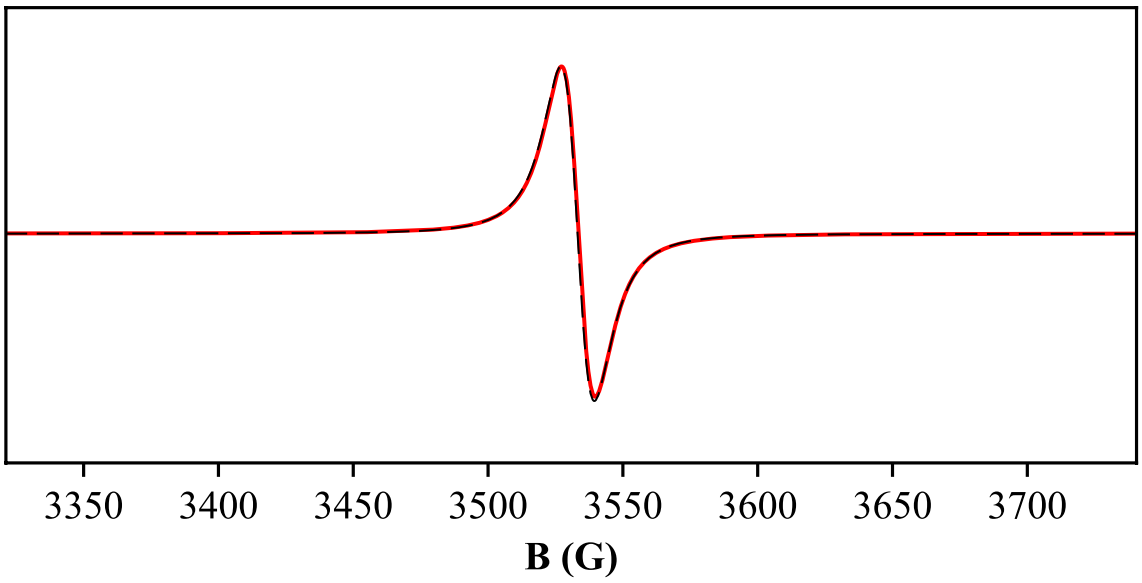

Figure 22.5. Room-temperature X-band EPR spectrum (red) and simulated spectrum (black dashes) of the products of reaction of $[Gd^{II}Cp'_3]^{1-}$ with $La^{III}Cp'_3(THF)$. Signals are present at g = 1.99 ($[Gd^{II}Cp'_3]^{1-}$).

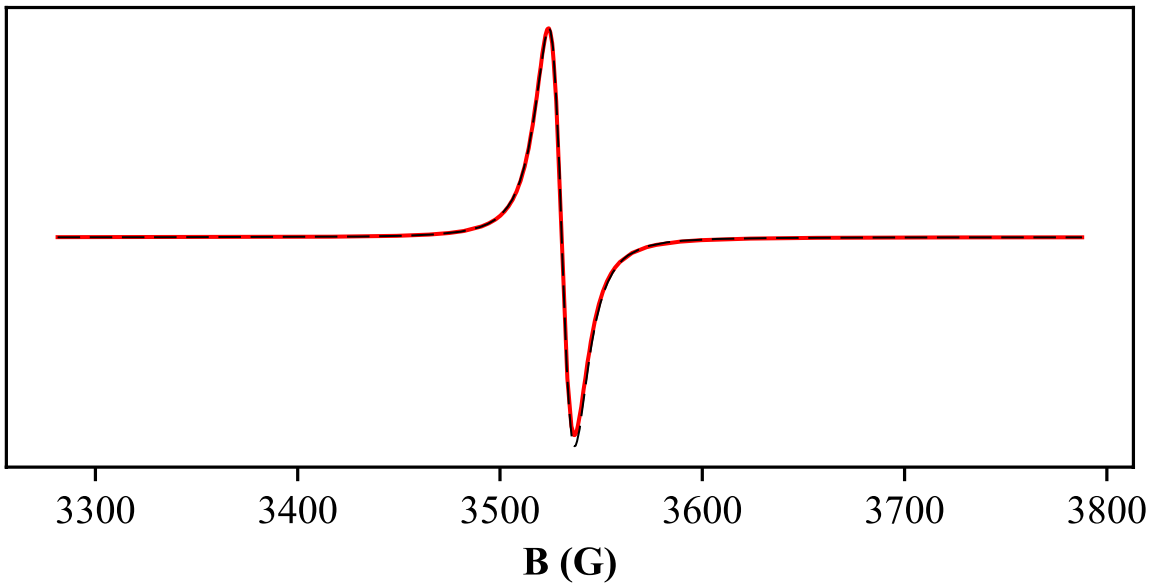

Figure 23.5. Room-temperature X-band EPR spectrum (red) and simulated spectrum (black dashes) of the products of reaction of $[Gd^{II}Cp'_3]^{1-}$ with $Lu^{III}Cp'_3$. Signals are present at g = 1.99 ($[Gd^{II}Cp'_3]^{1-}$).

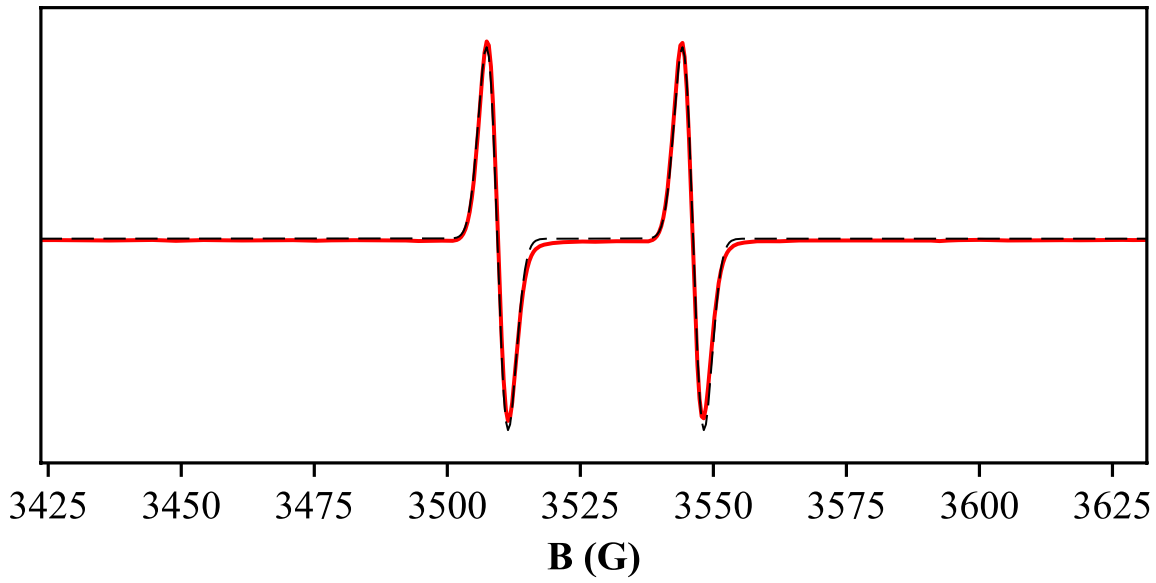

Figure 24.5. Room-temperature X-band EPR spectrum (red) and simulated spectrum (black dashes) of the products of reaction 8.5. Signal is present at $g = 1.99$, $A = 36.7$ G ($[Y^{II}Cp'_3]^{1-}$).

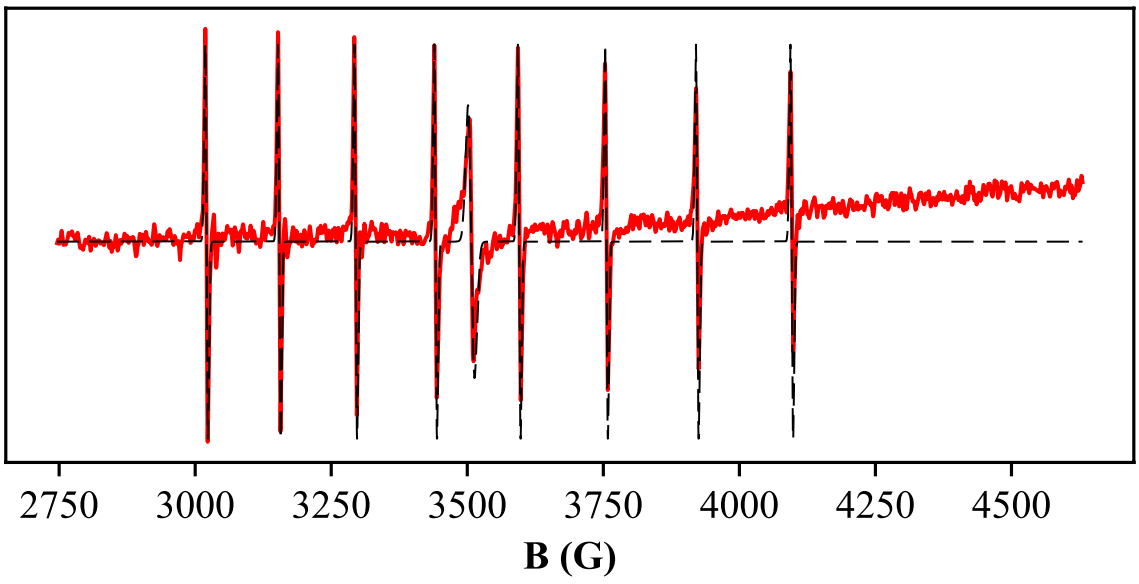

Figure 25.5. Room-temperature X-band EPR spectrum (red) and simulated spectrum (black dashes) of the products of reaction 9.5. Signals are present at $g = 1.97$, $A = 153.5$ G ($[La^{II}Cp'_3]^{1-}$) and $g = 2.00$ (an unknown species, likely electride).

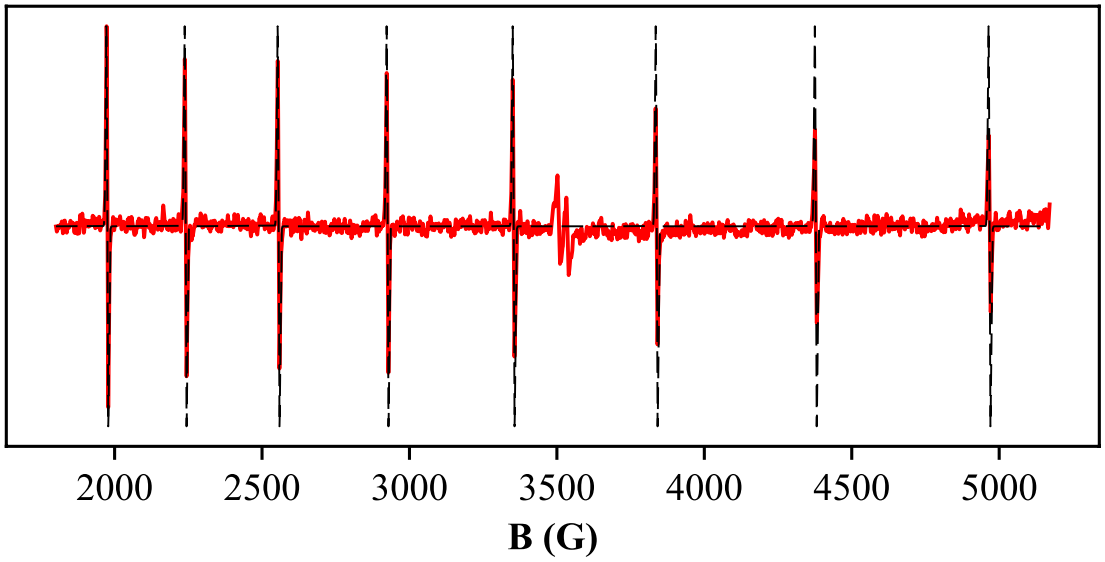

Figure 26.5. Room-temperature X-band EPR spectrum (red) and simulated spectrum (black dashes) of the products of reaction 10.5. Signals are present at $g = 1.97$, $A = 425.9$ G ($[Lu^{II}Cp'_3]^{1-}$) and ~3500 G (an unknown species).

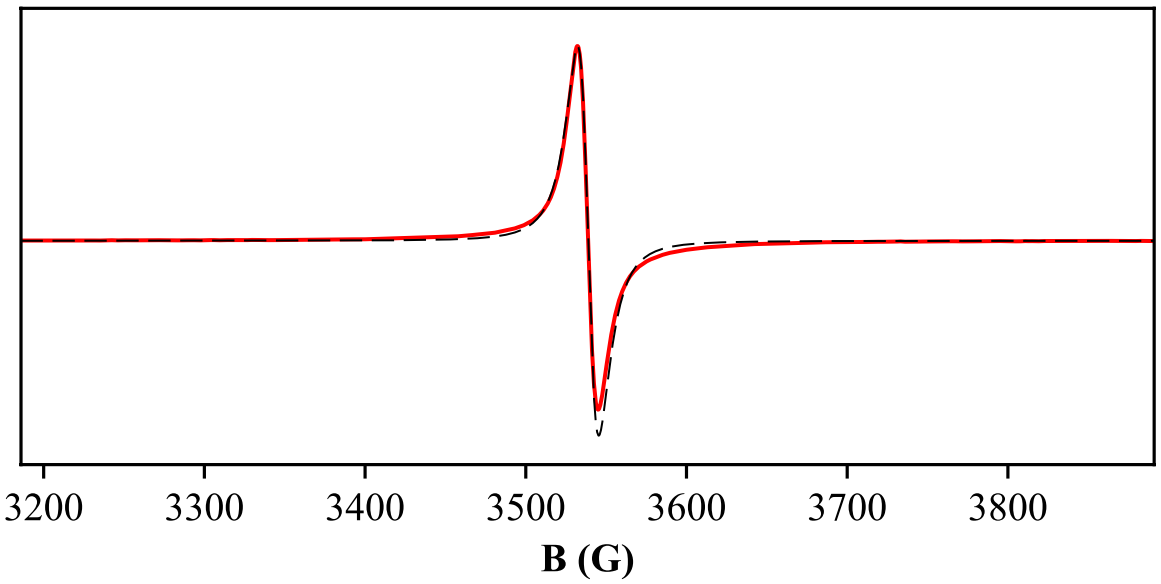

Figure 27.5. Room-temperature X-band EPR spectrum (red) and simulated spectrum (black dashes) of the products of reaction 11.5. Signal is present at $g = 1.98$ ($[Gd^{II}Cp'_3]^{1-}$).

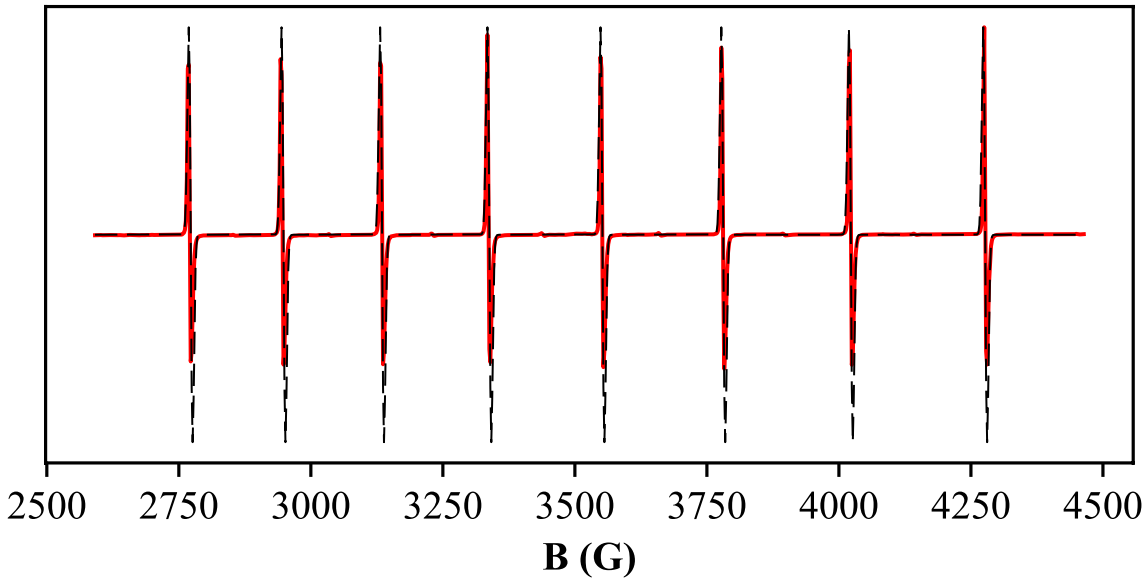

Figure 28.5. Room-temperature X-band EPR spectrum (red) and simulated spectrum (black dashes) of the products of reaction 12.5. Signal is present at $g = 1.98$, $A = 214.7$ G ($[Sc^{II}(NR_2)_3]^{1-}$).

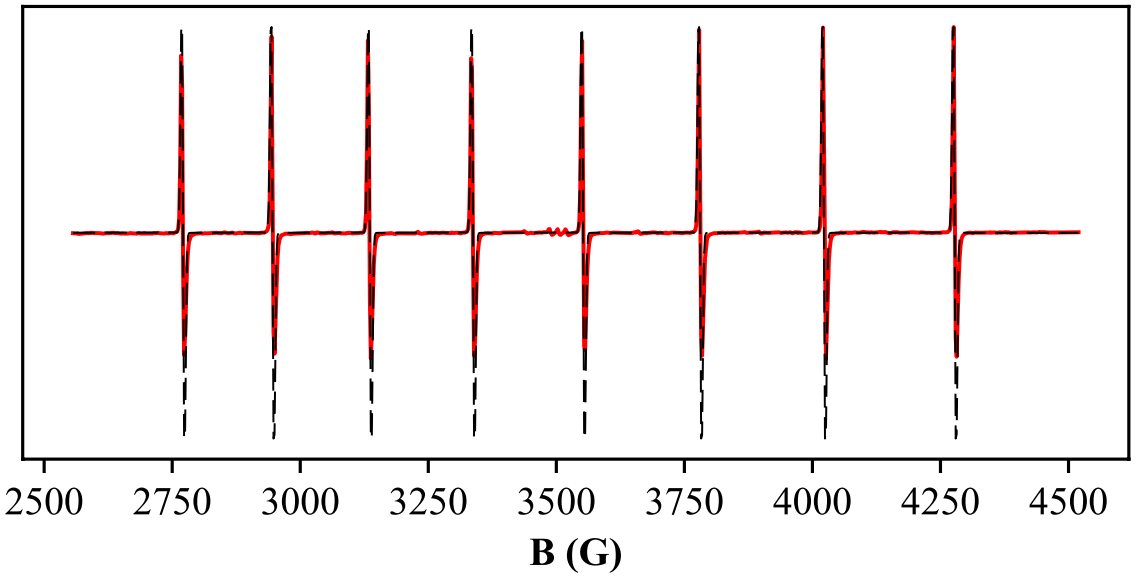

Figure 29.5. Room-temperature X-band EPR spectrum (red) and simulated spectrum (black dashes) of the products of reaction 13.5. Signal is present at $g = 1.98$, $A = 214.9$ G ($[Sc^{II}(NR_2)_3]^{1-}$). Small signals near 3500 G are not consistent with $[Y^{II}(NR_2)_3]^{1-}$ ($g = 1.97$, $A = 110.5$ G).

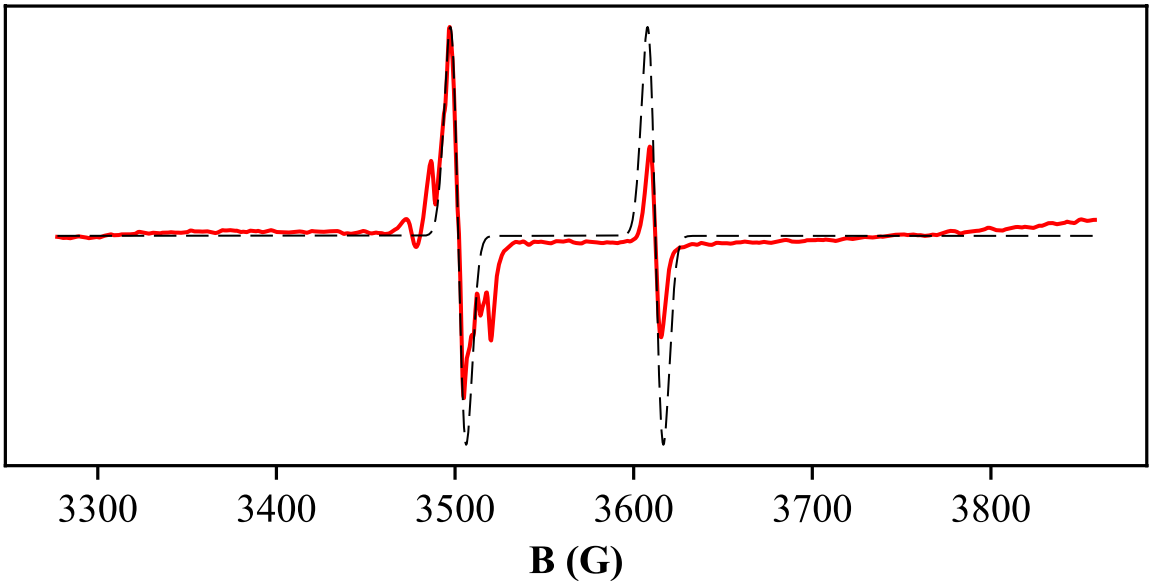

Figure 30.5. Room-temperature X-band EPR spectrum (red) and simulated spectrum (black dashes) of the products of reaction 14.5. Signal is present at $g = 1.97$, $A = 110.5$ G ($[Y^{II}(NR_2)_3]^{1-}$) with other, unsimulated signals around 3500 G (unknown species).

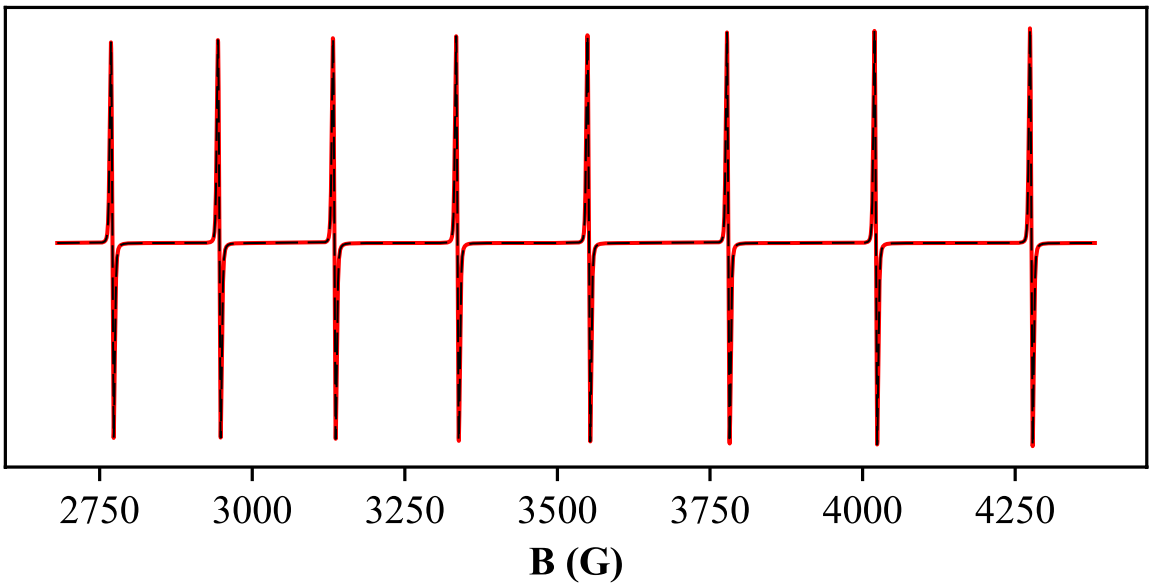

Figure 31.5. Room-temperature X-band EPR spectrum (red) and simulated spectrum (black dashes) of the products of reaction of $[Gd^{II}(NR_2)_3]^{1-}$ with $Sc^{III}(NR_2)_3$. Signal is present at $g = 1.98$, $A = 214.9$ G ($[Sc^{II}(NR_2)_3]^{1-}$).

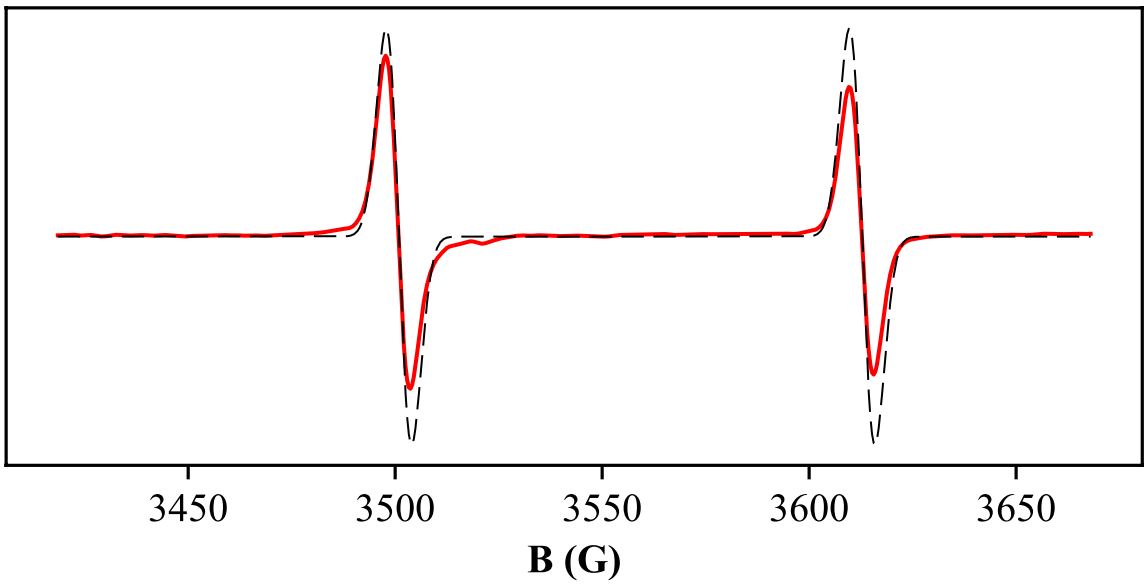

Figure 32.5. Room-temperature X-band EPR spectrum (red) and simulated spectrum (black dashes) of the products of reaction of $[Tb^{II}(NR_2)_3]^{1-}$ with $Y^{III}(NR_2)_3$. Signal is present at $g = 1.97$, $A = 111.9$ G ($[Y^{II}(NR_2)_3]^{1-}$).

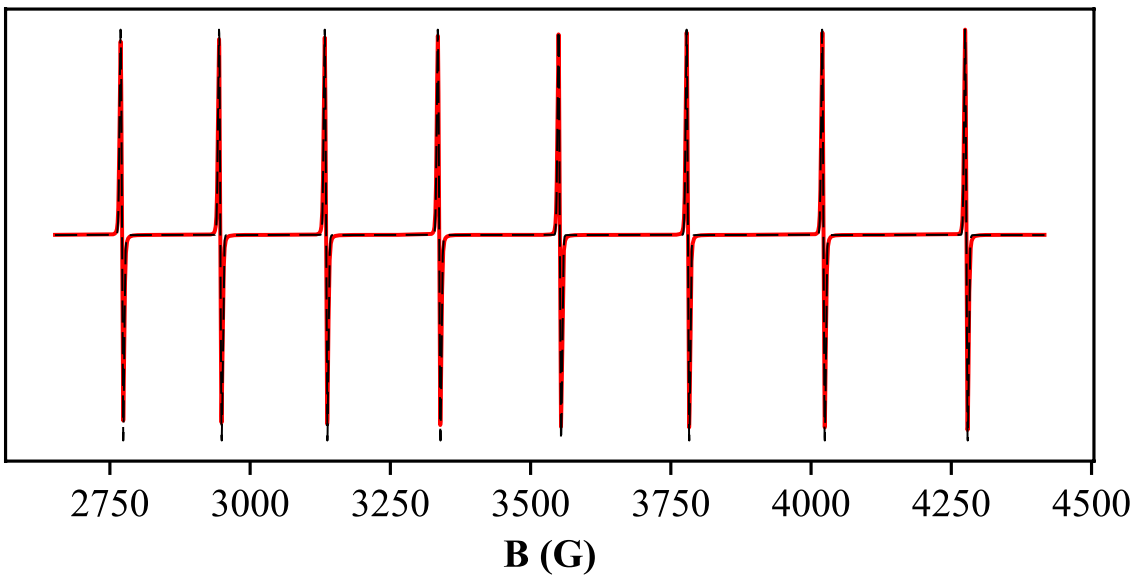

Figure 33.5. Room-temperature X-band EPR spectrum (red) and simulated spectrum (black dashes) of the products of reaction of $[Tb^{II}(NR_2)_3]^{1-}$ with $Sc^{III}(NR_2)_3$. Signal is present at $g = 1.98$, $A = 214.8$ G ($[Sc^{II}(NR_2)_3]^{1-}$).

$[Ln^{II}A_3]^{1-}$ Reactions with $Ln^{III}A'_3$ Complexes

Ln = Y

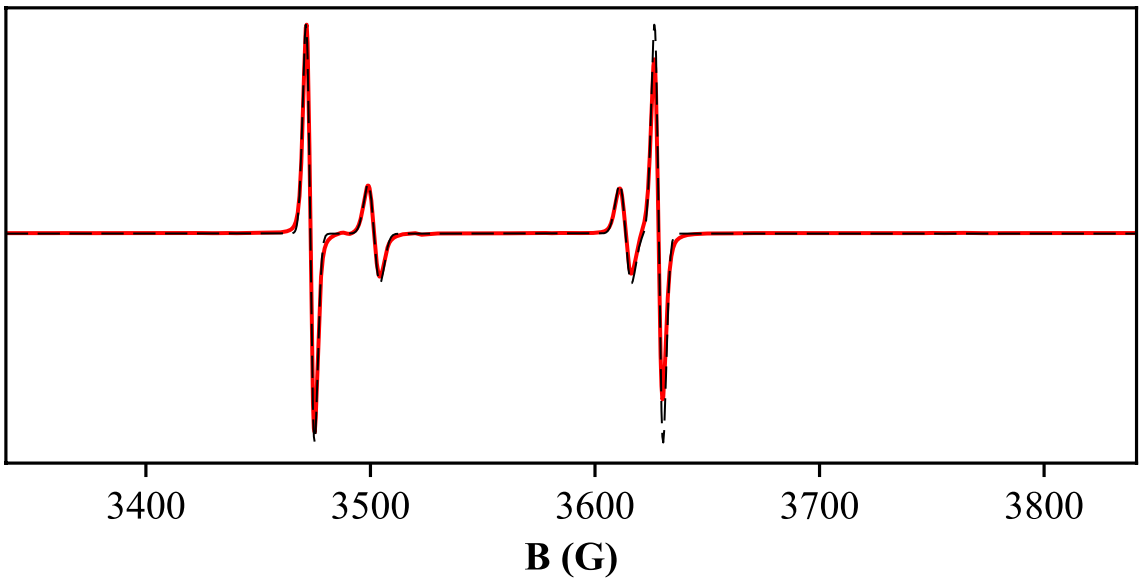

Figure 34.5. Room-temperature X-band EPR spectrum (red) and simulated spectrum (black dashes) of the products of reaction 20.5. Signals are present at $g = 1.97$, $A = 111.8$ G ($[Y^{II}(NR_2)_3]^{1-}$) and $g = 1.98$, $A = 155.1$ G ($[Y^{II}(OAr')_3]^{1-}$).

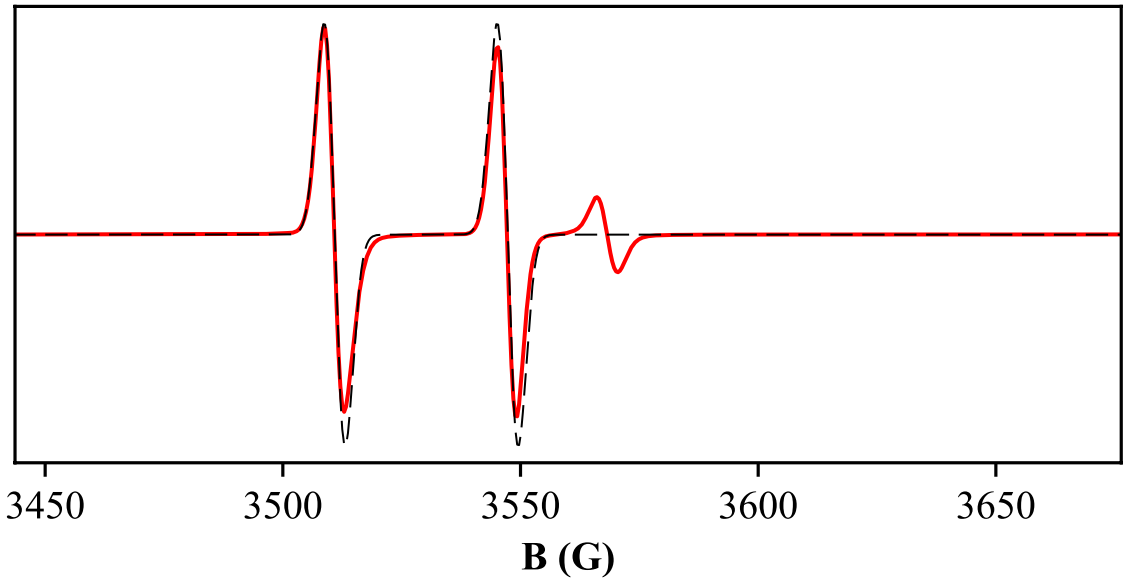

Figure 35.5. Room-temperature X-band EPR spectrum (red) and simulated spectrum (black dashes) of the products of reaction 17.5. Signals are present at $g = 1.99$, $A = 36.5$ G ($[Y^{II}Cp'_3]^{1-}$) and ~3575 G (an unknown species).

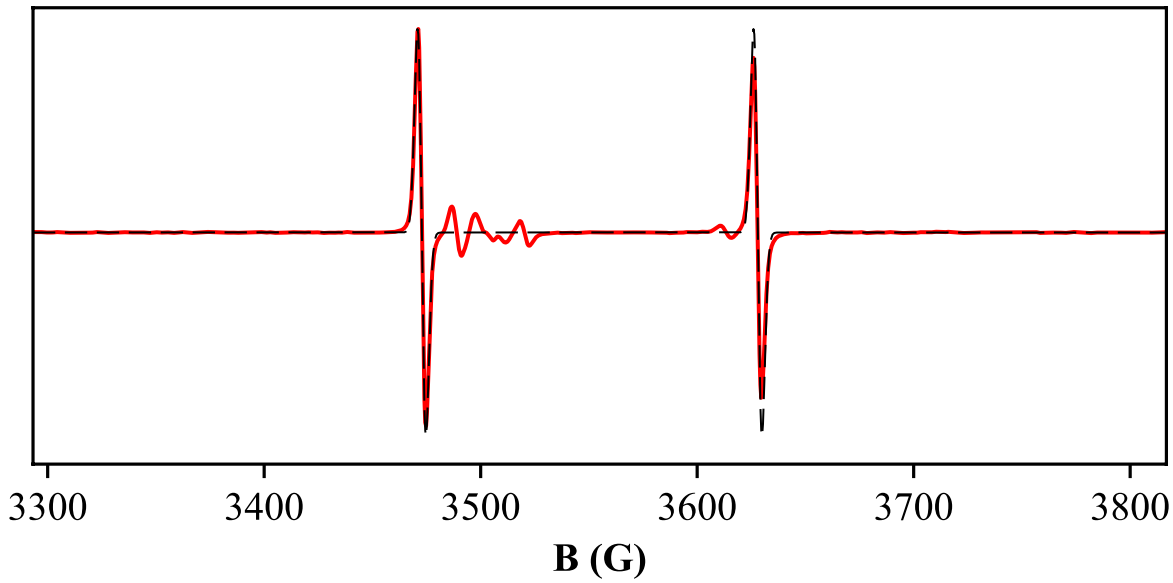

Figure 36.5. Room-temperature X-band EPR spectrum (red) and simulated spectrum (black dashes) of the products of reaction 19.5. Signals are present at $g = 1.98$, $A = 155.2$ G ($[Y^{II}(OAr)_3]^{1-}$) and ~3500 G (unknown species).

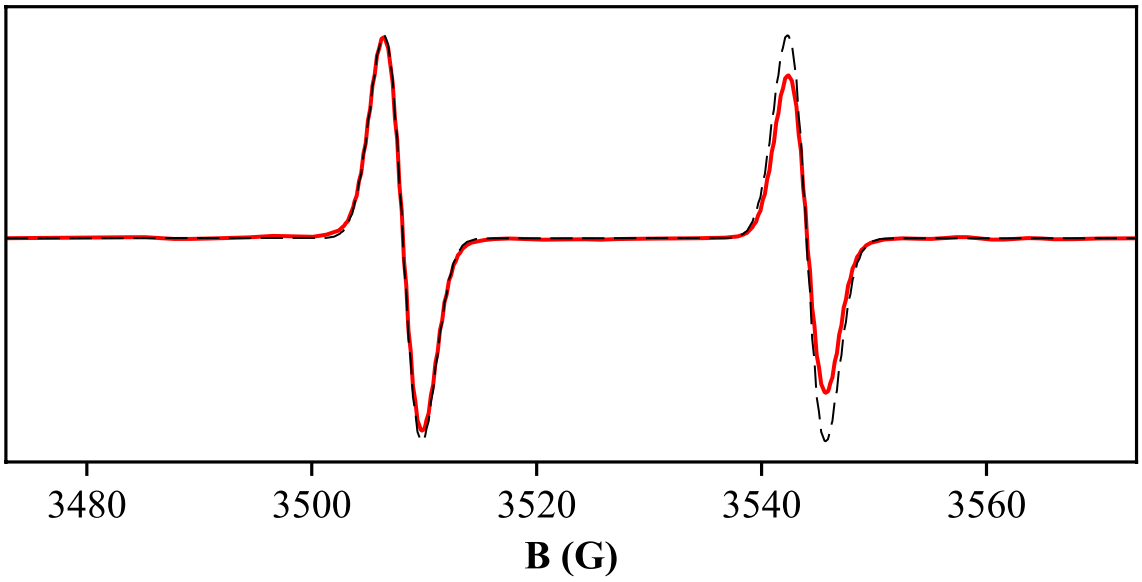

Figure 37.5. Room-temperature X-band EPR spectrum (red) and simulated spectrum (black dashes) of the products of reaction 18.5. Signals are present at $g = 1.99$, $A = 35.9$ G ($[Y^{II}Cp'_3]^{1-}$).

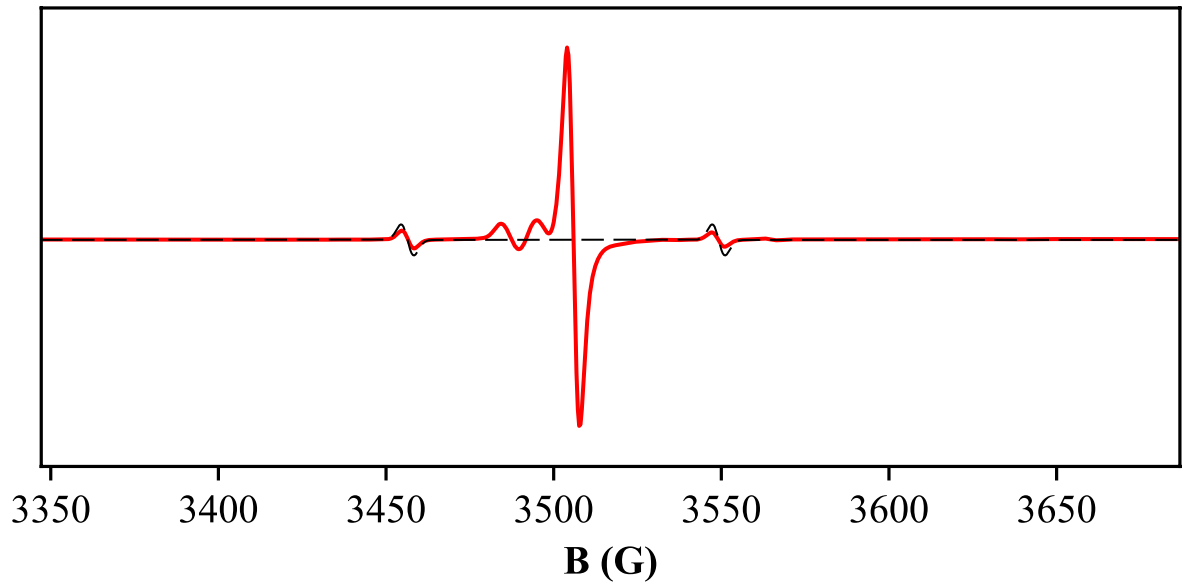

Figure 38.5. Room-temperature X-band EPR spectrum (red) and simulated spectrum (black dashes) of the products of reaction 15.5. Signals are present at $g = 2.00$ (an unknown species) and $g = 2.00$, $A = 92.8$ G (the highest A value that could be simulated for this data, an unknown Y(II) species).

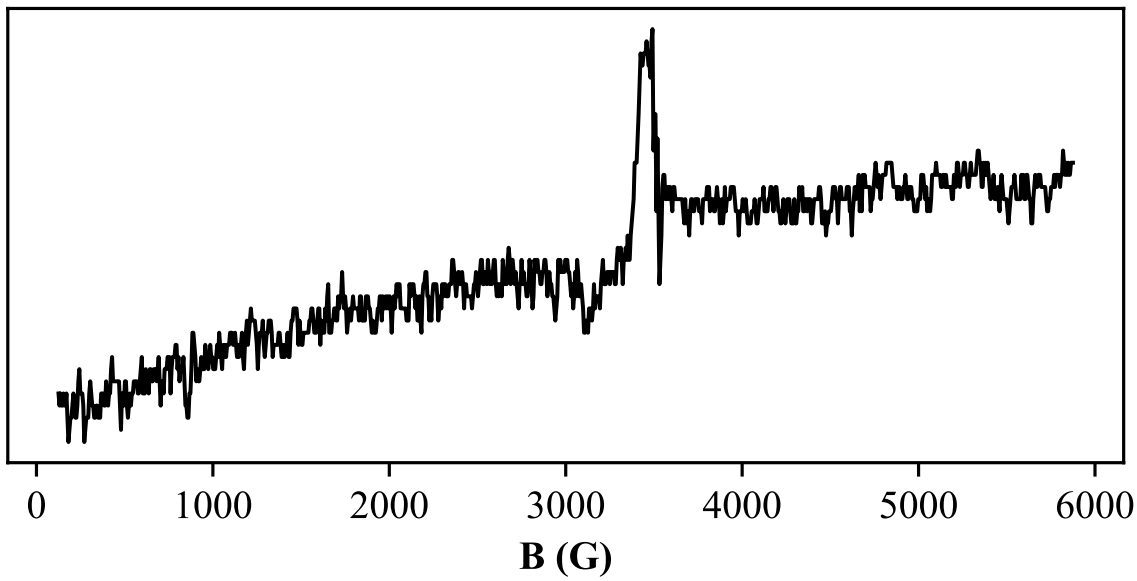

Figure 39.5. Room-temperature X-band EPR spectrum of the products of reaction 16.5. Signal is present at ~3500 G (unattributable to any Y(II) species).

Ln = Sc

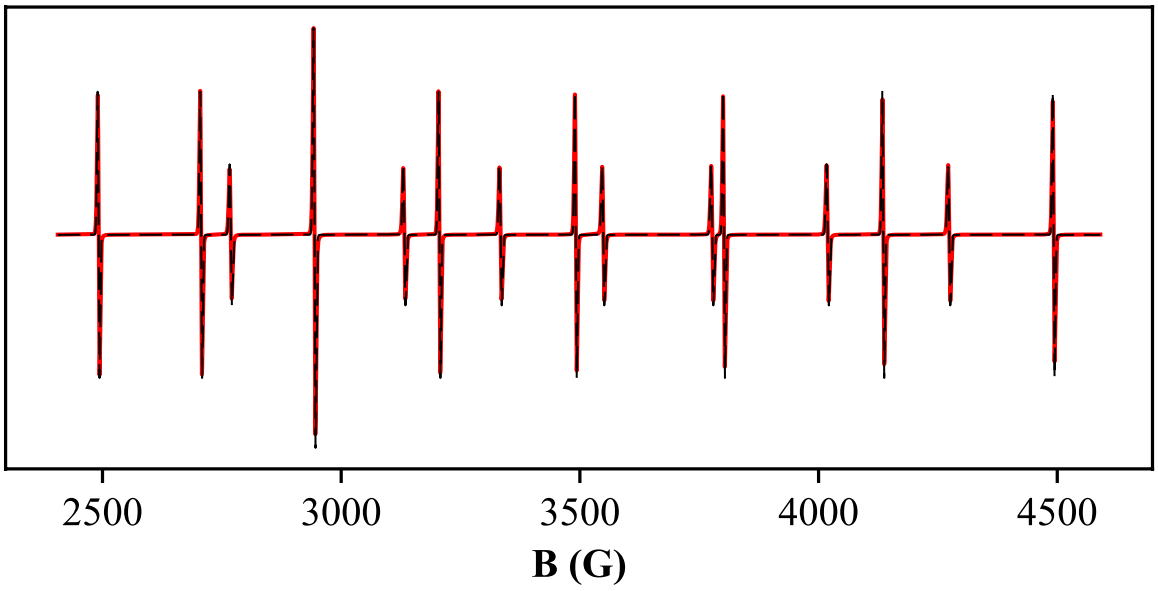

Figure 40.5. Room-temperature X-band EPR spectrum (red) and simulated spectrum (black dashes) of the products of reaction of $[Sc^{II}(OAr')_3]^{1-}$ with $Sc^{III}(NR_2)_3$. Signals are present at g = 1.98, A = 214.8 G ($[Sc^{II}(NR_2)_3]^{1-}$) and g = 1.99, A = 285.3 G ($[Sc^{II}(OAr')_3]^{1-}$).

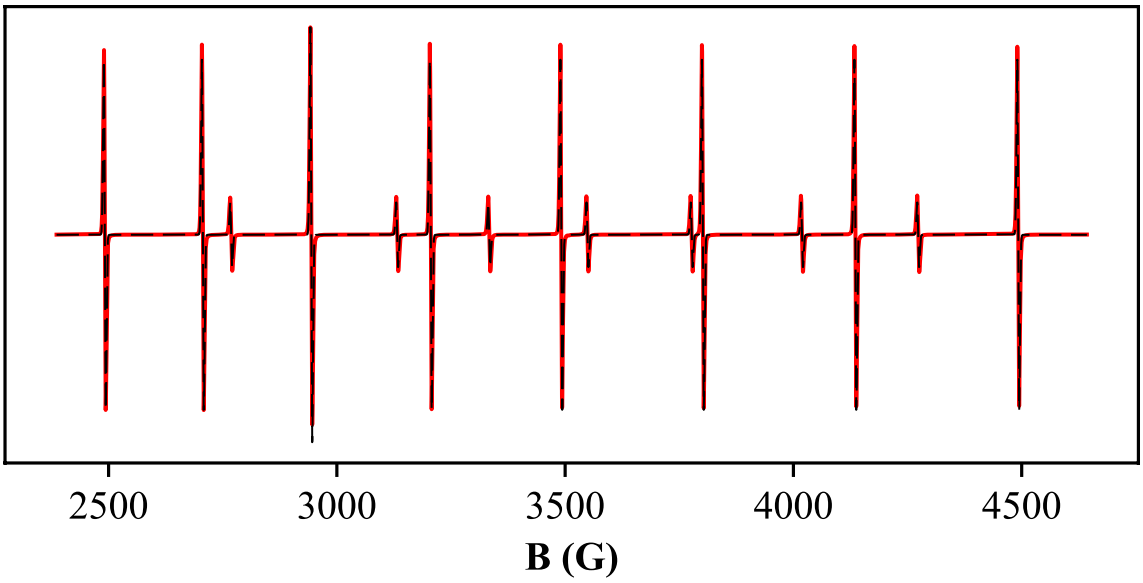

Figure 41.5. Room-temperature X-band EPR spectrum (red) and simulated spectrum (black dashes) of the products of reaction of $[Sc^{II}(NR_2)_3]^{1-}$ with $Sc^{III}(OAr')_3$. Signals are present at g = 1.98, A = 214.8 G ($[Sc^{II}(NR_2)_3]^{1-}$) and g = 1.99, A = 285.4 G ($[Sc^{II}(OAr')_3]^{1-}$).

Ln = La

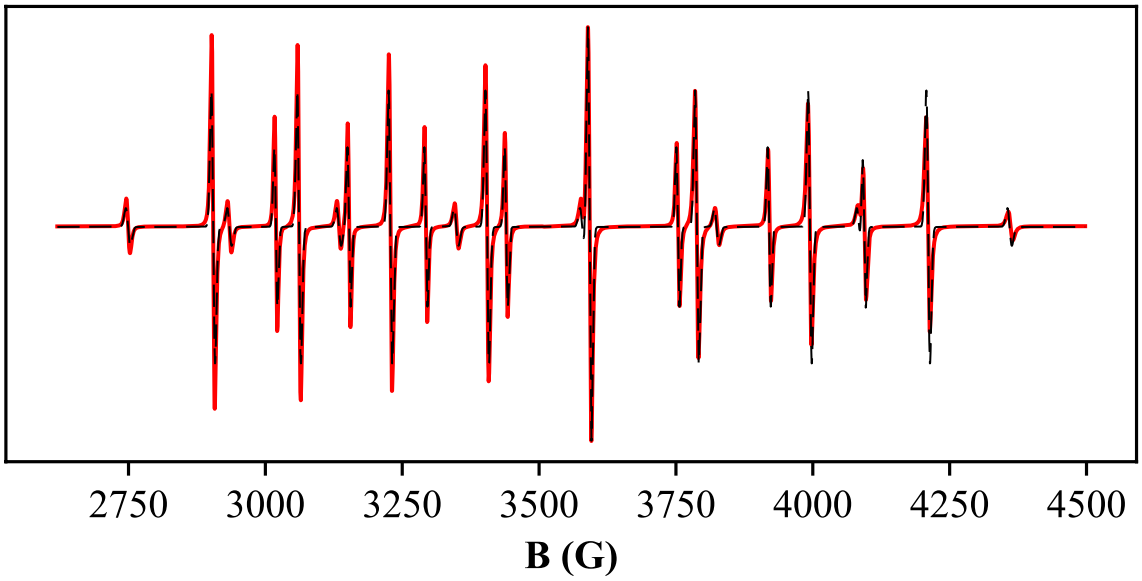

Figure 42.5. Room-temperature X-band EPR spectrum (red) and simulated spectrum (black dashes) of the products of reaction 22.5. Signals are present at $g = 1.97$, $A = 153.4$ G ($[La^{II}Cp'_3]^{1-}$), $g_A = 1.96$, $A_A = 186.5$ G (**La-A**) and $g_B = 1.96$, $A_B = 229.8$ G (**La-B**).

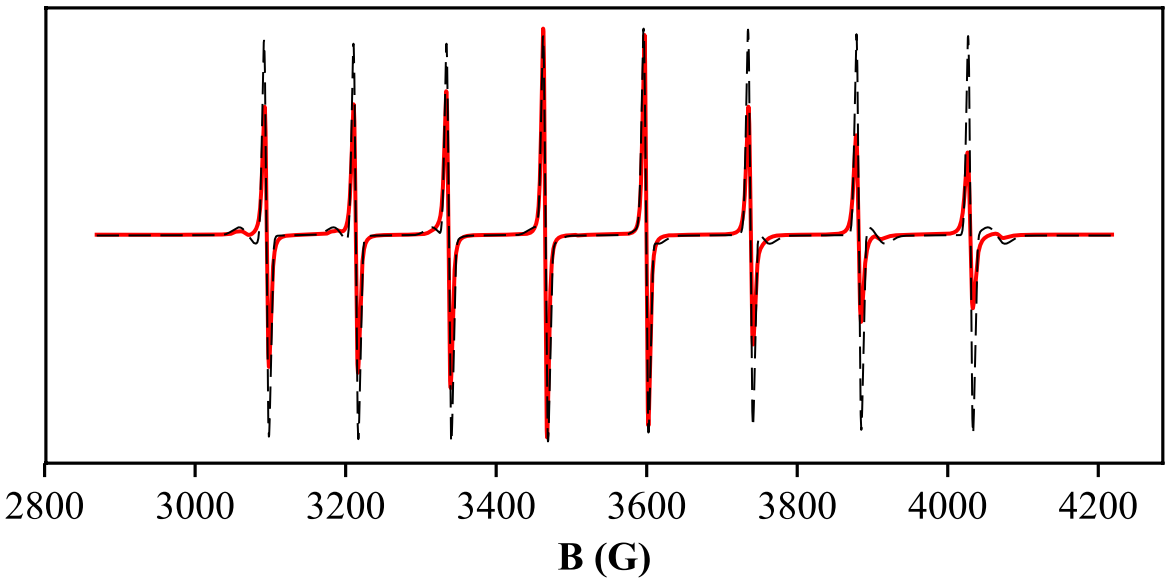

Figure 43.5. Room-temperature X-band EPR spectrum (red) and simulated spectrum (black dashes) of the products of reaction 24.5. Signals are present at $g = 1.97$, $A = 133.6$ G ($[La^{II}Cp''_3]^{1-}$) and $g = 1.96$, $A = 142.0$ G (an unknown La(II) species).

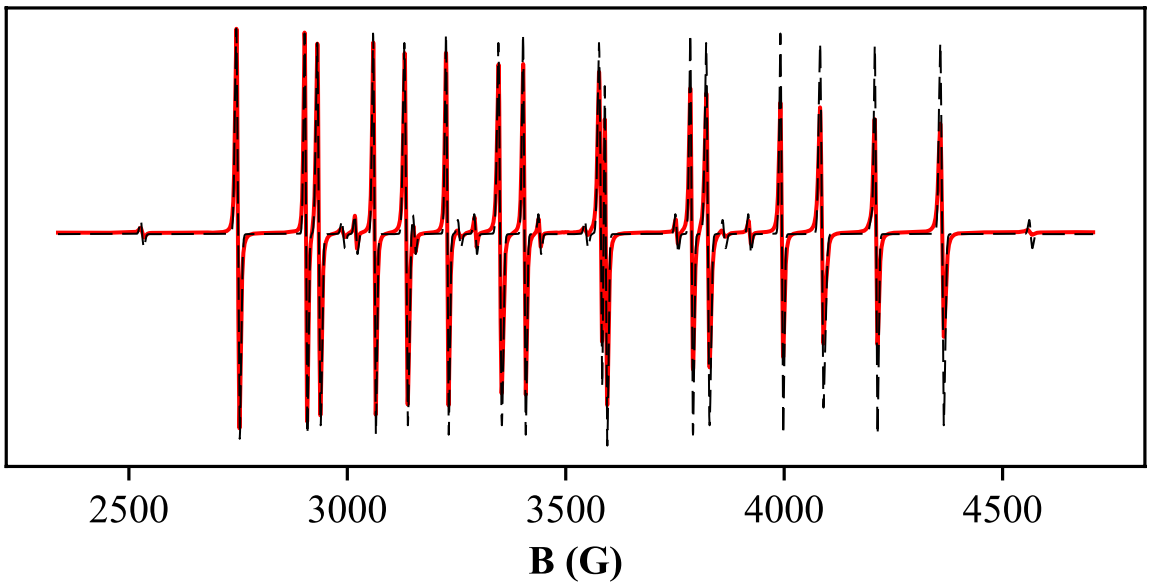

Figure 44.5. Room-temperature X-band EPR spectrum (red) and simulated spectrum (black dashes) of the products of reaction 23.5. Signals are present at $g = 1.97$, $A = 153.4$ G ($[La^{II}Cp'_3]^{1-}$), $g_A = 1.96$, $A_A = 186.3$ G (**La-A**), $g_B = 1.96$, $A_B = 230.0$ G (**La-B**), and $g = 1.96$, $A = 290.1$ G ($[La^{II}Cp^{tet}_3]^{1-}$).

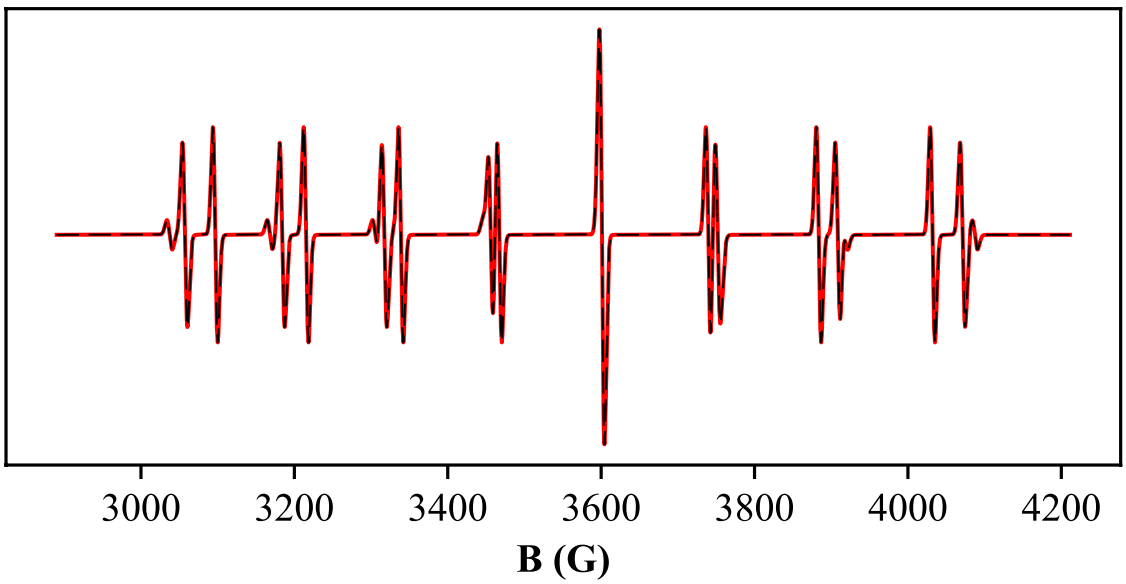

Figure 45.5. Room-temperature X-band EPR spectrum (red) and simulated spectrum (black dashes) of the products of reaction 25.5. Signals are present at $g = 1.96$, $A = 133.6$ G ($[La^{II}Cp''_3]^{1-}$), $g_C = 1.96$, $A_C = 144.8$ G (**La-C**) and $g_D = 1.96$, $A_D = 150.0$ G (**La-D**).

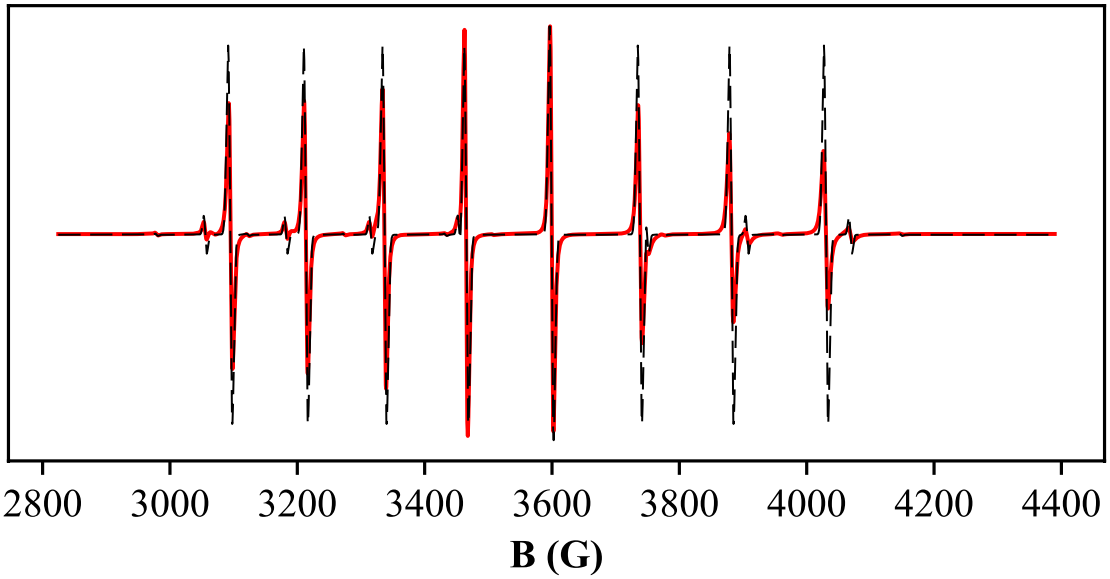

Figure 46.5. Room-temperature X-band EPR spectrum (red) and simulated spectrum (black dashes) of the products of reaction of $[La^{II}Cp''_3]^{1-}$ with $La^{III}Cp^{tet}_3$. Signals are present at $g = 1.97$, $A = 133.6$ G ($[La^{II}Cp''_3]^{1-}$), $g_1 = 1.96$, $A_1 = 144.7$ G (an unknown La(II) species) and $g_2 = 1.96$, $A_2 = 166.9$ G (an unknown La(II) species).

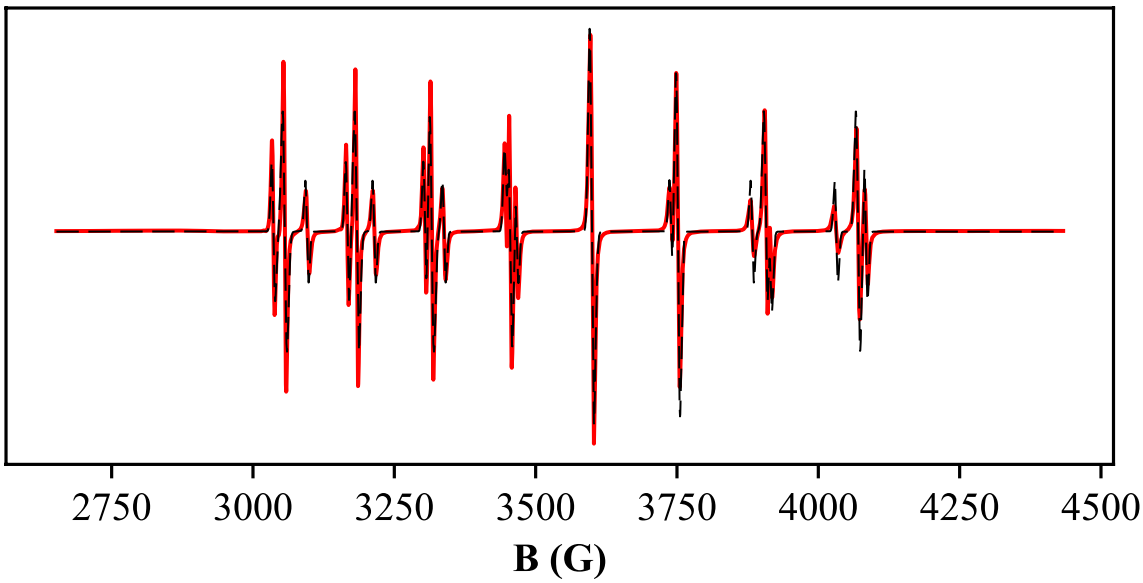

Figure 47.5. Room-temperature X-band EPR spectrum (red) and simulated spectrum (black dashes) of the products of reaction 26.5. Signals are present at $g = 1.96$, $A = 133.7$ G ($[La^{II}Cp''_3]^{1-}$), $g_C = 1.96$, $A_C = 144.8$ G (**La-C**) and $g_D = 1.97$, $A_D = 149.6$ G (**La-D**).

$[La^{II}Cp''_3]^{1-}$ + KA : Ligand Exchange Reactions.

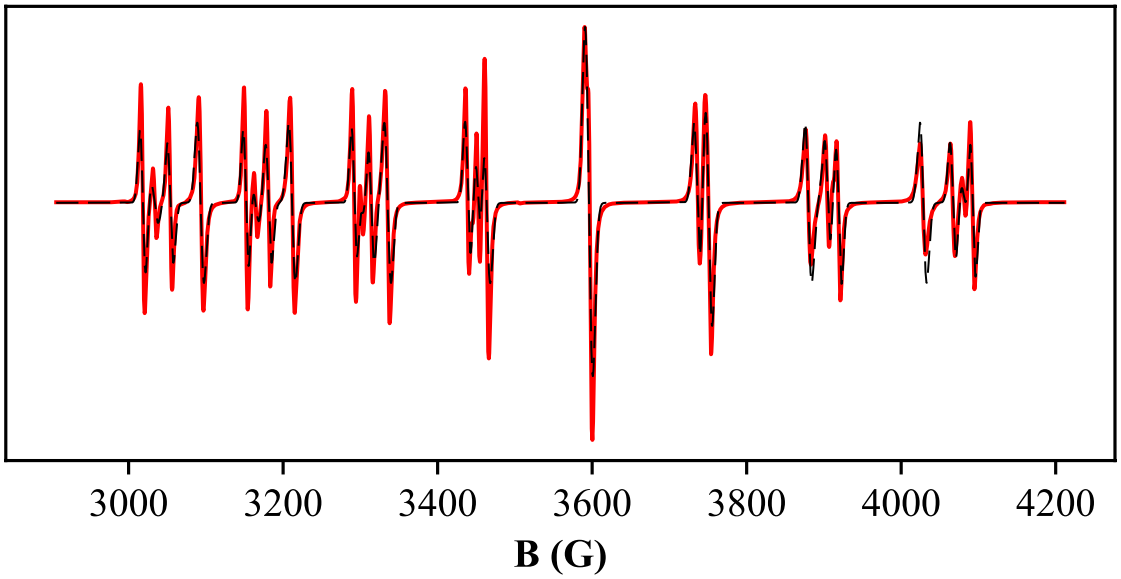

Figure 48.5. Room-temperature X-band EPR spectrum (red) and simulated spectrum (black dashes) of the products of reaction 27.5. Signals are present at $g = 1.97$, $A = 133.6$ G ($[La^{II}Cp''_3]^{1-}$), $g_C = 1.97$, $A_C = 144.6$ G (**La-C**) and $g_D = 1.97$, $A_D = 149.7$ G (**La-D**), and $g = 1.97$, $A = 153.4$ G ($[La^{II}Cp'_3]^{1-}$).

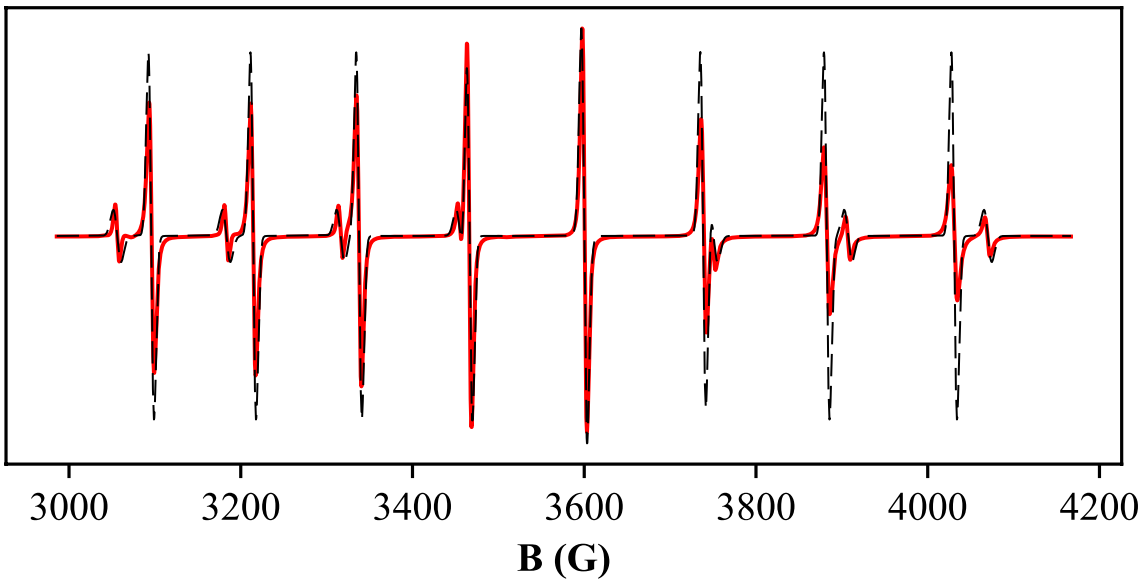

Figure 49.5. Room-temperature X-band EPR spectrum (red) and simulated spectrum (black dashes) of the products of reaction 28.5. Signals are present at $g = 1.97$, $A = 133.6$ G ($[La^{II}Cp''_3]^{1-}$) and $g = 1.96$, $A = 144.8$ G (an unknown La(II) species).

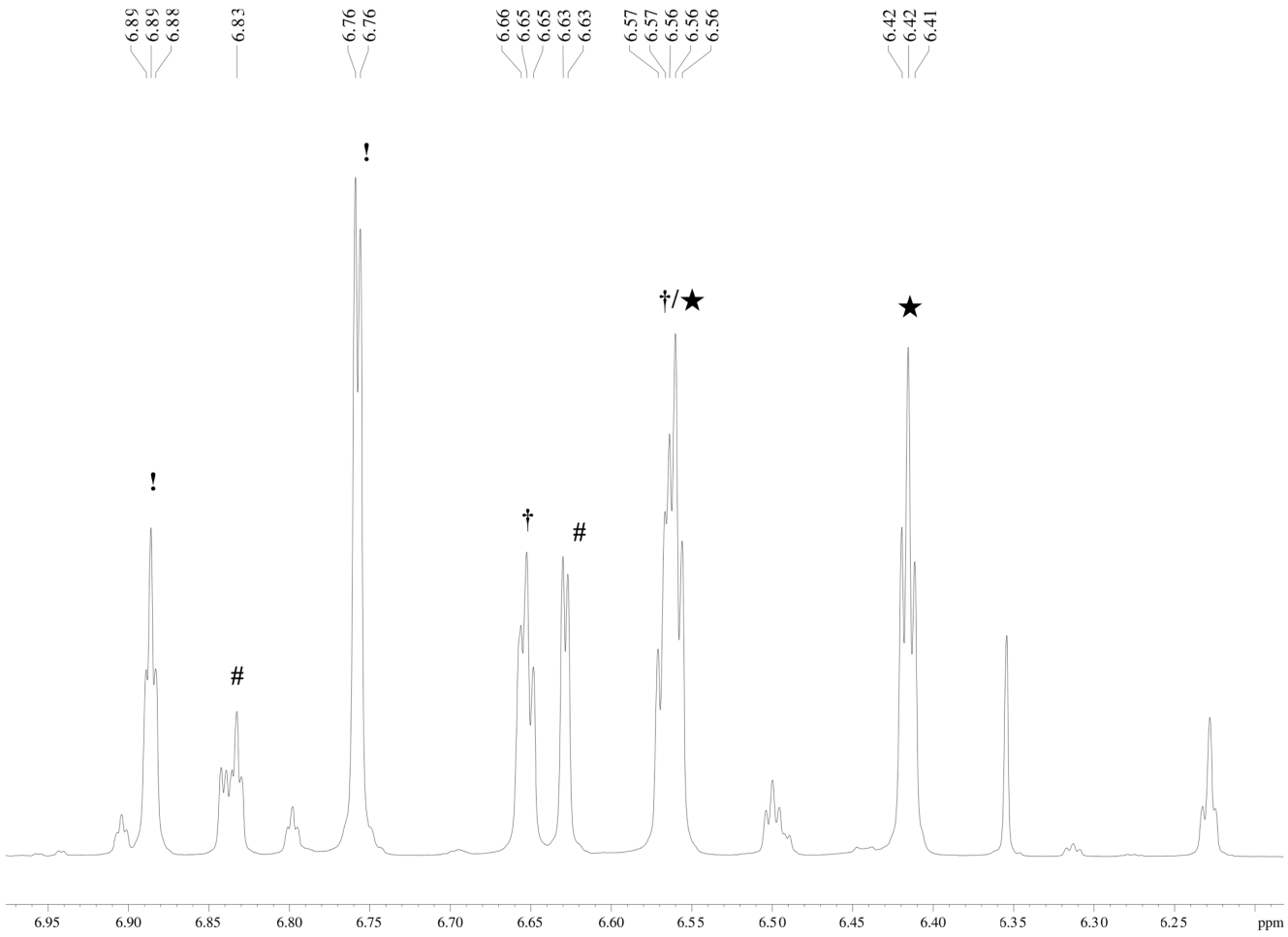

Figure 50.5. ^{1}H NMR spectrum of a 1:1 equimolar mixture of $La^{III}Cp''_3$ with $La^{III}Cp'_3(THF)$ in C_6D_6. ! =new Cp″ resonance, # = new Cp″ resonance, † = new Cp′ resonance, ★ = new Cp′ resonance. Multiplet at ~6.56 ppm is two overlapping Cp′ signals.

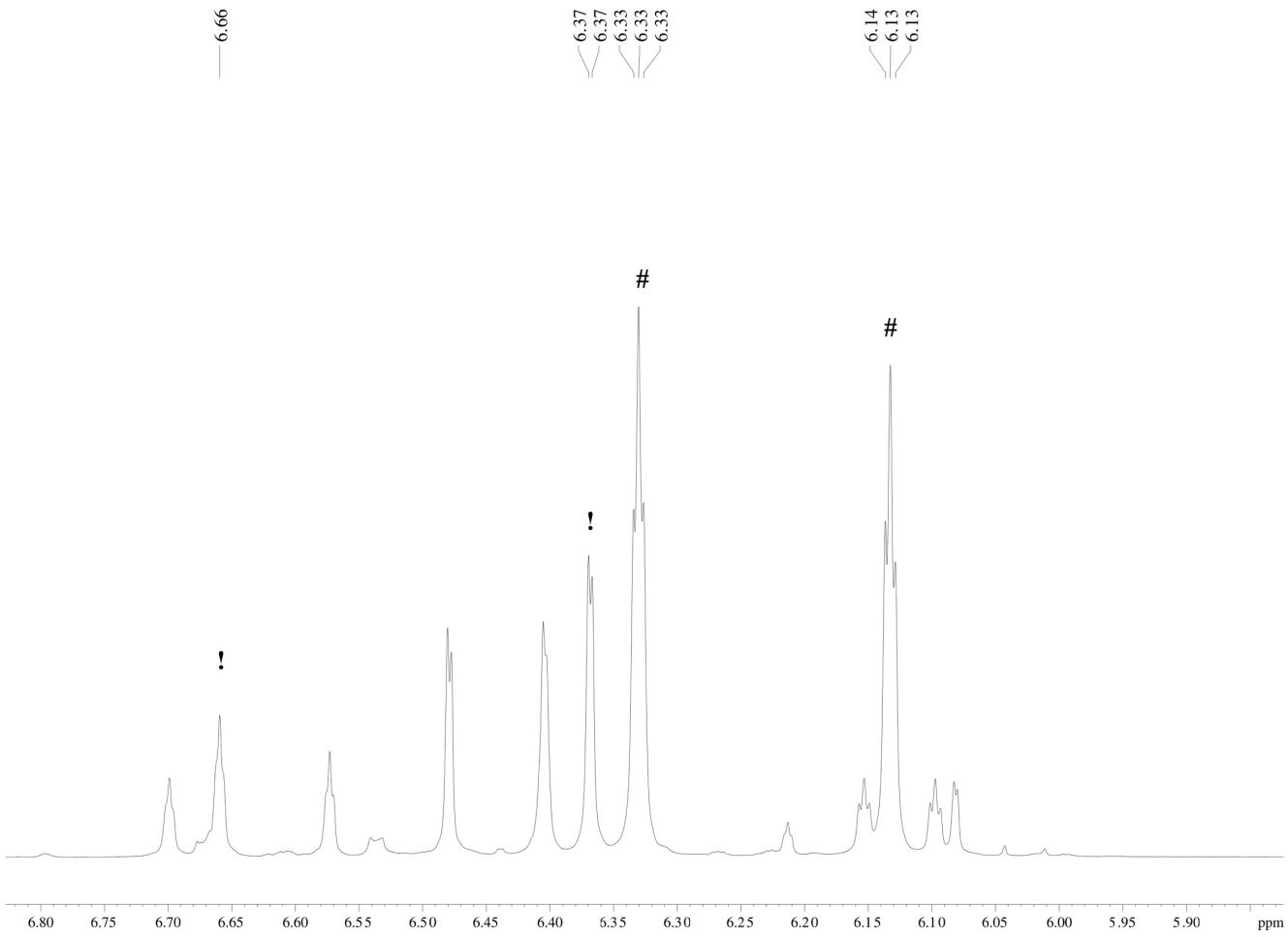

Figure 51.5. ^{1}H NMR spectrum of a 1:1 equimolar mixture of $La^{III}Cp''_3$ with $La^{III}Cp'_3(THF)$ in THF-d_8. ! =new Cp″ resonance, # = new Cp′ resonance.

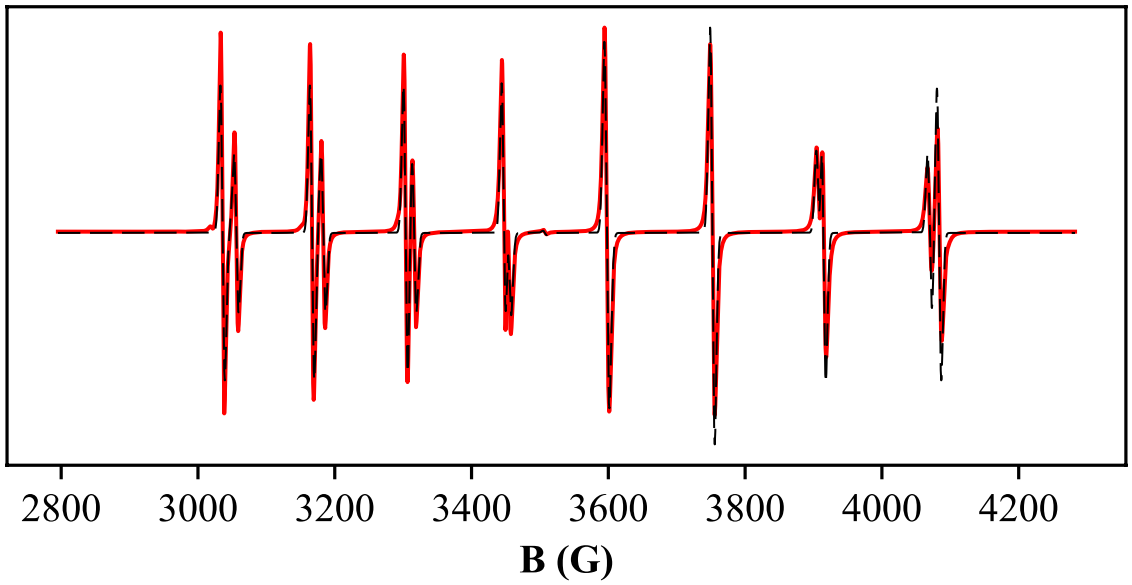

Figure 52.5. Room-temperature X-band EPR spectrum (red) and simulated spectrum (black dashes) of the products of the reduction of a 1:1 equimolar mixture of $La^{III}Cp''_3$ with $La^{III}Cp'_3(THF)$ and 1 equiv of crypt in THF-d_8. Signals are present at $g_C = 1.96$, $A_C = 144.8$ G (**La-C**), $g_D = 1.97$, $A_D = 149.6$ G (**La-D**), and $g = 2.00$ (an unknown species, likely electride).

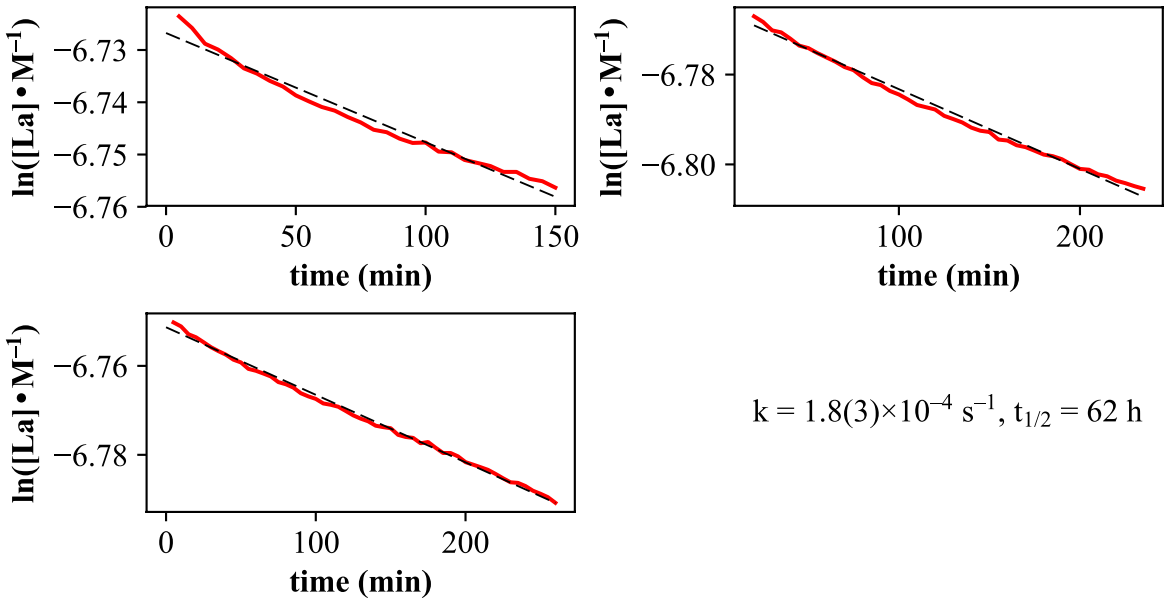

Figure 53.5. First-order kinetics plots for the determination of the rate constant for thermal decomposition of [K(crypt)][La^{II}Cp′$_3$] in THF at room temperature. [La] = concentration of [K(crypt)][La^{II}Cp′$_3$] in M.

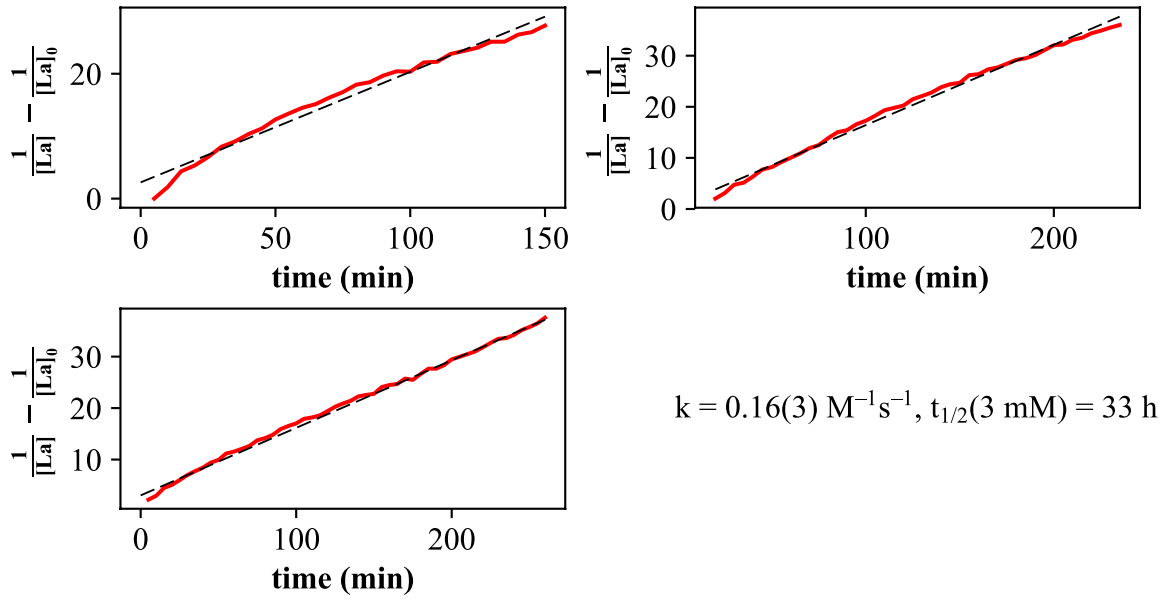

Figure 54.5. Second-order kinetics plots for the determination of the rate constant for thermal decomposition of [K(crypt)][La^{II}Cp′$_3$] in THF at room temperature. [La] = concentration of [K(crypt)][La^{II}Cp′$_3$] in M; $[La]_0$ = initial concentration of [K(crypt)][La^{II}Cp′$_3$] in M.

REFERENCES

(1) Hitchcock, P. B.; Lappert, M. F.; Maron, L.; Protchenko, A. V. *Angew. Chem. Int. Ed.* **2008**, *47*, 1488–1491.
(2) MacDonald, M. R.; Ziller, J. W.; Evans, W. J. *J. Am. Chem. Soc.* **2011**, *133*, 15914–15917.
(3) MacDonald, M. R.; Bates, J. E.; Fieser, M. E.; Ziller, J. W.; Furche, F.; Evans, W. J. *J. Am. Chem. Soc.* **2012**, *134*, 8420–8423.
(4) MacDonald, M. R.; Bates, J. E.; Ziller, J. W.; Furche, F.; Evans, W. J. *J. Am. Chem. Soc.* **2013**, *135*, 9857–9868.
(5) Fieser, M. E.; MacDonald, M. R.; Krull, B. T.; Bates, J. E.; Ziller, J. W.; Furche, F.; Evans, W. J. *J. Am. Chem. Soc.* **2015**, *137*, 369–382.
(6) Woen, D. H.; Chen, G. P.; Ziller, J. W.; Boyle, T. J.; Furche, F.; Evans, W. J. *Angew. Chem. Int. Ed.* **2017**, *56* (8), 2050–2053.
(7) Evans, W. J. *Organometallics* **2016**, *35*, 3088–3100.
(8) Woen, D. H.; Evans, W. J. Expanding the + 2 Oxidation State of the Rare-Earth Metals, Uranium, and Thorium in Molecular Complexes. In *Handbook on the Physics and Chemistry of Rare Earths*; Elsevier, 2016; Vol. 50, p 337–394.
(9) Gould, C. A.; McClain, K. R.; Yu, J. M.; Groshens, T. J.; Furche, F.; Harvey, B. G.; Long, J. R. *J. Am. Chem. Soc.* **2019**, *141*, 12967–12973.
(10) Kelly, R. P.; Maron, L.; Scopelliti, R.; Mazzanti, M. *Angew. Chem. Int. Ed.* **2017**, *56*, 15663–15666.
(11) Fieser, M. E.; Palumbo, C. T.; La Pierre, H. S.; Halter, D. P.; Voora, V. K.; Ziller, J. W.; Furche, F.; Meyer, K.; Evans, W. J. *Chem. Sci.* **2017**, *8*, 7424–7433.
(12) Ryan, A. J.; Darago, L. E.; Balasubramini, S. G.; Chen, G. P.; Ziller, J. W.; Furche, F.; Long, J. R.; Evans, W. J. *Chem. Eur. J.* **2018**, *24*, 7702–7709.
(13) Moehring, S. A.; Beltrán-Leiva, M. J.; Páez-Hernández, D.; Arratia-Pérez, R.; Ziller, J. W.; Evans, W. J. *Chem. Eur. J.* **2018**, *24*, 18059–18067.
(14) Jenkins, T. F.; Woen, D. H.; Mohanam, L. N.; Ziller, J. W.; Furche, F.; Evans, W. J. *Organometallics* **2018**, *37*, 3863–3873.
(15) Angadol, M. A.; Woen, D. H.; Windorff, C. J.; Ziller, J. W.; Evans, W. J. *Organometallics* **2019**, *38* (5), 1151–1158.
(16) Huh, D. N.; Ziller, J. W.; Evans, W. J. *Dalt. Trans.* **2018**, *47* (48), 17285–17290.
(17) Woen, D. H.; Huh, D. N.; Ziller, J. W.; Evans, W. J. *Organometallics* **2018**, *37*, 3055–3063.
(18) Electrochemical Series. In *CRC Handbook of Chemistry and Physics, 100th Edition (Internet Verison 2019)*; John R. Rumble, Ed.; CRC Press/Taylor & Francis: Boca Raton, FL.
(19) Huang, R. H.; Faber, M. K.; Moeggenborg, K. J.; Ward, D. L.; Dye, J. L. *Nature* **1988**, *331*, 599–601.
(20) Dye, J. L. *Science* **1990**, *247* (4943), 663–668.
(21) Bochkarev, M. N.; Fagin, A. A. *Chem. Eur. J.* **1999**, *5* (10), 2990–2992.
(22) Stoll, S.; Schweiger, A. *J. Magn. Reson.* **2006**, *178*, 42–55.
(23) Palumbo, C. T.; Darago, L. E.; Windorff, C. J.; Ziller, J. W.; Evans, W. J. *Organometallics* **2018**, *37*, 900–905.
(24) Evans, W. J. .; Drummond, D. K.; Zhang, H.; Atwood, J. L. *Inorg. Chem.* **1988**, *27* (3), 575–579.
(25) Tilley, T. D.; Andersen, R. A.; Zalkin, A. *Inorg. Chem.* **1984**, *23*, 2271–2276.
(26) Ryan, A. J.; Ziller, J. W.; Evans, W. J. *Submitted* **2019**.

(27) Fang, M.; Lee, D. S.; Ziller, J. W.; Doedens, R. J.; Bates, J. E.; Furche, F.; Evans, W. J. *J. Am. Chem. Soc.* **2011**, *133*, 3784–3787.
(28) Corbey, J. F.; Woen, D. H.; Palumbo, C. T.; Fieser, M. E.; Ziller, J. W.; Furche, F.; Evans, W. J. *Organometallics* **2015**, *34*, 3909–3921.
(29) Kotyk, C. M.; Macdonald, M. R.; Ziller, J. W.; Evans, W. J. *Organometallics* **2015**, *34*, 2287–2295.
(30) Cristina Cassani, M.; Lappert, M. F.; Laschi, F. *Chem. Commun.* **1997**, 1563–1564.
(31) Finke, R. G.; Keenan, S. R.; Schiraldi, D. A.; Watson, P. L. *Organometallics* **1986**, *5*, 598–601.
(32) Anderson, L. B.; Macero, D. J. *J. Phys. Chem.* **1963**, *67*, 1942.
(33) Evans, W. J.; Gummersheimer, T. S.; Ziller, J. W. *J. Am. Chem. Soc.* **1995**, *117*, 8999–9002.
(34) Evans, W. J.; Hunter, W. E.; Grate, J. W.; Choi, H. W.; Bloom, I.; Atwood, J. L. *J. Am. Chem. Soc.* **1985**, *107*, 941–946.
(35) Evans, W. J.; Hughes, L. A.; Hanusa, T. P. *J. Am. Chem. Soc.* **1984**, *106*, 4270–4272.
(36) Evans, W. J.; Keyer, R. A.; Ziller, W. *J. Organomet. Chem.* **1990**, *394*, 87–97.
(37) Bochkarev, M. N.; Fedushkin, I. L.; Fagin, A. A.; Petrovskaya, T. V.; Ziller, J. W.; Broomhall-Dillard, R. N. R.; Evans, W. J. *Angew. Chem. Int. Ed.* **1997**, *36*, 133–135.
(38) Evans, W. J.; Lee, D. S.; Lie, C.; Ziller, J. W. *Angew. Chem. Int. Ed.* **2004**, *43*, 551– – 5519.
(39) Evans, W. J.; Allen, N. T.; Ziller, J. W. *Angew. Chem. Int. Ed. Ed.* **2002**, *41* (2), 359–361.
(40) Huh, D. N.; Ziller, J. W.; Evans, W. J. *Inorg. Chem.* **2018**, *57*, 11809–11814.
(41) Evans, W. J.; Ulibarri, T. A. *J. Am. Chem. Soc.* **1987**, *109*, 4292–4297.
(42) Boyle, T. J.; Ottley, L. A. M. *Chem. Rev.* **2008**, *108* (6), 1896–1917.
(43) Evans, W. J.; Walensky, J. R.; Champagne, T. M.; Ziller, J. W.; Dipasquale, A. G.; Rheingold, A. L. *J. Organomet. Chem.* **2009**, *694*, 1238–1243.
(44) Peterson, J. K.; MacDonald, M. R.; Ziller, J. W.; Evans, W. J. *Organometallics* **2013**, *32*, 2625–2631.
(45) Bradley, D. C.; Ghotra, J. S.; Hart, F. A. *J. Chem. Soc., Dalton Trans.* **1972**, 1021–1023.
(46) Steele, L. A. M.; Boyle, T. J.; Kemp, R. A.; Moore, C. *Polyhedron* **2012**, *42* (1), 258–264.
(47) Schumann, H.; Glanz, M.; Hemling, H.; Hahn, F. E. *Z. Anorg. Allg. Chem.* **1995**, *621*, 341–345.
(48) Laschi, F.; Hitchcock, P. B.; Gun'ko, Y. K.; Cassani, M. C.; Lappert, M. F. *Organometallics* **1999**, *18*, 5539–5547.
(49) Bergbreiter, D. E.; Killough, J. M. *J. Am. Chem. Soc.* **1978**, *100* (7), 2126–2134.